Active X-ray optics for the next generation of X-ray space telescopes

Carolyn Atkins

Thesis submitted for the Degree of Doctor of Philosophy
of the University College London

Department of Physics & Astronomy
UNIVERSITY COLLEGE LONDON

October 2009

I, Carolyn Atkins, confirm that the work presented in this thesis is my own. Where information has been derived from other sources, I confirm that this has been indicated in the thesis.

To my parents, with love.

”I showed my masterpiece to the grown-ups and asked them if my drawing frightened them. They answered: ‘Why should anyone be frightened by a hat?’ My drawing did not represent a hat. It was supposed to be a boa constrictor digesting an elephant. So I made another drawing of the inside of the boa constrictor to enable the grown-ups to understand. They always need explanations. . . . ”

— Antoine de Saint-Exupéry (1944)

ABSTRACT

Described within is the design, manufacture, metrology and X-ray testing of an active X-ray prototype intended for the next generation of X-ray telescopes. One of the challenges faced by the X-ray telescope community is how to combine high resolution and high sensitivity into one system, as weight limitations place constraints on the optics that can be launched. Therefore the mandate of the active X-ray prototype is to provide high sensitivity through the ability of the optics to be nested and to deliver high angular resolution through the active control of the optic's form. Piezoelectric unimorph actuators provide the active component: it is intended that they will correct for figure errors within the optic and therefore increase the angular resolution capability.

The prototype's design is based upon an ellipsoidal segment which provides point-to-point focussing of an X-ray source. The prototype itself is composed of an electroformed nickel optic where the non-reflective surface is populated with 30 piezoelectric actuators and it is the production of the prototype that is the core of the presented research. Metrology of the actuators' influence functions is presented and highlight the prototype's ability to deform its optic surface by microns. In addition, the measured influence functions are compared against finite element models and a distinct similarity between the functions is observed.

The prototype was tested at an X-ray beamline facility in November 2008 and the results showed the prototype's ability to correct the optic to achieve an improved angular resolution: from 0.786 arc-minutes to 0.686 arc-minutes in terms of full width half maximum. Finally, difficulties in the manufacture of the prototype and X-ray testing shall be presented alongside future work in conclusion to this thesis

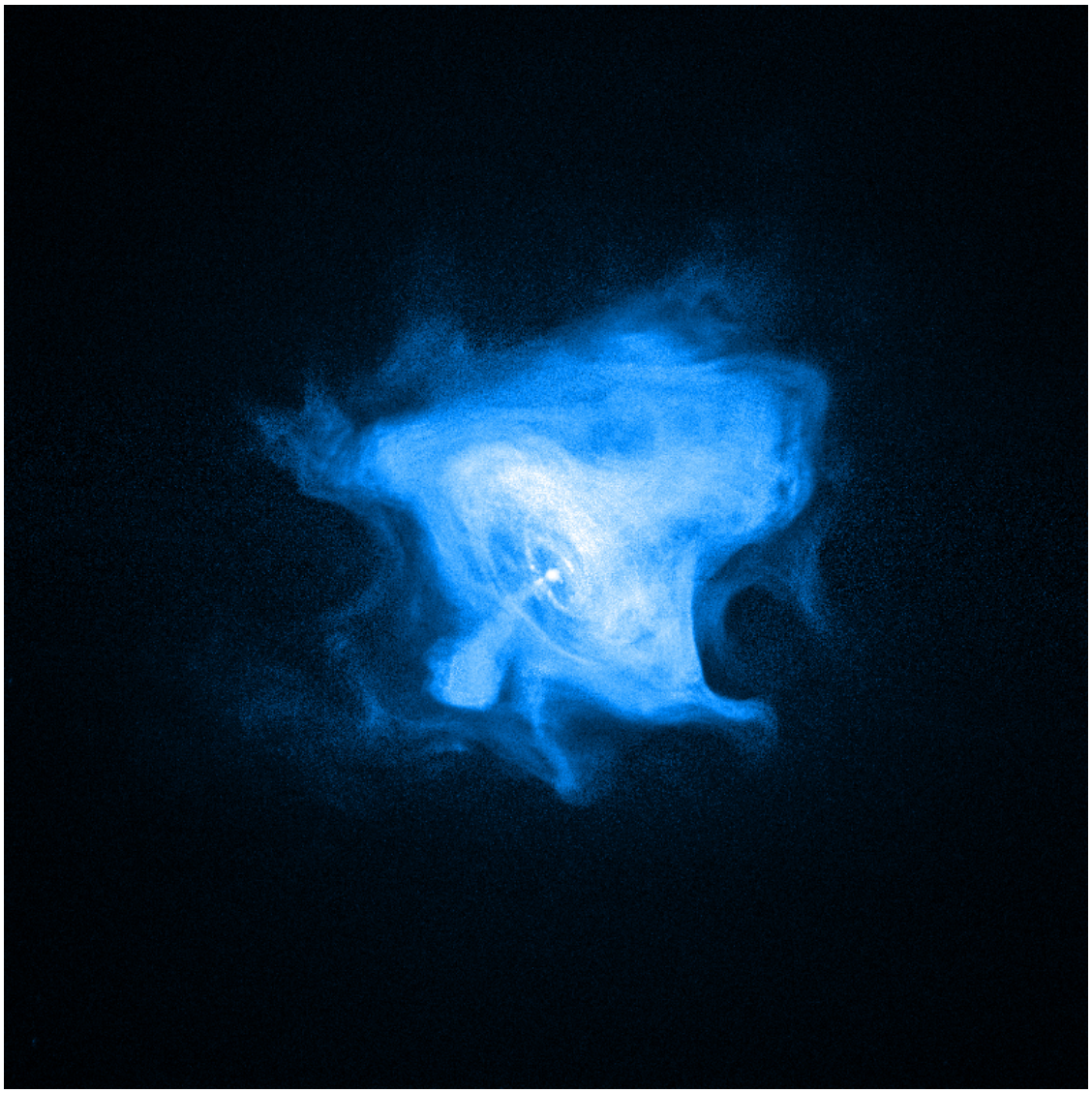

The Crab nebula as seen by the Chandra X-ray Observatory (NASA/CXC/SAO/F.Seward et al)

CONTENTS

Abstract v

Table of Contents vii

List of Figures xiii

List of Tables xxiv

Preface xxvi

1 Introduction 1

1.1 Production of an active X-ray prototype . . . 2

1.1.1 X-rays . . . 2

1.1.2 X-ray interaction with matter . . . 2

1.1.3 Grazing incidence . . . 5

1.1.4 Scattering . . . 7

1.1.5 Kirkpatrick-Baez . . . 7

1.1.6 Wolter Geometries . . . 8

1.2 Production of X-ray optics . . . 10

1.2.1 Monolithic optics . . . 11

1.2.2 Replicated optics . . . 11

1.2.3 Foil optics . . . 12

1.2.4 Future technologies . . . 13

1.3 Astronomical X-ray telescopes . . . 16

1.3.1 The Chandra X-ray Observatory - summary . . . 17

1.3.2 XMM-Newton - summary . . . 17
1.3.3 High Resolution versus high sensitivity . . . 18
1.3.4 Generation-X . . . 19
1.3.5 What is the science case for Generation-X? . . . 20
1.4 Active X-ray optics - the synchrotron community . . . 22
1.4.1 Piezoelectric bimorph mirrors . . . 22
1.4.2 Synchrotron versus the telescope . . . 23
1.5 Chapter summary . . . 24

2 The smart X-ray optics prototype for astronomical applications 26
2.1 The smart X-ray optics' active X-ray prototype . . . 26
2.1.1 The ellipsoidal prototype . . . 26
2.1.2 Development of manufacturing methods - cylindrical pre-prototype . . . 30
2.1.3 The optical form of the ellipsoidal prototype - University of Leicester . . . 31
2.1.4 Actuator design and fabrication - University of Birmingham . . . 33
2.1.5 Optic fabrication, optical testing and actuator control - University College London . . . 35
2.1.6 Support structure - Mullard Space Science Laboratory . . . 36
2.2 Finite element analysis . . . 39
2.2.1 A simple finite element analysis example . . . 39
2.2.2 Finite element models for the University of Leicester's Ray tracing code . 42
2.2.3 An FEA representation of the prototype's distortions caused by the effect of gravity . . . 43
2.2.4 An FEA representation of the piezoelectric nature of the prototype system 45
2.3 Chapter summary . . . 51

3 Cylindrical prototype 53
3.1 An overview of the cylindrical prototype's production methods . . . 53
3.2 The science of nickel electrodeposition . . . 55
3.2.1 Introduction to the theory of electrodeposition . . . 55
3.2.2 Deposition of metal with no applied potential . . . 59
3.2.3 Polarisation . . . 59
3.2.4 Transport of metal ions within the electrolyte . . . 60
3.2.5 Current density and the deposition of metal ions . . . 61

3.2.6 Stress within the electrodeposit . . . 61
3.2.7 Adhesion and passivation . . . 63
3.2.8 The effect of impurities . . . 64
3.3 The OSL electroforming facility . . . 64
3.3.1 Electrodeposition equipment set-up . . . 65
3.3.2 The chemical composition of the nickel sulphamate bath . . . 67
3.3.3 Additional equipment and safety concerns . . . 67
3.3.4 Operational procedure - production of a nickel electroform . . . 69
3.3.5 Early experimentation . . . 71
3.3.6 Current density anistropy . . . 72
3.3.7 Sacrificial electrodes . . . 76
3.3.8 A comparison of the experimental and FEA results . . . 79
3.3.9 An FEA model of the cylindrical prototype . . . 83
3.4 Production of the cylindrical mandrel . . . 88
3.4.1 Mandrel fabrication . . . 89
3.5 Production of the cylindrical optic . . . 91
3.5.1 General method for cathode preparation . . . 92
3.5.2 Cylindrical optic 1 . . . 93
3.5.3 Cylindrical optic 2 . . . 94
3.5.4 Cylindrical optic 3 and 4 . . . 95
3.5.5 Metrology of the replicated optics . . . 98
3.6 Actuator bonding, harnessing and the cylindrical prototype's completion . . . 103
3.6.1 The University of Birmingham's actuators . . . 103
3.6.2 Adhesive . . . 104
3.6.3 Actuator bonding . . . 104
3.6.4 Actuator harnessing . . . 105
3.6.5 Cylindrical prototype summary . . . 107
3.7 Chapter Summary . . . 108

4 The ellipsoidal prototype **109**
4.1 Fabrication of the ellipsoidal mandrel . . . 109
4.1.1 Materials choice . . . 109
4.1.2 Mandrel production . . . 113

4.2 Mandrel metrology . . . 119
4.2.1 Surface roughness . . . 119
4.2.2 Azimuthal radius of curvature . . . 120
4.2.3 Axial curvature . . . 120
4.2.4 Mandrel summary . . . 121
4.3 Optic replication . . . 124
4.3.1 Gold deposition . . . 124
4.3.2 Nickel deposition . . . 125
4.3.3 Optic removal . . . 127
4.4 Optic Metrology . . . 128
4.4.1 Surface roughness measurements using the RST 500 . . . 129
4.4.2 Surface roughness measurements taken at the Daresbury Laboratory . . . 129
4.4.3 Long trace profiler (LTP) traces along the axial length . . . 130
4.4.4 The inner azimuthal radius of curvature . . . 133
4.4.5 The outer azimuthal radius of curvature . . . 134
4.4.6 Thickness . . . 135
4.4.7 Optic summary . . . 137
4.5 Actuator bonding and harnessing . . . 141
4.5.1 Actuators for the ellipsoidal prototype . . . 141
4.5.2 Actuator Bonding . . . 142
4.5.3 Problems encountered . . . 143
4.5.4 Harnessing . . . 144
4.5.5 The completed prototype . . . 144
4.6 Chapter summary . . . 147

5 Prototype control and actuator influence functions 148
5.1 Actuator hardware . . . 148
5.1.1 Amplifier noise/ power supply stability . . . 149
5.1.2 Amplifier gain . . . 150
5.2 Software - Actuator control . . . 154
5.2.1 Requirements of the actuator control software . . . 154
5.2.2 The graphical user interface of the prototype's control software . . . 156
5.2.3 Operation of the virtual instrument graphical user interface . . . 158

5.2.4 Summary of the prototype's hardware and software 163
5.3 Prototype morphology and actuator influence functions 163
5.3.1 The finite element analysis model of the ellipsoidal prototype 163
5.3.2 FEA model considerations 164
5.3.3 Axial LTP measurements - zero volts 165
5.3.4 Axial LTP measurements - displacement per voltage 168
5.3.5 Axial LTP measurements - individual actuators 172
5.3.6 Axial LTP measurements - neighbouring effects 178
5.3.7 Axial LTP measurements - active to dormant decay in form 182
5.3.8 Prototype morphology and actuator influence functions summary 182
5.4 Chapter summary 186

6 X-ray testing at the University of Leicester 187
6.1 The University of Leicester's X-ray tunnel test facility 187
6.1.1 Specifications of the X-ray TTF 187
6.1.2 The X-ray source 188
6.1.3 The MCP detector 189
6.1.4 Integration of the prototype within the facility 191
6.2 The optimisation routine 191
6.3 X-ray testing at the X-ray TTF 192
6.3.1 Week 1 - Integration of the prototype within the X-ray facility and initial optical alignment 193
6.3.2 Week 2 - X-ray first light, realignment of the prototype and initial actuator measurements 194
6.3.3 Week 3 - Testing the optimisation routine and the development of new actuator patterns 197
6.3.4 Week 4 - Prototype optimisation 199
6.4 Data analysis 199
6.4.1 Optimisation of the Prototype's form 199
6.4.2 Prototype stability 202
6.4.3 Deformation of the optic over time 204
6.5 Chapter summary 206

7 Discussion and future work **207**

7.1 Chapters - review 207

7.2 The active X-ray prototype and X-ray results - review 208

7.3 Development of a second generation active X-ray prototype 209

7.4 An active X-ray telescope? 213

Bibliography **214**

List of Publications **221**

Acknowledgements **223**

LIST OF FIGURES

1.1 The Crab Nebula seen at different X-ray spatial resolutions: **(a)** - the Einstein Observatory 1978 (NASA/MSFC); **(b)** - ROSAT 1990 (S. L. Snowden (USRA, NASA/GSFC)) and **(c)** - the Chandra X-ray Observatory 1999 (NASA/CXC/SAO) 1

1.2 An X-ray incident upon a surface. 4

1.3 A ray incident upon a surface showing the effects of Snell's law 5

1.4 A schematic of the Kirkpatrick-Baez telescope system. Image **(a)** highlights the two mirror combination where incident X-rays are first focussed to line (reflection one) and then focussed to a point (reflection two). Image **(b)** depicts how the two mirror system can be nested to increase the effective area of the system. 8

1.5 The Wolter optical configurations, Type I is most commonly used in astronomical X-ray telescopes. 9

1.6 Image **(a)** highlights a 180 ° cross-section through a Wolter 1 geometry used for astronomical telescopes. Image **(b)** depicts how the optics are nested co-axially to increase the effective area of the system. 10

1.7 Production of XMM Newton's telescope optics via nickel electroforming. (1) The superpolished mandrel is cleaned. (2) The mandrel is gold coated to provide a release agent for the nickel deposit. (3) Nickel ions are electrodeposited upon the mandrel until the desired thickness is obtained. (4) The optic is released and the mandrel can be used to replicate further optics (the optic shown in the figure is a cross section of a complete optic revolution). 12

1.8 Flat sheets of glass (indicated as blue within the figure), $\sim 400\mu m$ thick, are placed upon a mandrel of the inverse form of the optic required (t_1), the optic is then uniformly heated (t_2) and the sheet deforms to the shape of the (t_3). The mandrels can be recycled and used to produce many optics. 14

1.9 Optics being produced at the NASA's Goddard Space Flight Centre (GSFC) for the forth coming NuSTAR mission. In the photo the optics have just been removed from the oven and have formed to the shape of the mandrel; the mandrels are quartz cylinders leading to a cylindrical optical profile. Figure courtesy of CHF. 15

1.10 The production of a silicon pore optic. **(a)** - The silicon wafers have channels cut into them. **(b)** The silicon plates are then stacked and in addition they are wedged as shown in image **(c)** (the orientation of image **(c)** is along the channel walls). . . 15

1.11 The mirrors of the Chandra X-ray Observatory, (NASA/CXC/SAO) 17

1.12 The aperture of one of the three XMM-Newton telescopes, courtesy of ESA. . . . 18

1.13 A section of a PBM: highlighting the composite structure and the electrode arrangement. 23

1.14 Image **(a)** highlights the poling of the PZT material in relation to the electric field. Due to the alignment of the electric fields with respect to the poling axis, the application of a driving voltage V_D causes an expansion of one PZT layer and a contraction within the other, resulting in an overall bending of the system, image **(b)**. 24

2.1 A schematic of the ellipsoidal prototype. 27

2.2 Definitions of the ellipsoidal form 28

2.3 The ellipsoidal prototype situated within the X-ray beam line at the UoL, image courtesy of CT from MSSL 31

2.4 Ray tracing performed at the University of Leicester to demonstrate the ellipsoidal form of the prototype's optic, courtesy of the CHF from UoL. 32

2.5 The fast Fourier transform patterns as developed by the UoL, each square represents an actuator and the shade between white and black refers to 1 to -1 respectively, courtesy of CHF from UoL. 33

2.6 A description of a unimorph actuator with respect to the material's poling axis. . 34

2.7 An example of the unimorph actuators as developed by the UoB for the SXO prototype. Figure 2.7(a) (not to scale) highlights the ground electrode (green) which has been wrapped around the PZT ceramic and allows its electrode to be accessed from the non-bonded surface. Figure 2.7(b) displays a completed curved actuator 35

2.8 Hysteresis within a piezoelectric actuator sample 36

2.9 Definition of pitch and yaw for the ellipsoidal prototype's support structure: pitch is a rotation about axis X and yaw is a rotation about axis Z. 37

2.10 The complete prototype support structure is composed of three components. First is the flange support (Figure 2.10(a)) which is fitted externally to the the X-ray TTF and has three adjustable legs that extend within the tunnel, normal to the surface. The active component is shown in Figure 2.10(b); it forms a kinematic mount with the flange support and provides optical alignment in terms of pitch and yaw. The final component is the optic's cradle (Figure 2.10(c)) and the prototype will rest upon its foam supports. 38

2.11 An example of an aluminium bar fixed at one end, with a 10N point force acting at the other. 40

2.12 The 2-dimensional object is first drawn to its physical dimensions 40

2.13 The 2-dimensional object is then meshed to divide the object into smaller segments, each segment represents an equation at that point 41

2.14 Boundary conditions are applied; these provide the model with point(s) to react against and the initial force 41

2.15 The solution for the FEA model of the aluminium bar with a point force 42

2.16 The elliptical prototype support structure (the optic cradle), an aluminium framework with two $5mm$ thick polyimide foam strips. 44

2.17 A view normal to the optic's surface showing the effects due to gravity caused by the optic cradle. 45

2.18 Piezoelectric coordinates 47

2.19 A 2D representation of a flat piezoelectric actuator affecting an aluminium substrate: the Cartesian and Piezoelectric coefficients are correctly aligned. The deformed colour map highlights the change in displacement of the substrate caused by the actuator. 48

2.20 A 2D representation of a curved actuator bonded to a curved substrate: within a Cartesian coordinate system the piezoelectric coefficients do not align correctly leading to an asymmetry in the resultant influence function. 49

2.21 A description of the cylindrical coordinate system used within COMSOL MULTIPHYSICS 50

2.22 An FEA generation influence function for a central actuator at -10V, Figure 2.22(a) indicates the magnitude of the y-displacement of the actuator (the displacement normal to the optic's surface) and Figure 2.22(b) highlights the form of the influence function with respect to the optical surface. 51

2.23 The half energy width, and the full width at half maximum, of the modelled detector image as a function of iteration number, image courtesy of CHF from UoL 52

3.1 A simplified description of the production of the nickel optic via electroforming. 54

3.2 A simple electrolytic cell, where electrical energy is used to produce a chemical change that would not otherwise occur spontaneously (Zumdahl 1989) 55

3.3 Example of nodule growths, Figure 3.3(a) displays a ring of nodules resulting from a tiny gap in the masking material and Figure 3.3(b) highlights the nodules and pitting formed at the corners of a deposit as a result of high current density. . . . 62

3.4 An example of a dendrite/tree formation courtesy of the UCLA mineral physics laboratory (`www.igpp.ucla.edu/minphys`) 62

3.5 Stresses within the metal deposit: tensile stress pulls itself away from the cathode and compressive stress forces itself upon the cathode. 63

3.6 The OSL electroforming facility 65

3.7 A schematic of the UCL electrodepositing facility 66

3.8 The titanium ring test used to determine the surface tension of the electrolyte. If a thin film is not produced after removing the ring from the electrolyte then additional electrolyte should be added. 70

3.9 A preparation of a simple mandrel prior to electrodeposit 70

3.10 The electrodeposition power supply: the power supply is turned on using the on/off switch in the bottom left-hand corner, the constant current output is then selected and the dial used to select the desired current output. Finally, the current is output to the electrolyte cell using the power output button. 71

3.11 The variation in deposition thickness as a function of position. Figure 3.11(a) displays the electrodeposit upon a kanigen mandrel (the relevence of the kanigen mandrel is explained in Chapter 4). Figure 3.11(b) highlights the measured thickness, where A and B refer to Figure 3.11(a). 73

3.12 An electric field existing between two oppositely charged plates: the condensation of field lines at the tips of the two plates indicate an area of greater electric field strength. 74
3.13 The potential boundary conditions applied upon the FEA model to produce a representation of the current density. 75
3.14 The resultant current density from the FEA boundary conditions as outlined in Figure 3.13 75
3.15 Schematic of the square test piece, with the mandrel labelled B and the sacrificial electrode labelled A. The thin polypropylene insulator ($250\mu m$) fits between A and B. 77
3.16 Nickel growth across an insulating bridge and the requirement to extrude the insulator. 77
3.17 These images show the mandrel and sacrificial electrode with electrical insulation supplied by a thin polypropylene layer ($250\mu m$). Figure 3.17(a) shows how the insulator has been extruded in height above the mandrel plane to provide a distinct boundary over which the nickel will not be able to deposit. Figure 3.17(b) highlights the reverse of the mandrel and two connectors are shown: first the connector to the external cathode bus bar, and second, a connector to provide an electrical junction between the sacrificial electrode and the mandrel. 78
3.18 An FEA representation of the mandrel described in Figure 3.17. The anode facing component is shown in Figure 3.18(a) and the reverse of the mandrel is seen in Figure 3.18(b) 79
3.19 The comparison between the measured thickness of the cathode (mandrel and sacrificial electrode) and the FEA current density map. 81
3.20 The comparison between the measured thickness of the mandrel and the FEA current density map. 82
3.21 The mandrel's wasters are 1cm extensions in width of the mandrel's form, Figure 3.21(c) highlights the position of the polypropylene insulators between the mandrel and the wasters in an expanded view. 84
3.22 The FEA representation of the cylindrical mandrel within the electroforming facility: the red lines indicate the electric field between the anode and mandrel. 85
3.23 A current density map of the surface from which the cylindrical optic will be replicated 86
3.24 A schematic of the cylindrical mandrel, including wasters and screw holes, courtesy of DB 88

3.25 The surface of the cylindrical mandrel after milling 89
3.26 The surface of the cylindrical mandrel during the polishing process. 90
3.27 Microscope interferometer image of the mandrel, indicating a surface roughness of 4.01nm Ra 90
3.28 The completed cylindrical mandrel 91
3.29 A schematic of the cylindrical mandrel within the electrodeposition facility . . . 92
3.30 Preparation of the cathode for the replication of the first cylindrical optic 93
3.31 Replication of the first cylindrical optic 94
3.32 Preparation of the cathode for the replication of the second cylindrical optic . . . 95
3.33 The electroform (figure 3.33(a)), including the sacrificial nickel directly post removal from the bath. Figure 3.33(b) shows the optical surface of the nickel electroform after being rinsed using distilled water. Figure 3.33(c) highlights the problem due to nodules that the sacrificial electrode was designed to remove. 96
3.34 The effect on the electric field caused by a centralised mandrel with respect to the anode (Figure 3.34(a)) and a non-centralised mandrel with respect to the anode (Figure 3.34(b)). 96
3.35 Addition of polypropylene edges to reduce the nickel growth at the edge of the cylindrical mandrel 97
3.36 Preparation of the cathode for the replication of the third cylindrical optic 97
3.37 The third replication run highlighting the cylindrical mandrel directly after removal from the bath 98
3.38 The fourth and final replication run of the cylindrical mandrel: the optic formed in this run was used as the optical component of the cylindrical prototype. 99
3.39 Surface roughness measurements of the final optic surface taken with the RST500 Interferometer. Figure 3.39(a) displays the raw interferometric data indicating the cylindrical form of the optic. Figure 3.39(b) shows the removal of the cylindrical term from the interferometric data, leaving a flat surface allowing a determination of surface roughness for the optic. 100
3.40 Comparison between measured and theoretical results for the nickel optic, Figure 3.40(a), displays the theoretical current density distribution over the mandrel's surface. Figure 3.40(b) displays the measured thickness variation along the optic. 102
3.41 A scanning electron microscope image of the cross section through an early prototype, courtesy of the University of Birmingham. 105

3.42 Figure 3.42(a) displays the process in which the actuators were bonded, in columns, with the actuators' wires leading out away from the optic. The completed bonding is shown in Figure 3.42(b): when completed the optic was under a cover to minimise access to detritus. 106
3.43 The harnessed actuators upon the reverse of the nickel optic 107

4.1 Initial experiment investigating gold as a viable passivation mechanism. 112
4.2 An investigation of the use of potassium dichromate as a possible release agent. . 113
4.3 A computer aided design of the ellipsoidal mandrel, including wasters, courtesy of DB. 115
4.4 The ellipsoidal mandrel being turned on the lathe, courtesy of Jim Percival 115
4.5 The ellipsoidal mandrel measured upon the Talysurf profilometer, courtesy of DB. 116
4.6 The surface roughness of the mandrel as taken by the RST 500 117
4.7 The finished mandrel, gold coated and prior to nickel electroforming. 117
4.8 Electroplating nickel to fill the scratch on the ellipoidal mandrel 118
4.9 A stitched surface profile of the ellipsoidal mandrel, indicating a surface roughness Ra of 2.16nm, (image 4.9(a) courtesy of Anthony Gleeson from DL) 121
4.10 The azimuthal radius of curvature of the ellipsoidal mandrel and its deviation from the desired form 122
4.11 The axial form of the ellipsoidal mandrel 123
4.12 The vacuum chamber used for the gold deposition of the mandrel and wasters . . 126
4.13 The current density map of the ellipsoidal mandrel 127
4.14 The ellipsoidal mandrel prior to nickel electrodepostion 128
4.15 A RST 500 surface profile of the second ellipsoidal shell, the ripples indicate that vibrations are present in the profile 130
4.16 2 and 3D profiles of the optical surface taken using the microscope interferometer at the DL (images courtesy of Anthony Gleeson from DL) 131
4.17 1D surface roughness data taken from the second ellipsoidal shell (position 3) . . 132
4.18 A 270mm by 6mm area of second ellipsoidal optic 134
4.19 The experimental set-up of the optic and cradle allowing the measurement of the optic's radius of curvature in two sections, A and B. 135
4.20 The radius of curvature of second ellipsoidal optic 137

4.21 The measured outer, and the calculated inner, radius of curvature of the ellipsoidal optic used in the prototype . . . 138
4.22 The measured thickness of the 2^{nd} ellipsoidal optic and its comparison to the FEA simulated current density map . . . 139
4.23 Peaks created on the optic's surface caused by the major scratch upon the mandrel 140
4.24 Measured axial profiles for the different methods of mounting for ellipsoidal shell 3 141
4.25 The bonding of the actuators in groups of 10 using the EP30-glass bead suspension. 143
4.26 The final stage of the prototype fabrication was: **(a)** the harnessing of the actuators and **(b)** the completed prototype awaiting integration within the X-ray test tunnel facility. . . . 145
4.27 The axial curvature of the prototype . . . 146

5.1 A schematic of the prototype's hardware . . . 149
5.2 An example of the noise generated upon channel AO4 for a 10 second duration, the scale in the vertical direction is one tick equals 20mV . . . 150
5.3 A histogram displaying the rms noise as a function of number frequency at 10V . . 151
5.4 A histogram displaying the rms noise as a function of number frequency at 100V . 151
5.5 The effect of the 50Hz mains frequency power supply . . . 153
5.6 An example of the hysteresis loop and use of the the reference voltage . . . 155
5.7 A practical example of the hysteresis and the use of the reference voltage . . . 155
5.8 The user interface of the virtual instrument as developed by HCW. . . . 157
5.9 Step 1: Initiation . . . 159
5.10 Step 2: Reference voltage . . . 160
5.11 Step 3: Input voltage . . . 161
5.12 Step 4: Finish . . . 162
5.13 The FEA representation of the ellipsoidal prototype system . . . 165
5.14 Displacement as a function of adhesive thickness with Actuator 15 set to 10V . . 166
5.15 A 1D azimuthal profile of the of Actuator 15 at 10V, indicating the decrease in displacement with distance from the actuator central point . . . 166
5.16 The axial profile of the ellipsoidal prototype . . . 167
5.17 The influence functions of Actuator 17 operated between +50V and -50V, displaying raw and zero-subtracted data: all other actuators are at 0V . . . 169

5.18 the profiles for Actuator 18 for the voltage range +20V to -20V in 5V steps that have been zero-subtracted and a tilt removed 171
5.19 An FEA comparison applied to the active region of the LTP trace. 171
5.20 The influence functions of Actuators 18 to 11 operated at 25V one at a time while all other actuators are at 0V 173
5.21 Zero-subtracted and cut data for each actuator between 11 and 20 operated at 25V one at a time, including an FEA comparison 176
5.22 Zero-subtracted and cut data for each actuator between 11 and 20 operated at -25V one at a time, including an FEA comparison 177
5.23 Raw LTP data taken over Actuator 17 to 19, centralised upon Actuator 18 179
5.24 Zero-subtracted data compared against FEA simulations. 180
5.25 Actuator 8 and 28's effect upon Actuator 18 and its neighbours (zero-subtracted and compared to FEA data) 181
5.26 Relaxation of the prototype from 0V power on to 0V power off 183
5.27 A comparison of full width half maximum measurements of the Actuator 17 profile at 50V for the LTP (Figure 5.27(a)) and FEA (Figure 5.27(b)) data. 185

6.1 A schematic of the the X-ray tunnel test facility at the University of Leicester . . 188
6.2 Figure 6.2(a), courtesy of Dr J. Pearson from UoL, depicts the view from the X-ray source towards the detector, Figure 6.2(b), courtesy of CHF from UoL, displays the copper anode coated with NaCl which is used to generate the X-rays. 189
6.3 Figure 6.3(a) displays the MCP detector at the UoL with a face guard protecting the detector. The detector is positioned upon two rails that provide the 0.8m of axial travel, photo courtesy of CHF from UoL. Figure 6.3(b) outlines a schematic of an individual channel of an MCP detector, where an incident X-ray liberates an electron and starts an electron cascade. 190
6.4 A pin hole image taken using the MCP detector demonstrating the pin cushion effect that has to be compensated for. The image mask used in this figure is a square array of pin holes, image courtesy of CHF from UoL 190
6.5 A schematic of the ellipsoidal prototype within the X-ray tunnel test facility: the prototype is located approximately 4.5m from the detector (when the detector is in the middle of its travel). The red line represents an incident X-ray upon the optic. . 191
6.6 Fast fourier transform patterns, image courtesy of CHF from UoL. 192

6.7 The photo on the left highlights the prototype positioned within the X-ray TTF as viewed from the detector towards the source (photo courtesy of CHF), the image on the right depicts the components of the prototype and support structure as seen in the photo. 193
6.8 The laser interacting with the prototype's optic to produce a reflected image, photo courtesy of CHF from UoL 194
6.9 The first light X-ray image 195
6.10 The improved realignment of the prototype using the optical laser. 195
6.11 The first X-ray image of the realignment of the prototype. The image is centralised upon the detector and smaller than the previous first light image. 196
6.12 The realigned X-ray image brought into focus using the axial travel of the MCP detector. 196
6.13 Image **a** represents the zero volts X-ray image, image **b** represents the effect of applying 50V to the 15 actuators located closest to the X-ray source while the other 15 actuators are at 0V. There is a marked difference in the form of the detected image. 197
6.14 Local patterns as developed during X-ray testing, image courtesy of CF from UoL 198
6.15 The graphical user interface of the detector control, the FWHM-input for the optimising routine is calculated from the x and y components of the image. . . . 198
6.16 The analysis of the optimisation routine data. The half energy width (HEW) and the full width half maximum (FWHM) are shown against the iteration number of the optimisation routine, graphs provided by CHF. 200
6.17 The voltage configuration of the prototype at the end of the optimisation routine. The black line indicates the trace of the LTP along the actuators. Green represents 100V and red represents -100V 201
6.18 An LTP trace compared against finite element analysis data for the voltage pattern as determined by the optimising routine. 202
6.19 An analysis of the stability of the prototype over 5 hours given in terms of HEW and FWHM, graphs provided by CHF. 203
6.20 Stability of the power supply over 5 hours 203

6.21 An analysis of the HEW and FWHM of the zero volts applied to the prototype during the 5 days of the X-ray optimisation. The images on the left display the variation in HEW of the prototype over number of day (top-left figure) and number of actuations (bottom-left figure). The images on the right are a FWHM representation of the HEW figures. The annotation within the figures relates to the type of zero volts measurement obtained as recorded within the log. `power off` is a zero volts image with the high voltage amplifier turned off. `Start` and `end` are zero volt images with the power on taken at the start and the end of the day respectively. `Piezos on` is identical to `Start`. Graphs provided by CHF from UoL. 205

7.1 A vacuum chuck used to position actuators upon the non-reflective surface of the optic. Image **(a)** highlights the surface of the chuck which is figured to the same form as the optic, vacuum channels are then used to hold the actuator prior to bond. Image **(b)** depicts the actuator arranged upon the chuck. It is hoped that the vacuum will deform the actuators to the form of the chuck and therefore the optic, as a result improving the curvature mismatch. 210

7.2 The effect of inter-actuator kinking represented as a function of prototype axial length and inter-actuator spacing. 211

7.3 The double electrode actuator to decrease the number of inter-actuator kinks. . . 212

LIST OF TABLES

1.1 An overview of the X-ray telescopes (Willingale 1999) 16

2.1 An overview of the ellipsoidal prototype 27
2.2 The optical specifications of the ellipsoidal prototype 28
2.3 An overview of the cylindrical prototype 30
2.4 Converting Cartesian coordinates to cylindrical coordinates 47

3.1 The components of the nickel sulphamte electrolytic solution 68
3.2 Cylindrical optic production 91
3.3 Azimuthal radius of curvature measurements of the 2^{nd} cylindrical optic taken using the Talysurf profilometer 101
3.4 Average radius of curvature profilometer measurements of five actuator samples . 103

4.1 The surface roughness as measured using DL's microscope interferometer 120
4.2 Ellipsoidal shell production 124
4.3 The surface roughness (Ra) measurements taken from the second ellipsoidal shell 133
4.4 Radius of curvature of the 2^{nd} ellipsoidal optic 136
4.5 Comparison between the measured thickness data and that of the FEA data . . . 138

5.1 The power supply stability with each channel operated at 10V 152
5.2 The power supply stability with the odd channels operated at 100V 153
5.4 The components of the FEA model describing the prototype system in terms of dimension. 164
5.5 The maximum displacement of Actuator 17 operated between 50V to -50V in 25V steps 168
5.6 Actuator 18 operated in the voltage range +20V to -20V in 5V steps 170

5.7 The maximum displacement of actuator operated at 25V one at a time 172
5.8 The maximum displacement of actuators 11 - 20 each operated at +25V and -25V one at a time 175

PREFACE

The development of the active X-ray prototype was far from an individual endeavour; it was based upon the collaborative effort of the Smart X-ray Optics consortium members and this preface will outline the contribution from each member and the author's participation within the project.

The Smart X-ray Optics consortium consists of seven UK institutions (presented below) investigating two branches of active X-ray research with applications in medical and astronomical instrumentation:

- University College London (UCL)
- University of Leicester (UoL)
- University of Birmingham (UoB)
- Mullard Space Science Laboratory (MSSL)
- STFC [1] Daresbury Laboratory (DL)
- King's College London (KCL)
- University of Edinburgh (UoE)

MEDICAL - The prototype system for medical applications is based upon applying piezoelectric actuators to X-ray focussing micro optical arrays (MOAs) (Michette *et al.* 2007) with the goal to focus an X-ray source upon single cells. This research is directed by KCL with direct input from UoL, UoB, MSSL, DL and UoE.

ASTRONOMICAL - The prototype for astronomical applications, and the topic of this thesis, aims to achieve high resolution and high sensitivity through active control and an ability to be

[1] Science Technology Facilities Council

nested respectively. The prototype is based upon an optic, similar to XMM Newton's optics, whose non-reflective side is populated with 30 piezoelectric actuators and it is the actuators that provide the prototype's ability to improve its optical form. The development of the astronomical prototype is lead by Dr Peter Doel from UCL and the contributing consortium members are outlined below:

Peter Doel (APD)	Principle Investigator	UCL
David Brooks (DB)	Senior experimental officer	UCL
Samantha Thompson (SJT)	Postdoctoral researcher[a]	UCL
Jun Yao (JY)	Postdoctoral researcher[b]	UCL
Hongchang Wang (HCW)	Postdoctoral researcher[c]	UCL
Carolyn Atkins (CA)	PhD Student	UCL
Richard Willingale (RW)	Co-Investigator	UoL
Charlotte Feldman (CHF)	PhD student	UoL
Tim Button (TB)	Co-Investigator	UoB
Dou Zhang (DZ)	Postdoctoral researcher	UoB
Daniel Rodiguez Sanmartin (DRS)	PhD student	UoB
Ady James (AJ)	Project manager	MSSL
Craig Theobald (CT)	Mechanical design	MSSL
Graham Willis (GW)	Electronic design	MSSL
Andrew D. Smith (AS)	Co-Investigator	DL

[a] April 2004 - March 2005

[b] August 2006 - June 2007

[c] November 2007 - March 2009

The University of Leicester was responsible for: the optical modelling of the prototype within the X-ray facility; the optical geometry of the prototype; the optimising routine; directing the X-ray tests and analysing the X-ray data. The fabrication and the characterisation of the piezoelectric actuators were undertaken by the School of Materials and Metallurgy at the University of Birmingham. The mechanical design of the prototype's support structure and the wiring of the prototype's electronics were managed by MSSL. Metrology of the prototype, and subsequent optics, was performed at DL. Finally UCL's role, and the foundation of this thesis, was to manufacture the prototype's optics, assemble the optic and actuators into a prototype system and design the actuator

control software and finite element analysis of the prototype system. To ensure that each member of the consortium, both astronomical and medical, were working in harmony, the management of the SXO was undertaken by AJ from MSSL.

Much of the work undertaken at UCL, especially in regard to the optic's manufacture, was a collaborative effort between DB, HCW and the author; as such only the finite element analysis is the sole responsibility of the author. Where work is attributed to other persons this is highlighted within the relevant text.

CHAPTER 1

INTRODUCTION

The objective of this reseach is to produce an active X-ray optic prototype intended for astronomical applications; as such the introduction shall begin with an investigation into the science and production methods required to reach this goal. Furthermore, a description of two current astronomical X-ray telescopes shall be given and their limitations highlighted, therefore leading to a discussion of future X-ray observatories and the science case for improving both angular resolution and sensitivity of a system. Finally, active X-ray optics used within synchrotron facilities shall be described and differences between the technologies highlighted.

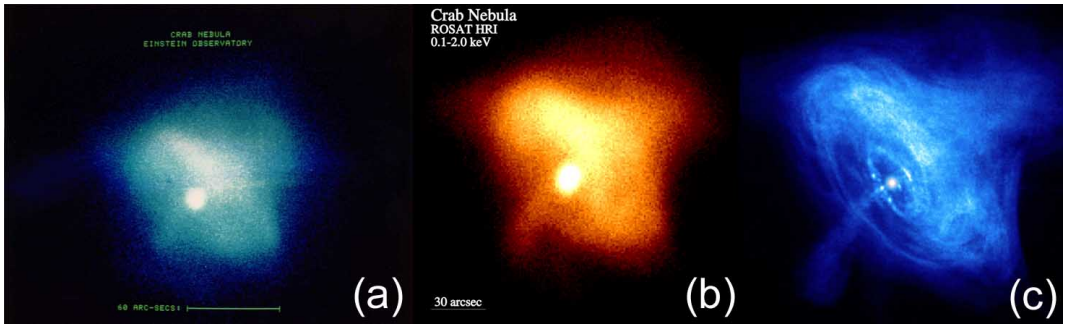

Figure 1.1: The Crab Nebula seen at different X-ray spatial resolutions: **(a)** - the Einstein Observatory 1978 (NASA/MSFC); **(b)** - ROSAT 1990 (S. L. Snowden (USRA, NASA/GSFC)) and **(c)** - the Chandra X-ray Observatory 1999 (NASA/CXC/SAO)

1.1 Production of an active X-ray prototype

Before introducing X-ray telescopes, their current limitations and the drive for future telescope development, the science behind X-ray interactions with matter shall be presented to provide a foundation to X-ray reflecting optics.

1.1.1 X-rays

X-rays were discovered at the end of the nineteenth century by the German physicist Wilhelm Röntgen, the wavelength, energy and frequency ranges are provided below (Willingale 1999).

Wavelength - $124\text{Å} \longrightarrow 0.124\text{Å}$

Frequency - $2.4 \times 10^{16}\text{Hz} \longrightarrow 2.4 \times 10^{19}\text{Hz}$

Energy - $0.1\text{keV} \longrightarrow 100\text{keV}$

1.1.2 X-ray interaction with matter

How an X-ray interacts with matter is paramount to developing successful X-ray optics. As this thesis considers the interaction of X-rays with an optic's surface only the macroscopic properties of the X-ray interaction with matter shall be discussed and not the X-ray's interaction upon an atomic scale. The manner in which X-rays interact with matter can be described using the complex refractive index $\tilde{n}$, as shown in Equation 1.1 (Aschenbach 1985; Michette & Buckley 1993):

$$\tilde{n} = 1 - \delta - i\beta \tag{1.1}$$

δ - refractive index decrement

β - absorption index

The refractive index decrement δ and the absorption index β have values that range from $10^{-2} \longrightarrow 10^{-5}$ and $10^{-2} \longrightarrow 10^{-6}$ in the X-ray domain (Michette & Buckley 1993) and they are calculated using Equation 1.2:

$$\delta = Kf_1 \text{ and } \beta = Kf_2 \tag{1.2}$$

Where f_1 and f_2 are the atomic scattering factors defined in Equations 1.3 and 1.4:

$$f_1(E) = Z + \frac{4\epsilon_0 m_e c}{he^2} \int_0^\infty \frac{W^2 \sigma(W)}{E^2 - W^2} dW - \Delta_{rel} \tag{1.3}$$

$$f_2(E) = \frac{2\epsilon_0 m_e c}{h} E\sigma(E) \tag{1.4}$$

E - photon energy

W - the energy over which the f_1 is integrated

Z - atomic number of the scatterer

$\sigma(E)$ - atomic photoabsorption cross section for the photon energy E

$\sigma(W)$ - atomic photoabsorption cross section for the integrated energy W

m_e - electron rest mass

h - Planck's constant

ϵ_0 - Permittivity of free space

Δ_{rel} - the relativistic correction factor

c - the speed of light

e - electron charge

The constant K from Equation 1.2 is defined by the X-ray and interacting material's physical properties and is shown in Equation 1.5:

$$K = \frac{r_0 \lambda^2}{2\pi} \frac{N_A}{A} \rho \tag{1.5}$$

r_0 - the classical electron radius $2.1879 \times 10^{-15} m$

λ - the wavelength of the incident X-ray

N_A - Avagadro's number

A - the atomic weight of the material

ρ - the density of the material

REFRACTION - Equation 1.5 highlights the dependence on X-ray wavelength and material properties of the interacting surface and it is the combination of these conditions that provides the small values of δ and β. In turn δ and β result in a complex refractive index that deviates only slightly from unity and therefore when considering the use of lenses to focus X-rays, an extremely long focal length would be required and this leads them to being unattractive as a telescope system (not to mention the weight of such a system). However, despite the long focal lengths, X-ray missions have been proposed to use lenses (Skinner *et al.* 2008), but these generally require the need for two space craft flying in formation.

REFLECTION - If refraction is impractical to focus an X-ray source, then reflection is the only alternative. The amount of reflectance provided by a surface is governed by the Fresnel equations (Michette & Buckley 1993) (Aschenbach 1985), which divide the incident ray (at angle θ_i from the surface) into the reflected (angle θ_r) and transmitted (angle θ_t) components. Equations 1.6 and 1.7 (angles in reference to Figure 1.2) describe the parallel and perpendicular component of reflectivity from the Fresnel equations (transmission is omitted due to the emphasis on reflectance within this thesis); these equations illustrate the scenario for an X-ray incident from a vacuum upon a surface and this is appropriate considering the vacuum environment in which an X-ray telescope operates. The total reflectivity (or reflected intensity) for an unpolarised X-ray source is given by $R = (R_p + R_s)/2$ where $R_p = r_{\|} r_{\|}*$[1] and $R_s = r_{\perp} r_{\perp}*$.

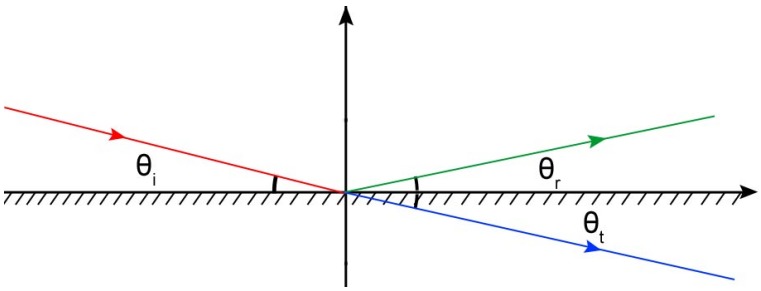

Figure 1.2: An X-ray incident upon a surface.

$$r_{\|} = \frac{\tilde{n}^2 sin\theta_i - [\tilde{n}^2 - cos^2\theta_i]^{\frac{1}{2}}}{\tilde{n}^2 sin\theta_i + [\tilde{n}^2 - cos^2\theta_i]^{\frac{1}{2}}} \tag{1.6}$$

[1] the asterisk denotes the conjugate complex value

$$r_{\perp} = \frac{sin\theta_i - [\tilde{n}^2 - cos^2\theta_i]^{\frac{1}{2}}}{sin\theta_i + [\tilde{n}^2 - cos^2\theta_i]^{\frac{1}{2}}} \tag{1.7}$$

The Fresnel equations highlight the significance of θ_i and $\tilde{n}$, and through $\tilde{n}$ the dependance upon wavelength and atomic weight, for achieving reflection. Plots of R against θ_i and wavelength for different material properties, as presented within Zombeck (2007), highlight decreased reflectivity in the X-ray domain for angles of $\theta_i \geqslant 1^\circ$ and for low atomic number elements. This leads to an X-ray reflective surface that must be almost parallel to the incidence X-rays and have a high atomic number.

The reflectance of X-rays, particularly in the high energy domain, can be enhanced with the use of multilayers. Multilayers work on the principle of Bragg crystal reflectance, where the spacing between layers in the crystal acts to enhance the reflectivity. These coatings allow X-ray energies less than 1 or 2 keV to be reflected at normal incidence and they significantly increase the reflectance at 100keV at grazing incidence (Zombeck 2007). Examples where these coating are being employed in future X-ray missions are Astro-H (Furuzawa *et al.* 2009) and NuSTAR (Koglin *et al.* 2009) (further discussed in Sections 1.2.3 and 1.2.4).

1.1.3 Grazing incidence

The shallow angles required to achieve X-ray reflectance, as described in Section 1.1.2, are termed *grazing angles* and the resultant reflectance is based upon total external reflection. The definition of grazing angle orginates with Snell's law (Equation 1.8: angles in reference to Figure 1.3 (Hecht 2002)):

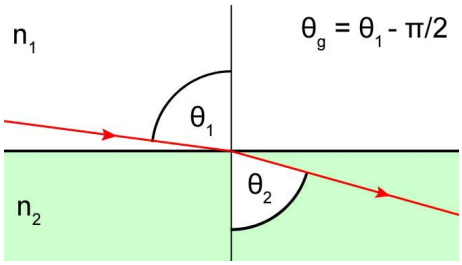

Figure 1.3: A ray incident upon a surface showing the effects of Snell's law

$$n_1 sin\theta_1 = n_2 sin\theta_2 \tag{1.8}$$

Assuming that the incident X-ray propagates from vacuum (n_1 = 1), the angle of incidence θ_i normal to the surface is defined as the angle from the surface to the normal minus the grazing angle θ_g (i.e. $\frac{\pi}{2} - \theta_g$) and that θ_2 is equal to $\pi/2$ (the limit for reflectance), Equation 1.8 simplifies to:

$$sin(\frac{\pi}{2} - \theta_g) = n_2 sin(\frac{\pi}{2}) \tag{1.9}$$

Which in turn can be simplified to the equation for grazing incidence (Equation 1.10):

$$cos\theta_g = 1 - \delta \tag{1.10}$$

θ_g - the grazing angle

δ - refractive index decrement

Equation 1.10 can be further simplified to Equation 1.11 when $\delta \ll 1$.

$$\theta_g = \sqrt{2\delta} \tag{1.11}$$

Finally the Equation 1.11 can be combined with a simplification of the refractive index decrement as shown in Equation 1.12 (where Z is the atomic number) (Aschenbach 1985),

$$\delta = N_A \frac{r_0 Z}{A 2\pi} \rho \lambda^2 \tag{1.12}$$

to form Equation 1.13 (assuming a Z/A ratio of ~ 0.5).

$$\theta_g = 5.6\lambda\sqrt{\rho} \tag{1.13}$$

In reference to Equation 1.13: λ is in ångströms and ρ in g/cm^2. However it should be stressed that this is a simplification and that Equations 1.2 and 1.3 provide a better representation of δ; Equation 1.13 does highlight the dependence of wavelength and density of interacting material upon grazing angle. In conclusion, Equation 1.10 highlights that for $\delta \ll 1$, which is the case for X-rays, the grazing angle θ_g is typically around 1 °. These shallow grazing angles require the development of telescope optics which are almost parallel to the incident X-rays. The geometries of such optics shall be presented in Sections 1.1.5 and 1.1.6.

1.1.4 Scattering

The Fresnel equations assume a perfectly smooth reflective surface; this condition is impossible to obtain in a practical working environment. Therefore it is inevitable that some of the incident X-rays will become scattered by their reflective surface. The roughness of a surface is measured using metrology instruments; several examples are provided within this thesis and they typically provide an evaluation of the roughness in terms of Ra and Rq. Ra is the deviation of the surface from a mean value and Rq is the root mean square (rms) of Ra: both notations are used within this thesis. When estimating the scatter from a surface, the total integrated scatter (TIS) equation can be used (Equation 1.14 (Driggers 2003; Elson *et al.* 1983))[2]. The equation assumes that the roughness (Rq) is a gaussian distribution and the same in both in-plane directions (Friedman & Miller 2004), therefore the equation provides an estimation rather than a definitive answer for the scatter experienced by an incident ray. The equation, as shown, predicts the fraction of the incident rays that will be scattered from a surface. For example, if 10% scatter was acceptable by a surface then the resultant roughness (Rq) would have to be 1.54nm rms (for θ_i = 1.163 °, λ = 1.19nm). A rule-of-thumb would be that a surface should not have roughness that exceeds the wavelength of the incident ray:

$$TIS = 1 - exp\left[-\left(\frac{4\pi sin\theta_i \sigma}{\lambda}\right)^2\right] \tag{1.14}$$

θ_i - the angle of incidence of the system

σ - the rms roughness of the surface

λ - the wavelength of the incidence wave

1.1.5 Kirkpatrick-Baez

The Kirkpatrick-Baez (KB) configuration was first proposed in 1948 in the paper Kirkpatrick & Baez (1948). The system consists of two orthogonally positioned cylindrical mirrors each of which provides a line focus, as shown in Figure 1.4. To increase the collecting area of the system the optics can be stacked/nested. An advantage of the KB system is that the optics are relatively easy to manufacture due to curvature in a single direction. Although the KB system is not generally used in X-ray telescopes, primarily due to its lack of axial symmetry, it is still considered as a viable

[2]The TIS equation can be used at all wavelengths

technology. Papers by Willingale & Spaan (2009) and Rajan & Cash (2005) highlight different uses of KB optics for future X-ray missions.

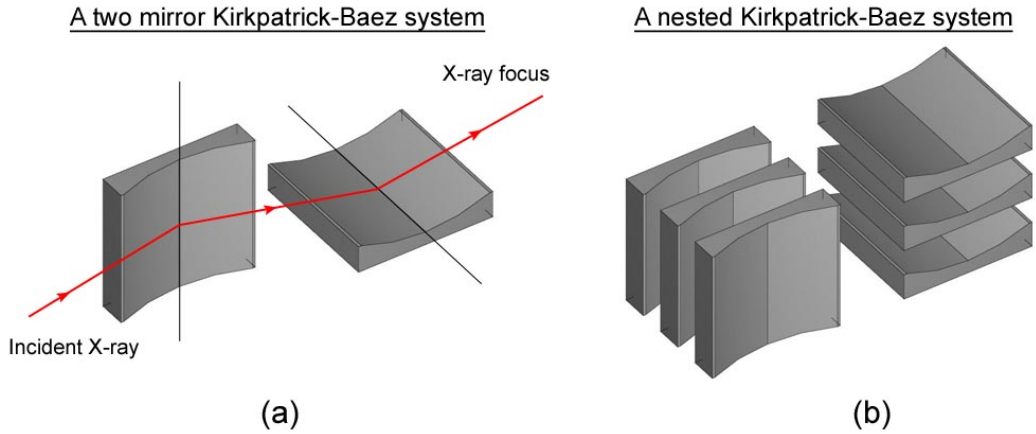

Figure 1.4: A schematic of the Kirkpatrick-Baez telescope system. Image **(a)** highlights the two mirror combination where incident X-rays are first focussed to line (reflection one) and then focussed to a point (reflection two). Image **(b)** depicts how the two mirror system can be nested to increase the effective area of the system.

1.1.6 Wolter Geometries

The Wolter geometries (Figure 1.5) were first proposed in 1952 in the paper by Wolter (1952). The advantage of the Wolter system is the axial symmetry along which the optics operate. The Wolter system uses two reflective surfaces to remove the effect of aberrations, the two optics are co-axially aligned and there are three configurations (Figure 1.5[3]):

Type I - involves two internal reflections from a parabola followed by a hyperbola.

Type II - uses an internal reflection from a parabola followed by an external reflection from a hyperbola.

Type III - has an external reflection from a parabola followed by an internal reflection from an ellipsoid.

The Type I geometry is most commonly used within astronomical optics and this is due to the ability of the optics to be fabricated out of a single piece of material and to be nested. Figure 1.6

[3]This figure was originally obtained from the website `www.roe.ac.uk/~jcm/thesis/node44.html`; however a similar representation can be found in Aschenbach (1985)

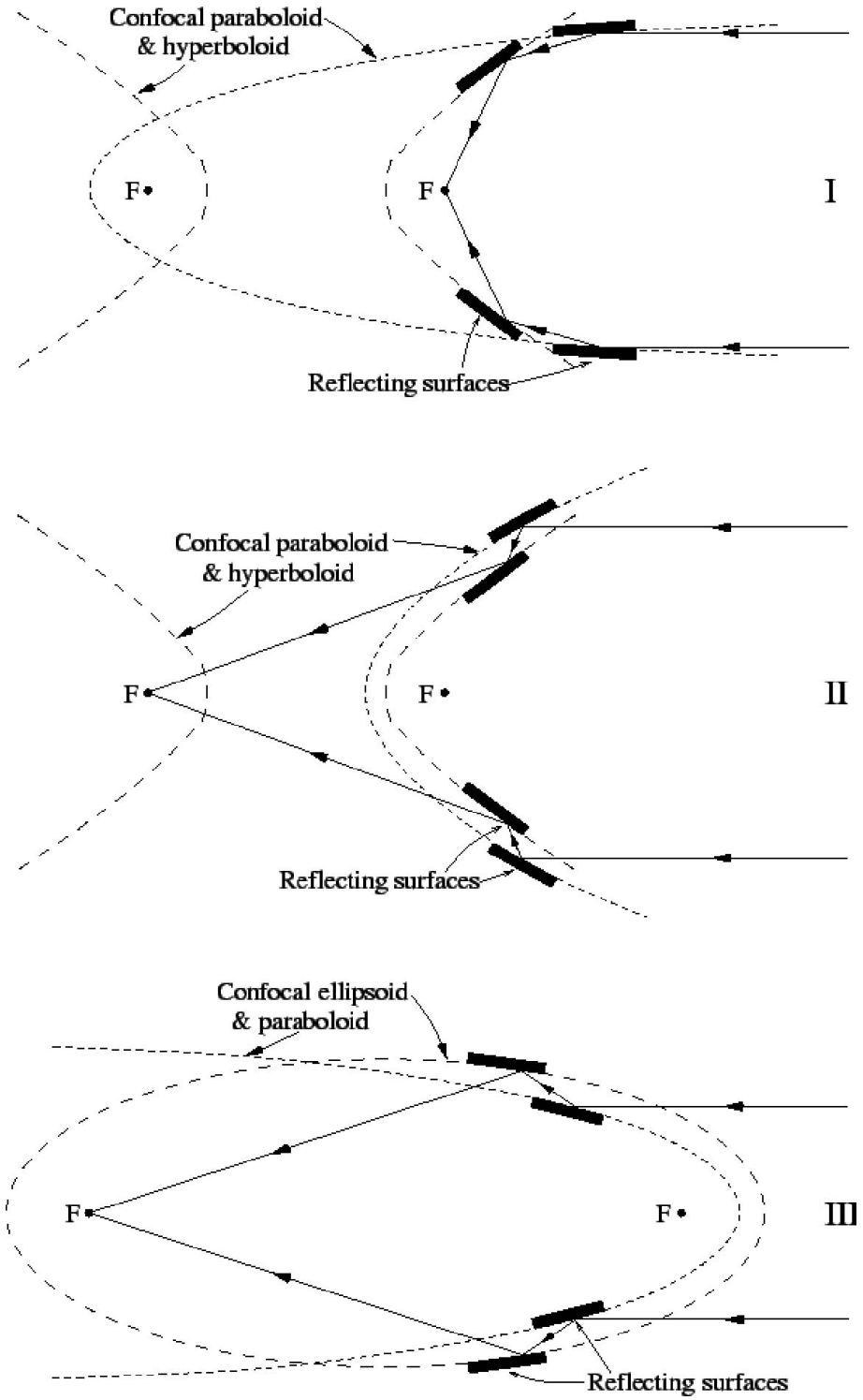

Figure 1.5: The Wolter optical configurations, Type I is most commonly used in astronomical X-ray telescopes.

highlights how the Wolter geometries are used within a telescope system. The geometries are revolved around 360 ° (only 180 ° is shown in the figure). The geometries are then nested, so that optics with decreasing radii of curvature are positioned inside each other and they are aligned co-axially. Nesting the optics increases the effective area (the area viewed from the X-rays' perspective) and as a result the intensity of the imaged object; however, there is a limit between increasing the effective area and decreasing the open area available to incident X-rays.

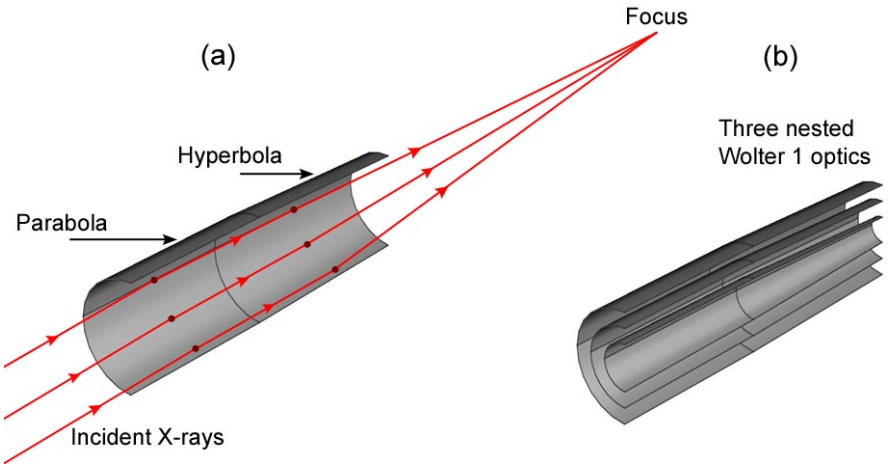

Figure 1.6: Image **(a)** highlights a 180 ° cross-section through a Wolter 1 geometry used for astronomical telescopes. Image **(b)** depicts how the optics are nested co-axially to increase the effective area of the system.

1.2 Production of X-ray optics

X-rays from astronomical sources cannot be detected from the ground due to their absorption within the Earth's atmosphere, therefore X-ray telescopes are space borne observatories (Zeilik & Gregory 1998). In addition, the flux from X-ray sources often tends to be low due to vast distances between source and observer. These considerations have to be taken into account when developing optics for X-ray observatories. This Section will present the past, present and future technologies for X-ray telescope optics. The first three methods, which are summarised in the paper by Willingale (1999), have been used in the production of X-ray telescopes to date, the later two are examples of technology development intended for future X-ray missions.

Prior to the discussion on X-ray telescope optics it would be prudent to outline the two methods in which angular resolution is defined. The full width at half maximum (FWHM) and the half energy width (HEW) are both used to describe angular resolution and the distinction between the

widths is outlined below for the function $f(x)$:

FWHM - is the width x_1 to x_2, whose points are defined as being half the of the maximum of function $f(x)$

HEW - is the width x_a to x_b, whose points are defined as containing half of the integral, between $+\infty$ and $-\infty$, of function $f(x)$.

It should noted that both widths are used throughout this thesis.

1.2.1 Monolithic optics

Monolithic optics are produced from a single piece of material: the material tends to be a ceramic glass, such as Zerodur, due to its thermal stability. The Wolter I geometry is drilled out of the glass and then ground to achieve the correct thickness and optical figure [4]. Afterwards the optic is superpolished to achieve a high quality surface finish to minimise the effect of scattering. Finally, the reflective surface of the optic is coated in a heavy element metal to provide increased X-ray reflectivity.

These optics have excellent form after production (leading to high angular resolution) and this is a result of the optics' structural stability. However, monolithic optics are heavy in comparison to the optics discussed in Sections 1.2.2 to 1.2.4, therefore fewer can be used per given weight budget and their thickness prevent the optics from being heavily nested. Examples of missions that have employed monolithic optics are ESA's ROSAT mission (Aschenbach *et al.* 1982) and NASA's Chandra X-ray Observatory mission (Weisskopf & O'Dell 1997).

1.2.2 Replicated optics

These optics are created via depositing metal ions upon a mandrel (mould) with the inverse form of the optic required: typically by electroforming. Nickel (Pareschi *et al.* 2005) or nickel-alloy (Ramsey 2005) is generally used as the deposited metal, as it offers low stress within the replicated optic. The optics replicate the surface form and roughness of the mandrel, therefore production of a high quality mandrel is paramount to obtain good quality optics. The optics are removed from the mandrel with the use of a release agent and a mechanical or thermal shock. Once the optics have been released from the mandrel no further finishing processes are required as the reflective surface is replicated from the mandrel. An advantage of this system is that a single

[4] *figure* and *form* are used throughout this thesis to describe the shape of an optic.

mandrel can be used to replicate multiple optics. The method of replication is demonstrated in Figure 1.7, using the X-ray telescope XMM Newton as an example.

Replication via metal deposition is capable of producing sub-mm thick optics which can be nested to increase the effective area without significantly sacrificing the available aperture. However, the optics tend to have a poor form in comparison with their monolithic counterparts and this is a result of residual stress within the deposited metal and reduced structural stability. Nevertheless, with careful integration of the optics within the telescope mounting, acceptable resolution can be obtained and a prime example of such a system is the European Space Agency's (ESA) XMM-Newton mission.

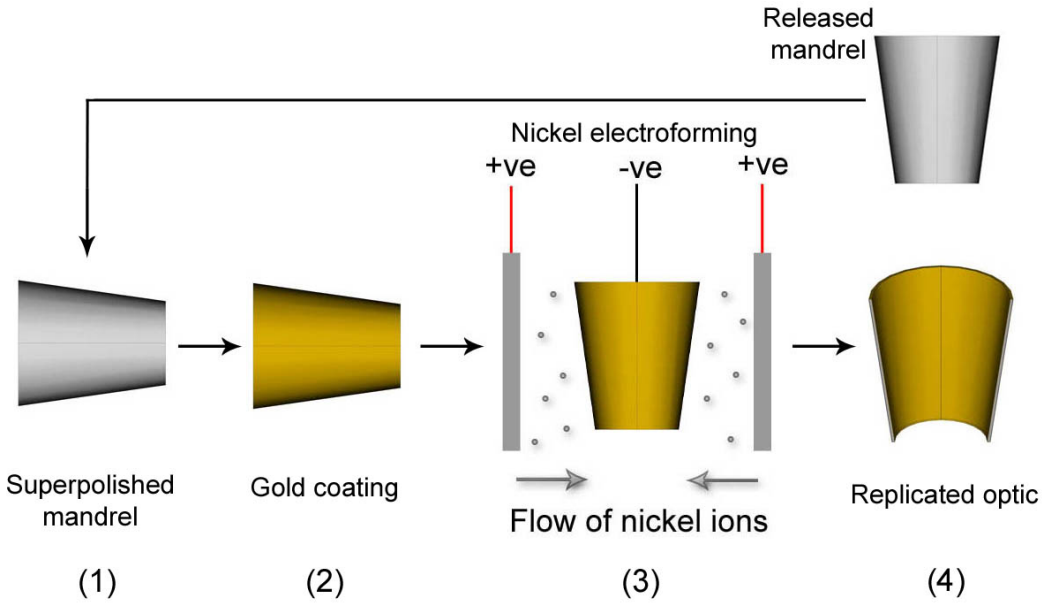

Figure 1.7: Production of XMM Newton's telescope optics via nickel electroforming. (1) The superpolished mandrel is cleaned. (2) The mandrel is gold coated to provide a release agent for the nickel deposit. (3) Nickel ions are electrodeposited upon the mandrel until the desired thickness is obtained. (4) The optic is released and the mandrel can be used to replicate further optics (the optic shown in the figure is a cross section of a complete optic revolution).

1.2.3 Foil optics

Foil optics are exceptionally thin and tend to be a conical approximation of the actual desired Wolter I geometry. They are produced via epoxy replication. The optic's coating (for example gold) is deposited upon a mandrel (of the inverse form) and epoxy is used to bond thin aluminium sheet

to the reflective coating. The resulting thickness can range from $\sim$130 μm to $\sim$ 200 μm allowing the optics to be heavily nested to provide a large effective area. These optics are not replicated with angular resolution as a priority and therefore further alignment concessions can be made by not replicating the optics in full revolutions, but rather as a fraction of the total 360 °. Examples of this technology employed within X-ray telescopes would be Japan's ASCA mission (Inoue 1993) and its up and coming Astro-H mission (Furuzawa *et al.* 2009).

1.2.4 Future technologies

The development of new technologies is being driven by the next generation of X-ray telescopes and in particular the International X-ray Observatory (IXO) is at the fore front of this technology drive. IXO is collaboration between NASA, ESA and JAXA[5] and it aims to achieve an effective area of $3m^2$ at 1.25keV with a resolution of 5 arc-seconds. However it requires a new optics technology to achieve the sensitivity without exceeding the weight budget. The two contenders are silicon pore optics (SPO) and slumped glass optics (SGO) and both shall be presented within this section.

SLUMPED GLASS OPTICS - The fabrication of optics via the slumped glass process is described in Figure 1.8; the method shown is employed at NASA's Goddard Space Flight Centre; however, variations on the method are also available (Ghigo *et al.* 2009). Commercially available flat glass sheets (400 μm thick) are placed upon mandrels with the correct optical figure. They are then placed within an oven and heated to 600 °C and the glass sheet deforms under its own gravity to take the form of the mandrel. An anti-sticking agent is used to prevent the glass bonding to the mandrel. The cooled optics are then cut using a hot wire to the desired geometry: the edges of the glass are avoided as they do not conform accurately to the mandrel. The optics are then coated with a high atomic number element, such as iridium, to enhance the optic's X-ray reflectivity (Zhang *et al.* 2009*c*).

It is hoped that the technology will provide similar optical properties to that of nickel replication, with advantages being that the glass sheet is cheap, commercially available and significantly lighter than nickel. This style of optics is currently being produced for the NuSTAR X-ray mission (Zhang 2009), where cylindrical optics are being manufactured which are then deformed to a conic approximation while being integrated within the optic's housing. An example of NuSTAR's optics taken from the oven is shown in Figure 1.9. NuSTAR is a high energy X-ray mission aiming to achieve an angular resolution of 46 arc seconds with a large effective area above 7keV and it will focus the high energy X-rays through multilayer coatings upon the slumped glass optics (Koglin

[5]Japanese Space Agency

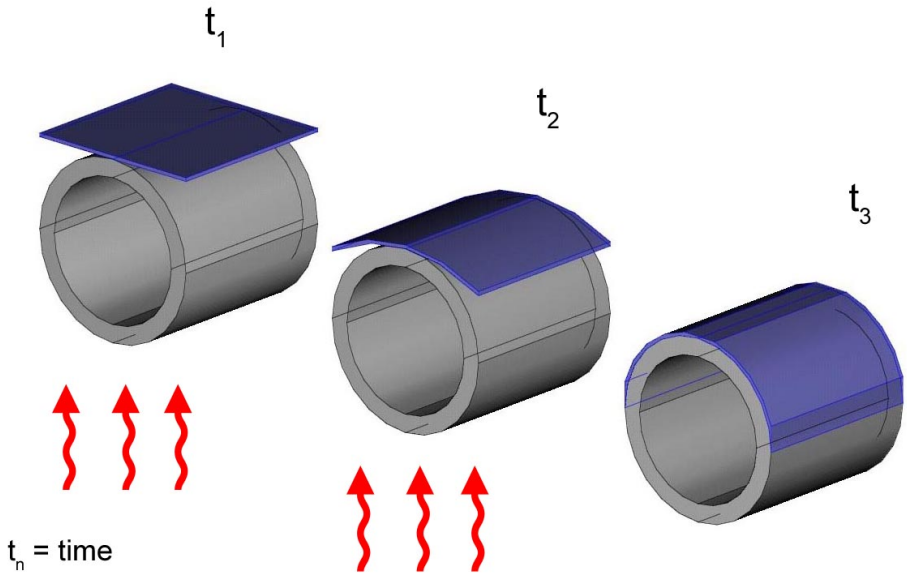

Figure 1.8: Flat sheets of glass (indicated as blue within the figure), $\sim 400\mu m$ thick, are placed upon a mandrel of the inverse form of the optic required (t_1), the optic is then uniformly heated (t_2) and the sheet deforms to the shape of the (t_3). The mandrels can be recycled and used to produce many optics.

et al. 2009).

SILICON PORE OPTICS - These optics are significantly different from the previous technologies discussed in Sections 1.2.1 to 1.2.3. Instead of nested shell segments, 'ribbed' silicon wafers are bonded in stacks, providing the X-rays with channels to interact against; however the system is still based upon a Wolter I geometry. The manufacture of silicon pore wafers is outlined by Riekerink *et al.* (2009). Commercial silicon wafers are diced into square plates of the required size and then 'ribbed' to form parallel channels down the length of the plate. The plates are then stacked and wedged (Figure 1.10); this is done to provide increased reflective area (similar to nesting) and to position the plates in a conical Wolter I approximation, respectively.

For IXO it is proposed that each mirror module is composed of two sets of SPO mounted to provide a parabola and hyperbola approximation to a Wolter I geometry. The mirror models are then integrated within 8 petals, which are 45 ° of a 360 ° aperture. The advantage of SPO is their structural stability due to the monolithic structure of the mirror modules in comparison with their slumped glass counterparts. Current X-ray measurements of this technology indicate a resolution of 4" half energy width (HEW) for a single SPO pore and 17" HEW for four mirrors (Wallace *et al.* 2009). This is very much a developing technology.

Figure 1.9: Optics being produced at the NASA's Goddard Space Flight Centre (GSFC) for the forth coming NuSTAR mission. In the photo the optics have just been removed from the oven and have formed to the shape of the mandrel; the mandrels are quartz cylinders leading to a cylindrical optical profile. Figure courtesy of CHF.

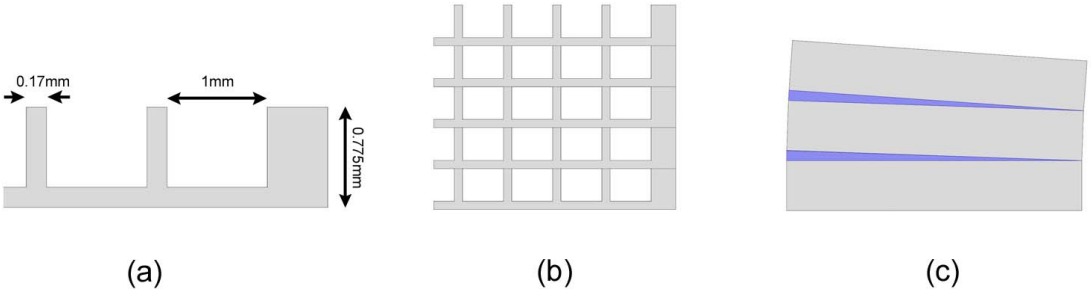

Figure 1.10: The production of a silicon pore optic. **(a)** - The silicon wafers have channels cut into them. **(b)** The silicon plates are then stacked and in addition they are wedged as shown in image **(c)** (the orientation of image **(c)** is along the channel walls).

Table 1.1: An overview of the X-ray telescopes (Willingale 1999)

	Chandra	XMM Newton
Launch date	1999	1999
Optical configuration	Wolter I	Wolter I
Shell material	Zerodur	Nickel
Reflective coating	Iridium	Gold
Focal length	10.069m	7.5m
Angular resolution	0.5 arc-seconds	8 → 15 arc-seconds
Outermost mirror diameter	1200mm	700mm
Innermost mirror diameter	620mm	300mm
Mirror shell thickness	20mm → 40mm	0.4mm → 0.72mm
Number of mirror shells per telescope	4	58
Optic production method	Monolithic	Replicated

1.3 Astronomical X-ray telescopes

The origin of X-ray astronomy lie in the rocket missions of the 1940s/50s that identified the Sun as a source of X-rays. The first X-ray source outside our solar system was identified in 1962 as Sco-X1, which is a low mass X-ray binary star (Shklovsky 1967). All the early X-ray observations were via collimated X-ray detectors, not X-ray telescopes; therefore it was not until 1978 with the launch of NASA's Einstein Observatory (Giacconi *et al.* 1979) that the first X-ray images were obtained. In comparison with optical telescopes, X-ray telescopes are still in their infancy; however there has been a continual development in the past decades, leading to such notable telescopes as EXOSAT (de Korte *et al.* 1981), ROSAT (Aschenbach *et al.* 1982), ASCA (Inoue 1993), XMM Newton (Jansen *et al.* 2001) and the Chandra X-ray Observatory (Weisskopf 2003).

This section will not provide a detailed account of each telescope system, but rather focus on the two most recent observatories: XMM Newton and the Chandra X-ray Observatory. By comparing these telescopes (Table 1.1), the current limitations in astronomical X-ray optics will be identified and the advantages of an active X-ray telescope, which is foundation of this thesis, will be presented.

1.3.1 The Chandra X-ray Observatory - summary

NASA's Chandra X-ray Observatory was launched in 1999 and is still providing the X-ray astronomical community with high resolution X-ray images to date. Chandra has a highly elliptical orbit of 63.5 hours and it capable of obtaining data for 70% of that time (Weisskopf 2003). The optical component (Figure 1.11) of the observatory consists of 4 monolithic Wolter I optics which provide an impressive angular resolution of 0.5 arc-seconds. The Zerodur substrate of the optics was coated in iridium to provide X-ray reflectance. The effective area of the optics is 800cm^2 at 0.24keV, 400cm^2 at 5.0keV and 100cm^2 at 8.0keV.

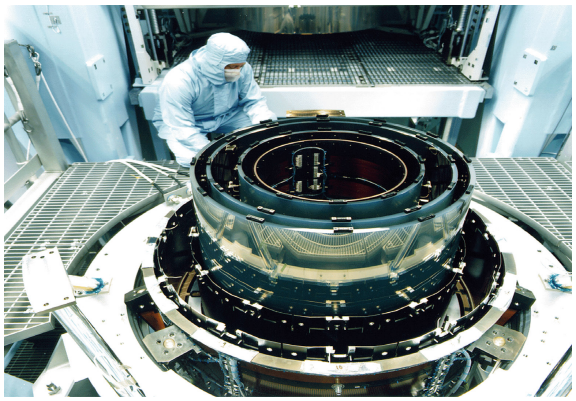

Figure 1.11: The mirrors of the Chandra X-ray Observatory, (NASA/CXC/SAO)

1.3.2 XMM-Newton - summary

The XMM Newton observatory was launched in the latter part of 1999 as part of the ESA's Horizon 2000 program. The observatory consists of three identical X-ray telescopes each containing 58 mirror shells (174 shells/optics in total). The optics were fabricated via the replication method as outlined in Section 1.2.2 and an example of one end of one of the telescopes is shown in Figure 1.12. Gold was the release agent for the optics from the mandrel and therefore is the X-ray reflective coating upon the optics. The thickness of the optics (0.4mm $\rightarrow$ 0.72mm) allows them to be heavily nested without significant loss in aperture area and this leads to an increase in the effective area, 1475 cm^2 at 1.5keV and 580 cm^2 at 8keV per telescope, and therefore sensitivity. Although the sensitivity is greater than that of Chandra, its angular resolution is limited to 8 - 15 arc-seconds (HEW).

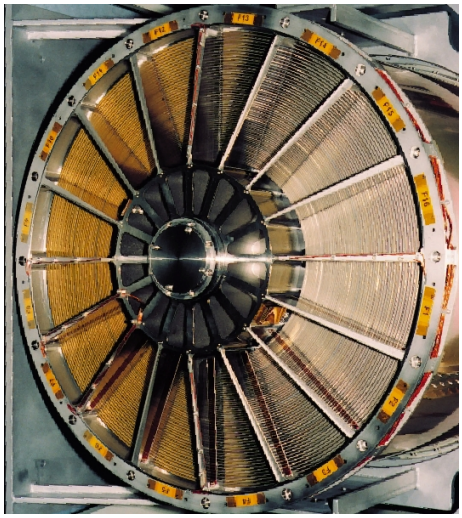

Figure 1.12: The aperture of one of the three XMM-Newton telescopes, courtesy of ESA.

1.3.3 High Resolution versus high sensitivity

The launch of both Chandra and XMM Newton in 1999 provided the astronomical X-ray community with two complementary telescopes, providing high resolution and high sensitivity respectively. Their different optical performance stems from the production methods used to manufacture the optics and as a result neither telescope could offer both attributes. The problem of combined resolution and sensitivity will not be solved in the immediate future of X-ray telescopes, with mission proposals such as the International X-ray Observatory only looking to improve upon sensitivity. The core of the problem is weight constraints imposed by the launch vehicles used to elevate the observatories into orbit. Monolithic optics, which provide excellent resolution, are heavy and therefore a limited number of optics can be nested; conversely, replicated optics are relatively light but structurally weaker and can be heavily nested to increase the effective area.

This is the problem that the Smart X-ray Optics' (SXO) prototype is investigating, to produce a lightweight optic that can be heavily nested but also provide high angular resolution. The proposed prototype design can be considered as a synergy between traditional X-ray optic technology and adaptive optics (AO) used in ground based telescopes. AO improves the resolution of a ground based telescope by correcting for the distortions caused by the turbulence within the atmosphere in real-time. However, an X-ray telescope has no atmosphere to correct for, instead the active element will correct for distortions within the form of the optic, therefore lightweight structurally weaker optics can be used and their figure corrected through active control. This technology is

active rather than adaptive as there is no requirement to continuously adapt the optic for real-time distortions, instead the active nature will be used to optimise the form of the optics and hold them in that position.

Although the concept of actively adjusting a large number of actuators upon a large number of nested optics is a daunting task, the research is not without support. In early 2000 NASA proposed the Generation-X mission (Gen-X). This mission aims to achieve a 50 m^2 effective area with a resolution of 0.1 arc-seconds and it intends to attain this resolution through active control of its optical elements.

1.3.4 Generation-X

The Generation-X mission proposal is part of NASA's Vision Missions for the decade 2020 - 2030. It is thought that the mission will aim to achieve a resolution of 0.1 arc seconds while providing an effective area of 50 m^2 (Schwartz *et al.* 2008), in comparison with XMM Newton's effective area which is approximately 0.15m^2 at 1.5keV (Stockman *et al.* 1999). It is expected that the optics will follow the traditional Wolter I geometry, having a paraboloid primary and a hyperboloid secondary. The focal length is expected to be in the range 50 - 60 m and the aperture diameter in the range 8 - 16 m. Rather than having the traditional complete nested shells, Generation-X proposes the use of small segments (1 m $\times$ 1 m), which combined produce the full 360 $^\circ$ revolution of the shell. Iridium coated glass slumped segments are currently favoured for the optical component of the system as glass has a significantly lower density than XMM Newton's nickel optics.

The active nature of the optics will be attained through the addition of piezoelectric actuators; currently two distinct styles are being considered: 'bimorph' and 'radially adjustable' mirrors (Reid *et al.* 2008). In the bimorph[6] configuration a thin layer of piezoelectric material is directly deposited upon the the reverse of the optic (i.e. the non reflecting surface), then combined with a sectioned electrode pattern. A displacement is generated in-plane with the the optical surface. It is thought in total, a range of $10^6 - 10^7$ separate actuator regions is required. Radially adjustable mirrors rely on actuators being placed at distinct intervals and they move normal to the optic's surface. The active nature of both designs is for the occasional correction of the telescope system. The initial optimisation of the system would occur during the deployment phase of the telescope and further corrections could be applied infrequently to correct for drift over time.

[6] bimorph refers to the two layers in the optic-piezoelectric composite

1.3.5 What is the science case for Generation-X?

Inevitably the development of any new technology must have precursory science objectives. To gain future funding for the Generation-X mission proposal, a series of *White Papers* were produced for the United States' Decadal Survey[7]. The following White Papers were submitted in February 2009 and they outline the science case for Generation-X:

- The Formation and Growth of the First Black Holes (Lehmer *et al.* 2009)
- Active Galaxies and Quasars (Elvis *et al.* 2009)
- Supernovae and Their Consequences: Studies with the Generation-X Mission (Slane *et al.* 2009)
- Accreting Binary Populations and ISM Evolution in Galaxies (Zezas *et al.* 2009)
- X-Ray Studies of Stars and Planets with Ultrahigh Sensitivity and Resolution (Wolk *et al.* 2009)

Presented below is a summary of the white papers and examples where high resolution and high sensitivity are both required to further the understanding of a variety of astrophysical processes.

THE FORMATION AND GROWTH OF THE FIRST BLACK HOLES - It is theorised that the first populations of black holes were formed at a redshift between z$\sim$15-20, caused by the death of the first massive stars. Interactions of these first black holes with dense nebulous gas and other black holes leads to the creation of the first galaxies and the continuing growth of the black holes through accretion. X-rays are an extremely effective method in probing the immediate vicinity of an accreting black hole as X-rays can penetrate through obscuring material. The International X-ray Observatory (IXO) will be capable of probing red-shifts of z$\sim$7-8. However to view the creation of these first black holes at z$\sim$8-15 requires the detection of extremely faint sources and the ability to distinguish between them. Lehmer *et al.* (2009) suggests that to achieve this goal, a telescope with an effective area of 50 - 100 m^2 and an angular resolution of 0.1" (arc-seconds) will be required.

ACTIVE GALAXIES AND QUASARS - Active galaxies and quasars (quasi-stellar objects) are both forms of galaxies that have an active galactic nuclei (AGN) (quasars are an extreme example of active galaxies). The AGN occurs primarily due to mass accreting upon the central super massive black hole (SMBH) and subsequently releasing vast amounts of energy. The majority of galaxies, like our own, have SMBH at their hearts, the difference is that the SMBHs in the majority of

[7] an assessment of the allocation of funds for the up-coming decade

galaxies are dormant and don't expel the vast amount of energy observed from active galaxies and quasars. Although active galaxies and quasars have been studied for several decades many questions still remain, in particular regarding: the growth of the SMBH; the reason why the majority of SMBHs are dormant; how quasars accelerate matter up to the highest energies and how an AGN affects galaxy evolution. In the case of how do SMBHs grow, the high sensitivity that Generation-X will provide would allow the growth phase when $z > 7$ to be studied. In addition, the high angular resolution offered by Generation-X could probe the growth path of SMBH mergers. For two SMBHs separated by 1kpc this distance represents approximately $\sim$0.17" at $z > 1$, therefore to study these merger events $\sim$0.1" resolution is required.

SUPERNOVAE AND THEIR CONSEQUENCES: STUDIES WITH THE GENERATION-X MISSION - A supernova is the final stage in the lifetime of a massive star and is characterised by a rapid core collapse followed by violent explosion. Supernovae events can be used to determine a number of astrophysical phenomena, for example in their use as *standard candles* and in the chemical evolution of galaxies, to name but a few. The study of the aftermath of the supernova, the supernova remnant (SNR), provides a description of the form of the ejecta (both in terms of shape and composition), the shock waves and winds they create, and the compact object that remains at the core of the SNR. One particular use stated in the paper by Slane *et al.* (2009) would be the use of Generation-X in the determination the progenitor systems in type Ia supernovae which are the standard candles used in cosmology to study the expansion of the universe. The investigation of X-ray emission when the supernovae are young provides a description of the circumstellar material (CSM) in which the binary pair inhabited and therefore allowing a description of the binary pair themselves. However, to study this faint X-ray emission and to be able to distinguish it from other galactic X-ray sources requires both the high sensitivity and resolution proposed by Generation-X.

ACCRETING BINARY POPULATIONS AND ISM EVOLUTION IN GALAXIES - The paper by Zezas *et al.* (2009) discusses the opportunity to observe individual X-ray sources (such as accreting X-ray binaries, supernovae remnants and the hot interstellar material (ISM)), not just within our own galaxy but within more distant galaxies. One of the difficulties in observing these discrete X-ray sources comes from the X-ray background, a combination of hot ISM and fainter X-ray sources. By increasing both sensitivity and resolution the number of sources which can be observed will be significantly increased. One of the examples voiced within the paper is a discussion on the chemical enrichment of the hot ISM due to star formation regions and how this is diffused from the star formation region into interstellar space. This is particularly interesting as the metal rich gas can then form part of the next generation of stars and planets. In this case high

resolution is paramount to study the gas close to where it has been energised and to isolate it from contaminating X-ray binary emission.

X-RAY STUDIES OF STARS AND PLANETS WITH ULTRAHIGH SENSITIVITY AND RESOLUTION - One of the closest X-ray sources to Earth is that of the Sun and its hot X-ray emitting corona. Within the paper by Wolk *et al.* (2009) a study of the X-ray emission from individual stars and planets is discussed. One particular example is an investigation of the X-ray emission from stars which have close orbiting hot Jupiters. Stars which have hot Jupiters orbiting at a distance greater than 1.5AU[8] have reduced X-ray activity compared with stars which have hot Jupiters orbiting at a distance less than 0.5AU. While future telescopes, such as IXO, will be able to statistically study this effect, the physical nature of the interaction between star and planet cannot be determined without the sensitivity offered by Generation-X.

Further to the examples presented, a summary of the science case for Generation-X can be found within the papers by Wolk *et al.* (2008) and Windhorst *et al.* (2006).

1.4 Active X-ray optics - the synchrotron community

The previous sections have discussed: the science of X-ray telescope; the fabrication of their optics; current and future X-ray observatories and the science case for continued research into X-ray telescope technology. This final section will discuss how active X-ray optics are currently being employed within synchrotron facilities; in particular highlighting the differences/similarities between the synchrotron and telescope technologies.

1.4.1 Piezoelectric bimorph mirrors

In recent years many new Synchrotron facilities have been built. These more powerful facilities offer a larger range of X-ray experiments that can be undertaken, for example: X-ray spectroscopy, microscopy and microanalysis. Therefore these applications require flexible X-ray optics to focus the synchrotron source upon the instrument. Many facilities employ mechanically bent optics: where a flat mirror substrate is bent to provide an ellipsoidal mirror (Howells *et al.* 2000). However, an alternative approach uses piezoelectric bimorph mirrors (PBM), which alter the focussing capability of the optics via piezoelectric control (Signorato *et al.* 1998).

A PBM has two layers of piezoelectric material, typically lead zirconate titanate (PZT), sandwiched between two silica layers. The composite is created by first bonding one PZT layer to a silica

[8] 1AU (Astronomical unit) = $\sim 1.5 \times 10^{11}$ m, the average distance between the Earth and the Sun

layer and polishing the silica surface to a concave form; this is done to both PZT-silica components. The piezoelectric material is then poled normal to their surface: this determines the direction of the expansion and contraction within the piezoelectric material. Finally, the two external faces of the piezoelectric material are bonded to form a silica - PZT - PZT - silica composite mirror, as shown in Figure 1.13. There are three electrodes that provide the potential difference to the system. The 'ground' electrodes are at the interfaces between the silica and PZT layers and the driving potential is supplied by an electrode at the PZT - PZT interface (Signorato & Ishikawa 2001).

Figure 1.14 highlights the orientation of the poling axis **P** in relation to the direction of the electric field **E**. When a driving potential V_D is applied, the different orientation of the electric fields in comparison with the poling axis in the PZT material causes one PZT layer to contract and the other to expand. The result is an overall bending of the PBM system and this is the foundation of active X-ray optics within synchrotron facilities.

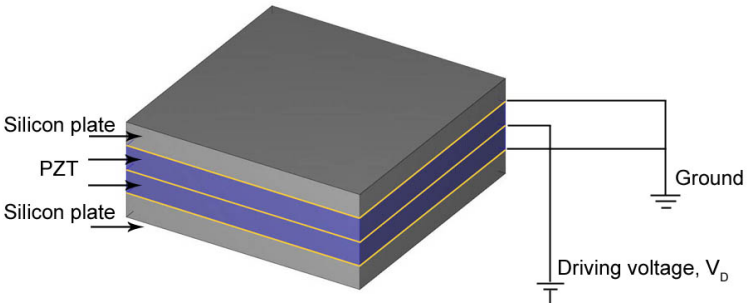

Figure 1.13: A section of a PBM: highlighting the composite structure and the electrode arrangement.

1.4.2 Synchrotron versus the telescope

The synchrotron community has been using PBMs for almost a decade to provide active X-ray focussing; however an X-ray telescope has different constraints and these are outlined below.

WEIGHT - Synchrotron PBMs are not restricted to a weight budget imposed by a launch vehicle.

X-RAY SOURCE - Synchrotrons have a powerful X-ray source, whereas the X-ray flux from astronomical objects tends to be low.

SINGLE OPTIC - Only a single optic is required within a synchrotron facility in comparison with X-ray telescopes which require optics to be nested to increase their collecting area.

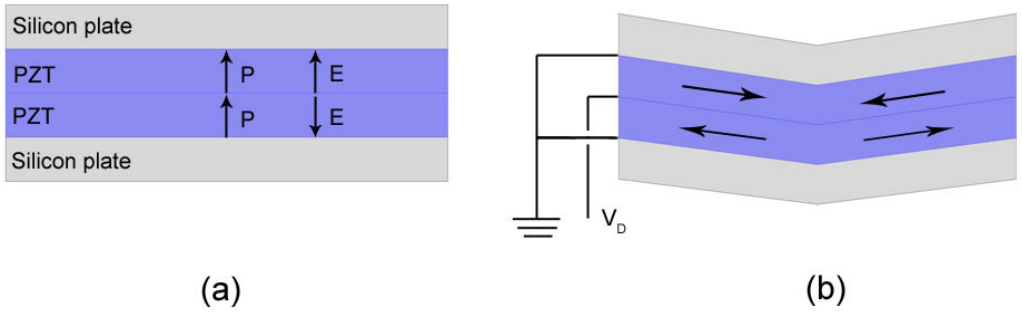

Figure 1.14: Image **(a)** highlights the poling of the PZT material in relation to the electric field. Due to the alignment of the electric fields with respect to the poling axis, the application of a driving voltage V_D causes an expansion of one PZT layer and a contraction within the other, resulting in an overall bending of the system, image **(b)**.

MANUFACTURING METHODS - In a PBM the PZT is first bonded to the silica substrate before the composite is polished to the correct figure to remove errors incurred due to the bonding. However, this would be difficult to implement for a telescope optic which are often produced via a replication process.

Despite the differences between the technologies there are points of common interest. Signorato *et al.* (1998) states the presence of *junction effects* between the PZT actuators (there are several actuators within a PBM), the precise cause of these junction effects are not given; however, it is possible they stem from shrinkage within the bonding layer as they are visible in a 0V profile. There are also characteristics, such as piezoelectric hysteresis and an optimising routine which are applicable in both systems. Therefore there are similarities within the two systems; however, the design of the optics and their implementation will be different.

1.5 Chapter summary

This introduction has looked to outline the drivers and methods for the production of an active X-ray prototype intended for astronomical applications. The optical constraints upon an X-ray focussing system have been described and production methods of astronomical X-ray optics investigated. The need for development of this research has been explained and the application of the prototype examined. Finally active X-ray optics within synchrotron facilities have been discussed and the difference between the technology development established. The following chapter presents the

SXO prototype, its design, intended manufacturing methods and its eventual operation within an X-ray facility.

CHAPTER 2

THE SMART X-RAY OPTICS PROTOTYPE FOR ASTRONOMICAL APPLICATIONS

This chapter is divided into two sections. The first will outline the Smart X-ray Optics' (SXO) large scale prototype highlighting: the collaborative nature in its design; the intended production methods and its operation within the X-ray environment. The second section will describe finite element analysis models investigating the prototype's gravitation sag and the actuators' influence functions and how these have been used by the University of Leicester within their ray-tracing code to determine the effect upon the detected X-ray image.

2.1 The smart X-ray optics' active X-ray prototype

The design of the SXO prototype was built upon a proof-of-concept study undertaken by the consortium from 2004 to 2005 (Doel *et al.* 2006; Atkins *et al.* 2007), which highlighted the ability to use thin ($500\mu m$) actuators, bonded upon the reverse of a substrate, to manipulate the substrate's optical form. The following section will outline the design and proposed fabrication methods for the ellipsoidal prototype and the role of each SXO consortium member in its development. In addition, the work undertaken within this thesis will be placed in context within the large scale prototype development as a whole.

2.1.1 The ellipsoidal prototype

An overview of dimensions of the prototype is shown in Table 2.1 and a schematic of the system is shown in Figure 2.1. The prototype is a 300 mm $\times$ 100 mm section from an ellipsoid where X-rays

Table 2.1: An overview of the ellipsoidal prototype

The dimensions of the ellipsoidal prototype			
The optic		The actuators	
Axial length	300 mm	Axial length	29 mm
Azimuthal length	100 mm	Azimuthal length	32 mm
Thickness	0.4 mm	Thickness	∼0.2 mm
Optical form	ellipsoidal off-axis	Actuator arrangement	Grid
Material	Nickel	Material	PZT

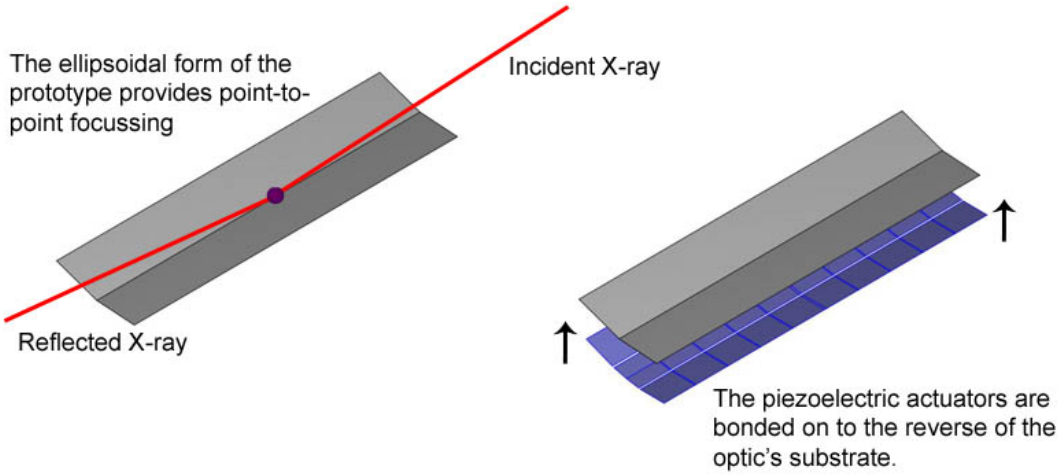

Figure 2.1: A schematic of the ellipsoidal prototype.

reflect from the interior surface and the actuators are bonded to the exterior. The nomenclature for the prototype system is outlined in Figure 2.2, the axial length/curvature is in the direction of the semi-major axis and the azimuthal length/curvature is in the direction of the semi-minor axis.

The optical form of the prototype's ellipsoid is outlined in Table 2.2. The ellipsoid has been fitted to the dimensions of the X-ray tunnel test facility (X-ray TTF) which will be used to test the completed prototype. The ellipsoid locates the X-ray source and the X-ray detector at the two foci therefore supplying point-to-point focussing of the optical system. Further information regarding the prototype's operation within the X-ray TTF will be presented in Section 2.1.3.

The optical component (the ellipsoidal reflector) will be nickel. To produce an optic with

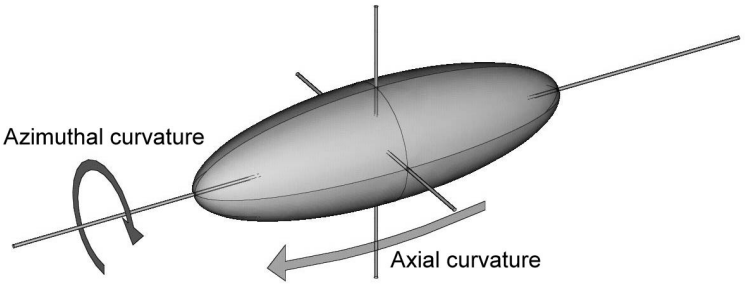

Figure 2.2: Definitions of the ellipsoidal form

Table 2.2: The optical specifications of the ellipsoidal prototype

Ellipsoidal prototype's optical prescription	
Semi major axis	14145 mm
Semi minor axis	228 mm
Position of the front of the optic (from the centre)	9442.5 mm
Position of the rear of the optic	9742.5 mm
Position of the rear from the detector	4402.5 mm
Radius at the front of the optic	169.761 mm
Radius at the rear of the optic	165.298 mm
Grazing angle	1.163°
Angle at the front	33.751°
Angle at the rear	34.662°
Sagital distance from a cone	0.0325 mm

the desired thickness and form electroforming shall be employed: the same method used by the European Space Agency (ESA) in the fabrication of XMM Newton's telescope mirrors. The selection of nickel was based on the X-ray reflective nature of the metal as well as the nickel electroforming facility based in-house at University College London (UCL). Production of X-ray optics via nickel electroforming, requires a low stress mechanism for nickel deposit (the electrolyte used in UCL's electrodeposition facility offers the lowest stress for any nickel deposit) and a mandrel, or mould, upon which to deposit the nickel. The mandrel will be made to the inverse form of that required, so that when the optic is released from the mandrel it has the desired optical form. The optical component of the ellipsoidal prototype will be fabricated at UCL to allow the electrodeposition process to be accurately monitored and adjustments to be easily made.

In addition to the constraints of optic form upon the mandrel, the surface must be polished to a quality that will provide X-ray reflectance. Using the total integrated scatter equation in Section 1.1.4, the maximum surface roughness can be calculated for given conditions. Therefore for the optic to provide a maximum scattering of 10% at 1.04keV (the energy used within the X-ray TTF and is equivalent to λ = 1.19nm) and at a grazing angle of 1.163 °, the maximum surface roughness allowed is 1.54nm root mean square (rms). This is therefore the bench-mark to which the mandrel will be polished.

The actuators that provide the active component of the prototype will be fabricated at the University of Birmingham's (UoB) School of Materials and Metallurgy. The piezoelectric material will be lead zirconate titanate (PZT), which is a polycrystalline ceramic often used in the production of actuators. The difficulty in the fabrication of the actuators lies in the requirement for thin ($200\mu m$) actuators that have the same azimuthal curvature as the optical component: this is to ensure a close fit between the actuators and the optical form and a minimal thickness for the prototype system as a whole.

The number of actuators was determined by the control capability already available at UCL. A 32-channel voltage output card is used to control the 30 actuators plus a common ground, therefore 31 channels out of 32 are used. The output of the voltage is multiplied by a factor of 20 to achieve a final voltage output of 0V - 200V. This is the same actuator control method as employed in the proof-of-concept project presented by Doel *et al.* (2006). However, improvements have to be made to the control system to operate all 30 actuators within the X-ray TTF.

The development of this novel technology required the production methods to be tested, prior to the completion of the ellipsoidal prototype. The production of X-ray reflecting nickel optics is a new area of research at UCL. Therefore the precise method with which to replicate optics

Table 2.3: An overview of the cylindrical prototype

The dimensions of the cylindrical prototype			
The optic		The actuators	
Axial length	200 mm	Axial length	19 mm
Azimuthal length	100 mm	Azimuthal length	32 mm
Azimuthal RoC	155mm	Azimuthal RoC	155mm
Angle	37 °		
Thickness	0.4 mm	Thickness	∼0.2 mm
Optical form	cylindrical	Actuator arrangement	Grid
Material	Nickel	Material	PZT

from the mandrel was unknown and due to the complexity in the production of the ellipsoidal mandrel any mistakes made using the ellipsoidal mandrel would be damaging in terms of time and cost. Therefore, it was decided to produce a pre-prototype with a cylindrical form. The loss of the curvature in the axial direction simplified the production of the mandrel and would allow the replication of the optics on a quicker timescale, it would also provide an evaluation of all the production methods prior to their application to the ellipsoidal prototype. The following section provides an overview of the cylindrical prototype and Chapter 3 is dedicated to its development.

2.1.2 Development of manufacturing methods - cylindrical pre-prototype

The dimensions of the cylindrical pre-prototype are outlined in Table 2.3. The prototype is 100 mm shorter in the axial direction and the curvature in the azimuthal curvature is tighter, at 155mm radius of curvature (RoC): this curvature was chosen due to a cylindrical lens that could be bought to measure the optical profile of the mandrel. The pre-prototype is essentially a scaled-down version of the ellipsoidal prototype.

The lack of the curvature in the axial direction makes the production of the mandrel significantly easier as only one curvature has to be accounted for. Furthermore, the smaller geometry requires less nickel to be used in the optics' production. Methods for actuator bonding and harnessing are also untested and will therefore benefit from a practice pre-prototype.

The cylindrical pre-prototype has been discussed in this section to provide a thorough description of the manufacturing steps to achieve the final goal of the ellipsoidal prototype and for clarity

the remainder of this chapter is dedicated to the ellipsoidal prototype. The pre-prototype will be further discussed in Chapter 3.

2.1.3 The optical form of the ellipsoidal prototype - University of Leicester

The prescription of the optical form of the ellipsoidal prototype was determined by the dimensions of the X-ray tunnel test facility (TTF) at the University of Leicester (UoL). The facility is a 28 m horizontal pipe, with the X-ray source at one end and a microchannel plate (MCP) detector at the other. The geometry of the optical component of the prototype (Table 2.2) is governed by an ellipsoid that was fitted to the TTF dimensions, situating the source and MCP detector at either foci. Along the length of the pipe are a series of flanges that provide access to the interior. The prototype is located over such a flange at a distance of approximately 4.5 m from the detector. The prototype and associated support structure is too large itself to be inserted directly through the flange; instead it is gently pushed down the 4.5 m of pipe from the detector using an extendable pole. Figure 2.3 highlights the prototype situated upon its support structure above an access flange through which the electronics exit.

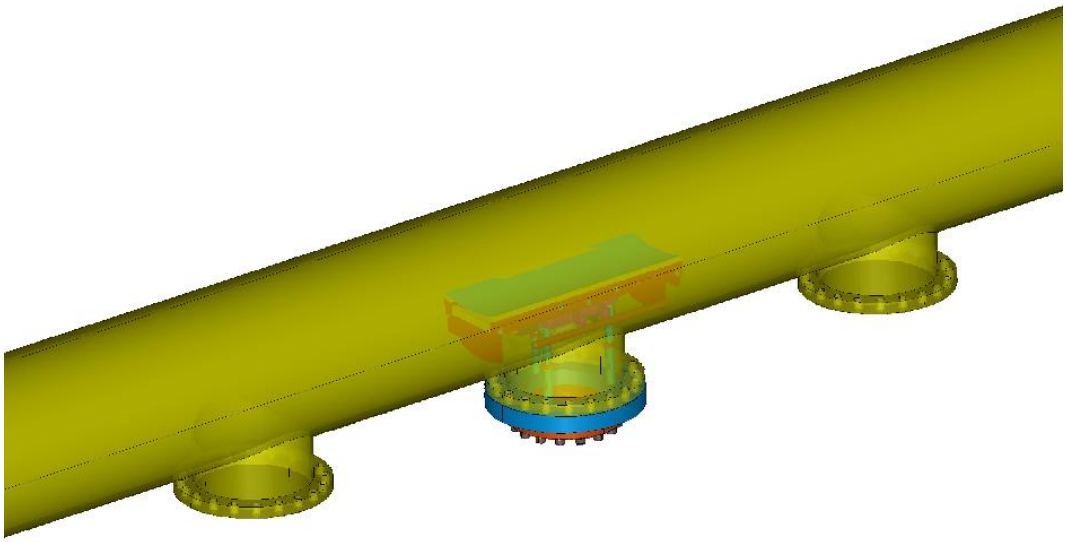

Figure 2.3: The ellipsoidal prototype situated within the X-ray beam line at the UoL, image courtesy of CT from MSSL

Ray-tracing of the optical form of the ellipsoidal prototype within the software 'Q'[1], demon-

[1]The software Q was developed in-house at UoL by Dr R. Willingale

strated how the optic would interact with the X-rays to produce the detected image (Figure 2.4). The top-left image from Figure 2.4 highlights the axial length of the X-ray TTF (not to scale) and the ellipsoid fitted to it. The foci of the ellipse represent the X-ray source and the MCP detector. The incident X-rays are shown in red and they can be seen to transverse the majority of the tunnel's length before their interaction with the optical component of the prototype. The image at the bottom-left shows an increased magnification in the region of the optic and the detector. Most of the X-rays are transmitted through the optic: only those at grazing incidence angles of $\leqslant 1.163\,^{\circ}$ will reflect from the optic's surface. The images on the right highlight the image as seen from the detector's plane and the top-right image displays an 500mm^2 plane, the red rectangle at the bottom of the plots are the X-rays that were transmitted through the prototype rather than being reflected from it. The small red circle (radius 2.5mm) indicates the reflected X-rays that have been focussed by the optic and this circle in increased magnification can be seen in the bottom-right image.

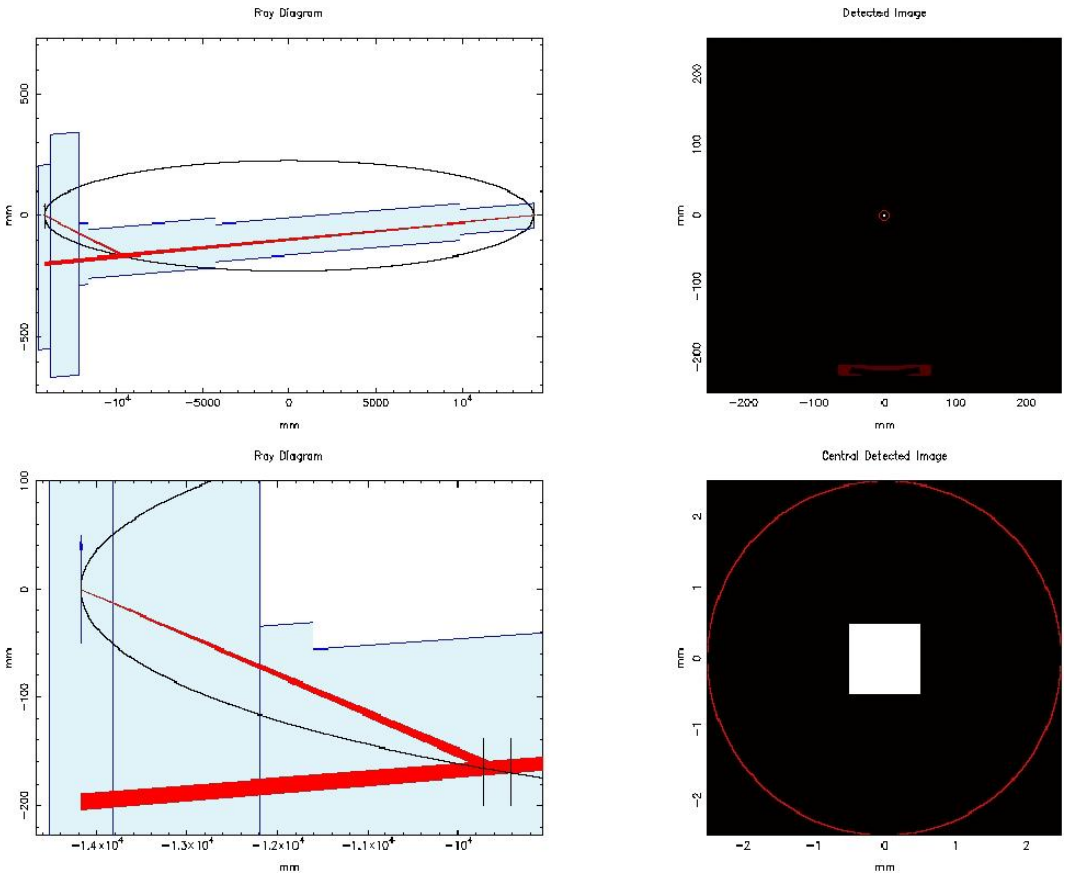

Figure 2.4: Ray tracing performed at the University of Leicester to demonstrate the ellipsoidal form of the prototype's optic, courtesy of the CHF from UoL.

UoL is responsible for the operation of the prototype while in the X-ray facility; this involves

management of the X-ray source and the MCP detector. The *optimising routine*, which is designed to improve the initial resolution of the optic, has been developed at UoL and benefits from their direct knowledge of the MCP detector. The optimising routine corrects for the prototype's optic distortions by using a series of patterns as shown in Figure 2.5 (a thorough discussion of the optimising routine shall be provided in Chapter 6). Each of these patterns are multiplied by 10 voltages between -100V and 100V in 20V steps with a detected image taken at each voltage. The optimum voltage for that pattern is then calculated and added to the next pattern at each of the 10 voltages: the final optimised voltage pattern is therefore the cumulative effect of all the voltage patterns at their optimum. Chapter 6 will provide a complete account of the X-ray testing performed at the UoL and the results obtained.

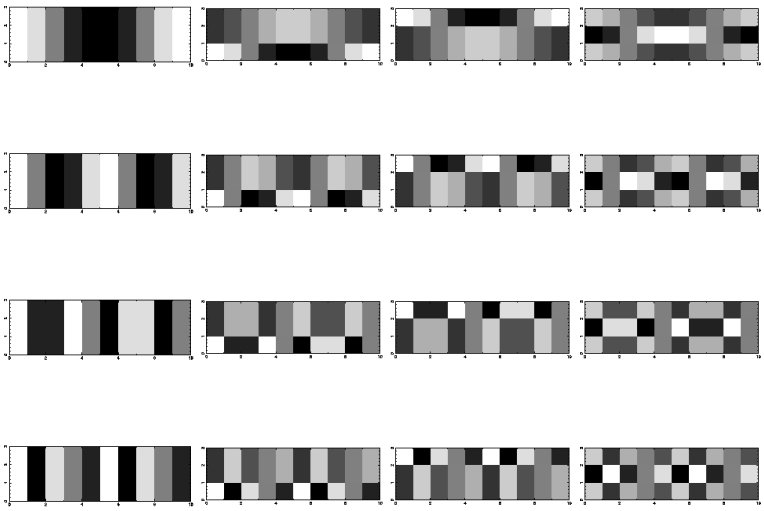

Figure 2.5: The fast Fourier transform patterns as developed by the UoL, each square represents an actuator and the shade between white and black refers to 1 to -1 respectively, courtesy of CHF from UoL.

2.1.4 Actuator design and fabrication - University of Birmingham

Actuators are devices that cause a movement/displacement upon another system. In context with SXO, the actuators are causing an optical surface of an X-ray system to change shape to produce an improved resolving capability of the optic. Actuators have been used for many years in ground based telescopes, where an adaptive optics (AO) system is used to correct the wavefront for distortions caused by the Earth's atmosphere (Glindermann *et al.* 2000). The difference between AO and the system developed in the SXO project is non-dependence upon real-time adjustment: the optical surface is not being corrected to compensate for atmospheric distortions. X-ray telescopes operate

in space and therefore do not have to accommodate for the atmosphere, instead the actuators are correcting for manufacturing errors in the optics themselves and therefore real-time adjustment is not required.

Piezoelectric materials are used commercially as sensors and actuators. Sensors use the direct piezoeletric effect, where, upon the application of a force, an electric field is produced. Actuators use the converse piezoelectric effect where the application of an electric potential difference results in a strain being induced within the material. Many materials display piezoelectric properties: quartz, tourmaline and Rochelle salt are all natural piezoeletric materials that demonstrate a small piezoelectric effect. An improved effect can be attained from lead-zirconate-titante ceramics (PZT), which are commonly used in the production of actuators, and the polyvinylidene fluoride polymer (PVDF) is primarily used for sensoring materials (Sirohi & Chopra 2001).

For the piezoelectric material to be utilised in an actuator/sensor application, the PZT crystals are required to be poled in the same direction. The poling direction is determined by the application of a potential difference, which aligns the crystals due to their dielectric nature. For the case of most actuators this poling direction is aligned normal to the main actuator surface (i.e. the surface with the largest area); traditionally this axis is labelled by a 3. The two axes within the plane are labelled 1 and 2. The value of d_{33} describes the displacement caused in the 3-axis due to the electric field being present in 3-axis and d_{31} denotes the displacement in the 1-axis due to the electric field being in the 3-axis: these values are quoted in m/V (Figure 2.6). Generally the value of d_{33} is positive (expansion) and the d_{31} negative (contraction).

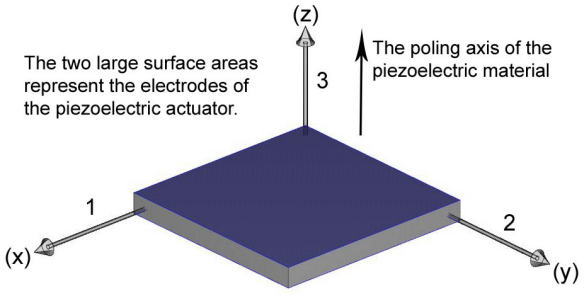

Figure 2.6: A description of a unimorph actuator with respect to the material's poling axis.

The actuators for the SXO prototypes are produced at the School of Materials and Metallurgy at the University of Birmingham (UoB) and this allows the azimuthal curvature of the prototype to be replicated upon the actuator. The curvature in the axial direction is negligible in comparison to the azimuthal curvature and therefore is not considered within the actuator's design. Although

alternative actuator technologies were investigated, such as active fibre composites (AFCs) (Bowen *et al.* 2006), the SXO's actuators will be unimorph in design (Zhang *et al.* 2009*a*). A unimorph actuator is one that has a single layer of PZT sandwiched between two parallel electrodes. An advantage of the UoB's actuators is the direct access to the ground electrode (the electrode bonded to the substrate) from the non-bonded surface: this is achieved through removing a small section of the top electrode and wrapping the bottom electrode around to fill the gap, as shown in Figure 2.7.

The actuators will be $150\mu m$ - $200\mu m$ in thickness. It is important to minimise the thickness of the actuators and the bonding layer, as within a telescope system a thick optic limits the number of optics per available aperture. The SXO prototype is designed to be no greater than $\sim 700\mu m$ in thickness; this is comparable with XMM-Newton's optics.

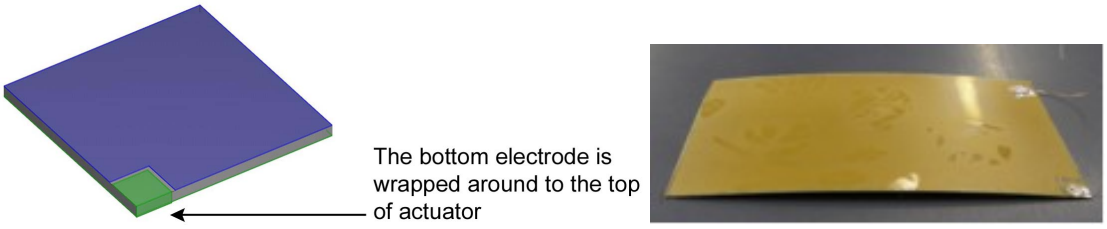

(a) A schematic of UoB's actuator's electrodes

(b) An example of an actuator fabricated at the UoB

Figure 2.7: An example of the unimorph actuators as developed by the UoB for the SXO prototype. Figure 2.7(a) (not to scale) highlights the ground electrode (green) which has been wrapped around the PZT ceramic and allows its electrode to be accessed from the non-bonded surface. Figure 2.7(b) displays a completed curved actuator

An inherent characteristic of piezoelectric materials is their hysteresis, which results in a variation in displacement per voltage depending upon the position within the loop. An example of an hysteresis loop produced by the UoB's piezoelectric material can be seen in Figure 2.8: this effect will have to be compensated for within the control program to obtain reliable displacements per voltage.

2.1.5 Optic fabrication, optical testing and actuator control - University College London

University College London (UCL) was responsible for the production of the prototype's optic and this would be via an electroforming method using a low stress electrolyte. The production of the mandrels for the cylindrical and ellipsoidal optics were to be undertaken by DB in-house at UCL. In

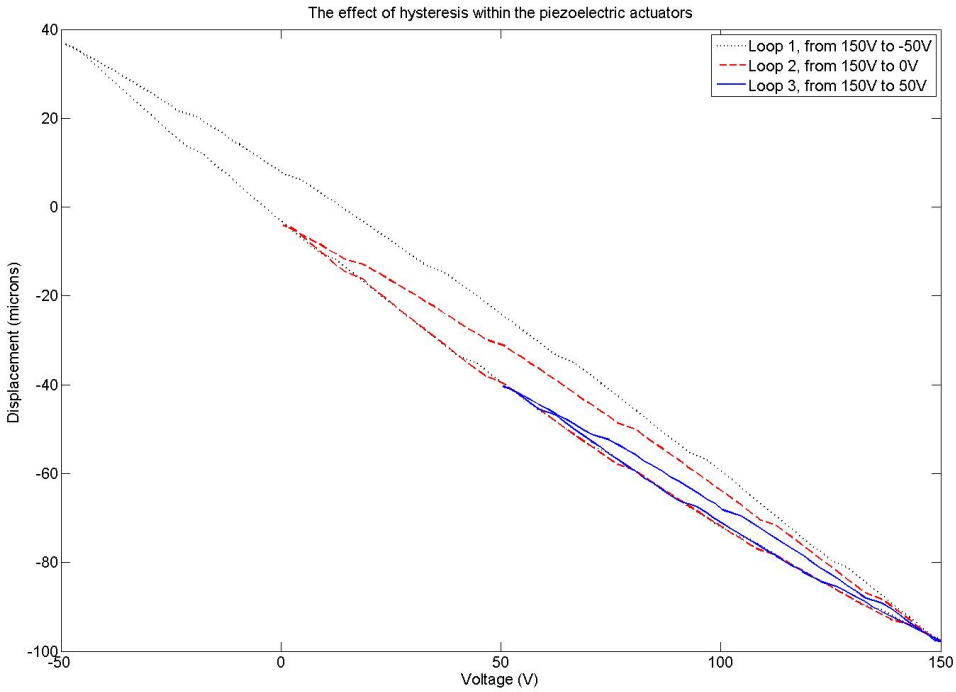

Figure 2.8: Hysteresis within a piezoelectric actuator sample

addition to the optics fabrication the actuator bonding was to be carried out at UCL and Chapters 3 and 4 outline the production of the cylindrical and ellipsoidal prototypes respectively.

To complement the fabrication undertaken at UCL, finite element analysis (FEA) was used to investigate several characteristics of the prototype system such as: gravitation distortions and actuator influence functions (as presented in Section 2.2). FEA was also employed in the modelling of the electrostatic environment of the electrodeposition facility as outlined in Chapter 3.

The graphical user interface (GUI) for the actuators' control software was developed at UCL owing to the hardware having been established previously at UCL. This is outlined in Chapter 5.

2.1.6 Support structure - Mullard Space Science Laboratory

The support structure which holds the prototype in the correct position within the X-ray TTF was designed and predominantly fabricated at the Mullard Space Science Laboratory. Outlined below are constraints that had to be accommodated within the support structure design:

- The vacuum environment of the X-ray TTF

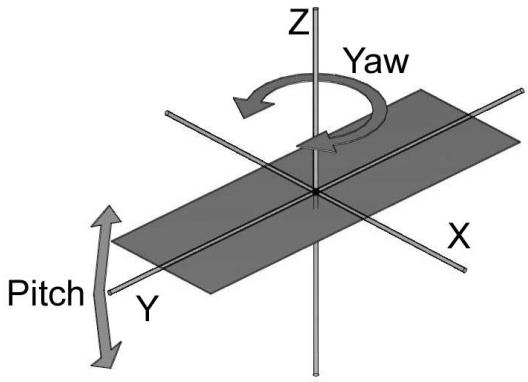

Figure 2.9: Definition of pitch and yaw for the ellipsoidal prototype's support structure: pitch is a rotation about axis X and yaw is a rotation about axis Z.

- An ability to actively adjust the position of the prototype in terms of pitch and yaw (as defined in Figure 2.9) to ensure accurate positioning.
- To provide an exit for the prototype's electronics through the flange
- To ensure a repeatable positioning of the support structure each time it is integrated within the X-ray TTF.
- To minimise high spatial frequency distortions upon the prototype's optic

The support structure can be divided into three sections: first is the flange support (Figure 2.10(a)), which provides three points that extend normal to the pipe's surface. It is on top of these three points that the second component of the support structure sits and together they form a kinematic support. In addition, the prototype's electronic's cabling exits directly through this flange support, allowing it to be externally connected to the driving computer. The second component provides the active positioning of the prototype within the X-ray environment (Figure 2.10(b)); it has two motors that move the prototype in pitch and yaw by sub-micron steps. The final piece of the support structure is the optic cradle (Figure 2.10(c)): an aluminium framework with a radius of curvature approximately matching that of the prototype, on top of which are bonded two foam strips and it is upon this foam that the prototype rests unconstrained. All of the components of the support structure are vacuum compatible, including the foam used to directly hold the prototype.

The design criterion of the optic cradle was based upon ensuring only low spatial frequency distortions caused from the effect of gravity. By holding the prototype with two strips along the axial length, the gravitational sag experienced by the prototype would be of low spatial order frequencies that could be corrected using the actuators or the active support structure. The magnitude of the

gravitational sag could have been reduced by using multiple struts along the azimuthal curvature of the prototype, but this would have introduced high spatial order frequencies which may have been beyond the capability of the actuators to correct for.

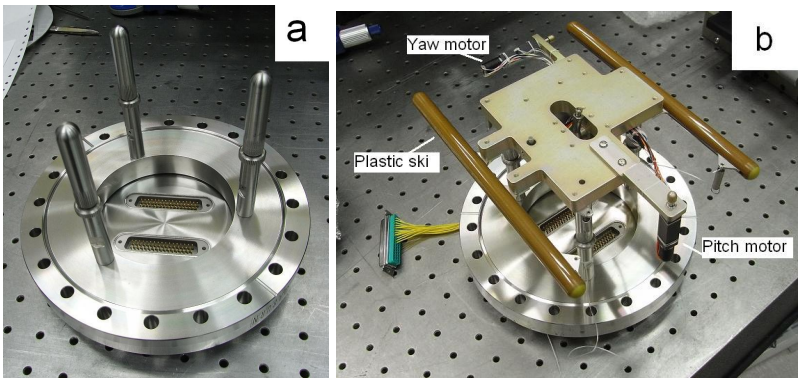

(a) Flange support (b) Active support

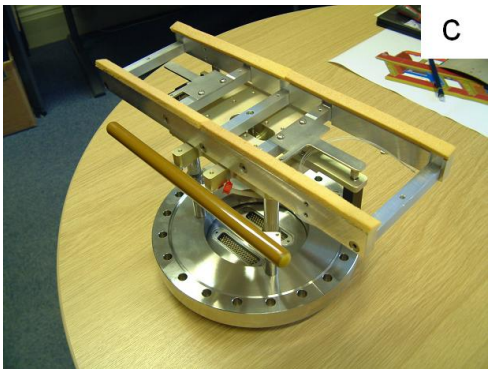

(c) Total support structure

Figure 2.10: The complete prototype support structure is composed of three components. First is the flange support (Figure 2.10(a)) which is fitted externally to the the X-ray TTF and has three adjustable legs that extend within the tunnel, normal to the surface. The active component is shown in Figure 2.10(b); it forms a kinematic mount with the flange support and provides optical alignment in terms of pitch and yaw. The final component is the optic's cradle (Figure 2.10(c)) and the prototype will rest upon its foam supports.

2.2 Finite element analysis

Finite element analysis (FEA) is a tool that allows a physical object to be modelled within the software and then apply a set of physics equations to determine, for example, the thermal expansion experienced by an iron girder for a 10K temperature gradient. Within this thesis FEA has been used to model gravitational sag, piezoelectric actuator influence functions and the current density distribution upon a mandrel within the electroforming facility.

There are several software options available to produce FEA models, for example COMSOL MULTIPHYSICS , I-DEAS, ANSYS etc.; however, COMSOL MULTIPHYSICS has been used throughout this thesis. COMSOL MULTIPHYSICS was selected for the SXO project owing to its ability to solve simultaneous physics equations, for example thermal expansion and gravitation sag at the same time, COMSOL MULTIPHYSICS also has a specific piezoelectric module allowing the piezoelectric actuators to be accurately represented. An example where FEA has been implemented in modelling piezoelectric structures is outlined in the paper by Poizat & Benjeddou (2006).

Section 2.2.1 describes how FEA is used to solve a simple physics problem involving mechanical bending and the example presented is not related to the ellipsoidal prototype. The following Sections 2.2.3 and 2.2.4 describe two models which were produced to form part of the optical ray-tracing models undertaken by the University of Leicester and discuss the effect of gravity and the actuator influence functions upon the ellipsoidal prototype.

2.2.1 A simple finite element analysis example

To provide a simple explanation in the use of FEA to solve a mechanical problem, an example of a supported beam with a loaded end shall be described. Figure 2.11 highlights the case of a 2-dimensional (2D) aluminium bar (2m $\times$ 0.1m), fixed at one end so that the end cannot move from its original position. At the opposite end of the bar is a 10N point source acting normal to the bar's surface. The question to be answered is, 'What is the total displacement experienced by the bar due to a 10N point source?' The finite element method to solve this problem is outlined below.

STEP 1 - DRAW - A computer aided design (CAD) representation of the object is produced; generally this is a simplification of the object's real geometry. A 2D representation of a 3-dimensional (3D) object is useful in reducing the number of mesh elements (discussed in the following paragraph) within the object and therefore processing time. Figure 2.12 displays a 2D representation of the aluminium bar. The object against which the bar is fixed is not represented. As the boundary between the bar and the object is fixed, the object will not affect the end result.

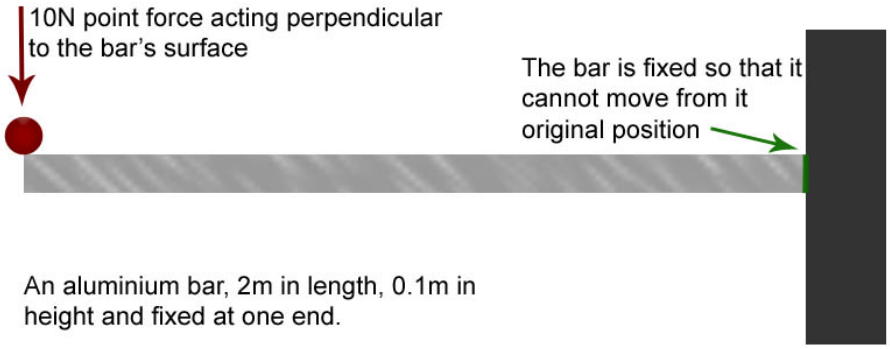

Figure 2.11: An example of an aluminium bar fixed at one end, with a 10N point force acting at the other.

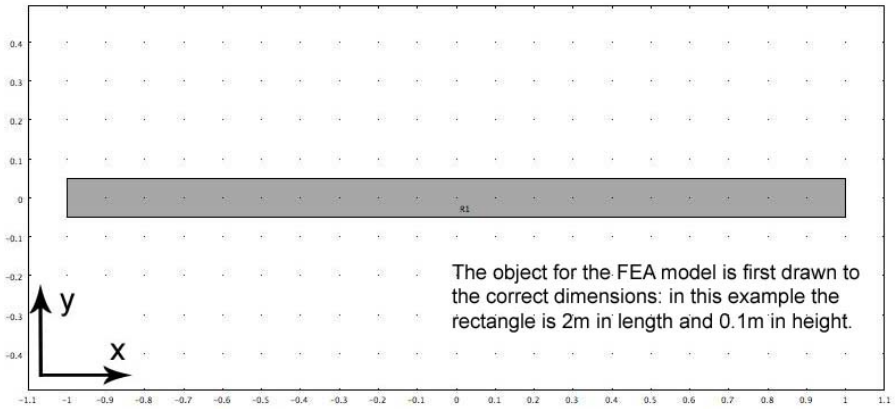

Figure 2.12: The 2-dimensional object is first drawn to its physical dimensions

STEP 2 - MESH - The object is divided into small segments called a mesh. Each mesh element represents an area to be be evaluated within the partial differential equations. Within COMSOL MULTIPHYSICS mesh elements can have either a triangular or quadrangular form depending upon the geometry of the object. Figure 2.13 demonstrates a mesh generated for the geometry of the aluminium bar. The mesh can be fine or coarse depending on the accuracy of the results required; however, a fine mesh takes longer to solve. In practice both a coarse and fine mesh can be used within one model and this optimises the accuracy of the results against the time to solve the equations.

STEP 3 - PHYSICS - The physics of the FEA model describes the physical characteristics of the problem to be solved and there are four forms: SUBDOMAIN, BOUNDARY, EDGE and POINT. Using the example of a 3D object, the SUBDOMAIN describes the object as a whole, specifying such

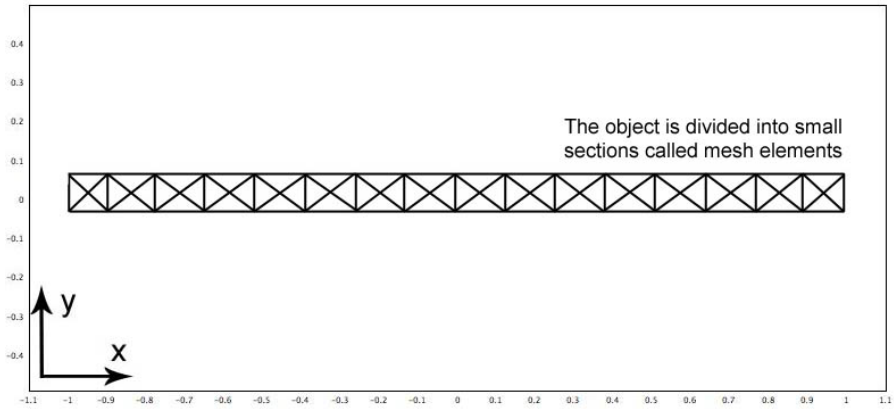

Figure 2.13: The 2-dimensional object is then meshed to divide the object into smaller segments, each segment represents an equation at that point

physical parameters as density, coefficient of thermal expansion, Poisson's ratio etc., in addition physical conditions relating to the whole object are applied, i.e. gravity affects the entire object. The BOUNDARY represents a 2D surface of the 3D object, for example if one surface of an object is fixed that would be applied in the BOUNDARY condition. EDGE conditions are 1-dimensional (1D) lines that form part of the geometric structure and POINT conditions describe the physics of a single point. When selecting the PHYSICS to be applied to a 2D model, the model should be considered as a cross-section through a 3D object and therefore the above example of applying physics conditions applies. For example, a line represented in a 2D format is actually a BOUNDARY condition seen edge on. Figure 2.14 demonstrates how the physical characteristics of the problem have been implemented within the FEA model.

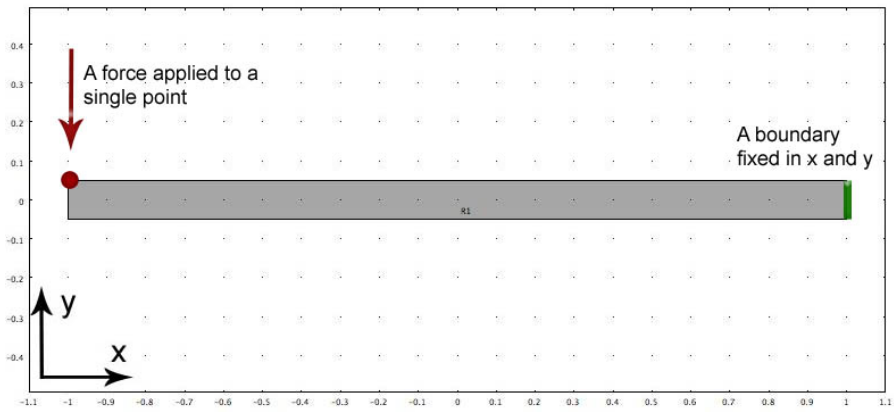

Figure 2.14: Boundary conditions are applied; these provide the model with point(s) to react against and the initial force

STEP 4 - SOLVE - The SOLVER ties together the MESH, which is a representation of the object, with the PHYSICS which is affecting the object. Figure 2.15 highlights the solution to the aluminium bar problem. The results show that for 10N point force the end of the aluminium bar has displaced by 0.0005m ($500\mu m$).

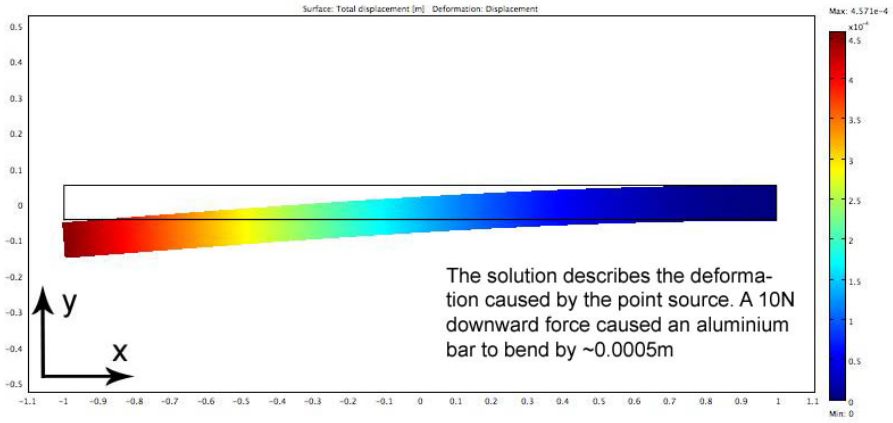

Figure 2.15: The solution for the FEA model of the aluminium bar with a point force

The above example has outlined the basic steps required to generate a finite element model and these four steps have formed the basis of all the FEA models presented within this thesis. The remainder of this chapter shall outline two FEA models developed to investigate the effect of gravitation sag upon the optical form of the prototype and the actuators' influence functions. Additional use of FEA can be found in Chapters 3 and 4, where the electrostatic environment of the electrodeposition facility has been modelled. Chapter 5 presents actuator influence functions compared against measured results. The FEA influence functions are based upon the foundation of those developed in Sections 2.2.4.

2.2.2 Finite element models for the University of Leicester's Ray tracing code

Section 2.1.3 has introduced the optical modelling performed at the UoL. In addition to modelling the optical form of the prototype, the distortion caused by gravity was investigated; this required a synergy between the ray-tracing software at the UoL and the FEA software at UCL. The FEA model used to predict the gravitation sag experienced by the prototype is detailed in Section 2.2.3.

The optical modelling was combined with the optimisation routine to provide a means to predict the improvement that may be obtained using the piezoelectric actuators upon a deformed optic. UCL therefore produced a series of FEA actuator influence functions that would predict

the magnitude and the form of the function for each of the 30 actuators. These functions were represented within the voltage patterns and used to predict the improvement in resolving power obtained through the actuators' use. Feldman *et al.* (2008) presents optical modelling described in this section.

A requirement for the FEA models with respect to the optical modelling at UoL was to use a standard coordinate-map for each of the FEA outputs. The coordinate maps generated by COMSOL MULTIPHYSICS do not match from model to model, therefore a standard map was generated within MATLAB to export the data.

2.2.3 An FEA representation of the prototype's distortions caused by the effect of gravity

DRAW - In modelling the effect of gravity of the prototype within the X-ray facility, certain approximations were made. The ellipsoidal form of the prototype was approximated to a cylinder, to keep it in line within the actuator influence functions model as outlined in Section 2.2.4. The actuators were not displayed as individual segments, but rather a single piece of piezoelectric material, this being done primarily to reduce the complexity of the model and to allow it to solve. A glue layer was not modelled, as its thickness was considered negligible compared to the nickel optic and the actuators: it also removed an additional element of complexity. Only the immediate aluminium framework of the support structure was modelled (Figure 2.16) and this allowed the effect of gravity on the prototype to be determined without modelling the complex support structure in contact with the tunnel.

MESH - Both a triangular and a quadrangular mesh were used for the gravitation model. Due to the high aspect ratios within the optic (the length of the optic is 750 times greater than its thickness) a triangular mesh was too fine and would not solve. Therefore a triangular mesh was used for the support structure and controlled quadrangular mesh was used for the prototype. The disadvantage of using two meshes is the requirement to provide a PHYSICS link, to ensure that the physics conditions applied to one mesh will propagate into the other mesh: this link was established using the IDENTITY CONDITIONS within the software.

PHYSICS - the subdomain for the model described the aluminium frame and the BP101 foam[2] of the support structure, and the nickel optic and PZT-5H of the actuators. Gravity is a global effect requiring it to be applied in the subdomain. The effect of gravity was applied by adding a downward force perpendicular to the optic's surface which has a magnitude equivalent to the

[2] purchased from Upilex (`www.upilex.jp`)

density of the material multiplied by the acceleration due to gravity. The model is fixed, in terms of BOUNDARY conditions, at the junction between the active component of the support structure and the aluminium frame work. In Figure 2.16 the boundary conditions were applied to the three aluminium bars in the centre of the framework which are perpendicular to the axial length..

SOLVE - The maximum displacement experienced was down the centre of the optic, exhibiting a displacement of $5.5\mu m$ in the direction of gravity. The edges of the optic (directly supported by the foam) displayed the minimum displacement of $2\mu m$ in the direction of gravity (Figure 2.17). It is thought that this change in radius of curvature and the lateral downward displacement should be able to be compensated for by the actuators and the precision drivers on the primary support structure respectively.

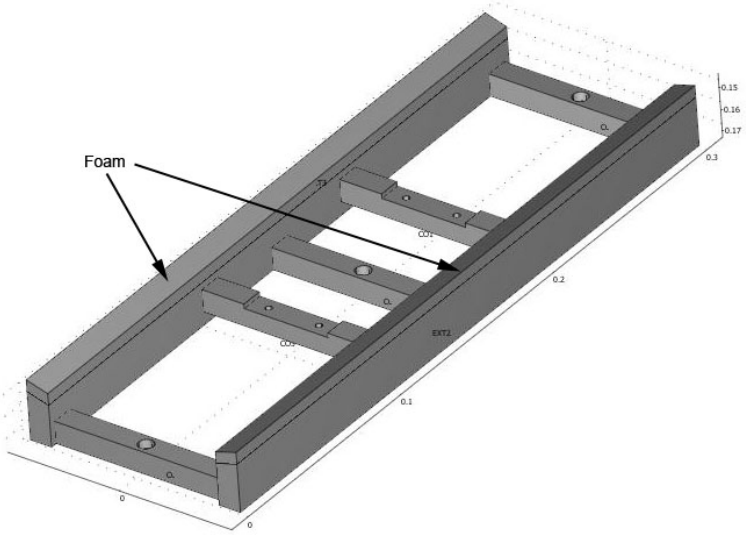

Figure 2.16: The elliptical prototype support structure (the optic cradle), an aluminium framework with two $5mm$ thick polyimide foam strips.

The displacements in the X, Y and Z axes were exported for the prototype's optical surface within a standard coordinates map. This data was then input within the optical tracing code at the UoL to determine the effect of gravitation distortion upon the theorised X-ray detected image. The results, as presented within the PhD thesis by Feldman (2009), indicate that there would be a 10.02" (arc-second) distortion created by gravity.

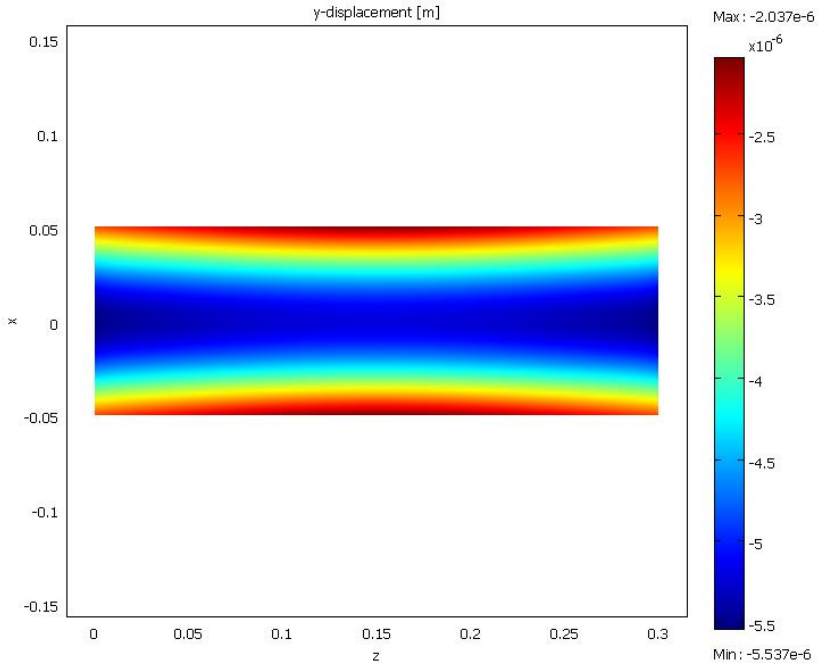

Figure 2.17: A view normal to the optic's surface showing the effects due to gravity caused by the optic cradle.

2.2.4 An FEA representation of the piezoelectric nature of the prototype system

The piezoelectric effect is modelled within COMSOL MULTIPHYSICS using the *structural mechanics module*, which is an add-on to the standard software. Prior to describing the development of the FEA model, by which the influence functions were produced, a brief introduction to the underlining equations will be made.

BACKGROUND - Two sets of equations can describe the piezoelectric effect; those that describe stress and those that describe strain. Within COMSOL MULTIPHYSICS both can be used; however, only the stress form detailed is in this thesis.

$$\{T\} = [c^E]\{S\} + [e]^T\{E\} \tag{2.1}$$

$$\{D\} = [e]\{S\} + [\epsilon^S]\{E\} \tag{2.2}$$

- $\{T\}$ - 6×1 stress vector
- $\{D\}$ - 3×1 electric displacement vector

- $\{S\}$ - 6×1 strain vector
- $\{E\}$ - 3×1 electric field vector
- $[c^E]$ - 6×6 elastic stiffness matrix
- $[e]$ - 3×6 piezoelectric coupling coefficient
- $[\epsilon^S]$ the 3×3 dielectric coefficients matrix

These equations form the basis of the finite element method simulations. The piezoelasticity of the material is commercially quoted in terms of its strain-charge form $[d]$ of the piezoelectric coupling coefficient and the relationship between $[e]$ (stress) and $[d]$ (strain) is given in Equation 2.3.

$$[e]^T = [c^E][d]^T \tag{2.3}$$

The following matrix displays the piezoelectric strain coefficients as obtained from a piezoelectric manufacturer. The values of d_{31} and d_{32} are identical, as are d_{15} and d_{24}: this is due to the symmetry of the piezoelectric material in the plane perpendicular to the poling axis.

$$Coupling\ matrix\ strain-charge\ form\ \mathbf{d} = \begin{pmatrix} 0 & 0 & 0 & 0 & d_{15} & 0 \\ 0 & 0 & 0 & d_{24} & 0 & 0 \\ d_{31} & d_{32} & d_{33} & 0 & 0 & 0 \end{pmatrix}$$

As mentioned in Section 2.1.4, a piezoelectric material is anisotropic as demonstrated by its d_{33} and $d_{31/32}$ coefficients; however, there are additional subscripts that describe displacement per voltage in terms of twist about an axis and these subscripts are highlighted in Figure 2.18. $d_{15/24}$ describe a twist (5/4) caused by an electric field in the 1/2-axis.

Unimorph piezoelectric actuators should be modelled to ensure that the d_{33} coefficient and the d_{31}/d_{32} coefficients are always normal and in-plane with the surface respectively. Early flat models represented the piezoelectric material well within a 2D Cartesian coordinate system where $x \longrightarrow d_{31}$ and $y \longrightarrow d_{33}$ (as highlighted in Figure 2.19).

However, the prototype has polar geometry, with curvature in two axes and therefore solving the curved geometry of the prototype within a Cartesian system leads to an asymmetry in the influence functions as highlighted in Figure 2.20. The Cartesian coordinate system does not ensure that the d_{33} coefficient is always normal to the actuator's surface and results in a poor representation of the displacement generated.

COMSOL MULTIPHYSICS does not support polar coordinates; however, there was an option to use cylindrical coordinates, although the geometry of the prototype would have to be approximated

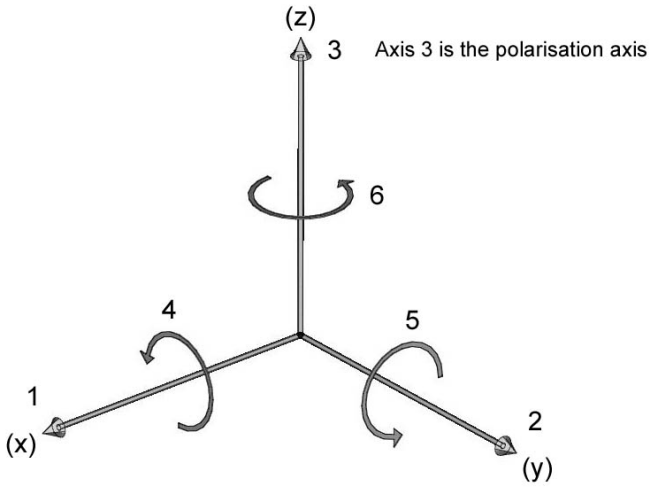

Figure 2.18: Piezoelectric coordinates

Table 2.4: Converting Cartesian coordinates to cylindrical coordinates

$cE_{11} \longrightarrow cE_{33}$	$sE_{11} \longrightarrow sE_{33}$	$d/e_{31} \longrightarrow d/e_{13}$
$cE_{33} \longrightarrow cE_{11}$	$sE_{33} \longrightarrow cE_{11}$	$d/e_{32} \longrightarrow d/e_{12}$
$cE_{12} \longrightarrow cE_{32}$	$sE_{12} \longrightarrow cE_{32}$	$d/e_{33} \longrightarrow d/e_{11}$
$cE_{13} \longrightarrow cE_{31}$	$sE_{13} \longrightarrow cE_{31}$	$d/e_{15} \longrightarrow d/e_{35}$
$cE_{23} \longrightarrow cE_{21}$	$sE_{23} \longrightarrow cE_{21}$	$d/e_{24} \longrightarrow d/e_{26}$
$cE_{44} \longrightarrow cE_{66}$	$sE_{44} \longrightarrow cE_{66}$	$\epsilon T/S_{33} \longrightarrow \epsilon T/S_{11}$
$cE_{66} \longrightarrow cE_{44}$	$sE_{66} \longrightarrow cE_{44}$	$\epsilon T/S_{11} \longrightarrow \epsilon T/S_{33}$

to a cylinder to ensure the coordinate system simulates the curved actuators correctly. This approximation was considered acceptable when considering the deviation from a conic form of $33\mu m$ and the 5mm difference in radius of curvature between the two ends of the prototype (Table 2.2). Therefore an accurate depiction of the prototype was sacrificed for a more accurate representation of the active nature of the piezoelectric material.

The cylindrical coordinate system within COMSOL MULTIPHYSICS is rigid: it cannot be altered to accommodate the piezoelectric coefficients, therefore the matrices that govern the piezoelectric material have to be altered. The cylindrical coordinate system, as shown in Figure 2.21, requires the piezoelectric material to be aligned such that (d_{33}, d_{32}, d_{31}) align with (r, θ, z); within the piezoelectric matrices this corresponds to $z \longleftrightarrow x$, $3 \longleftrightarrow 1$ and $6 \longleftrightarrow 4$.

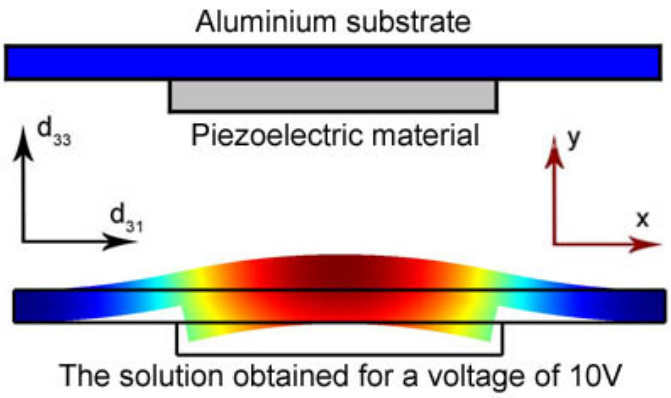

Figure 2.19: A 2D representation of a flat piezoelectric actuator affecting an aluminium substrate: the Cartesian and Piezoelectric coefficients are correctly aligned. The deformed colour map highlights the change in displacement of the substrate caused by the actuator.

$$Coupling\ matrix\ strain-charge\ form\ \mathbf{d} = \begin{pmatrix} d_{11} & d_{12} & d_{13} & 0 & 0 & 0 \\ 0 & 0 & 0 & 0 & 0 & d_{26} \\ 0 & 0 & 0 & 0 & d_{35} & 0 \end{pmatrix}$$

The matrix conversions as shown in Table 2.4 are used to convert the Cartesian coordinates to cylindrical coordinates, the strain-charge form of the piezoelectric coupling matrix converted to cylindrical coordinates is shown above. With the model now able to accurately represent the piezoelectric material the model for the ellipsoidal prototype could be developed.

DRAW - Due to the high aspect ratios for the components of the prototype system and the requirement of cylindrical coordinates, the prototype was drawn in 11 2D geometries which described the azimuthal plane of the prototype. Unlike the gravitation sag model, each of the actuators were individually represented and like the gravitational sag model the adhesive layer was omitted.

MESH - The high aspect ratio of the optic's length to its width prevented the use of a triangular mesh, therefore a mesh was created in the 2D azimuthal plane and extruded in to a 3D geometry. This resulted in 11 3D geometries being created, one for the optic and 10 for sets of 3 actuators. Each of the geometries had to be linked in terms of PHYSICS as described in Section 2.2.3. Within the 3D environment of each of the prototype's components, cylindrical coordinates were selected, over-riding the default Cartesian coordinate system.

PHYSICS - Within the SUBDOMAIN, only the physical properties of the materials were de-

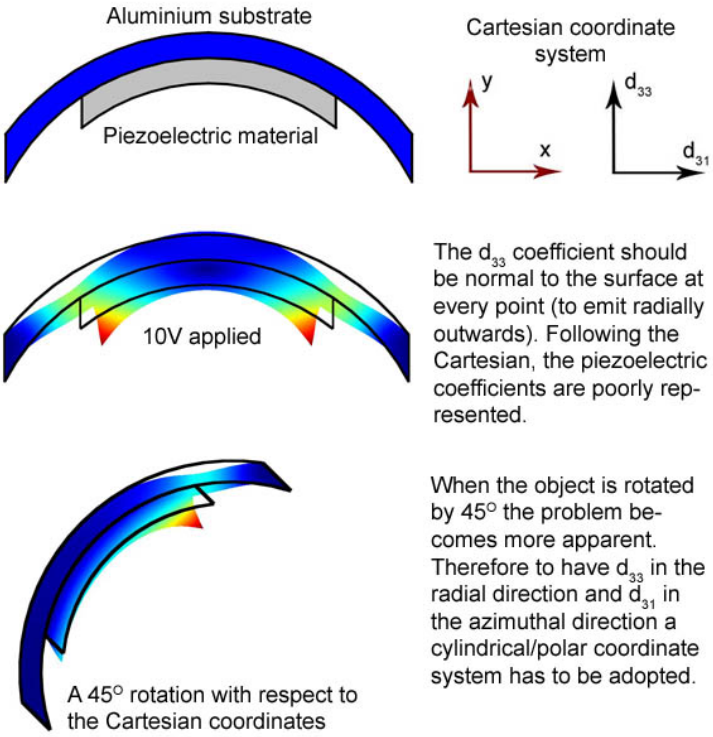

Figure 2.20: A 2D representation of a curved actuator bonded to a curved substrate: within a Cartesian coordinate system the piezoelectric coefficients do not align correctly leading to an asymmetry in the resultant influence function.

scribed, the optic $\longrightarrow$ nickel and the actuators $\longrightarrow$ the cylindrical form of the PZT-5H ceramic. From consultation with the UoB PZT-5H was considered the close approximation to the material properties of their own PZT. Surface BOUNDARY conditions determined the electrodes of the piezoelectric material. The boundary in contact with the nickel optic was designated ground and the external surface the driving potential. UoL required influence functions at both 10V and -10V, therefore two functions were created for a single actuator.

In the actual system, the prototype rests upon its support structure unconstrained; unfortunately this condition can not be represent accurately within FEA software as the model needs a point to react against. The decision was made to fix the model of the prototype at corner points, as this would provide a point to react against without fixing the edges of the prototype rigidly. In the case where the actuator is located at a corner, the point at that corner is not fixed, thus allowing a more accurate representation of the corner actuators.

SOLVE - Influence functions were generated for 10 of the prototype's actuators and this provided representation of all the actuators across the surface due to the symmetry of the model. An example

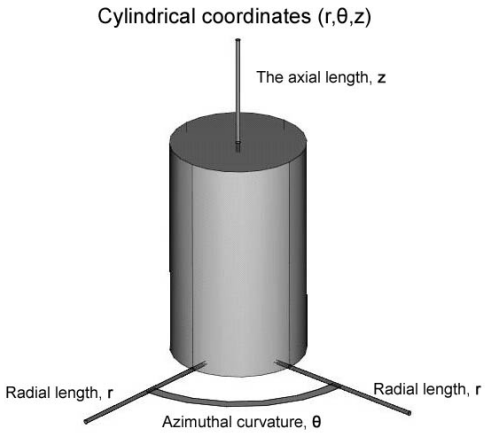

Figure 2.21: A description of the cylindrical coordinate system used within COMSOL MULTIPHYSICS

of a generated influence function at -10V can be seen in Figure 2.22. The 2D image highlights the magnitude of the influence function: the magnitude of the depression caused by the actuator is $\sim$-2μm and this is located in the immediate vicinity of the actuator, but a global view indicates that the 'wings' of the prototype experience a greater displacement of $\sim$2.7μm. Figure 2.22(b) highlights the local form of the influence functions and its effect upon the entire prototype; in particular it demonstrates the actuator's effect beyond its own physical dimensions.

UOL RAY-TRACING CODE - The UoL took the 20 influence functions generated and applied them to each of the 30 actuators: each actuator has two functions, one positive and one negative. The displacement per voltage was calculated using a linear relationship; this is appropriate when considering the small range of voltages over which the actuator operates when compared to the full voltage range of the piezoelectric ceramic. An optic was modelled with gross distortions in its form, including gravitation sag and effects due to actuator bonding (to be mentioned in Chapter 5). The FFT patterns (Figure 2.5) were multiplied by the actuator influence functions at voltages between -100V and 100V and the optimum voltage for that pattern calculated. The modelled results are seen in Figure 2.23. The image size shows a theoretical improvement of the prototype's resolution from 3.46' (arc-minutes HEW) to 1.83' (arc-minutes HEW). The optic model developed at UoL, highlighted the use of the optimising routine to lead to an improvement in the angular resolution of the prototype's system.

Section 2.2 has introduced the concept of finite element analysis and how it has been used to solve such mechanical questions as: the effect of gravitational sag and the actuators' influence functions. The following Chapters 3, 4 and 5 all continue to develop the FEA simulations of the

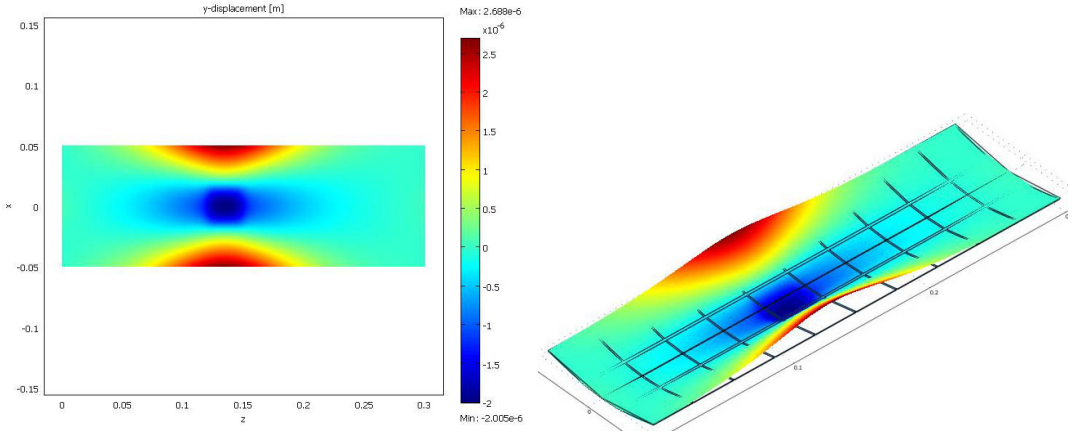

(a) A 2-dimensional representation of a central actuator at -10V

(b) A 3-dimensional representation indicating the form of the influence function

Figure 2.22: An FEA generation influence function for a central actuator at -10V, Figure 2.22(a) indicates the magnitude of the y-displacement of the actuator (the displacement normal to the optic's surface) and Figure 2.22(b) highlights the form of the influence function with respect to the optical surface.

prototype system and comparisons are made to measured results with correlations observed.

2.3 Chapter summary

Chapter 2 has presented the prototype development, the optical dimensions of the ellipsoidal prototype and its intended operation within the X-ray tunnel test facility at UoL. The use of finite element analysis has been presented in reference to ray-tracing code developed by the UoL, and has highlighted the theoretical operation of the prototype within the test facility. The following chapter outlines the development of the cylindrical prototype with particular emphasis on the optic replication via nickel electroforming.

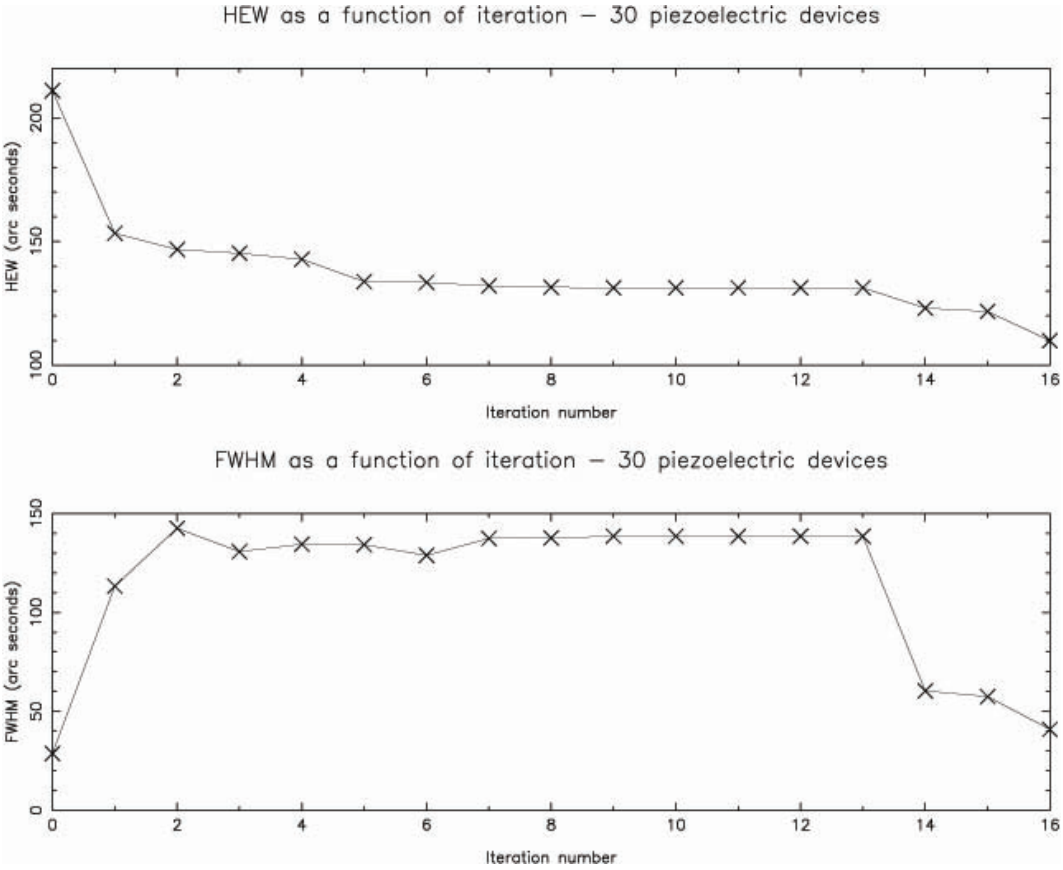

Figure 2.23: The half energy width, and the full width at half maximum, of the modelled detector image as a function of iteration number, image courtesy of CHF from UoL

CHAPTER 3

ELECTROFORMING AND THE DEVELOPMENT OF THE CYCLINDRICAL PRE-PROTOTYPE

This chapter outlines the development of the experimental procedures intended for the production of the ellipsoidal prototype that will be discussed in Chapter 4. This chapter will focus on the optic replication via nickel electroforming; an introduction to the science and practice of electroforming will be given, followed by the production of cylindrical nickel optics. Problems encountered, such as the anisotropy of current density upon a mandrel's surface, shall be discussed and their practical solutions investigated. The chapter concludes with the completion of the cylindrical prototype leading to a discussion of production-method developments required for the manufacture of the X-ray focussing ellipsoidal prototype.

3.1 An overview of the cylindrical prototype's production methods

The prototypes, both cylindrical and ellipsoidal, have two primary components: the optic and the actuators. X-ray optics intended for high sensitivity tend to be thin (sub mm) shells that can be heavily nested to achieve a large effective area. High sensitivity X-ray missions to date use thin electroformed nickel (or nickel-cobalt) shells or epoxy-aluminium films; however, the future of such missions is leaning towards the use of slumped glass optics. The choice of optical material in this project stemmed from the available resources within the Smart X-ray Optics (SXO) consortium. A nickel electrodeposition[1] facility was readily available at University College London (UCL) and therefore the decision was made to proceed with optic fabrication via nickel electroforming. A

[1] The process of depositing metal ions upon a surface

schematic of the intended production method is shown in Figure 3.1: here, a mandrel (a mould of the inverse form of that required by the optic) is placed within the facility until the desired nickel thickness is obtained. The mandrel and optic are then removed from the facility and the optic released with the mandrel's optical form. The first part of this chapter therefore introduces the method of electrodeposition and how it has been employed in the production of the prototype's optics

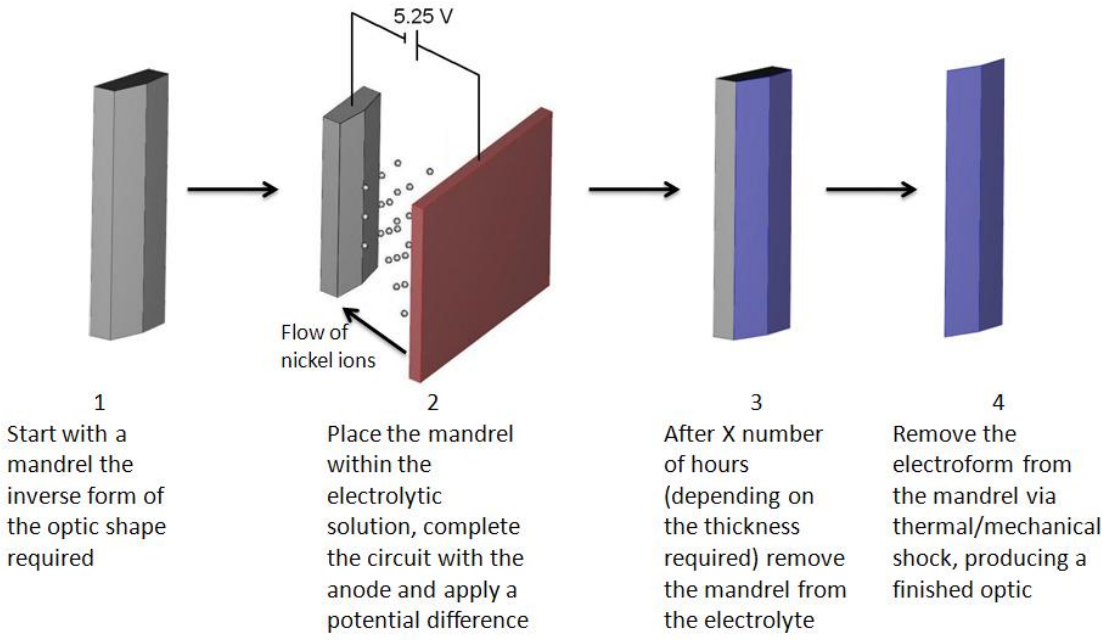

Figure 3.1: A simplified description of the production of the nickel optic via electroforming.

The actuators, as mentioned previously, are manufactured at the University of Birmingham (UoB) with the same curvature as the optical component; in the cylindrical prototype's case a radius of curvature of 155mm. It is intended that they will be bonded in a grid arrangement (3-azimuthal direction $\times$ 10-axial direction) populating the entire reverse of the optical surface. They are to be bonded using a low shrinkage adhesive to minimise the effect of actuator print-through; the wires of the actuators will be harnessed to the reverse of the optic and connected to a 37-D connector, where 30 pins represent the individual driving potential of the actuators and a single pin represents the common ground to all 30 actuators. The second part of this chapter will outline the bonding and harnessing of the actuators to form the completed cylindrical prototype.

3.2 The science of nickel electrodeposition

This section will introduce the science and experimental procedures required to produce an optic, with the required form, via electroforming. Electrodeposition (referring to the deposition of metals upon a surface through electrostatic attraction) is often described as a dark art, where tiny variations in the chemical composition of the bath (i.e. the electrolytic solution) can cause huge effects upon the deposited metal. Electroforming, in comparison with electroplating, electrorefining and other forms of electrodeposition, is the deposition of metal ions upon a mandrel/mould till the desired thickness is obtained, then the deposited metal (the electroform) is removed from the mould with desired geometry. Much of the theory from this section has been taken from Lowenheim (1974) and for the arrangement of the UCL electrodepositing facility the reader is directed to Hart (2000). To familiarise the reader with key chemistry terms pertinent within this chapter definitions will be given at the beginning of each section.

3.2.1 Introduction to the theory of electrodeposition

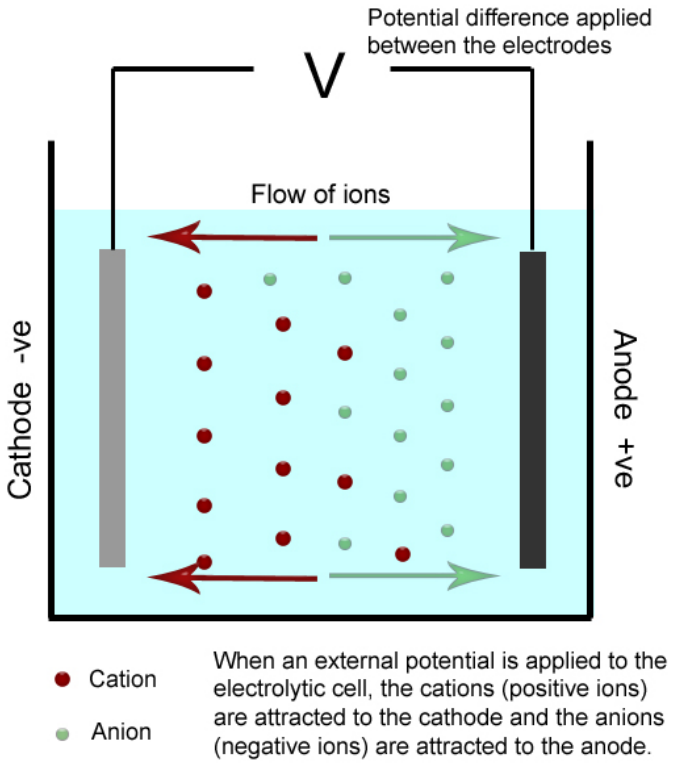

Figure 3.2: A simple electrolytic cell, where electrical energy is used to produce a chemical change that would not otherwise occur spontaneously (Zumdahl 1989)

ELECTROLYSIS - a process which involves forcing a current through a cell to cause a non spontaneous chemical reaction to occur [a]

CATHODE - the negative electrode

ANODE - the positive electrode

ELECTRODE - a collective term for both the cathode and the anode.

ELECTROLYTE - the aqueous solution of the electrodepositing facility

CATION - a positive ion (e.g. Ni^{2+})

ANION - a negative ion (e.g. OH^{-})

ION - a charged particle, a collective term for both the cations and the anions.

OXIDATION - is the increase in oxidation state (i.e. a loss of electrons) [a]

REDUCTION - is the decrease in oxidation state (i.e. a gain of electrons) [a]

a - definitions provided from Zumdahl (1989).

Due to nickel's role in the production of the prototype's optic, it shall be the example metal throughout the discussion of the theory of electrodeposition. The principle behind electrodeposition is that on the application of an electric potential, the cathode becomes dominately negative, and the anode positive; within the electrolytic solution, the nickel ions (cations) are attracted to the cathode, where they obtain two electrons (they are reduced) and become incorporated within the metal lattice following Equation 3.1. The crystalline structure of metal atoms have metal ions bonded in layers with a cloud of moving electrons: therefore, when a nickel ion becomes incorporated within the lattice it does not become a neutral nickel atom, but rather its ionic charge is balanced by the cloud of electrons moving throughout the metal.

$$Ni^{2+} + 2e^{-} = Ni \tag{3.1}$$

At the anode the opposite reaction to Equation 3.1 occurs. Electrons are removed from the nickel atom, causing it to break its bond with the anode lattice: these nickel cations then join the electrolyte and often bond with water molecules to form hydrated nickel ions.

The physics which governs the process of electrodeposition is attributed to Faraday's laws of electrolysis (1833), as detailed below:

- The weight of a substance formed at an electrode is proportional to the amount of current passing through the cell.
- The weights of different substances produced at an electrode by the same amount of current are proportional to the equivalent weights

Using the above laws, the quantity of a deposited metal can be calculated for a given current and duration. The following example calculates the thickness of the nickel deposit for the ellipsoidal mandrel as described in Chapter 4:

ATOMIC MASS, NICKEL 58.693g

DENSITY, NICKEL 8900Kg/m^3

APPLIED CURRENT 5.25A

TIME 40 hours

SURFACE AREA 0.0525m^2

STEP 1 - define the unit *Faraday*, which is the number of coulombs per mole of electrons.

$$\begin{aligned} 1\ Coulomb &= 1\ Ampere \times 1\ Second \\ Charge\ on\ 1\ electron &= 1.602176462 \times 10^{-19}\ C \\ Charge\ on\ 1\ mole\ of\ electrons &= 1.602176462 \times 10^{-19} \times 6.02214199 \times 10^{23} \\ &= 96485.3415\ Coulombs/Mole \\ &= 1\ Faraday \end{aligned} \tag{3.2}$$

STEP 2 Calculate the total number of coulombs of charge for the duration of the electrodeposit.

$$\begin{aligned} Total\ number\ of\ coulombs &= 5.25 \times 40\ \times\ 60\ \times\ 60 \\ &= 756000\ C \\ &= 7.560\ \times\ 10^5\ C \end{aligned} \tag{3.3}$$

STEP 3 Calculate the number of moles of electrons required to carry a charge of 7.560×10^5 C; from Equation 3.2 1 mole of electrons carries ~96485 C of charge.

$$\begin{aligned} moles\ of\ e^- &= \frac{7.560\ \times\ 10^5}{96485} \\ &= 7.835\ mol \end{aligned} \tag{3.4}$$

STEP 4 As each nickel atom requires two electrons, the number of moles of electrons produces half the number of moles of nickel atoms, $Ni^{2+} + 2e^- \longrightarrow Ni$

$$\begin{aligned} moles\ of\ Ni &= \frac{7.835}{2} \\ &= 3.918\ mol \end{aligned} \tag{3.5}$$

STEP 5 Calculate the mass of the deposited nickel

$$\begin{aligned} The\ molar\ weight\ of\ nickel &= The\ atomic\ mass\ of\ nickel \\ 1\ mol\ of\ Ni &= 58.693\ g \\ 0.7835\ mol\ of\ Ni &= 3.918\ \times\ 58.693 \\ &= 229.242\ g \\ &=\sim 0.230\ kg \end{aligned} \tag{3.6}$$

STEP 6 From the mass of nickel deposited the thickness of the deposit can be calculated from the surface area of the mould/mandrel.

$$\begin{aligned} Mass\ deposited &= Density\ of\ the\ material \times Surface\ area \times Thickness \\ Thickness &= \frac{Mass\ deposited}{Denisty \times Surface\ area} \\ &= \frac{0.230}{8900 \times 0.0525} \\ &= 4.921 \times 10^{-5} m \\ &=\sim 500 \mu m \end{aligned} \tag{3.7}$$

Equation 3.7 predicts that for a 0.525 m^2 surface area, with a duration of 40 hours at 5.25 A, the thickness of the deposit will be $\sim$500μm; however, there are several other factors that affect the rate of deposition and these shall be outlined in following sections.

3.2.2 Deposition of metal with no applied potential

LIGAND a neutral molecule or ion, having a lone pair of electrons that can be used to form a bond to a metal ion [2].

ADSORPTION atoms or molecules being held at a material's surface.

When an electrode is within an electrolytic solution and there is no applied external potential there is an equilibrium of reactions occurring at the surface of the electrode. The cloud of electrons within the metal lattice not only balances the charge of the metal ions within the lattice, but also attracts cations and water molecules (due to their dipole nature). The cations are held near the surface of the electrode via electrostatic attraction while the water molecules are held by adsorption forces and these ions/molecules form a *double layer*. From this layer the metal ions can release their ligands and bond to the metal lattice and neutralise their charge; simultaneously metal ions within the metal lattice can become loose and bond with water molecules from the double layer and become hydrated metal ions.

3.2.3 Polarisation

POLARISATION a term used to refer to the external potential that is applied to an electrolytic cell.

To disrupt the equilibrium state as outlined in the previous section and to initiate the deposition of metal ions upon the cathode, an external potential has to be applied, and this potential is termed *polarisation*. There are several forms of polarisation within an electrolytic cell and these are outlined below:

ACTIVATION POLARISATION This is the minimum potential required for deposition to occur: it is the energy required to move from the double layer and to become incorporated within the metal lattice.

CONCENTRATION POLARISATION When metal deposition has occurred for a finite amount of time, the concentration of metal ions within the double layer decreases as mass transport mechanisms (mentioned in the following section) are not sufficient to maintain the original concentrations and there is a shift in the equilibrium potential. This change in potential is termed concentration polarisation.

[2] definition from Zumdahl (1989)

RESISTANCE/OHMIC POLARISATION This is the potential required to produce a flow of current through the ohmic resistance of the electrolyte, also, if the cathode is covered in a thin film offering a resistance, then this component adds to the resistance polarisation of the electrolyte.

TOTAL POLARISATION This is the sum of these individual voltages and is the potential required to maintain a steady operation of current throughout the tank.

3.2.4 Transport of metal ions within the electrolyte

There are three mechanisms that transport metal ions from the electrolyte to the cathode's surface (similar mechanisms occur at the anode's surface). When the external potential is applied, an electric field is generated between the two electrodes; within this field the cations are attracted to the cathode and the anions are attracted to the anode: this electrostatic attraction is termed *ionic migration* and is the first transport mechanism.

Convection is the second mechanism and is found in several forms. At the cathode's surface metal ions are being removed from the electrolyte, decreasing the density of the solution, resulting in an upward flow of solution (the reverse occurs at the anode). This form of convection is termed *natural convection*. Baths are often heated to increase the rate of reaction and this heating provides a *thermal convection* within the electrolyte. To remove hydrogen bubbles (a by product of the cathode reaction) from the surface of the cathode, mechanical agitation is often employed: this is the final form and is termed *forced convection*. However, convection is not the dominant method of depositing metal ions upon a surface as friction forces between the metal ions and electrolyte oppose this method. In the immediate vicinity of the cathode's surface, ionic migration, and diffusion in particular, dominate.

The final transport mechanism is *diffusion*, which is the movement of molecules to equalise a concentration gradient: molecules will move from a high concentration to a low concentration to bring it into equilibrium. In the immediate vicinity of the cathode, metal ions have been removed, leaving not only a lower density, but also a lower concentration. This area of low concentration is termed the *diffusion layer* and it is defined as having a 1% decrease in concentration (of a specific chemical species) in comparison with the bulk solution (the total solution within the tank). This diffusion layer is not created instantaneously, but rather develops in a few seconds after the application of an external voltage. The rate of diffusion is inversely proportional to the thickness of the diffusion layer (Lowenheim 1974); agitation acts to decrease the diffusion and as a result the rate of diffusion and deposition increases, leading to diffusion being the dominant mechanism of

transport in the immediate vicinity of the cathode's surface.

3.2.5 Current density and the deposition of metal ions

Metal ions do not deposit themselves uniformly across a cathode; they deposit themselves preferentially in certain locations as defined by the current density distribution. A thorough analysis of the effect of current density shall be given in Section 3.3.6, therefore only a qualitative description shall be provided in this section. Sharp corners and edges of a cathode produce a higher current density than flat central regions: this is an effect caused by a non uniformity in the density of electric field lines, while recesses and hollows have a lower current density and as a result metal ions deposit preferentially at corner and edges as opposed to hollow and recesses.

Typically, assuming an even current density, the metal lattices of the metallic structure build evenly, one layer of metal ions upon another layer of metal ions. However, irregularities in the lattice growth do occur and two forms of these are called *nodules* and *trees*. Nodules occur in two instances, first due to the inclusion of a foreign particle upon the metal deposit, resulting in a deformation of the lattice growth, and second, in areas of high current density where the lattice growth is much larger than the cathode as a whole: examples can be seen in Figure 3.3. Trees or *dendrites* are angular structures that form at locations which provide a rapid supply of ions by diffusion: an example can be seen in Figure 3.4. These undesired growths increase over time, and therefore with thickness, and can place a practical limit on the thickness of electroformed objects.

A final problem that affects the growth of metal ions are hydrogen bubbles at the surface of the cathode. The electrolytic cell is not 100% efficient in its conversion of external potential to deposited metal; approximately 2 - 4% of the potential is used in the conversion of water to H_2 and OH^-. Without sufficient agitation these hydrogen bubbles fix to the cathode's surface causing the metal ions to bond around them and this results in small holes within the deposit called *pits* or *pitting*, an example of which can be seen in Figure 3.3(b).

3.2.6 Stress within the electrodeposit

Stress within the electrodeposit originates from either a mismatch in the lattice structure of the deposited metal, or from the incorporation of impurities within the deposit which disrupt the natural growth of the lattice.

The stress within the deposit can be defined as either tensile or compressive. Figure 3.5 highlights these effects for a thin cathode plate and electrodeposit. Tensile stress causes the deposit

(a) A ring of nodules (b) Corner nodules and pitting

Figure 3.3: Example of nodule growths, Figure 3.3(a) displays a ring of nodules resulting from a tiny gap in the masking material and Figure 3.3(b) highlights the nodules and pitting formed at the corners of a deposit as a result of high current density.

Figure 3.4: An example of a dendrite/tree formation courtesy of the UCLA mineral physics laboratory (`www.igpp.ucla.edu/minphys`)

to curl upwards and form a bowl: this form of stress often results in poor adhesion to the cathode. Compressive stress curls the plate downwards and forms a bump and this stress can be difficult to accomondate for within electroforms, as the stress fixes the plate to the mandrel/cathode (Stein 1996). Practical examples of both compressive and tensile stress are presented within the paper by Kim & Mentone (2006).

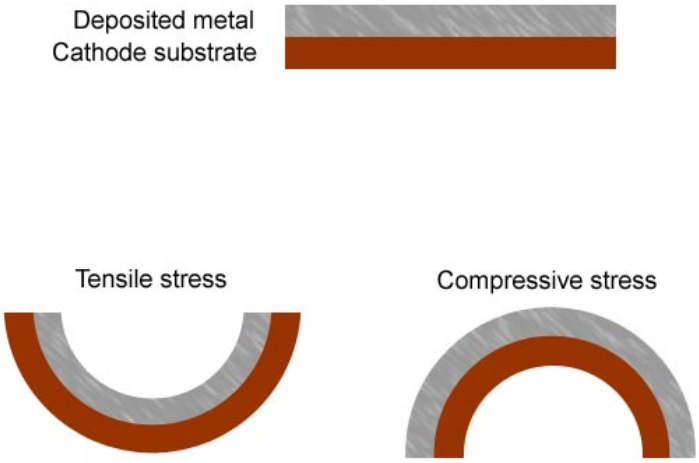

Figure 3.5: Stresses within the metal deposit: tensile stress pulls itself away from the cathode and compressive stress forces itself upon the cathode.

3.2.7 Adhesion and passivation

The adhesion of metal ions upon the cathode's surface is greatly affected by the the cleanliness of the surface. Residual films of material can act to insulate the cathode or disrupt the growth of metal ions causing the electrodeposit to peel away from the cathode. Therefore prior to the cathode entering the electrolyte its surfaces must be thoroughly cleaned to remove all traces of oil or grease, in addition to general detritus.

However, often a chemical film is beneficial, particularly in electroforming, where the objective is to remove the electroform from the mandrel. The mandrel's material can be chemically treated to produce an oxide film upon its surface; this layer does not contaminate the bath, but produces a barrier, preventing the metal ions from reaching the metal ions of the cathode. This introduction of an oxide layer is called passivation and it is a term that will also be applied to the oxide layer produced upon the titanium anode baskets mentioned in Section 3.3.1.

3.2.8 The effect of impurities

There are many different forms of impurities; there are those which are insoluble and form an electrolyte-impurity suspension, and there are those which are soluble and become incorporated within the electrolytic solution. The insoluble particles are caused by general dust and other detritus within the operating environment of the deposition facility. These particles can become attracted to the electrodes, and, in the case of the cathode, incorporated within the metal deposit to form nodules or pitting. In addition, agitation can bring up particles which had settled at the bottom of the tank, aggravating the effect of impurities.

Soluble contaminants, including organic compounds, have the effect of altering the metallic lattice of the deposited metal and affecting the overall structural properties of the metal, which is generally non-beneficial. The effect of metallic contaminants depends on the potential required to deposit the metal upon the cathode's surface. If the metal has a lower reduction potential than the external potential applied to the bath, the metal will readily deposit upon the cathode: this is quite damaging to the final metal deposit, but it is possible to remove these contaminants easily through plating-out upon a scrap cathode. Metals that have a higher reduction potential than the external potential cannot be directly deposited upon the metal lattice, unless they co-deposited with another molecule. Finally, other ions, such as sodium, potassium, ammonium and magnesium, cannot be deposited at the cathode, but they can have an effect at the double layer, which affects the internal stress of the deposit.

3.3 The OSL electroforming facility

The theory behind electrodeposition has been introduced; this section will present UCL's electrodeposition facility and how it will be operated in the production of the prototype's optic. The electrodeposition facility was originally developed for the deposition of nickel upon carbon fibre to produce lightweight optical mirrors (Thompson *et al.* 2008; Thompson *et al.* 2008). This electroplating procedure required a low stress deposit to minimise distortion within the carbon fibre. There are several different chemical composition of nickel deposition baths available; however, nickel sulphamate offered nickel deposits with the lowest stress, and therefore was deemed most suitable for optics production. Figures 3.6 and 3.7 display the facility as set-up within the laboratory and a schematic of the facility including dimensions respectively. The following sections outline the mechanical and chemical components of the bath, how the bath is operated to produce nickel electroforms and the problem of current density anisotropy.

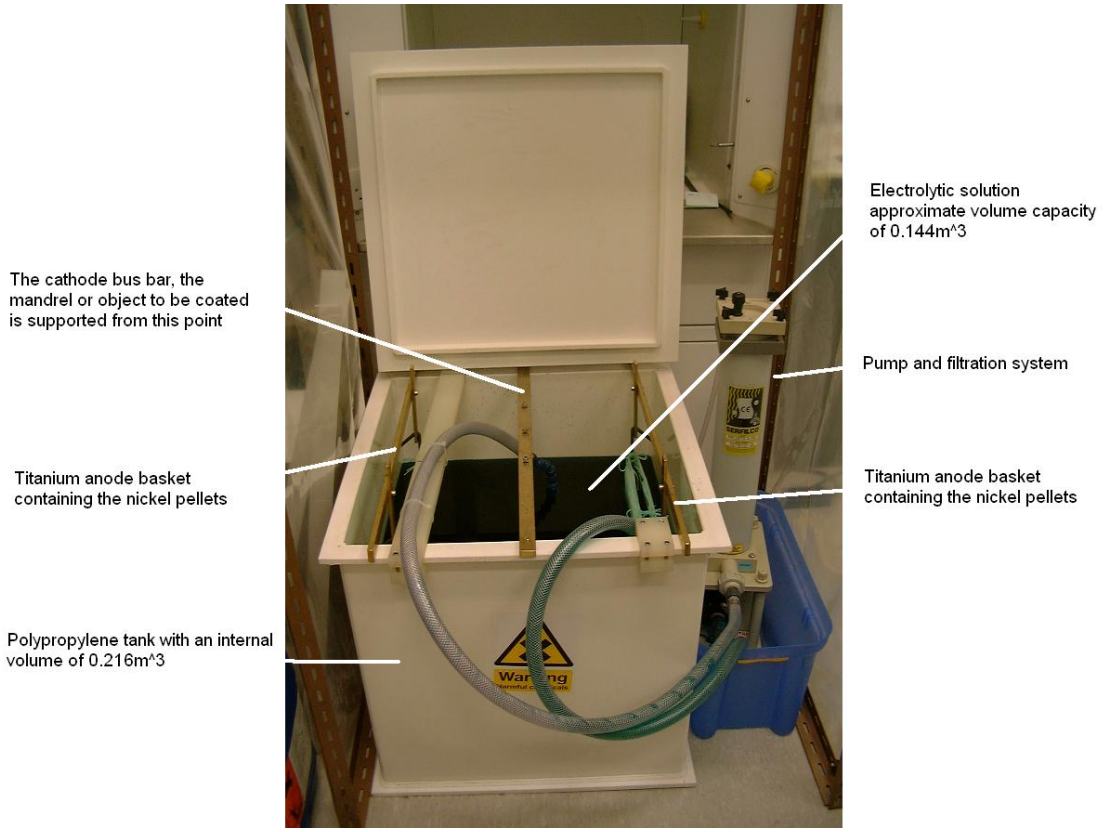

Figure 3.6: The OSL electroforming facility

3.3.1 Electrodeposition equipment set-up

The non-chemical components of the electrodeposition facility shall be described in the following section:

POLYPROPYLENE TANK - The white plastic tank is made from polypropylene as the material is inert when in contact with the electrolytic solution: it has a maximum internal volume of 0.216m^3.

FILTRATION PUMP - The pump acts both to agitate the solution, leading to an increase in deposition rate and a removal of hydrogen bubbles at the cathode's surface, and to filter the solution removing insoluble particles.

TITANIUM ANODE BASKETS - A titanium mesh provides the outer walls of the baskets and it allows the dissolved nickel to exit unhindered from the anode but retains the non dissolved nickel pellets. The material of the anode baskets must be electrically conductive and non-

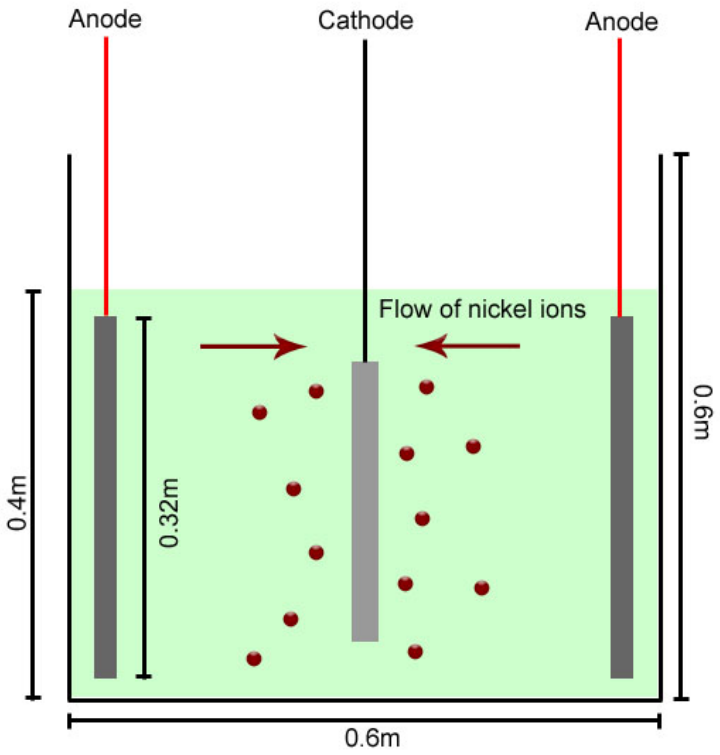

Figure 3.7: A schematic of the UCL electrodepositing facility

reactive within the electrolyte when a potential is applied. Titanium develops an oxide layer (passivation layer) immediately with potential, preventing undesired chemical interactions.

NICKEL PELLETS - The anode baskets are filled with Inco S-Nickel pellets, which is a sulphur activated nickel that allows the dissolution of the pellets without the addition of nickel chloride (discussed in Section 3.3.2); typically these pellets are ∼1cm in diameter.

ANODE BAGS - The dissolution of the nickel pellets produces a black residue which must be isolated from the bulk solution; polypropylene anode bags surround the entirety of the anode baskets, preventing the egress of the residue outside the immediate vicinity of the anode, but allowing the nickel cations to enter the solution unhindered.

POWER SUPPLY - The external potential is supplied using a PWR800L power supply from KIKUSUI: it maintains a constant current by altering the voltage to compensate for variations in the bath's resistivity.

3.3.2 The chemical composition of the nickel sulphamate bath

The chemical composition of the nickel sulphamate bath was first proposed in 1938. The original composition included nickel chloride to aid in the dissolution of the anode nickel; however, nickel chloride also had the effect of increasing the internal stress of the nickel deposit. A chloride-free solution was suggested in 1954, where the chloride's role in the dissolution of the anode nickel could be compensated for by using sulphur-activated nickel pellets (i.e. Inco S-Nickel). The resulting nickel deposits offer the least stress of any nickel bath and this condition leads it to being the favoured bath for electroforming. Table 3.3.2 describes the chemical composition and quantities required within the chloride-free nickel sulphamate bath; a description of their purpose within the solution is outlined below:

NICKEL SULPHAMATE - The primary source of nickel ions within the electrolytic solution

BORIC ACID - This acts as a buffer and stabilises the pH of the solution in the immediate vicinity of the cathode.

SULPHAMIC ACID - The pH of the solution increases over time (i.e. becomes more alkaline) due to the efficiency of the cathode deposition, ∼96-98% of the potential is used to deposit nickel, the additonal ∼4-2% is in the production of hydrogen gas from the water molecules (resulting in alkaline OH^- ions). Therefore, to preserve the required pH range of the bath, sulphamic acid is added.

DEIONISED/DISTILLED WATER - Over time the water within the solution evapourates and this is particularly noticable when left for long durations between operations. To preserve the correct concentrations, a quantity of water is added, determined by a physical marker on the side of the tank.

WETTING AGENT - to remove the hydrogen bubbles from the mandrel's surface, the surface tension of the solution has to be lowered through the addition of the wetting agent.

3.3.3 Additional equipment and safety concerns

The following is a list of additional laboratory equipment and safety precautions used in the experimental procedure of nickel electroforming,

DIGITAL PH METER - To measure the pH of the solution to ensure it is within the 3.9-4.1 operating range.

Chemical	Chemical formula	Quantity added
Nickel Sulphamate	$Ni(NH_2SO_3)_24H_20$	350 ml/l
Boric Acid	H_3BO_3	30 g/l
Sulphamic Acid	H_3NSO_3	Added over time to lower the pH as required
Distilled/Deionised water	H_2O	as required
Wetting agent		1 ml/l
pH range		4.1 - 3.9
Temperature of operation		$\sim 22\,^{\circ}\mathrm{C}$ (room temperature)

Table 3.1: The components of the nickel sulphamte electrolytic solution

TITANIUM METAL RING - To determine the surface tension of the electrolyte solution.

DE-GREASING AGENT - SD-Klene de-greasing agent is used in the preparation of the cathode prior to electrodeposit: it is a strong non-caustic detergent that removes oil and grease from a surface.

PUMP NOSSELS - Different nossels can be placed at the end of the pump/filter to agitate the solution to varying degrees.

POLYESTER INSULATING TAPE - This chemical/acid resistant tape is used to mask the areas of the mandrel that do not required metal deposition.

DISPOSABLE GLOVES - These are worn throughout the experiment, to ensure that no chemicals come in contact with the hands; they also have the benefit of preventing finger marks upon the clean mandrel surface.

LONG ARM RUBBER GLOVES - These are worn while positioning the mandrel within the facility and they are chemical/acid resistant.

RUBBER GLOVES - These are worn while mixing any chemicals.

GOGGLES - Splash resistant goggles are worn to protect the eyes while mixing chemical solutions and operating in the immediate vicinity of the electrolytic solution.

ARM GATERS - These are worn to offer extra protection while mixing the sulphamic acid (powered acid is added to deionised to produce a 10% acid solution)

FACE MASK - Worn to prevent the inhalation of powered acid grains during sulphamic acid production.

FUME CUPBOARD - The entire UCL electrodeposition facility is operated out of a plastic enclosure linked to a fume cupboard drawing air away from the immediate vicinity of the bath.

3.3.4 Operational procedure - production of a nickel electroform

The following is a narrative of the steps required to produce a nickel electroform.

STEP 1 - ELECTROLYTE PREPARATION - First, distilled water is added to compensate the effect of evaporation and the pump is activated to thoroughly mix the diluted solution. The pH of the bath is measured; if the pH is higher than 4.1, sulphamic acid is added in small 100 ml quantities until the desired pH is obtained ($\sim$3.9). Approximately 10-15 minutes is given between each acidic addition to ensure a thorough mixing of the acid within the solution; care should also be taken with the addition of sulphamic acid, as the pH can jump suddenly to a lower pH in the region of 3.9, leading to a more acidic bath than desired. The surface tension is then measured to determine the quantity of wetting agent to be added. The pump should be turned off and the solution allowed to settle. The titanium ring is dipped slowly into the solution and then slowly brought out. If there is a thin film of electrolyte within the ring then the surface tension is adequate and no additional wetting agent should be added; however, should the film test fail, then a small quantity (10ml) of wetting agent should be added until the test succeeds (Figure 3.8).

STEP 2 - CATHODE/MANDREL PREPARATION - The mandrel should first be thoroughly cleaned using the SD-Klene degreasing compound to remove all trace of oil/grease from its surface. Distilled/deionised water should be used to rinse the mandrel to ensure no degreasing compound can enter the electrolyte. The mandrel should be left to dry before the masking of regions that do not require nickel deposition. The degreased connector, the rod or wire used to connect the mandrel to the cathode bus bar, should be fixed to the mandrel and masked if required. Figure 3.9 depicts a plate mandrel with external potential connection supplied by a connector wire.

STEP 3 - POSITIONING THE MANDREL WITHIN THE ELECTROLYTE - Immediately before the mandrel is placed within the bath it should be thoroughly rinsed to remove any dust etc. which may have settled upon the surface after degreasing. The mandrel is placed within the facility, facing the anode, and the connector fixed to the cathode bus bar; conductivity between the bus bar and the connector should be verified to ensure that current will flow towards the mandrel. The pump should

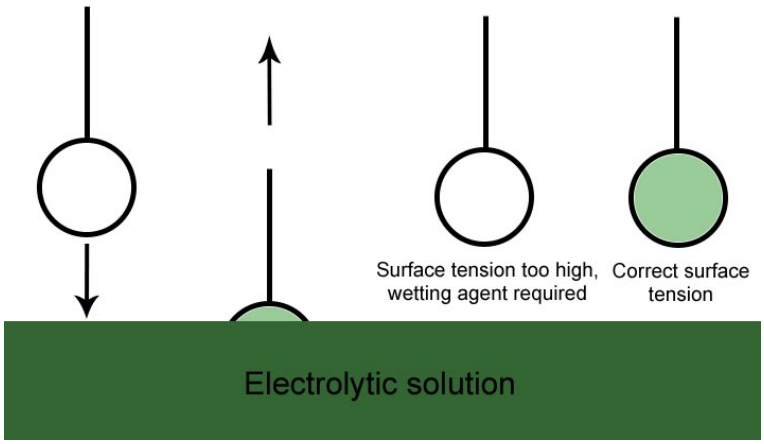

Figure 3.8: The titanium ring test used to determine the surface tension of the electrolyte. If a thin film is not produced after removing the ring from the electrolyte then additional electrolyte should be added.

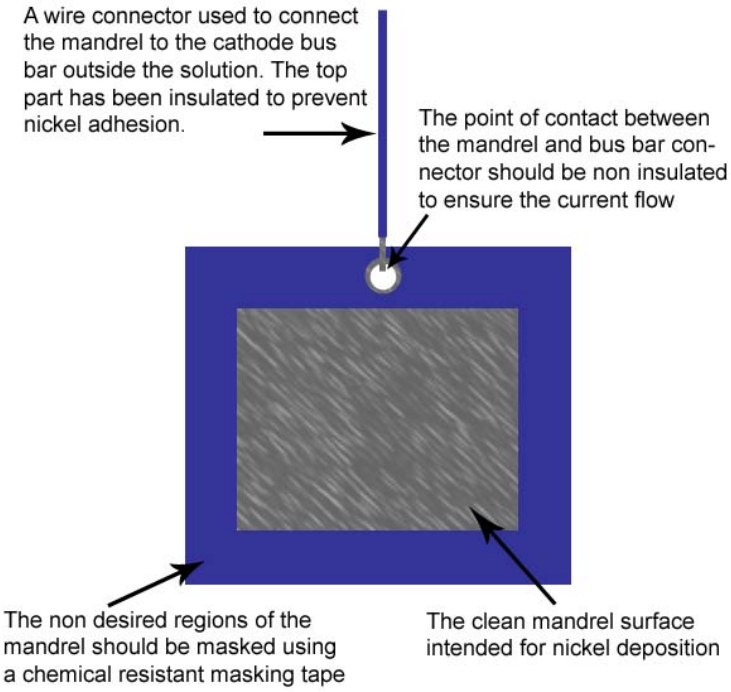

Figure 3.9: A preparation of a simple mandrel prior to electrodeposit

be turned on and positioned to provide an even flow of electrolyte in the vicinity of the mandrel.

STEP 4 - ELECTRICAL CONNECTION - If the mandrel has two faces that require deposition then both anodes in the facility are used; however, if only one face is required (the cylindrical prototype's mandrel), then one of the anodes is removed from the circuit. With conductivity established between the anode and cathode/mandrel through the use of a multimeter, the power supply is activated. Figure 3.10 depicts the power supply unit and the method of obtaining the desired current output. The amount of current output is determined by the surface area and the desired ideal current density upon the surface; typically the bath is operated at a low current density of 0.01A/cm^2 as this minimises the stress within the deposit, therefore the current output is calculated from $current\ density\ \times\ surface\ area\ (cm^2)$. Once a current is output, then the voltage between the anodes can be measured and compared against that of the power supply. Assuming no gross deviations are seen, the bath can be left to operate for the required duration.

Figure 3.10: The electrodeposition power supply: the power supply is turned on using the on/off switch in the bottom left-hand corner, the constant current output is then selected and the dial used to select the desired current output. Finally, the current is output to the electrolyte cell using the power output button.

STEP 5 - REMOVAL FROM THE BATH - The power supply is turned off (as mention in Figure 3.10) and the mandrel disconnected from the cathode bus bar. Removal of the electroform from the mandrel can be achieved through force or thermal shock (assuming different coefficients of thermal expansion (CTE)).

3.3.5 Early experimentation

The first trials practised the experimental method as outlined above. However, it soon became apparent that thickness anisotropy was greatly affecting the electroforms, making them stiffer than desired. An example can be seen in Figure 3.11: nickel was deposited for approximately 8 hours

and it produced edge deposits which were ∼10 times greater than the centre. This magnitude of anisotropy would have greatly affected the actuator influence functions across the surface of the optic and therefore a solution had to be devised to provide thickness uniformity across the optic.

3.3.6 Current density anistropy

The thickness variation encountered in Figure 3.11 stems from anisotropy within current density. Although the current supplied to the circuit assumes that a uniform density extends across the cathode's surface (0.01A/cm^2), this is rarely experienced upon any cathode and the actual current density is very non-uniform. As mentioned in Section 3.2.1, Faraday's laws dictate that the amount of metal deposited at the cathode is directly related to the current flowing through the system, therefore to solve the deposit thickness variation the current density in the region of the cathode has to be smoothed.

The current density upon the mandrel's surface is created upon the application of a potential difference and can be defined by Ohm's law (Serway & Beicher 2000), Equation 3.8, which states:

- *for many materials (including most metals) the ratio of current density to electric field is a constant σ that is independent of the electric field producing the current.*

$$\mathbf{J} = \sigma \mathbf{E} \tag{3.8}$$

$\mathbf{J}$ - current density with SI units A/m^2, vector quantity

σ - the conductivity of the conductor

$\mathbf{E}$ - the electric field, vector quantity

It is the current density's dependence upon the electric field which initiates the current density anisotropy: if one considers two plates opposite one another with a potential difference, the resultant electric field lines follow those in Figure 3.12. The plate's corner points experience a greater density of electric field lines than the centre of the plate. When this is coupled with Equation 3.8, the current density will be greater in the corner regions than the centre, assuming a uniform coefficient of conductivity σ.

Ohm's law also forms the foundation of the *Conductive media DC application mode* within COMSOL MULTIPHYSICS and thereby supplies a tool with which to visualise the current density

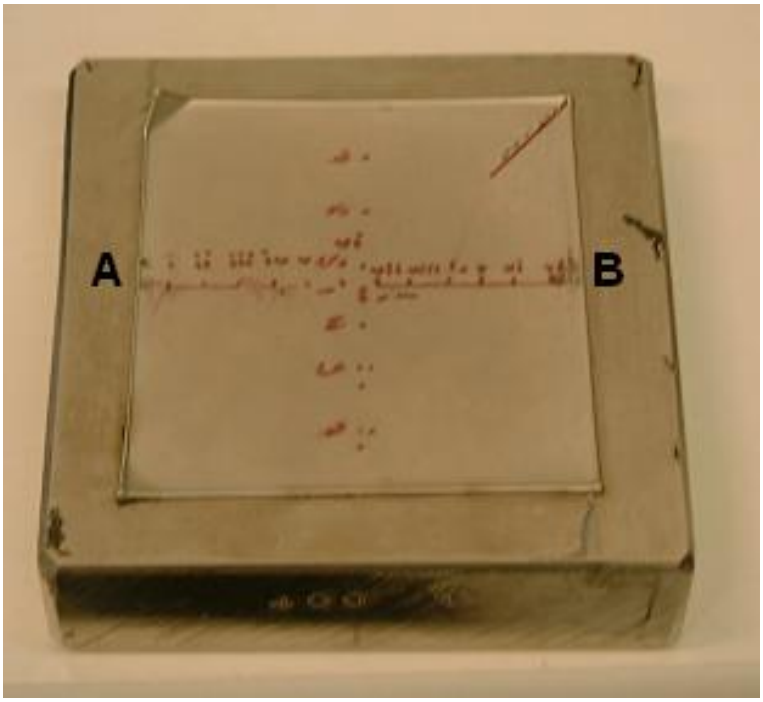

(a) Highlighting the effect of current anisotropy

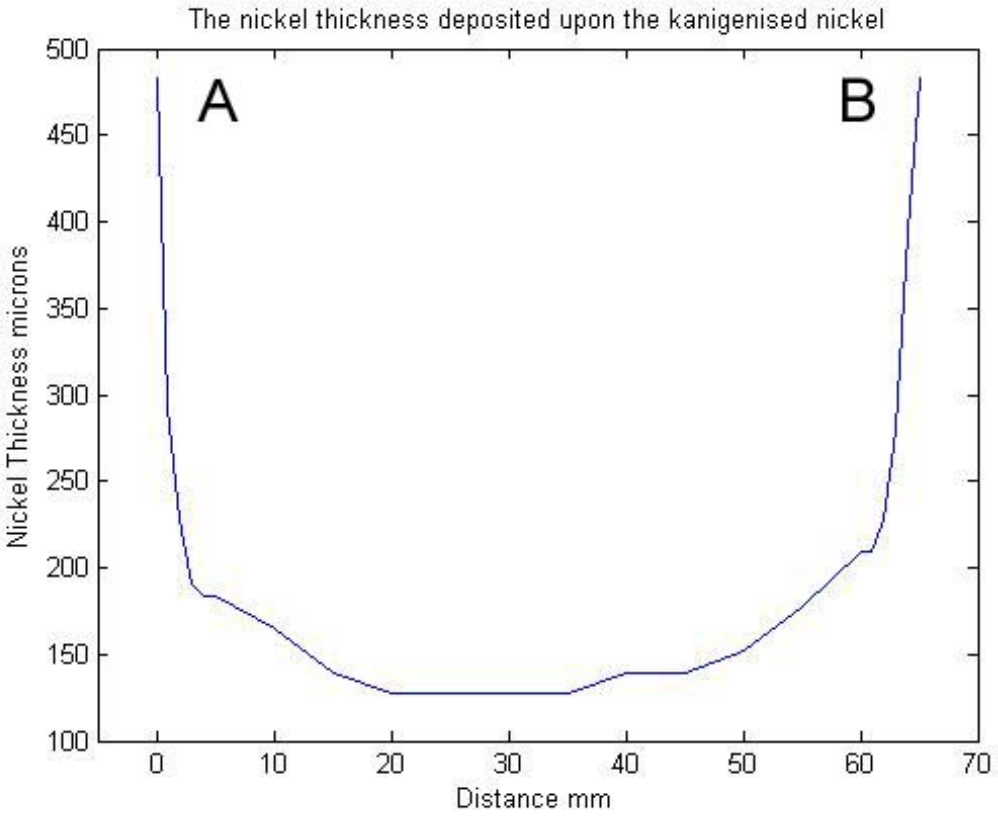

(b) A deposition thickness

Figure 3.11: The variation in deposition thickness as a function of position. Figure 3.11(a) displays the electrodeposit upon a kanigen mandrel (the relevence of the kanigen mandrel is explained in Chapter 4). Figure 3.11(b) highlights the measured thickness, where A and B refer to Figure 3.11(a).

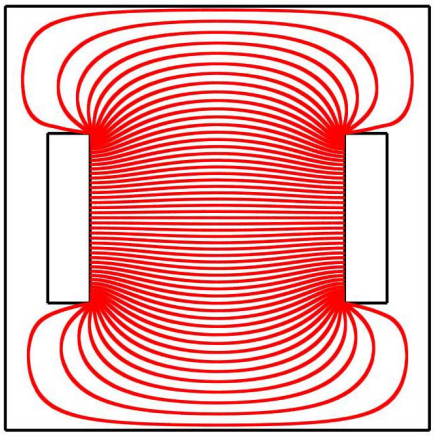

Figure 3.12: An electric field existing between two oppositely charged plates: the condensation of field lines at the tips of the two plates indicate an area of greater electric field strength.

anisotropy (COMSOL August 2006). Using the geometric arrangement in Figure 3.12, a finite element analysis (FEA) model was created which represented the conductive medium of the tank minus the two plates; the plates are subtracted as it is the boundaries between the plates and the electrolyte that are of interest, not the plate itself. Figure 3.13 highlights the applied boundary conditions, one plate boundary at ground, the other at 5V and all other boundaries are insulated. The mesh was selected to be finer in the boundary regions as this would provide a more detailed solution in the region of interest. The resultant current density upon the ground boundary is shown in Figure 3.14. When this figure is compared with the thickness measurements in Figure 3.11(b) there is a distinct similarity in the form, despite the differences in geometry between the experiment and the model.

Therefore, to remove the over deposition at the edges of the electroform, the electric field lines across the surface of the mandrel have to become uniform; in practice this is near impossible to obtain. The problem now becomes how to remove the worst of the over deposition within the constraints of the electrodeposition facility. The problem is well documented among electrodepositing specialists (Tan & Lim 22 April 2003; Yang *et al.* 2008). The general practice is to move the regions of high electric field line density to another part of the cathode which is not part of the desired electroform. The additional electrodes are often termed *sacrificial electrodes* or *secondary cathodes* (Yang & Kang May 2000) as they form no part of the mandrel but are present only to receive the high current density effect. An alternative method is to revolve the cathode within the electrolyte and this is often employed in mandrels which have 360 ° of azimuthal curvature;

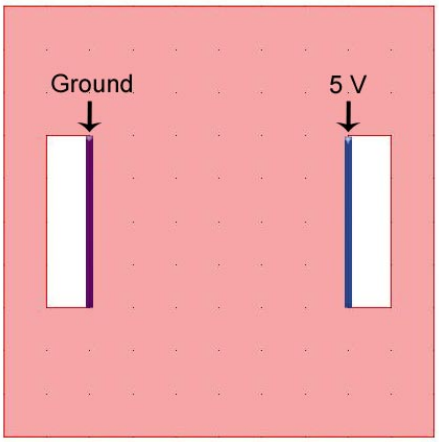

Figure 3.13: The potential boundary conditions applied upon the FEA model to produce a representation of the current density.

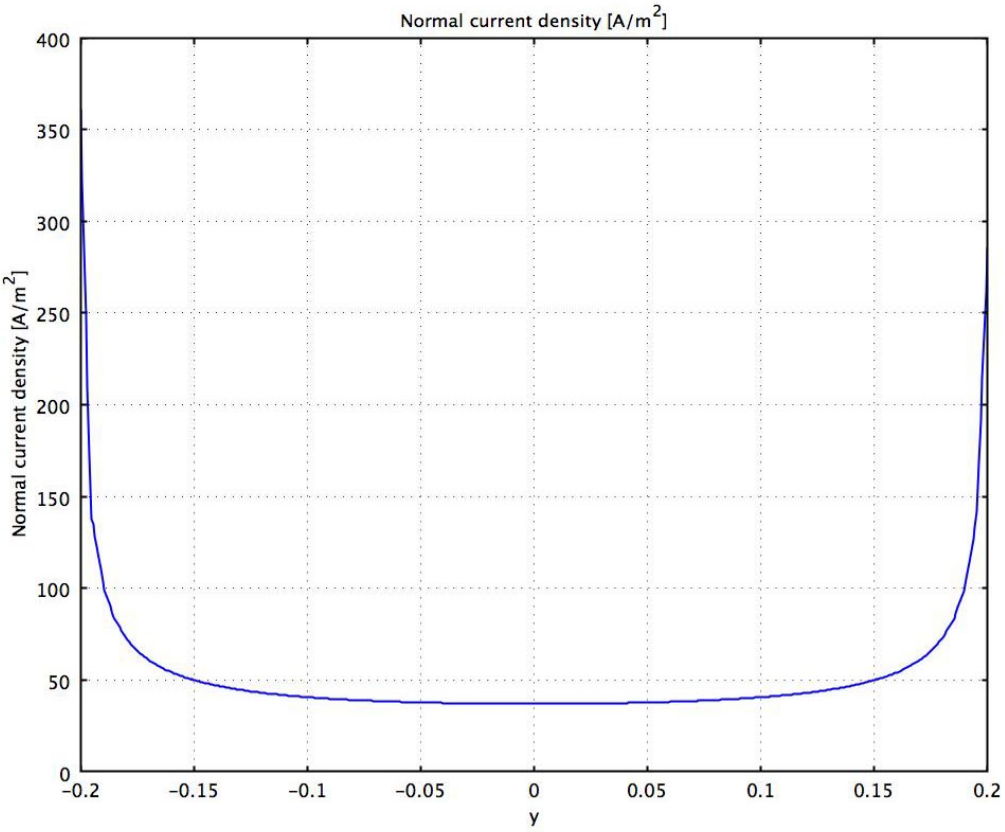

Figure 3.14: The resultant current density from the FEA boundary conditions as outlined in Figure 3.13

however, sacrificial electrodes are the easier to implement within a small in-house facility.

3.3.7 Sacrificial electrodes

Several forms of sacrificial electrodes have been proposed over the years; however, at UCL the simplest solution was investigated, that was, increasing the area of the cathode/mandrel and then removing the central region as the electroform, leaving the over-deposited regions upon the excess area. This approach required that the sacrificial electrode (the excess area) be in-plane with the mandrel and that it should be insulated from the mandrel to allow the electroform to be removed without cutting the deposit. The insulating layer would also have to be as thin as possible, to ensure that the cathode appeared as one single object and therefore minimise further edge effects.

An experiment was designed to investigate the practical implementation of such sacrificial electrodes: two stainless steel squares were cut, one with length 50mm and one with length 100mm. The smaller square was designed to fit within the large square with a $\sim$250μm gap around the perimeter, as shown in Figure 3.15. A $\sim$200mm length of polypropylene insulator, 5mm in height, was positioned between the mandrel and the sacrificial electrode. The insulator was extruded in height, to ensure a physical boundary over which the nickel could not deposit. Due to the form of nickel growth, a non-extruded boundary could be bridged by a growth in nickel deposit, therefore an extruded insulator would prevent this growth and allow the electroform to be removed from the sacrificial nickel (Figure 3.16).

The connection to the cathode bus bar was via a wire connection to the sacrificial electrode: to then share that connection with the mandrel a wire bridge was made from the sacrificial electrode to the mandrel and this was made on the reverse of the test piece to minimise the electric field disruptions upon the front of the mandrel. The wire was bonded to the stainless steel using a silver conductive epoxy; the experimental set-up is shown in Figure 3.17. The test piece has a total surface area (front and back) of 200cm^2 leading to a current of 2A (assuming 0.01A/cm^2). Nickel would be deposited for 8 hours to achieve a thickness of $\sim$100μm. Only one anode was used for the experiment, as only the front surface with the extruded insulator was of interest, therefore deposition upon the reverse of the test piece was not of concern.

An FEA representation of the experiment was produced; the mandrel, insulator, and all connectors were modelled and can be seen in Figure 3.18. The single anode was depicted as a 32cm $\times$ 32cm $\times$ 2cm rectangle, and the bath was represented as a 60cm $\times$ 60cm $\times$ 40cm block of electrolyte. The internal components of the bath (i.e. the mandrel, connectors, and anode) were subtracted from the bath, leaving the bath with the boundaries of the mandrel and anode. The mesh

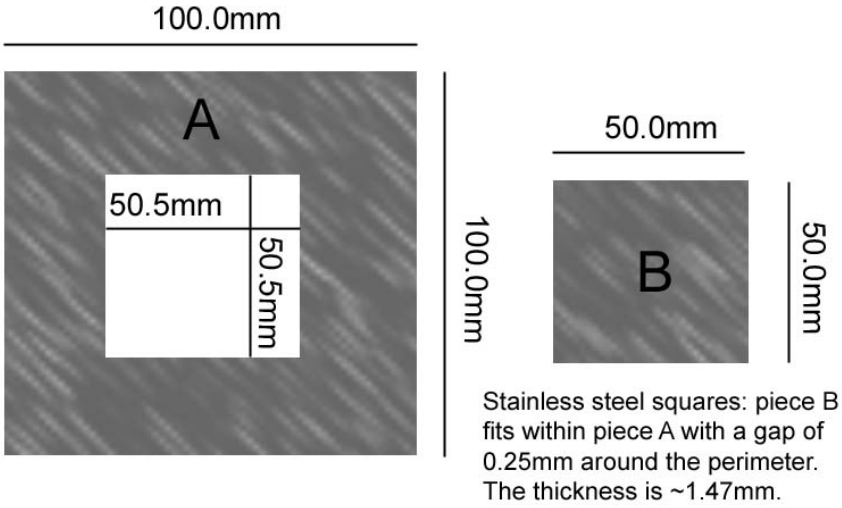

Figure 3.15: Schematic of the square test piece, with the mandrel labelled B and the sacrificial electrode labelled A. The thin polypropylene insulator ($250\mu m$) fits between A and B.

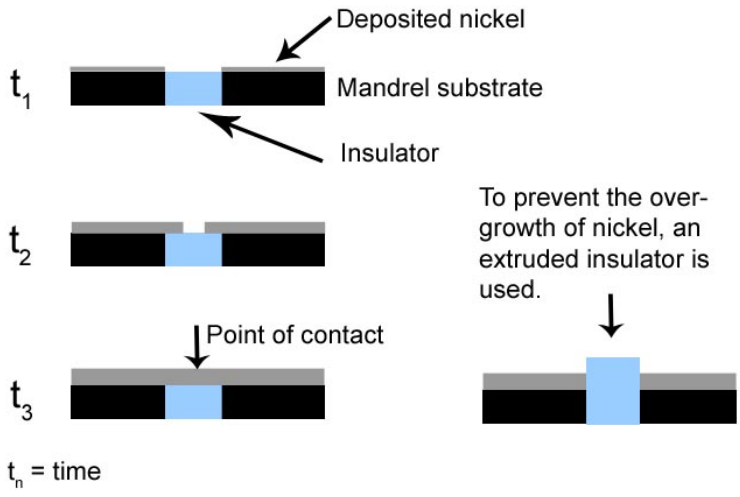

Figure 3.16: Nickel growth across an insulating bridge and the requirement to extrude the insulator.

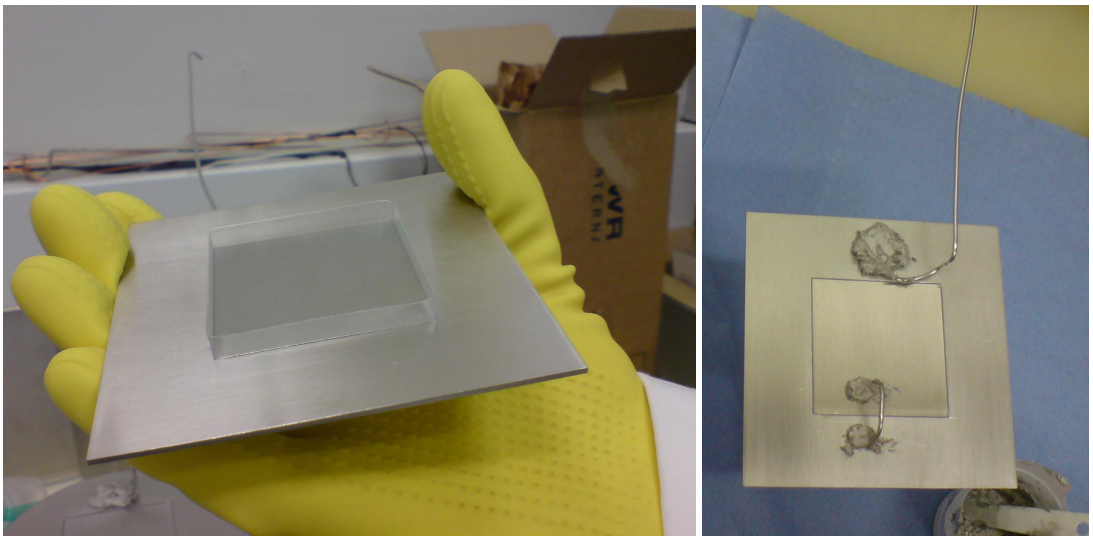

(a) The anode facing surface of the mandrel (b) The reverse of the mandrel

Figure 3.17: These images show the mandrel and sacrificial electrode with electrical insulation supplied by a thin polypropylene layer ($250\mu m$). Figure 3.17(a) shows how the insulator has been extruded in height above the mandrel plane to provide a distinct boundary over which the nickel will not be able to deposit. Figure 3.17(b) highlights the reverse of the mandrel and two connectors are shown: first the connector to the external cathode bus bar, and second, a connector to provide an electrical junction between the sacrificial electrode and the mandrel.

generated upon the mandrel was fine (maximum element size 5mm), the sides of the tank and the polypropylene layer were represented as an insulator, the anode was given a potential of $\sim$1.5V (the same as that measured with the voltmeter during the experiment) and the mandrel (including the sacrificial electrode) was set to ground.

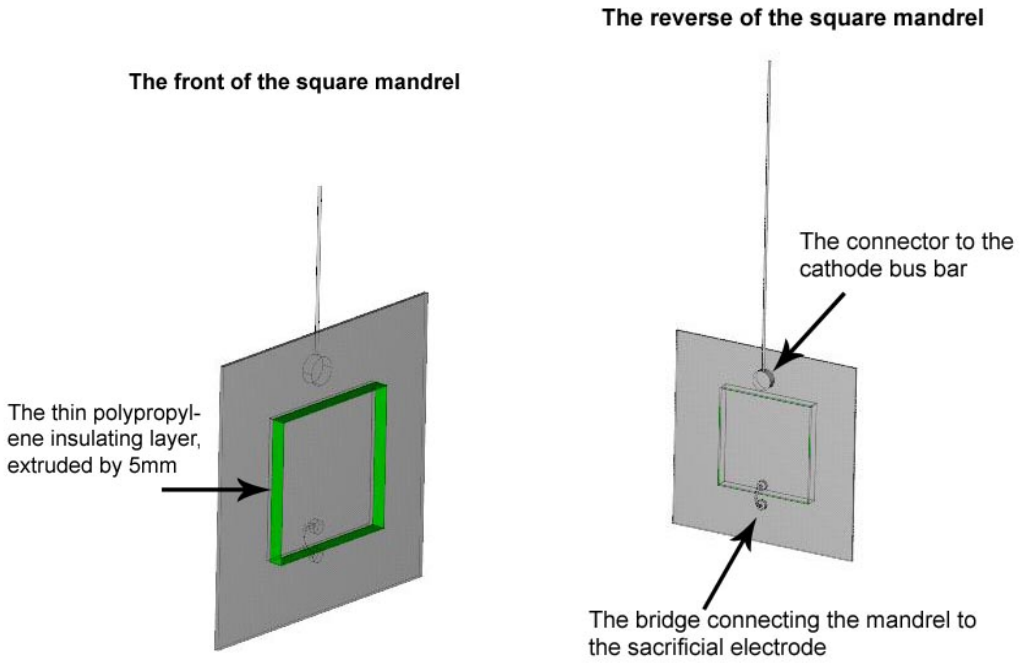

(a) The front of the mandrel (b) The reverse of the mandrel

Figure 3.18: An FEA representation of the mandrel described in Figure 3.17. The anode facing component is shown in Figure 3.18(a) and the reverse of the mandrel is seen in Figure 3.18(b)

3.3.8 A comparison of the experimental and FEA results

EXPERIMENTAL DATA - The thickness of the deposit was measured using a digital micrometer and then substracted against the thickness of the steel substrate. The results for the cathode's (mandrel and sacrificial electrode) surface and just the mandrel's surface are presented in Figures 3.19(a) and 3.20(a). The lack of data points, particularly taken from the sacrificial electrode prevent detailed 2D representation of the surface. Further, the measured thickness was a cumulative effect of the front and back nickel deposit. The back of the mandrel would suffer large deviations in current density caused by connecting wires and as a result affect the thickness of the nickel deposit.

FINITE ELEMENT ANALYSIS - The current density maps of the cathode and of just the mandrel's surface are presented in Figures 3.19(b) and 3.20(b) respectively. The images highlight an anisotropy within the current density, particularly evident within Figure 3.20(b): this is a probably a dual effect caused by the positioning of the cathode with respect to the anode and the effect of the uninsulated wire connector which provides an area of high current density at the upper region of the cathode.

A COMPARISON IN RESULTS - Figures 3.19 and 3.20 display the comparison between the

measured and FEA results. The number of points within the experimental data restricts a fair representation of cathode in respect to the FEA. However, Figure 3.19 highlights that the central region in both data sets has a lower current density/thickness than the corner regions. The top left hand corner of the mandrel has an over deposition in the measured results; thought to be a result of a gap in the polypropylene insulating layer. The insulator was folded around three corners and then the two ends brought to a point at the top right corner: the result of a gap at the join would create a greater over-deposition of nickel ions than would otherwise have occurred. In addition, the FEA data only represents the front of the mandrel, therefore for a true comparison the current density generated at both the front and the back of the mandrel should be considered.

Despite the lack of data points providing a reliable description of the measured thickness with respect to the FEA, the average results across the surface are encouraging. The sacrificial electrodes have removed the worst of the over-deposition from the mandrel's surface, except some anomalous data points at the centre of the mandrel which could have been the result of pitting.

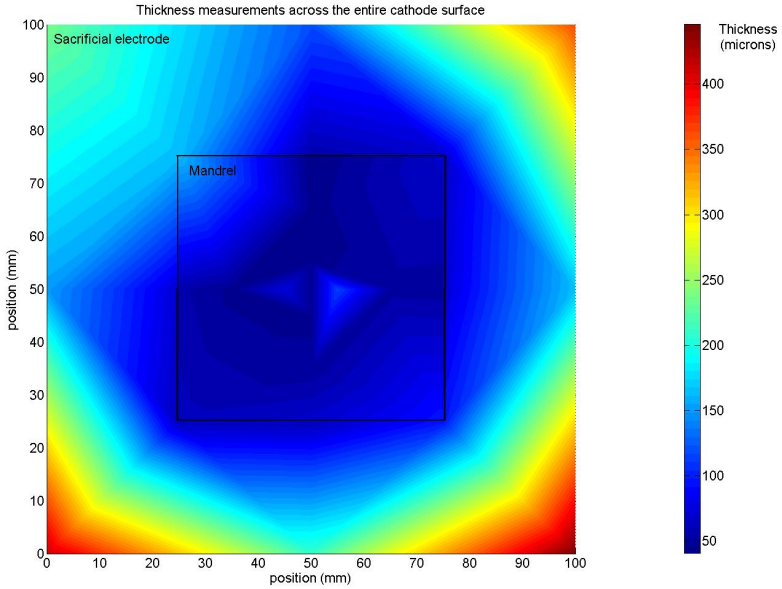

(a) Thickness measurements (μm)

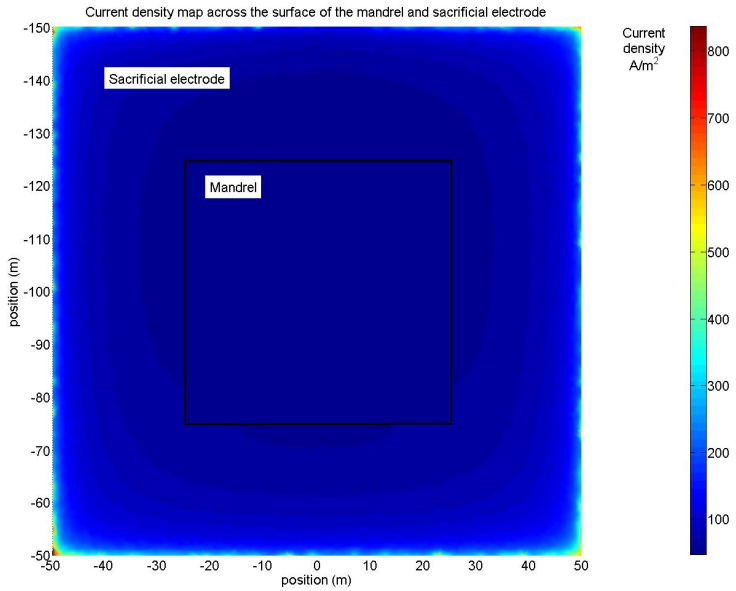

(b) Current density map (A/m^2)

Figure 3.19: The comparison between the measured thickness of the cathode (mandrel and sacrificial electrode) and the FEA current density map.

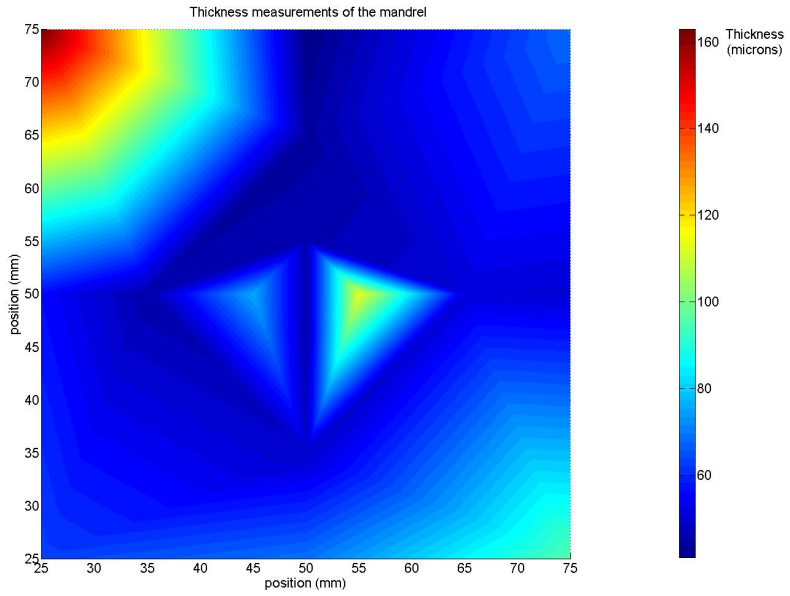

(a) Thickness measurements (μm)

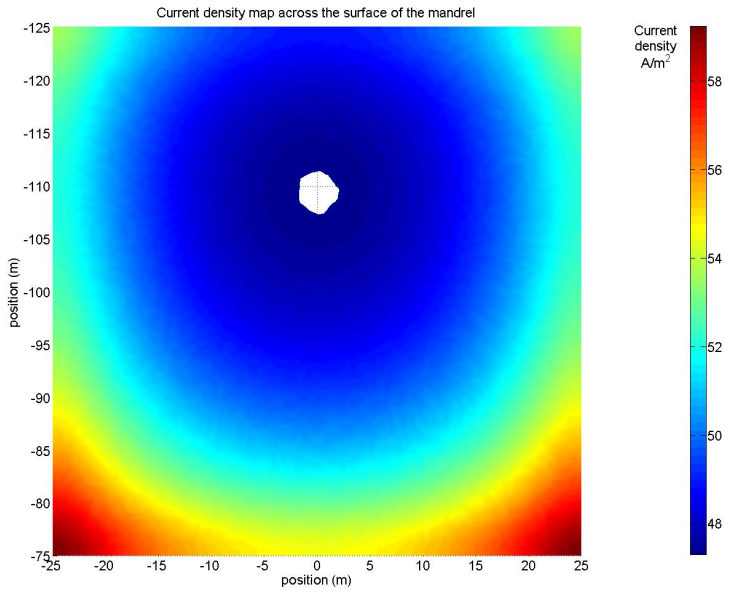

(b) Current density map (A/m^2)

Figure 3.20: The comparison between the measured thickness of the mandrel and the FEA current density map.

3.3.9 An FEA model of the cylindrical prototype

Further small experiments verified the results from Section 3.3.8, leading to an investigation on how to apply the method upon the mandrel for the cylindrical prototype. The primary problem was how to obtain a sacrificial electrode which was in-plane with the curved surface of the mandrel. The solution presented itself as the *wasters* which were used to protect the mandrel during production: they are an extension of the mandrel's form and are attached through screw and dowel joints (a full description of the wasters is presented in Section 3.4.1). Figure 3.21 highlights how the wasters are fixed to the mandrel's form and it is the curved surface of the mandrel that is to be used for nickel deposition. The proposed method is to position thin polypropylene insulating strips between the mandrel and the wasters; these strips will be extruded by 3mm above the surface of the mandrel and have holes punched to allow the screws to pass through and fix the mandrel and wasters together, as shown in Figure 3.21(c).

An FEA model was created to represent the mandrel and its sacrificial electrodes (i.e. its wasters) within the electroforming facility (Figure 3.22). The model represents the electroforming facility as operated in the production of optics for this project and therefore only a single anode is represented. The model is composed of three elements: the anode, the mandrel (the cathode) and the electrolytic solution. The mandrel is assumed to be 'free-floating' as the support rods are not modelled. Each component is drawn graphically in 3D and then the anode and the mandrel are subtracted from the bath, so that only the electrolytic solution is modelled, but there are geometric boundary interfaces with the electrodes. The electrolyte is given a conductivity, though this just acts as a multiplying factor and therefore doesn't dictate the current density across a surface. The boundary conditions are either potential (V), ground or insulator. The entire anode is set to a potential (i.e. a voltage) and the unmasked surface of the mandrel is to ground. The remaining boundaries: the outside walls of the tank, and the masked regions of the mandrel, are all set to insulator.

Figure 3.23 presents the current density map for surface from which the cylindrical optic will be replicated. Comparing the maximum and minimum current density regions $162A/m^2 \div 51A/m^2 =\sim 3$, indicates the corners of the optic should replicate with approximately three times increase in thickness compared with the centre. In terms of percentage increase from the corners to the centre this is $\sim$220%. When this result is compared to that of the mandrel without the wasters, $1456A/m^2 \div 37A/m^2 =\sim 40$, there is an approximate factor of 40 increase from the corners to the edge. Using the cylindrical mandrel's wasters as the sacrificial electrode significantly improves the

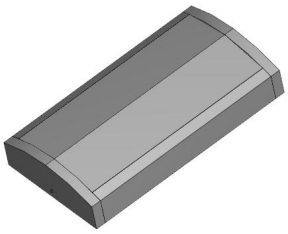

(a) The wasters fixed to the mandrel

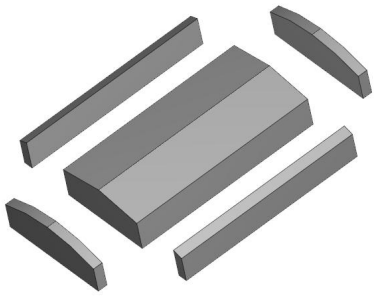

(b) An expanded view of the wasters and mandrel

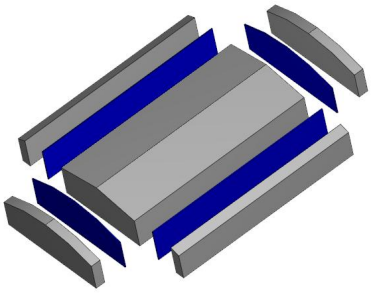

(c) The position of the insulator between the mandrel and the wasters

Figure 3.21: The mandrel's wasters are 1cm extensions in width of the mandrel's form, Figure 3.21(c) highlights the position of the polypropylene insulators between the mandrel and the wasters in an expanded view.

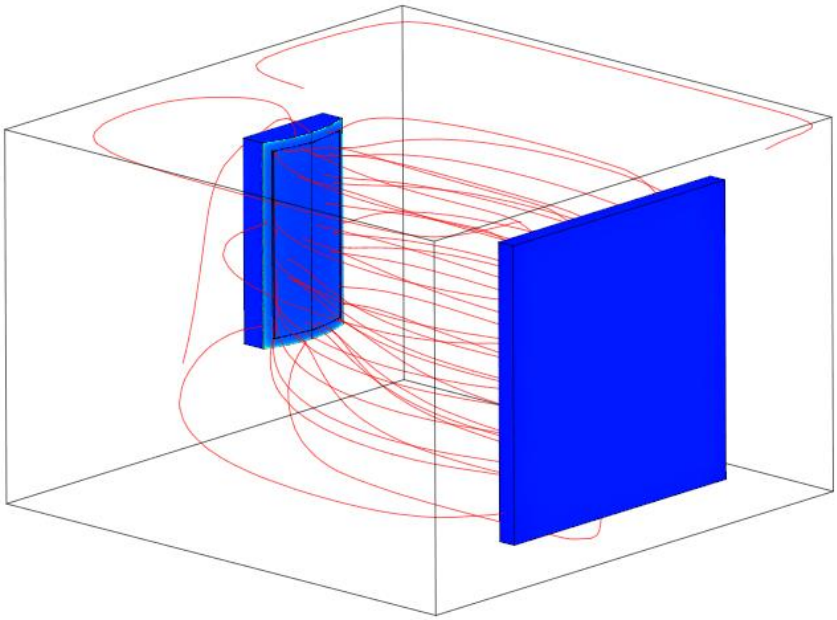

Figure 3.22: The FEA representation of the cylindrical mandrel within the electroforming facility: the red lines indicate the electric field between the anode and mandrel.

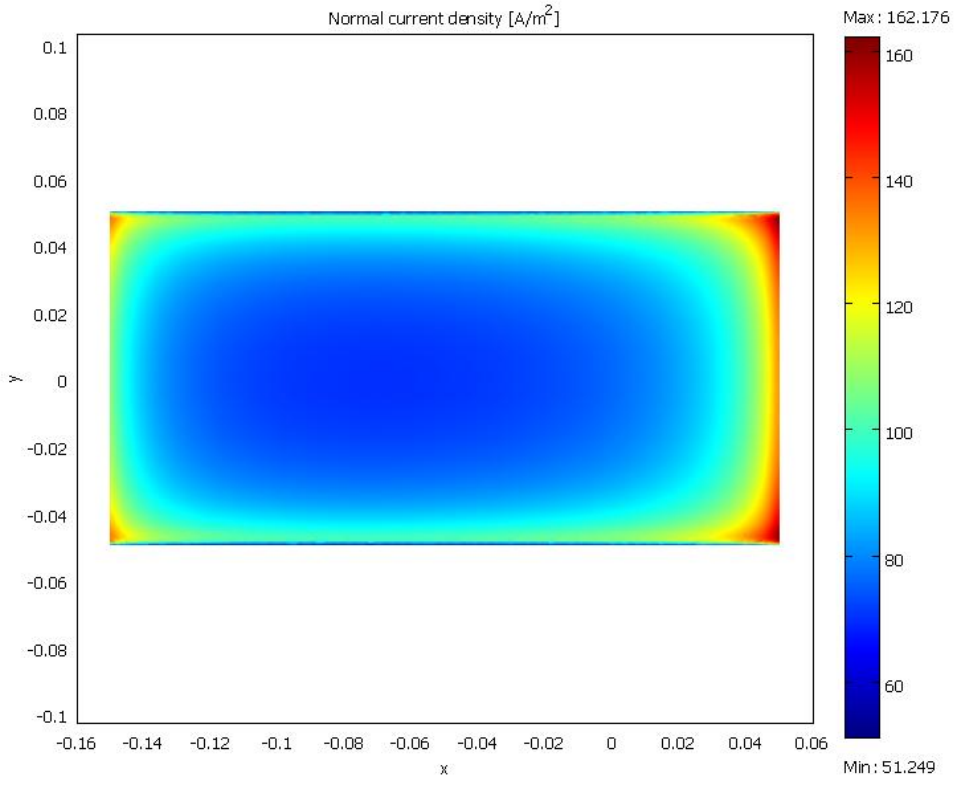

Figure 3.23: A current density map of the surface from which the cylindrical optic will be replicated

current density experienced across the mandrel's surface. The thickness gradient could be further reduced by increasing the dimensions of the wasters. However, the concept of using the wasters was proposed after their fabrication and production of a second set of wasters would not have been a simple procedure or time effective. Nevertheless, a viable method of producing an optic has been presented, though the optic will have a thickness gradient it is hoped that the experience gained in the optic's production will aid the development of the ellipsoidal optic, which is the objective of the cylindrical prototype's production.

3.4 Production of the cylindrical mandrel

The production of the cylindrical mandrel was performed in-house at UCL by DB and this section provides a narrative of the work undertaken. Due to the nature of electroforming, the mandrel must have the inverse form of the object required: a concave optic would require a convex mandrel. Therefore, to produce the 200mm $\times$ 100mm concave cylindrical optic with radius of curvature 155mm, a convex cylindrical mandrel of the identical dimensions must be produced and a schematic of the cylindrical mandrel can be seen in Figure 3.24.

There are four additional components connected to the outside of the mandrel within the figure; these are called wasters and they prevent a turned-down edge being created upon the edge of the mandrel due to the grinding and polishing processes. In addition they also provide an ideal sacrificial electrode: each component is perfectly aligned and in-plane. Within this chapter 'mandrel' shall refer to the component from which the optic is to be replicated and 'cylindrical mandrel' will refer to the mandrel and the wasters as a whole.

Stainless steel was selected as the cylindrical mandrel's material; not only does it offer physical properties allowing it to be figured to the desired optical form with a high surface quality finish, but it is also inert with the electrolyte, allowing nickel deposit to form at its surface without chemically attaching to the stainless steel lattice. The specific stainless steel grade 316L was used as it offers the chemical resistance required for a long duration within the electrolytic solution

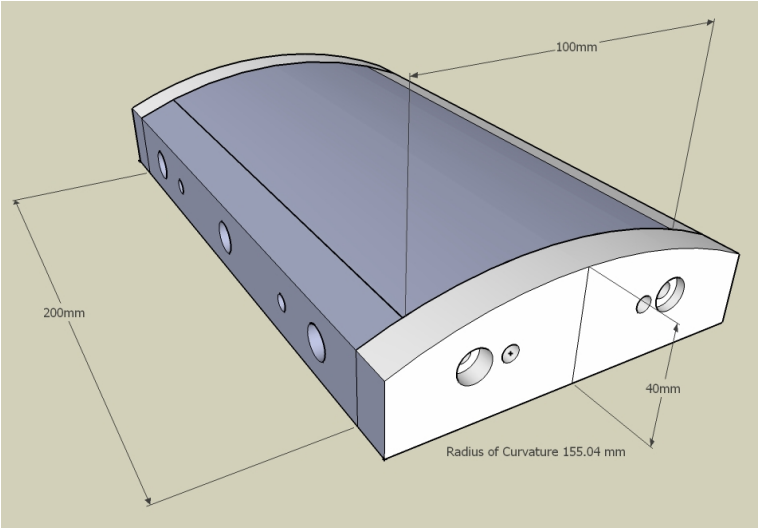

Figure 3.24: A schematic of the cylindrical mandrel, including wasters and screw holes, courtesy of DB

3.4.1 Mandrel fabrication

First, the five stainless steel components, which make up the cylindrical mandrel, were squared to ensure a clean join between the pieces. Steel dowels were used to align the mandrel to the wasters and to guarantee repeatability in their positioning, while screws were used to fix the wasters to the mandrel. The fixed stainless steel bricks of the cylindrical mandrel were milled to obtain the approximate curvature in the azimuthal direction: the result of this process can be seen in Figure 3.25.

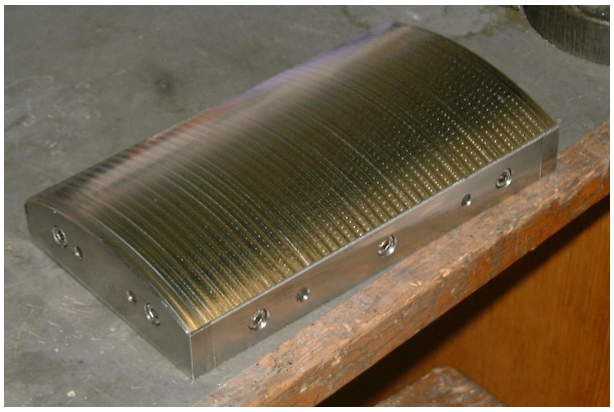

Figure 3.25: The surface of the cylindrical mandrel after milling

The cylindrical mandrel was then hand ground, using decreasing grain sizes of silicon carbide (SiC), till a final roughness of 0.5μm Ra was achieved. To ensure the correct form was produced, the azimuthal and axial profiles were measured using the Talysurf contact profilometer. The azimuthal form should highlight a radius of curvature of 155mm and the axial profile a flat line with no curvature.

The polishing process employed a TEXMET cloth[3] polishing tool and an aluminium oxide (Alox) slurry: the polishing tool maintains the form of the object while the aluminium oxide particles ($\varnothing$ 1μm) abrade the surface (Figure 3.26).

Microscope interferograms (1mm $\times$ 1mm), using the WYKO rough surface tester (RST) interferometer, provided a description of the surface roughness of the mandrel. Figure 3.27 highlights the final surface finish of the mandrel with a Ra of 4.01nm over the 2D image; this was the optimum finish that could be achieved upon the stainless steel. The interferometer figure highlights a Rq of 5.26nm rms; using this in conjunction with Equation 1.14 and the variables λ

[3] TEXMET purchased from South Bay Technology Inc. USA

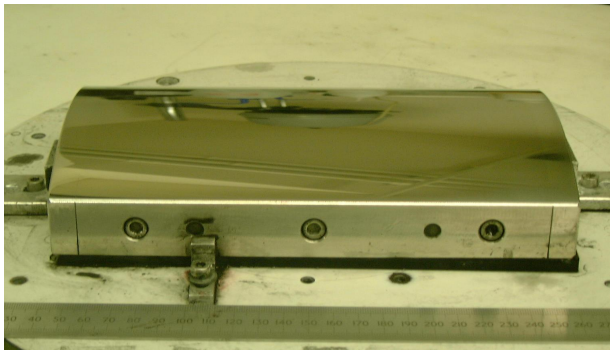

Figure 3.26: The surface of the cylindrical mandrel during the polishing process.

= 1.9nm and $\theta_g = 1.163\,^\circ$ (as mentioned in Section 2.1.1 of Chapter 2) an estimation of the total integrated scatter would be 70.8%. This is far above the acceptable limit of 10% and therefore alternative materials should be investigated for the ellipsoidal mandrel.

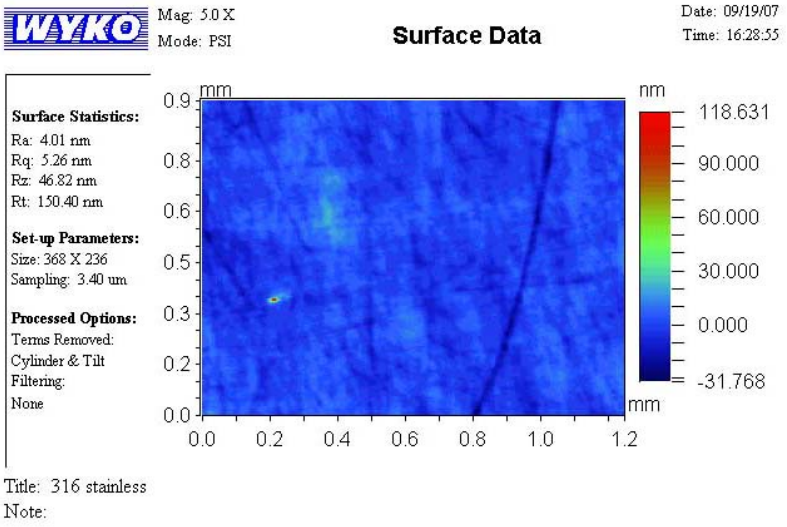

Figure 3.27: Microscope interferometer image of the mandrel, indicating a surface roughness of 4.01nm Ra

The completed mandrel can be seen in Figure 3.28 (the wasters are seen in the right of the photo); the final surface profiles indicated that the mandrel was made to form with the desired radius of curvature in the azimuthal direction.

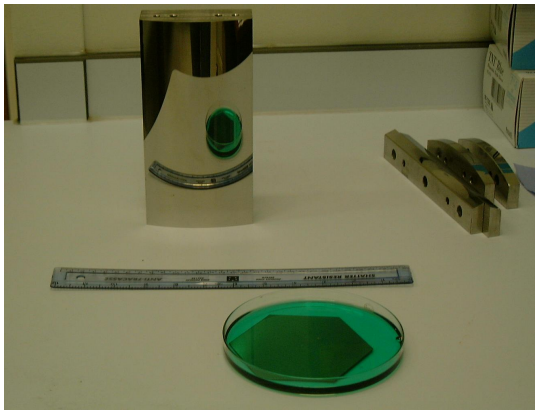

Figure 3.28: The completed cylindrical mandrel

Cylindrical optic no.	Manufacture date	Duration of deposition
Cylindrical optic 1	April 2008	plating time 36 hours
Cylindrical optic 2	May 2008	plating time 95 hours
Cylindrical optic 3	August 2008	plating time 40 hours
Cylindrical optic 4	September 2008	plating time 40 hours

Table 3.2: Cylindrical optic production

3.5 Production of the cylindrical optic

From April 2008 to September 2008, four cylindrical nickel optics were produced and a description of the optics can be found in Table 3.2. The objective of the cylindrical prototype was to investigate the production methods intended for the ellipsoidal prototype. Throughout the production of the optics, problems were encountered, therefore each optic represents a change in the replication procedure intended to correct for those problems. The cylindrical prototype was only completed a month before the completion of the ellipsoidal prototype, therefore time restrictions prevented a thorough investigation of the form of each of the optics and as a result only metrology data from Optic 2 is presented. In addition, Optic 2 had a 95 hour electrodeposition; this was a result of early prototype designs that suggested the use of a 1mm thick optic. However the thickness was decreased to 0.4mm as there was no direct benefit of a thicker optic.

Replication of the cylindrical optics following the electroforming practice as outlined in Section 3.3.4 and the set-up of the electroforming facility is shown in Figure 3.29. As each

cylindrical optic was produced in a slightly different manner, Section 3.5.1 will provide the general method in which the cylindrical mandrel was prepared prior to deposition. Sections 3.5.2 to 3.5.4 will present the modifications to the cylindrical mandrel's preparation for each optic.

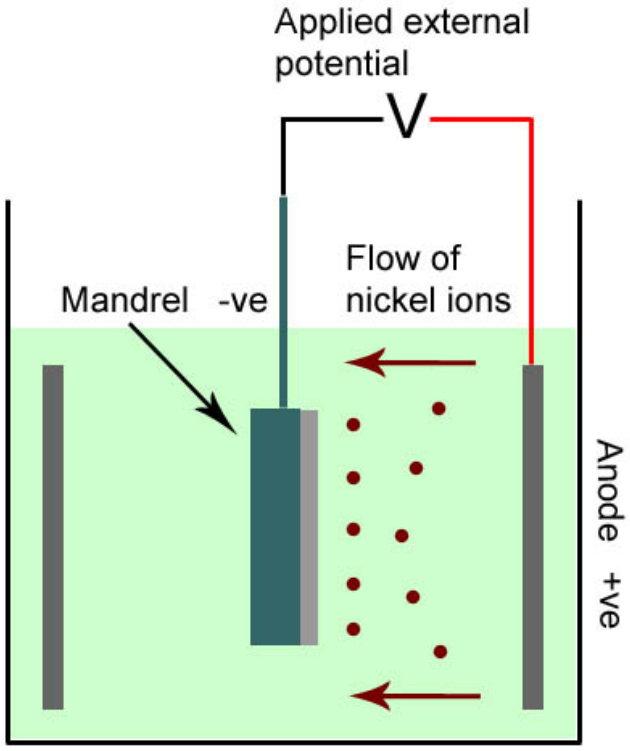

Figure 3.29: A schematic of the cylindrical mandrel within the electrodeposition facility

3.5.1 General method for cathode preparation

The cylindrical mandrel, stainless steel screws and stainless steel rods (providing the connection to the cathode bus bar, initially 30cm long) all were degreased as outlined in Section 3.3.4. The polypropylene insulators were leached using 5% sulphamic acid, to remove surface chemicals. The cylindrical mandrel and all other components were dried to ensure good adhesion between the insulating tape and stainless steel surface. The polypropylene insulators were positioned between the wasters and the mandrel and fixed using the stainless steel screws, producing a waster-insulator-mandrel arrangement. The polyester insulating tape was used to mask the connecting rods and all exposed areas of the cylindrical mandrel minus the optical surface. Connection was then made

between the rods and the cylindrical mandrel; however, the exact method changed from Optic 1 to Optic 2 and this will be outlined in the relevant sections. The current to be applied was calculated from the total surface area for the mandrel plus the wasters and a current density of 0.01A/cm^2, $surface\ area = 12cm \times 22cm = 264cm^2$, $applied\ current = 264 \times 0.01 = 2.64A$. Therefore to each of the four cylindrical optics a current of 2.64A was applied.

3.5.2 Cylindrical optic 1

The first cylindrical optic was produced in April 2008. During the cathode preparation the masked stainless steel rods were connected to the cylindrical mandrel before the cylindrical mandrel itself could be masked, as shown in Figure 3.30. To ensure that no nickel deposit could breach the join between the cylindrical mandrel and the connecting rods, excess insulating tape was used, but this resulted in insulating tape being on the surface of one of the wasters. The introduction of the tape upon the waster would cause variations in the current density in that region; however, without the immediate means to rectify the problem, the experiment proceeded to schedule.

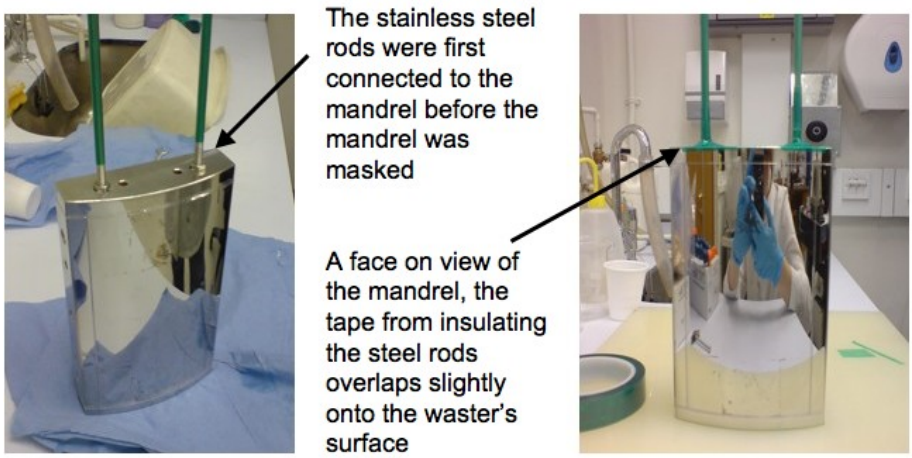

Figure 3.30: Preparation of the cathode for the replication of the first cylindrical optic

After 36 hours of continuous operation, the cylindrical mandrel was removed from the bath. Figure 3.31 shows the optic directly after removal from the bath and highlights a peeling of the electroform in the immediate vicinity of the overlapping tape, proving that a disruption in the current density can have a large effect upon the electroform. Despite the peeling of the electroform in the region surrounding the insulating tape, the cylindrical optic had remained attached to the mandrel with no obvious deformations; as a result, a second experiment was proposed to investigate

an alternative method for attaching the connecting rods and the effects of a longer plating duration would have upon the optic's form.

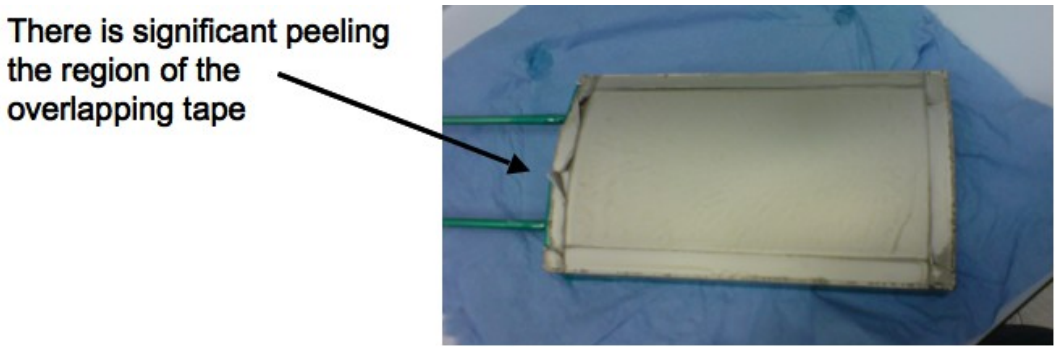

Figure 3.31: Replication of the first cylindrical optic

3.5.3 Cylindrical optic 2

For the second optic, the cylindrical mandrel and connecting rods were insulated separately before attaching one to the other. Two small holes were cut into the insulating layer where the rods would be positioned and the screws removed. The rods were only insulated in their non-threaded sections (i.e. the screw threads at the end of the rods were kept free from tape), the depth of thread within the cylindrical mandrel was approximated and a series of nylon nuts were positioned to mask any excess screw thread of the rod. A polypropylene washer was then placed between the nylons nuts and the cylindrical mandrel to mask the insulating tape cut when the screws were removed. The connecting rods were fastened to the cylindrical mandrel to form a tight joint. The cylindrical mandrel ready for nickel deposition can be seen in Figure 3.32.

Figure 3.33 displays the electroformed results for the second optic. No peeling of the electroform had occurred. The only surface features, produced on the non-reflecting side, were small pit marks in the regions immediately next to the polypropylene insulating layer. These pits were not unexpected, because the extruded insulator prevents the fluid flow in its immediate vicinity, therefore preventing the removal of hydrogen bubbles. However, the pitting effect was small and not viewed as a major problem. The increased plating time highlighted a discrepancy within the deposit which had not been apparent in the shorter duration deposit: there was a thickness gradient within the deposition increasing from the top of the tank to the bottom. This discrepancy was caused by the connecting rods which were too short to place the cylindrical mandrel centred upon the anode and therefore resulted in an anistropy in electric field lines across the surface, as visualised

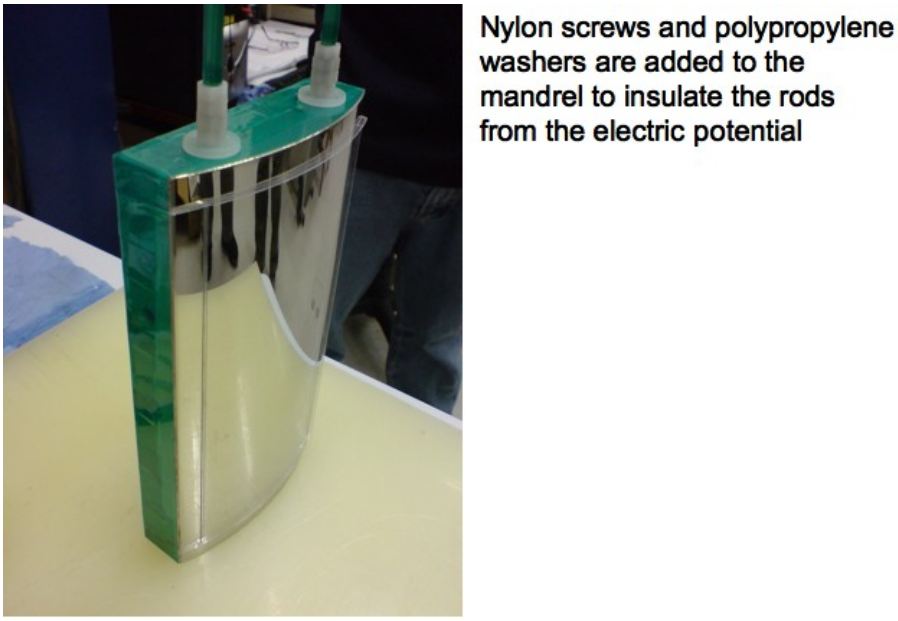

Figure 3.32: Preparation of the cathode for the replication of the second cylindrical optic

in Figure 3.34. By increasing the length of the rods from 30cm to 40cm, the mandrel should be positioned within the centre of the anode and this would therefore remove the thickness gradient.

3.5.4 Cylindrical optic 3 and 4

The third optic addressed the problem of the thickness anisotropy caused by non-centralised positioning of the mandrel with respect to the anode and thick nickel growths at the edge of the wasters. The outer edges of the wasters are the areas of highest current density and therefore result in the thickest deposits: these deposits form a 270° nickel formation, which fixes the deposit to the wasters leading to difficultly when removing the electroform. Due to the high growth rates of the deposits, the current density in these regions increases over time resulting in a decrease of current density in the central region of the mandrel. Therefore an outer barrier was suggested (Figure 3.35) which would prevent the 270° nickel formation and provide a more consistent current density over time.

The outer barrier was a 6mm thick layer of polypropylene which extruded 3mm above the edges of the wasters; its implementation can be seen in Figure 3.36. Nylon screws were used to replace the stainless steel screws which fixed the whole cylindrical mandrel together. Nylon screws were used to prevent undesired nickel growth regions which would affect the growth rate upon the mandrel.

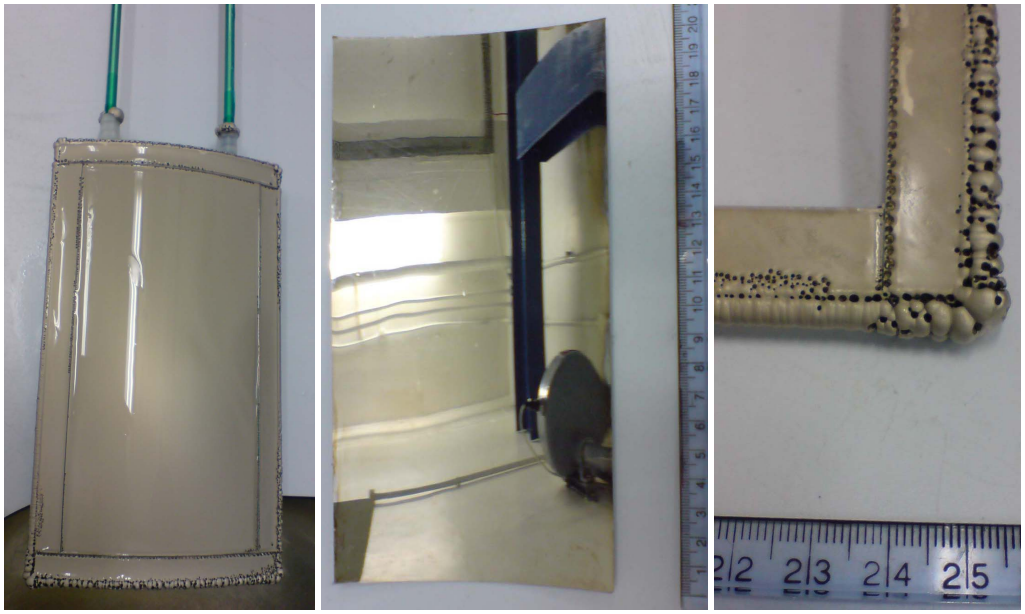

(a) Post removal (b) The optical surface (c) Nodules

Figure 3.33: The electroform (figure 3.33(a)), including the sacrificial nickel directly post removal from the bath. Figure 3.33(b) shows the optical surface of the nickel electroform after being rinsed using distilled water. Figure 3.33(c) highlights the problem due to nodules that the sacrificial electrode was designed to remove.

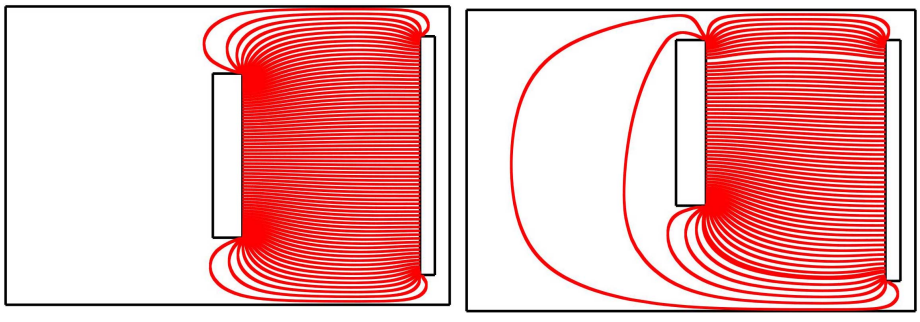

(a) A mandrel centralised with the anode (b) A mandrel off-centre with the anode

Figure 3.34: The effect on the electric field caused by a centralised mandrel with respect to the anode (Figure 3.34(a)) and a non-centralised mandrel with respect to the anode (Figure 3.34(b)).

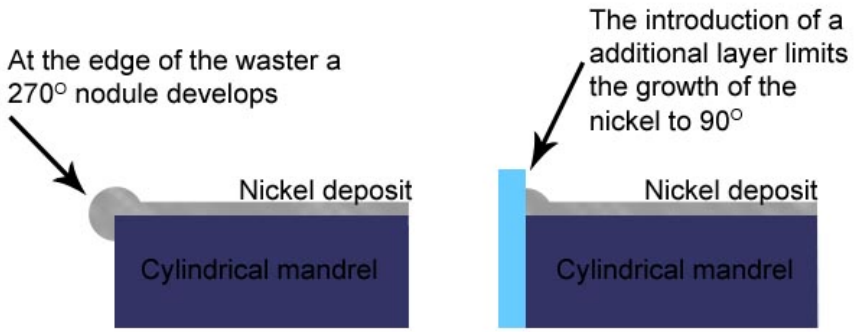

Figure 3.35: Addition of polypropylene edges to reduce the nickel growth at the edge of the cylindrical mandrel

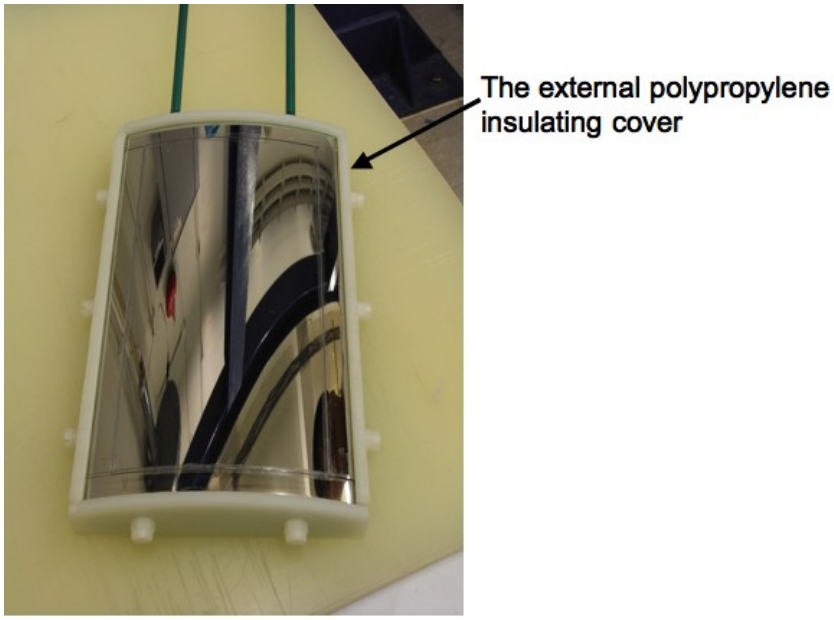

Figure 3.36: Preparation of the cathode for the replication of the third cylindrical optic

The cylindrical mandrel was plated for 40 hours and the results can be seen in Figure 3.37. The effect of the nylons screws was immediate; due to the thin insulating layer between the mandrel and the wasters, the stainless steel screws had previously bridged this insulator to distribute the current, therefore without a conductor only three of the four wasters would have direct access to a current source. Despite only one waster having direct current access, two additional wasters developed thin nickel films and these were a result of the nickel deposit bridging small gaps in the thin insulating to provide an electrical connection to the wasters.

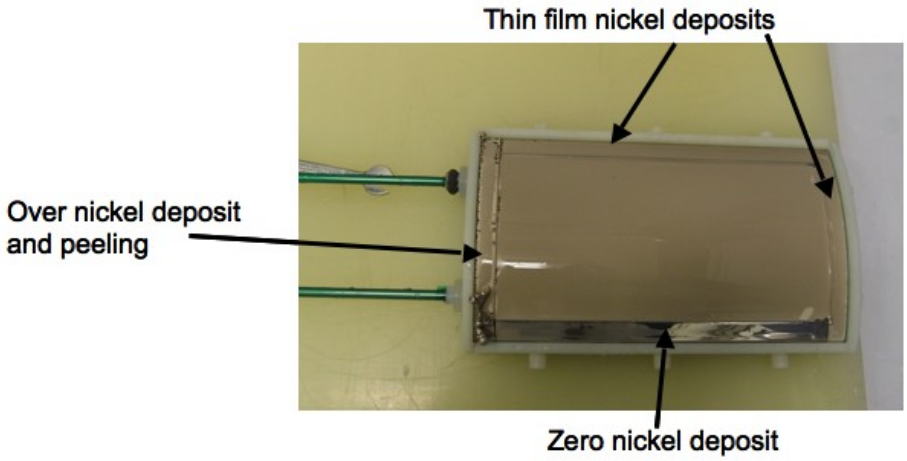

Figure 3.37: The third replication run highlighting the cylindrical mandrel directly after removal from the bath

Fortunately this oversight could be rectified by using the stainless steel dowel from the cylindrical mandrel's production; these would provide an electrical connection while the nylon screws could fix the outer polypropylene layer to the wasters and mandrel. The correction was implemented in the production of the fourth cylindrical optic and an even thickness across the wasters and the mandrel was observed (Figure 3.38). The removal of the nickel from the wasters was greatly aided by the extra polypropylene layer and the edge of the waste nickel in contact with the polypropylene layer indicated a slight reduction in thickness, possibly caused by a shadowing effect preventing the ready access of metal to the electric field. This fourth optic formed the optical component of the cylindrical prototype and provided the method in which the ellipsoidal optic would be replicated.

3.5.5 Metrology of the replicated optics

Only metrology from the second replicated optic was taken (results presented within the paper by Atkins *et al.* (2008)): this was primarily a result of time restraints preventing a thorough analysis

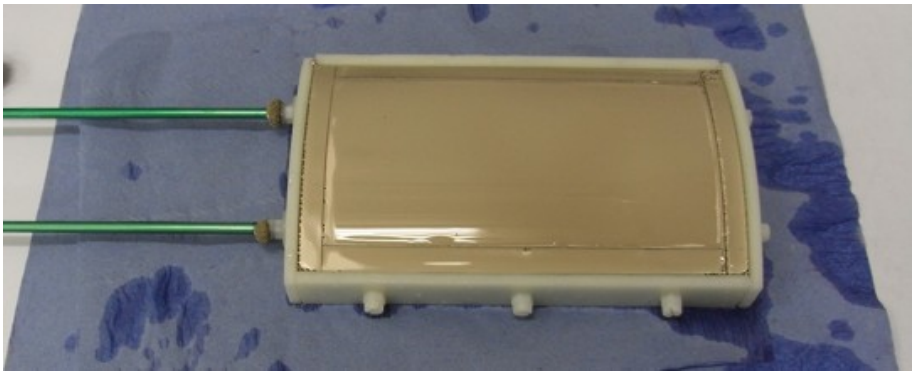

Figure 3.38: The fourth and final replication run of the cylindrical mandrel: the optic formed in this run was used as the optical component of the cylindrical prototype.

of Optic 4 before actuator bonding. Several measurements were taken investigating: the azimuthal radius of curvature; the surface roughness of the optic; and thickness of the optic and how this compares against the FEA simulations.

AZIMUTHAL RADIUS OF CURVATURE - The Talysurf profilometer was used to measure the curvature in the azimuthal direction; however, measurements were restricted by the maximum depth that the profilometer could record in one measurement. The curvature of the optic had to be halved, leading to two measurements along one axis of curvature (Table 3.3). Seven measurements were taken down the axial length. The ideal radius of curvature should have been 155mm, but the results indicate an increase in radius of curvature resulting from tensile stress (Section 3.2.6) within the deposit. The peak-to-valley measurement indicates the error on the measurement, by showing the variation of the optic's measured radius of curvature from the ideal scenario (i.e. the degree to which the measured radius of curvature deviates from a perfect arc).

SURFACE ROUGHNESS MEASUREMENTS - RST500 microscope interferometer was used to take 2D images of a 1mm^2 surface area. A 2D measurements of Ra across the surface indicated a variation in roughness from a maximum of 12.95 nm to a minimum of 6.49 nm (Figure 3.39), compared to the 4.01nm measurement that was originally attained from the finished mandrel. In addition, Figure 3.39 highlights an Rq of 9.86nm rms, using this in conjunction with total integrated scatter equation (Equation 1.14) and the variables mentioned in Section 2.1.1, the optic would provide 98% scattering at 1.04keV.

OPTIC THICKNESS - The thickness of the nickel optic was measured using a digital micrometer. Due to the reach of the micrometer only a distance of 2cm from the edge of the optic could be measured, therefore thickness data is lacking from the central area of the optic. Figure 3.40 displays

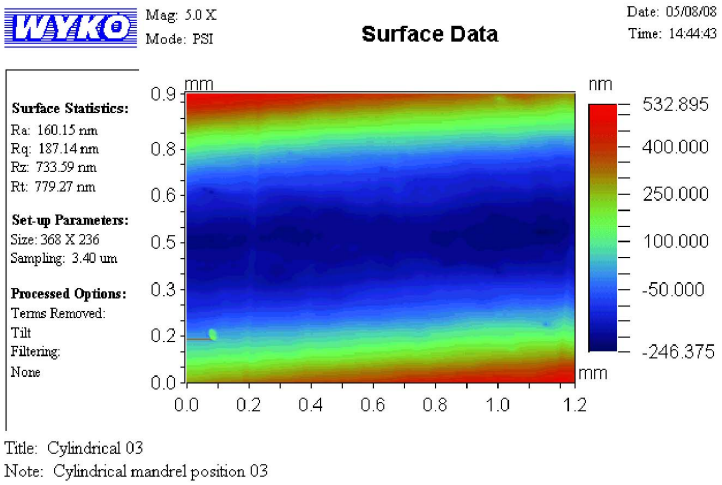

(a) The cylindrical form of the optic

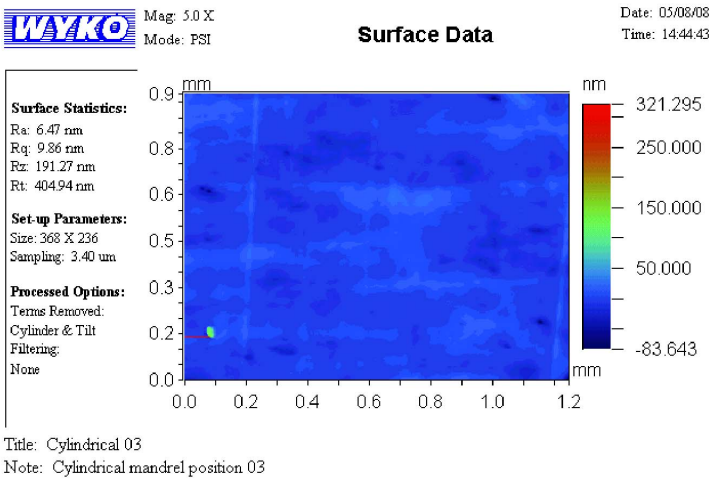

(b) The surface roughness of $6.47nm$

Figure 3.39: Surface roughness measurements of the final optic surface taken with the RST500 Interferometer. Figure 3.39(a) displays the raw interferometric data indicating the cylindrical form of the optic. Figure 3.39(b) shows the removal of the cylindrical term from the interferometric data, leaving a flat surface allowing a determination of surface roughness for the optic.

Azimuthal radius of curvature (RoC) of the 2^{nd} cylindrical optic				
	First Half		Second Half	
Position (cm)	RoC (mm)	Peak to Valley (μm)	RoC (mm)	Peak to Valley (μm)
1	173	14.500	174	8.935
4	175	29.684	173	22.518
7	176	27.890	170	18.845
10	174	26.006	169	26.266
13	164	31.820	172	12.831
16	166	15.221	171	14.104
19	168	10.771	168	6.012

Table 3.3: Azimuthal radius of curvature measurements of the 2^{nd} cylindrical optic taken using the Talysurf profilometer

the comparison between the FEA and measured results. The asymmetry in the results is an effect due to the position of the mandrel within the tank (as mentioned in Section 3.5.3). If positioned centrally in the tank, then two axes of symmetry should exist, however, in the experimental setup the mandrel was positioned approximately 50mm above the optimum position and this is represented in both the FEA and experimental data. As the centre of the optic could not be measured, a comparison between the theoretical and experimental data was taken at the maximum (a corner) and the minimum (the point closest to the centre). The theoretical ratio of current densities A/m^2 taken from the FEA was $162.176 \div 79.148 = 2.049$ compared to a measured thickness μm ratio of $1100 \div 541.5 = 2.031$. The close comparison in the FEA and measured data was encouraging for the future use of FEA in developing current density maps for the ellipsoidal mandrel.

The metrology results from the second cylindrical optic highlight a deviation in form and surface roughness compared to the cylindrical mandrel. Tensile stress caused the optic to produce a larger radius of curvature than that of the cylindrical mandrel

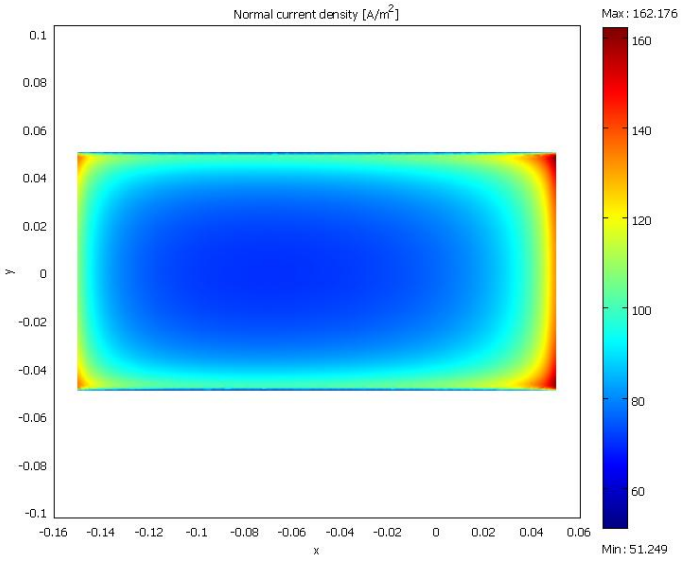

(a) Theoretical current density distribution

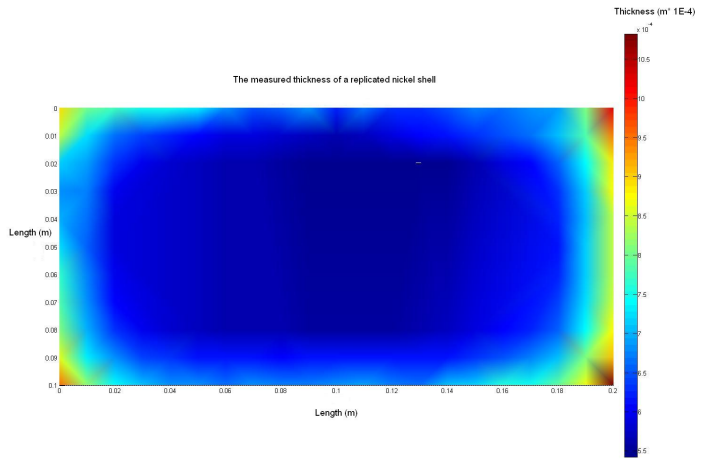

(b) Measured nickel thickness

Figure 3.40: Comparison between measured and theoretical results for the nickel optic, Figure 3.40(a), displays the theoretical current density distribution over the mandrel's surface. Figure 3.40(b) displays the measured thickness variation along the optic.

Actuator sample no.	Required RoC (mm)	measured average RoC (mm)
1	156	221
2	156	155
3	156	161
4	156	166
5	156	166

Table 3.4: Average radius of curvature profilometer measurements of five actuator samples

3.6 Actuator bonding, harnessing and the cylindrical prototype's completion

The bonding and harnessing of the cylindrical prototype's actuators was undertaken in September 2008. Unfortunately, due to the proposed X-ray testing in Novemeber 2008 of the ellipsoidal prototype, time constraints prevented a thorough analysis of the bonding and harnessing procedures, as well as the actuator influence functions created by the actuator upon the cylindrical optic. As a result, this section outlines the methods employed in the completion of the cylindrical prototype and the improvements required for the ellipsoidal prototype.

An anticipated problem was the effect of the radius of curvature mismatch. The curvature of the optic, as described in Section 3.5.5, deviated from the desired form due to tensile stress within the nickel deposit. Assuming the fourth optic suffers from a similar radius of curvature change, then there will be a mismatch in the radius of curvature between the actuators and the optic (assuming the actuators are produced to the required curvature).

3.6.1 The University of Birmingham's actuators

The University of Birmingham (UoB) produced a set of 30 actuators for the cylindrical prototype. These actuators were 32mm (azimuthal) $\times$ 19mm (axial) $\times$ 0.2mm (thickness) in dimensions and were intended to have a radius of curvature of 156mm. The azimuthal curvature of an actuator is achieved through heating the actuator to high temperature and forming it upon a zirconia former of the required radius of curvature (Zhang *et al.* 2009*b*). The UoB provided some actuator samples in April 2008 to measure the radius of curvature and the average radius of curvature can be seen in Table 3.4. The radii of curvature are several millimetres greater than the required RoC in all but

one instance.

3.6.2 Adhesive

The primary requirement for adhesive was that it should be of low shrinkage, as high shrinkage would readily deform the surface of the optic and create distortions on spatial frequencies that could not be accommodated for by the actuators. UV cure adhesives often offer extremely low shrinkage. However, due to the opaque nature of the two substrates (i.e. the nickel optic and the actuators), UV cure was unfeasible. The selected adhesive was Masterbond's EP30, which is a two part epoxy based glue with low viscosity and quoted to have exceptionally low shrinkage at 0.0003 inches/in [4].

A further consideration was how to isolate the actuator from the nickel optic to prevent the nickel optic from short-circuiting the actuators. To ensure a minimum thickness of glue a physical boundary would have to be applied. The simplest approach would be to add an insoluble and non reactive solid, with small dimensions, to the adhesive epoxy. Glass spacing beads are designed for this purpose; they offer diameters of $80\mu m$ to $150\mu m$ and they are directly mixed within the epoxy. To remove the air bubbles caused by the mixing (both with or without the glass beads), the EP30 is out-gassed within a vacuum chamber: the removal of these air pockets is important due to the eventual vacuum environment of the X-ray facility in which the ellipsoidal prototype would operate. Figure 3.41 displays a cross section of an actuator bonding test piece performed at the UoB: visible are the 150μm diameter glass beads which are maintaining the glue layer thickness and the nickel and actuator layers.

3.6.3 Actuator bonding

The actuators were bonded to the fourth nickel optic shortly after its completion in September 2008. A single quantity of EP30 was used, with $\varnothing 150\mu m$ glass beads forming an adhesive-bead suspension. The actuators supplied by the UoB all had thin, $\varnothing 90\mu m$, enamelled copper wire soldered to the actuators' electrodes, and care had to be taken not to break the fragile solder connection through handling. The bonding was undertaken within a clean environment in the laboratory: to minimise the exposure to dust particles. Figure 3.42 displays the bonded actuators.

There were two problems experienced when bonding the actuators: first, the soldered wires tended to pull the actuators once they had been positioned upon the optic, and as the actuators were 'floating' on a layer of low viscosity adhesive, accurate positioning of the actuators was difficult.

[4] Masterbond - technical data sheet (`http://www.masterbond.com/tds/ep30.html`)

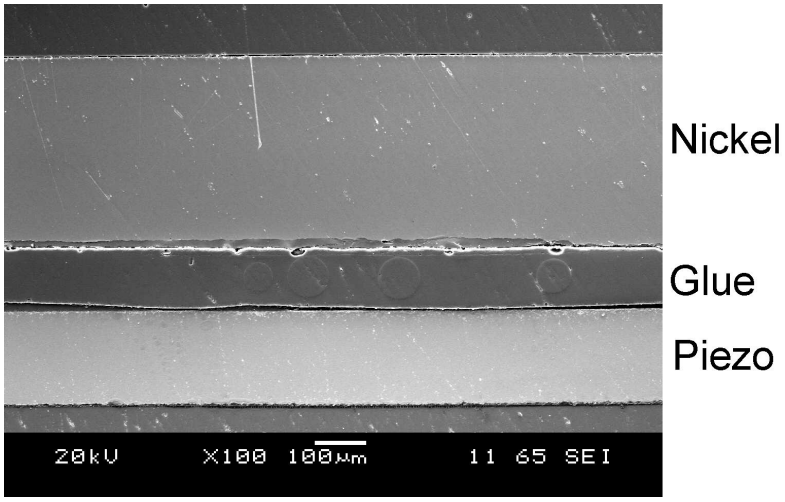

Figure 3.41: A scanning electron microscope image of the cross section through an early prototype, courtesy of the University of Birmingham.

The second problem was the working-life of the adhesive, which caused the viscosity to increase over time. The time taken to position the actuators was incorrectly estimated and as a result the actuators positioned later used adhesive of a higher viscosity than at the start.

3.6.4 Actuator harnessing

The final stage in the production of the prototype is the harnessing of the actuators, that is, collecting the actuators' wires, fixing them upon the reverse of the optic and soldering them onto a 37-D connector. The process of harnessing of actuators was undertaken by GW from the Mullard Space Science Laboratory: the wires were to be fixed upon the reverse of the optic using vacuum compatible acrylic tape. (Figure 3.43).

Two problems were encountered while harnessing: first, as the wires had already been soldered to the actuators, it was difficult to position the wires without causing stress upon the solder joint. The second problem was the non-adherent nature of the acrylic tape to the back of the actuators and the problem was not one which could be removed by wiping the back of actuators with propylene. Upon discussion with UoB, the problem originated from oils used in the production of the actuators and the removal of the oil had not been considered by either party prior to actuator dispatch.

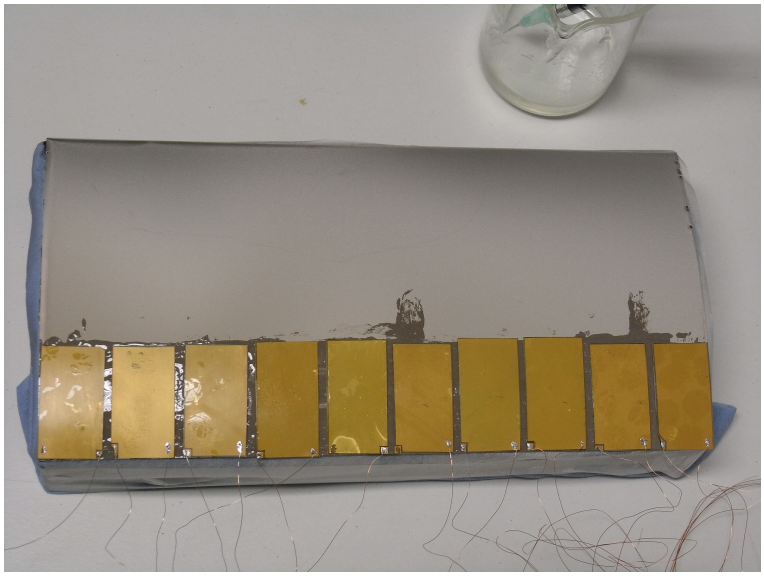

(a) Bonding strips of actuators

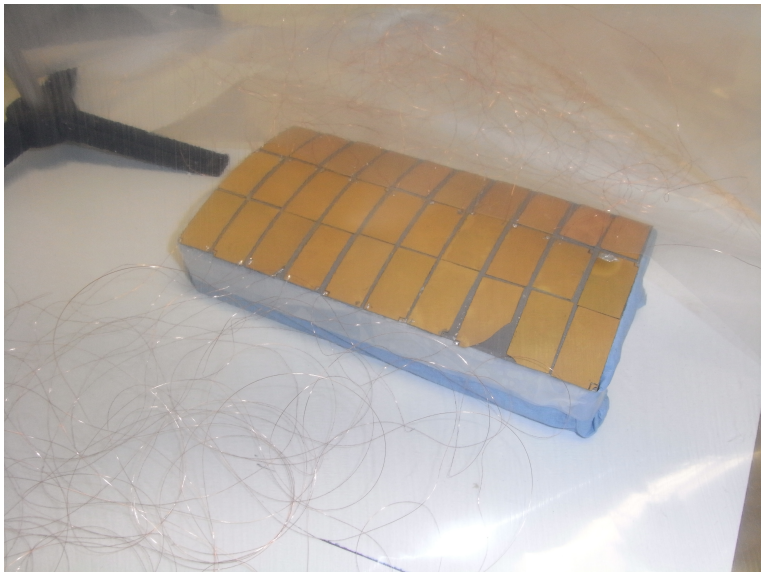

(b) The completed actuator bonding

Figure 3.42: Figure 3.42(a) displays the process in which the actuators were bonded, in columns, with the actuators' wires leading out away from the optic. The completed bonding is shown in Figure 3.42(b): when completed the optic was under a cover to minimise access to detritus.

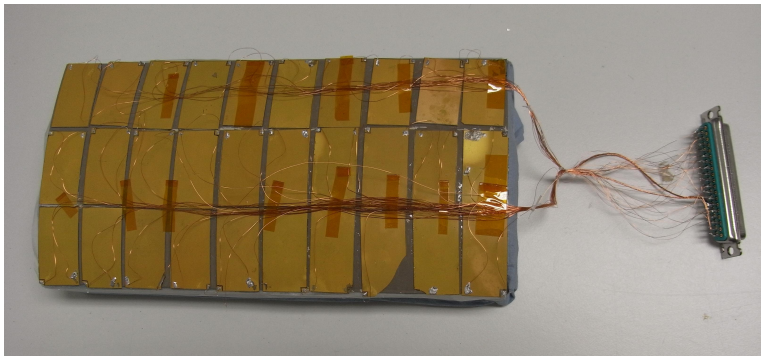

Figure 3.43: The harnessed actuators upon the reverse of the nickel optic

3.6.5 Cylindrical prototype summary

Fabrication of the cylindrical prototype prior to commencing the ellipsoidal proved invaluable in the assessment of intended production methods. Lessons learnt from the cylindrical prototype can be directly applied to the ellipsoidal prototype. The following is a list of actions to be applied or considered for the ellipsoidal prototype:

- MANDREL MATERIAL - although the cylindrical mandrel was made to form and operated well within the electrodeposition facility, there were disadvantages in the choice of material. The surface roughness obtained upon the mandrel was limited to 4.01nm Ra and this resulted in an optic with 98% scatter at 1.04keV. A selection of a harder material would improve the quality of the surface finish and reduce the scattering effect. A further disadvantage is from the perspective of the user: stainless steel is a heavy material, making the cylindrical mandrel cumbersome to handle. As the increased dimensions of the ellipsoidal mandrel would exaggerate the problem, an alternative material choice could alleviate this concern.

- WASTER DIMENSIONS - the use of the wasters as sacrificial electrodes provided optics with greater thickness uniformity which would not have otherwise been possible without their use. To improve the uniformity still further, the ellipsoidal mandrel's wasters could be increased in size to provide a larger surface area over which the nickel could deposit and thereby reduce the current density gradient across the mandrel's surface.

- ACTUATOR BONDING - to improve the actuator positioning upon the optic, the wires could be soldered after bonding; this would prevent the wires from pulling the actuators as they cure and disrupting their position. To prevent the adhesive from becoming too viscous, multiple

samples could be produced to ensure that the adhesive is used within its working-life.

- ACTUATOR HARNESSING - soldering the wires at the same time as harnessing allows the direction from which the wire exits the solder to be governed and therefore placed in the ideal position to be harnessed. From discussion with the UoB, the oil upon the actuators is to be removed prior to dispatch: this should provide the acrylic tape a clean surface to bond to and therefore securely fasten the wires to the actuators.

3.7 Chapter Summary

The dominant component of this chapter has been a description of the method of electrodeposition from a theoretical and practical view point and this led to the production of several cylindrical optics. The latter half of the chapter discussed the conversion of a nickel optic into a prototype system through addition of the piezoelectric actuators. In particular, the problems encountered have been highlighted and solutions proposed. Chapter 4 therefore outlines the production of the ellipsoidal prototype, building on the valuable experience gained within this chapter.

CHAPTER 4

THE ELLIPSOIDAL PROTOTYPE

Building upon the initial work in the production of the cylindrical prototype this chapter outlines the step-by-step production and metrology of the ellipsoidal prototype. The chapter begins with a review of the mandrel used for the optic replication process and concludes with the actuator bonding and harnessing.

4.1 Fabrication of the ellipsoidal mandrel

The specification of the ellipsoidal mandrel was determined by the dimensions of the X-ray tunnel test facility (TTF) as outlined in Table 2.2 in Chapter 2. Section 4.1.2 outlines a narrative of work undertaken by DB in the production of the mandrel.

4.1.1 Materials choice

The cylindrical mandrel was produced using stainless steel, but it was noted in the end of Chapter 3 that stainless steel would be unsuitable for the ellipsoidal mandrel due to its weight and final surface quality. This led to an investigation of alternative mandrel materials in an effort to alleviate these concerns.

Electroformed nickel optics have been used for the past 20 years in a variety of astronomical X-ray missions, both large and small, for example: XMM Newton (Egle 2000), Swift/Jet-X (Burrows *et al.* 2004; Citterio *et al.* 1996) and the balloon-borne Hero payload (Gubarev *et al.* 2005). Nickel replicated optics are far from old technology, with current mission proposals such as: Simbol-X (Pareschi *et al.* 2008) and the Focusing Optics X-ray Solar Imager (FOXSI) (Gubarev *et al.* 2009)

now under consideration. A common factor of all these missions is the use of a Al/electroless nickel (or kanigen) mandrel from which to replicate the optics. An Al/kanigen mandrel consists of a primary block of aluminium produced to the correct form, on the top of which kanigen is deposited. Kanigen is a nickel alloy which is deposited upon a surface through a catalyst aided chemical reaction, i.e. it is not driven by a potential difference and is therefore an electro-less process/material. Aluminium is a soft metal that can be easily figured to the desired form and it has a lower density than stainless steel, $\sim$2700Kgm^{-3} in comparison to $\sim$8000Kgm^{-3} respectively, this therefore makes the mandrel lighter and easier to handle. The kanigen coating provides the hard polishing surface and sub nano-meter roughness is a standard with this technology (XMM Newton's mandrels were $<$0.4nm rms Rq).

Al/kanigen optics have been made previously at OSL for alternative applications and good surface roughnesses have been achieved (Ra $\sim$0.5nm). In addition alternative stainless steels (manufacturing grade 420) were investigated for the ellipsoidal mandrel and methods to harden the steel through a heat treatment provided good surface roughness results ($\sim$0.5nm Ra was obtained), though weight still remained a concern. It was decided that an Al/kanigen hybrid would be the preferred material for the ellipsoidal mandrel as the reduced weight would make it significantly easier to handle during production and the electroforming phase. A disadvantage of an Al/kanigen mandrel is the requirement of a release agent between the kanigen and the nickel deposit: this prevents the nickel from ionically bonding to the kanigen, thereby allowing the optic to be released from the mandrel.

Possible release agents were investigated for application to the kanigen surface and two different approaches were considered: the addition of a thin metallic layer (e.g. Au, Ir, Pt etc) and through chemical passivation of the mandrel's surface. The thin metallic coating is applied through the vacuum deposition of a high atomic number (Z) metal upon the kanigen surface, then the nickel is electrodeposited upon the metallic layer, this approach was used in the production of XMM Newton's optics. In the second method, a chemical passivation technique is used, where a thin oxygen layer is chemically enforced upon the kanigen surface therefore providing a boundary between the kanigen and nickel (Gubarev *et al.* 2005).

The vacuum deposition of elemental gold[1] onto the mandrel's surface provides both a release agent and a reflective coating. After vacuum deposition the gold is physically bonded to the mandrel and could be removed with a small application of force (though obviously this is undesirable). The nickel ions of the electrodeposit ionically interact with the the gold atoms through the exchange

[1]Gold was selected for study due to it being easier and more economical to outsource to a local company

of electrons and thereby adhere themselves to the gold. When the electroform is removed from the mandrel the gold is transferred from the mandrel to the optic and therefore provides the optic's reflective coating.

The idea of using a gold coating as the release agent was tested to ensure it could be practically applied to the ellipsoidal mandrel. A small ($\varnothing$ 5.5cm) Al/kanigen concave mirror was coated with approximately 30nm of gold and the non reflective surfaces masked with a polyester insulating tape (Figure 4.1(a)). After a nickel deposition of 8 hours at 0.24A, providing a thickness of 80 - 100μm, the insulation was removed and the optic released. The deposited nickel was dull grey in appearance, this indicated that there were no impurities within either the bath or the gold layer. Removal of the optic required only minimal force at the edges and it could be seen that the gold had been transferred successfully from the mandrel to the optic, as shown in Figure 4.1(b). This experiment validated the use of gold as a possible release agent for the prototype.

Chemical passivation involves the production of an oxygen layer upon the kanigen surface and this is achieved by submerging the mandrel within a dichromate solution (either sodium or potassium dichromate can be used). The solution then interacts with the kanigen layer to produce oxygen on the surface. This oxygen layer acts as a barrier to prevent the electrodeposited nickel atoms from reaching the kanigen surface. This process was tested using a flat Al/kanigen mandrel ($9 \times 9\text{cm}^2$ reflective area): the mandrel was masked to provide a small $7 \times 7\text{cm}^2$ window for the nickel deposit. The mandrel was submerged in 0.068M of potassium dichromate (6.8×10^{-5}mol ml^{-1}) for 2 minutes to provide the oxygen layer[2]. The dichromate solution was thoroughly rinsed from the mandrel with distilled water before placement within the electroforming facility. The bath was operated for a duration of 8 hours at 0.49A and this led to typical thickness of 80 - 100μm. On removal from the bath, the masking was discarded and the electroform released. The electroform was not of the quality generally produced during a deposition, because the corners had peeled slightly from the mandrel's surface and further deposition was suspected underneath these regions. Figure 4.2 highlights these damaged regions and the corresponding damage to the mandrel's surface, however the optical surface did replicate well and the electroform did release unhindered from the mandrel's surface, therefore legitimising the use of chemical passivation as a possible release agent.

Gold was selected as the release agent for the Al/kanigen mandrel, based primarily on the quality of the final electroform, which was superior to the electroform from the chemical passivation method. The disadvantages of this method, however, were due to the outsourcing of the gold deposition,

[2]The concentration of the dichromate solution and the duration of submersion were provided through discussions with Tony Hart of Hart Coating Technology.

(a) Prior to nickel deposition

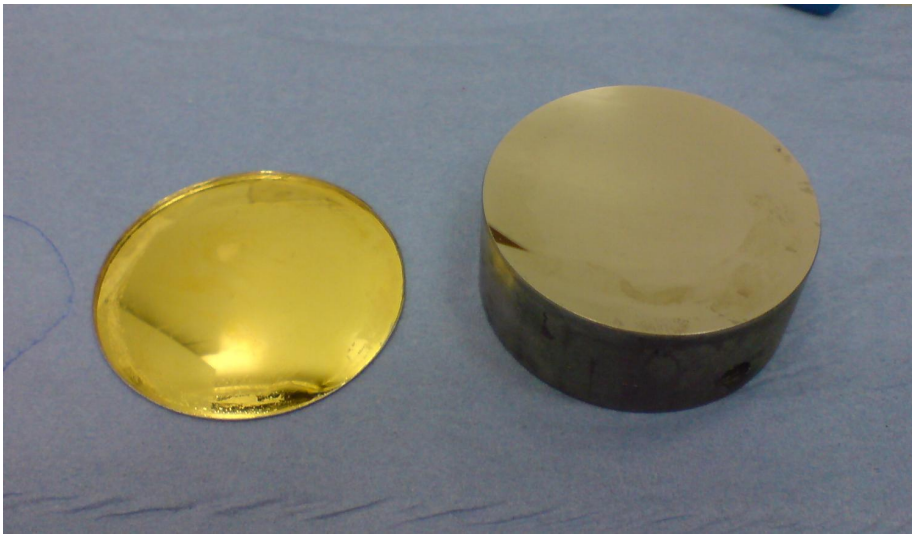

(b) The concave mirror and electroform

Figure 4.1: Initial experiment investigating gold as a viable passivation mechanism.

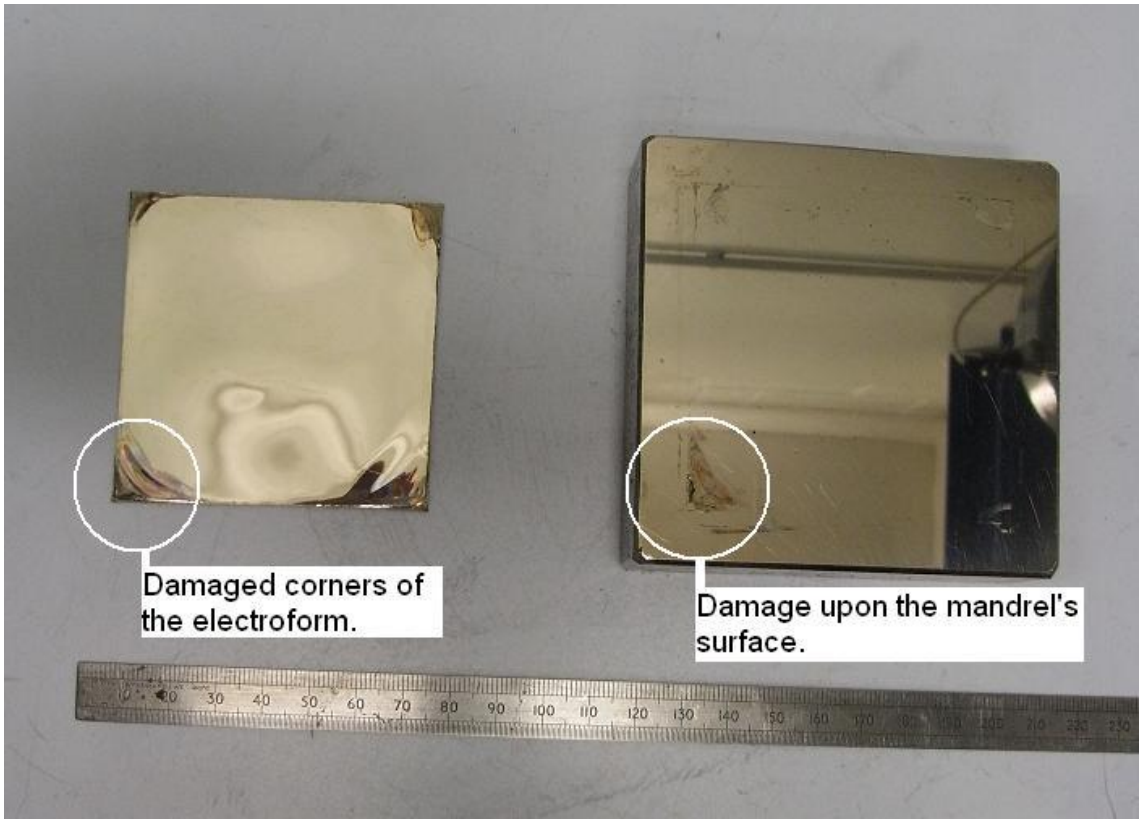

Figure 4.2: An investigation of the use of potassium dichromate as a possible release agent.

which prevented the ability to regulate the procedure in-house and the need to budget an increase in time and cost. These considerations were still favourable over the potassium dichromate, because even though the process is cheap and of short duration, the corner effect was undesirable. However, chemical passivation does remain a viable alternative.

4.1.2 Mandrel production

The ellipsoidal mandrel had the same 5 components as the cylindrical mandrel in Chapter 3, a central mandrel from which the optic would be electroformed and four wasters that surround the mandrel. Within this Chapter, 'mandrel' will be used to refer to the component from which the optic is replicated and 'ellipsoidal mandrel' will refer to the mandrel including the wasters. The components of the ellipsoidal mandrel have the same function as the cylindrical mandrel and a CAD representation of the mandrel can be seen in Figure 4.3. The primary difference in the components of the ellipsoidal mandrel to those of the cylindrical are that the wasters have been increased in width from 1cm to 2.5cm: this provides a larger sacrificial electrode and therefore an improved

optic thickness uniformity.

The five aluminium blocks which represent the wasters and the mandrel were first squared to ensure a clean join between pieces. Steel dowel was used to ensure repeatable alignment of the mandrel with the wasters, while screws were used to securely fasten the pieces together. A specific grade of aluminium, 5083 in the 'O' condition, was used for the production. The 'O' condition refers to the tempering of the material, implying that the material is in its most relaxed state and therefore less susceptible to losing its form during production due to residual internal stress. In between the wasters and the mandrel 200μm of aluminium foil was inserted and this mimicked the 100μm thickness of the kanigen layer that was to be deposited later on each of the faces, therefore guaranteeing that the curvature of the mandrel would be maintained after the kanigen deposition.

To provide the azimuthal curvature, the ellipsoidal mandrel was first turned on a lathe to the conical approximation of the ellipsoid (165mm to 170mm in radius of curvature), this process can be seen in Figure 4.4. The axial curvature was achieved through the grinding of aluminium at the two ends of the ellipsoidal mandrel while maintaining the curvature in the azimuthal direction. The grinding was peformed by hand using decreasing grain sizes of silicon carbide and the process required care and constant measurement (Figure 4.5) to ensure that the curvature provided in one direction did not counteract the curvature in the other. The mandrel was ground to the correct curvature down to grade 400 of SiC, providing a surface roughness of 0.7μm Ra, which was ideal for kanigen adhesion.

The kanigen deposition was outsourced to Nitec Ltd.; the foil between the mandrel and the wasters was removed to allow kanigen to be deposited upon every surface. The electroless nature of the deposition ensures thickness uniformity through the use of chemicals rather than an electric potential (as is the case in electroplating) and the final deposition is uniform to within $\pm$10%[3]. Further grinding of the mandrel was required to compensate for small variations in the form due to the kanigen deposit. Finer grades of SiC (400, 600, 1000) were used in this application and again constant profilometric measurements were required to ensure the form of the mandrel.

With the required ellipsoidal form, the mandrel was then polished using a pitch-faced polishing tool and an aluminium oxide (Alox) slurry. During the polishing process it is the aluminium oxide particles ($\varnothing \sim 1\mu$m) that abrade the surface while the polishing tool maintains the form. Throughout this process the surface of the mandrel is measured using a microscope interferometer to determine the surface quality and the final surface finish of the mandrel can be seen in Figure 4.6.

The mandrel was completed in early October 2008 (Figure 4.7): time constraints prevented

[3] As quoted by the Nitec product specfication

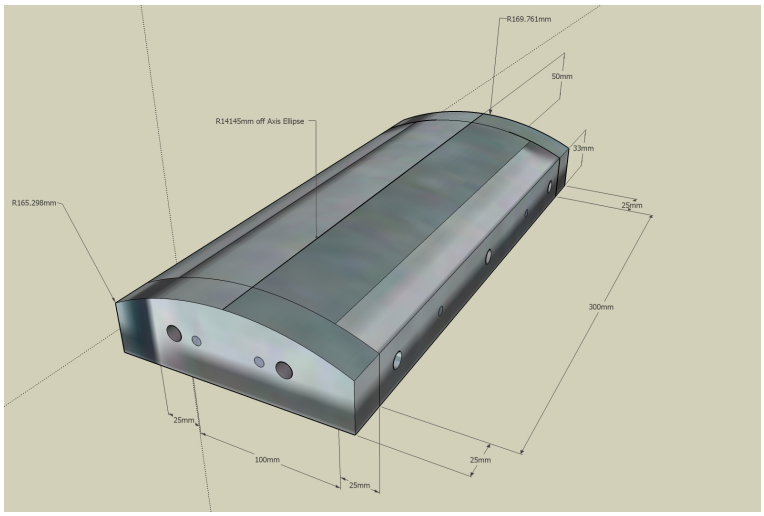

Figure 4.3: A computer aided design of the ellipsoidal mandrel, including wasters, courtesy of DB.

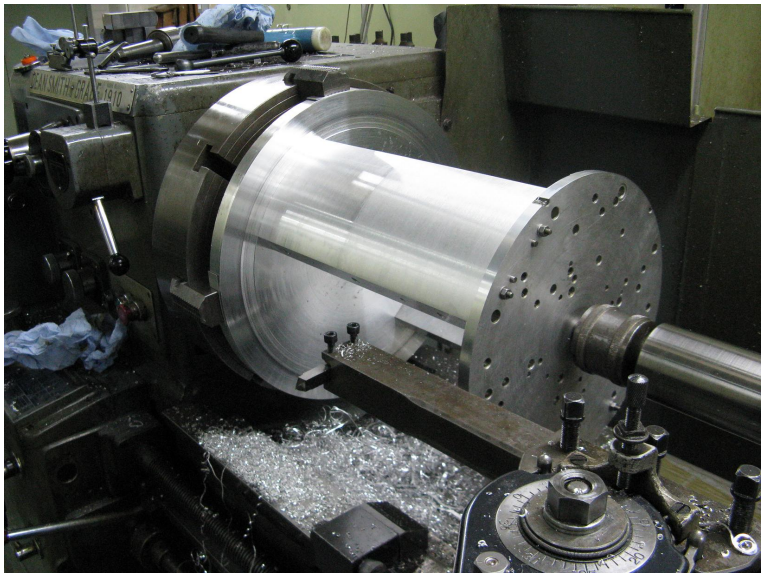

Figure 4.4: The ellipsoidal mandrel being turned on the lathe, courtesy of Jim Percival

Figure 4.5: The ellipsoidal mandrel measured upon the Talysurf profilometer, courtesy of DB.

measurements of the mandrel's form prior to gold deposition, therefore the measurements discussed in Section 4.2 were performed after the prototype's optic was replicated. In addition the mandrel was further polished in December 2008 and it was at this point that the final surface roughness of 1.33nm Ra was obtained.

During the production of the mandrel a single obvious defect occurred. During the polishing phase the tool cut into the kanigen, leaving a large deep scratch in the kanigen layer. Attempts were made to fill this scratch by using the electroforming facility to electroplate, rather than to electroform and therefore plate nickel within the kanigen scratch. The entirety of the mandrel, except for a thin rectangular window enclosing the scratch, was masked. The total duration of the deposition was approximately 2 hours and the electroplated nickel strip can be seen in Figure 4.8.

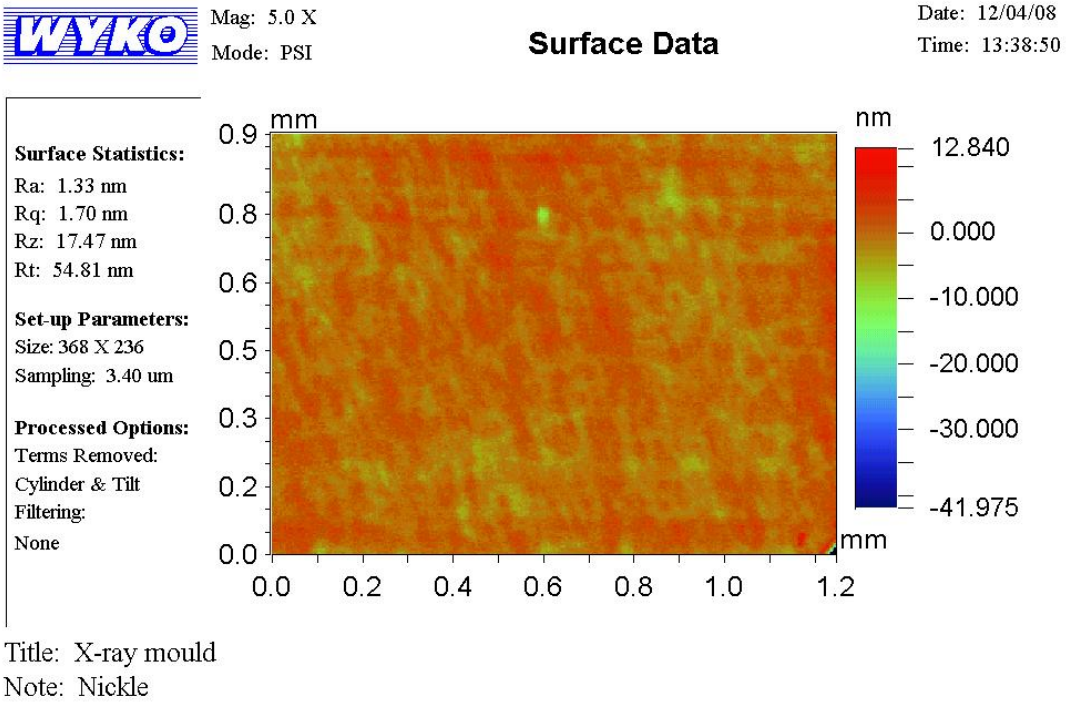

Figure 4.6: The surface roughness of the mandrel as taken by the RST 500

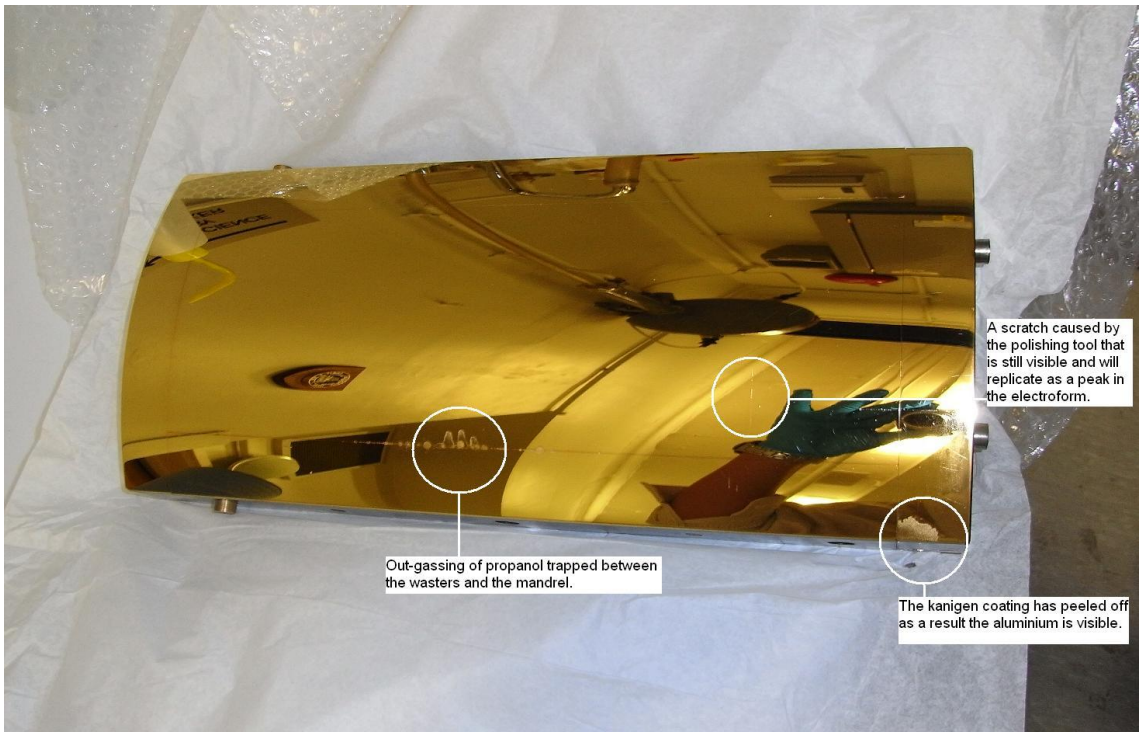

Figure 4.7: The finished mandrel, gold coated and prior to nickel electroforming.

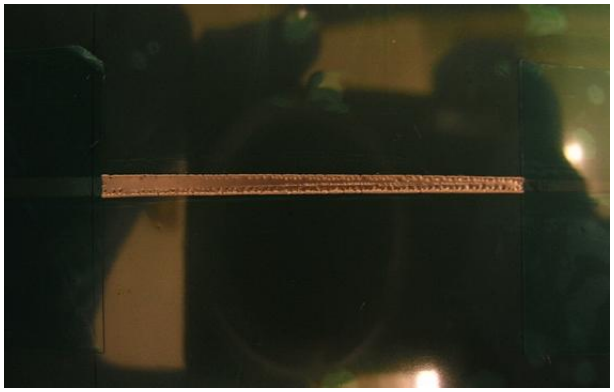

Figure 4.8: Electroplating nickel to fill the scratch on the ellipoidal mandrel

After deposition the nickel strip was ground and polished to keep the mandrel's form. Unfortunately the scratch was still visible, although to a lesser extent, and it was going to remain a feature of the mandrel and be replicated in subsequent optics. The scratch would have the effect of scattering the X-rays incident on that region, however as this is a small localised area the overall detected image should not be adversely affected.

4.2 Mandrel metrology

The mandrel's form was determined by a series of measurements performed at UCL and the STFC (Science and Technology Facilities Council) Daresbury Laboratory (DL) in Cheshire. The RST 500 microscope interferometer and the Talysurf profilometer were used to determine the surface roughness and the ellipsoidal curvature of the mandrel during fabrication. A long trace profiler (LTP) from Ocean Optics and a microscope interferometer (micro phase MicroXAM-5000-RP90 table mounted surface profiler) were used at DL under the supervision of Andy Smith (AS) and Anthony Gleeson (AG) respectively. An LTP is a non-contact laser displacement profiler that measures the form of an optic by comparing the reflected laser light from an object's surface to that of a reference and the MicroXAM-5000 interferometer provided additional surface roughness data over a smaller sample area. Therefore by combining surface form metrology and surface roughness metrology, the mandrel could be evaluated on both the large and small scale.

4.2.1 Surface roughness

The first set of measurements were taken during production using a WYKO RST 500 microscope interferometer. The interferogram has previously been shown in Figure 4.6: the sample size is 0.9mm $\times$ 1.1mm and the Ra over the area is 1.33nm (the software automatically corrects for tilt and cylindrical terms). Further analysis looked at Ra line profiles in the vertical and horizontal orientations as visualised in Figure 4.6; the average of 10 profiles gave an Ra of 1.55nm in the horizontal direction and an average of 13 line profiles produced a Ra of 1.63nm in the vertical. The interferogram also highlights the Rq at 1.70nm rms; calculating the total integrated scatter from Equation 1.14 for the variables λ = 1.19nm and θ_g=1.163 $^\circ$, 12.1% of the incident X-ray would be scattered. This is close to the desired 10%; however it is only an estimation from a single interferogram, but it does highlight a vast improvement from the expected scatter of the cylindrical mandrel at 70.8%.

To investigate the finer detail of the mandrel's surface the MicroXAM-5000 interferometer at the DL was used. The interferometer typically looks at surface area of 0.17mm by 0.13mm, however there is the capability to stitch several measurements together. The numerical results are presented in Table 4.1 and Figure 4.9 displays the stitched surface profile over an approximate 1.3mm length. From the corresponding 1D line profile (Figure 4.9(b)) it can be seen that deep scratches of the order of 20-30nm are present, although the majority of the scratches are in the order of 5-10nm. The data had been manually adjusted in terms of tilt and curvature (2^{nd} order

Position	Raw Ra(nm)	Tilt removed Ra(nm)	2^{nd} order polynomial removed Ra (nm)
1	1.4848	1.4735	1.4648
2	1.9731	1.8738	1.8646
3	3.7154	3.7027	3.3778
4	4.2209	4.1921	2.1600
Average	2.8486	2.8105	2.2168

Table 4.1: The surface roughness as measured using DL's microscope interferometer

polynomial) and the average Ra for the four data sets was approximately 2.22nm. When this is added to the average of the horizontal and vertical line data from the RST 500, a final surface roughness (Ra) for the mandrel of approximately 2.09nm is obtained.

4.2.2 Azimuthal radius of curvature

The azimuthal radius of curvature was determined using the Talysurf profilometer (data taken by HCW). Measurements indicated that there was a close agreement with the desired form and that the deviation was typically $\sim$350μm (Figure 4.10). As the optic is less sensitive in the azimthual direction in comparison to the axial direction, this small error is not expected to cause a major effect.

4.2.3 Axial curvature

The axial profile of the prototype was measured using the LTP; the profiler is non-contact and uses a laser to sample points along the surface of an object. Several axial measurements were taken at different azimuthal coordinates; these were done by carefully tilting the mandrel via the use of a kinematic mount. Figure 4.11, displays the averaged axial data from the measurements and indicates a good comparison with the desired form in terms of the magnitude of the axial curvature (33μm). However the figure highlights a tilting of the mandrel's profile in comparison with the required form. After consultation with the UoL, it was deemed that the descrepancy would not significantly affect the detected image.

(a) Surface profile of the ellipsoidal mandrel 2D image

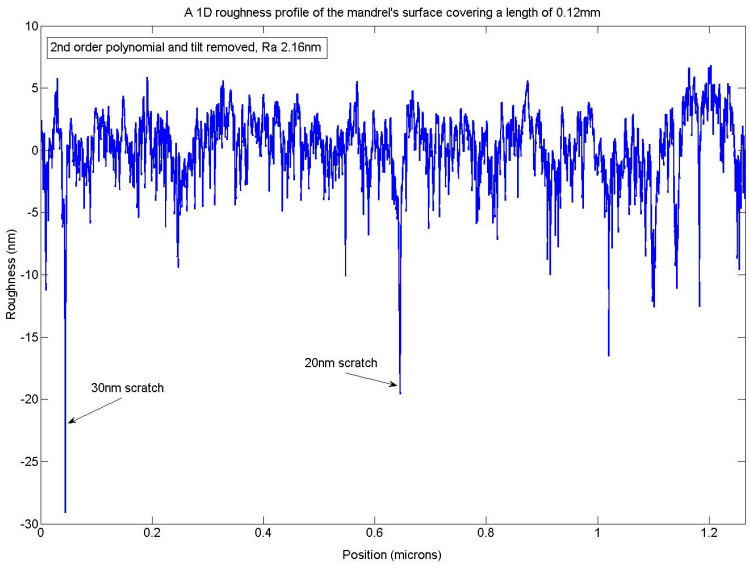

(b) Surface profile of the ellipsoidal optic 1D graph

Figure 4.9: A stitched surface profile of the ellipsoidal mandrel, indicating a surface roughness Ra of 2.16nm, (image 4.9(a) courtesy of Anthony Gleeson from DL)

4.2.4 Mandrel summary

The mandrel was completed a couple of weeks in advance of the scheduled Leicester delivery date (29$^{\text{th}}$ October) and was immediately taken to be gold coated to allow the production of the prototype to remain on schedule. The metrology presented in Sections 4.2.1 to 4.11 occurred after the replication of the prototype's optic and after the mandrel had been further polished; however, it is unlikely that either the optic replication or polishing would have altered the form of the mandrel dramatically from its pre-replication state. Considering the hand made nature of the mandrel and the difficulty in producing one curvature while not adversely affecting the other, the form of the mandrel is good. Both the azimuthal and axial curvature are close to their desired values and it is estimated that the surface roughness should limit the scattering to $\sim$12%.

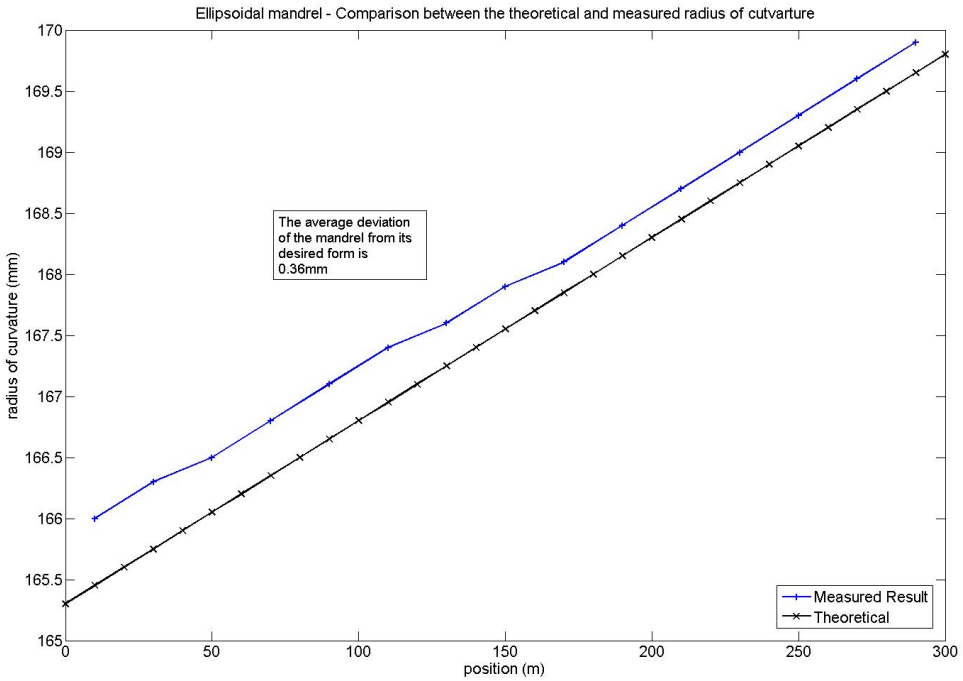

Figure 4.10: The azimuthal radius of curvature of the ellipsoidal mandrel and its deviation from the desired form

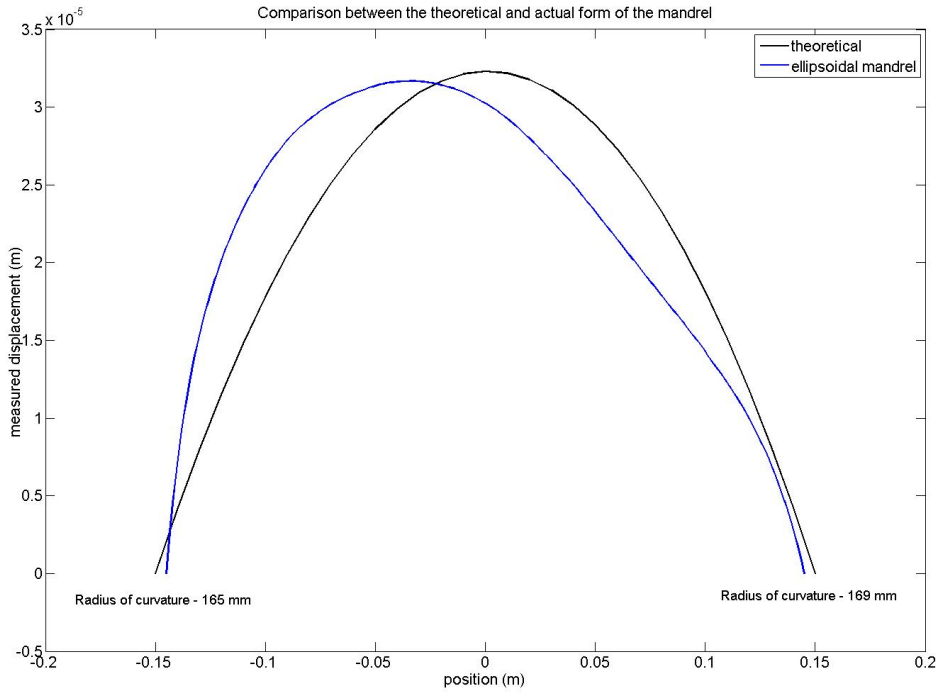

Figure 4.11: The axial form of the ellipsoidal mandrel

4.3 Optic replication

The replication of the optic followed approximately the same method as previously mentioned in Chapter 3, with differences caused by the gold release agent and the larger dimensions of the ellipsoidal mandrel. The prototype's optic was replicated in mid October 2008, and additional optics have been replicated through 2009. Table 4.2 highlights the ellipsoidal optics replicated to date, however the latter optics (4 - 6) are not detailed within this thesis.

4.3.1 Gold deposition

The vacuum deposition of a 30nm thick layer of gold was undertaken off site at Vacuum Coating Ltd in Walthamstow, London. The first deposition of gold upon the mandrel had the wasters and the mandrel in one complete piece: this was done to allow a single deposition rather than 5 individual depositions. Prior to installation within the vacuum chamber, the ellipsoidal mandrel was thoroughly cleaned with propanol to remove residual Alox slurry, grease and detritus. The exterior and the interior of the vacuum chamber can be seen in Figures 4.12(a) and 4.12(b) respectively. The gold to be deposited was situated in a small boat at the bottom of the chamber and the ellipsoidal mandrel was suspended above the boat: deposition occurs when a current is passed through the boat which melts and vapourises the gold.

During this first deposition, residual propanol outgassed and left bubble marks on a small area of the ellipsoidal mandrel (Figure 4.7) and this occured as a result of the ingress of propanol in the joint of the mandrel and waster. Although this effect was undesirable, it was small and localised, and should not severely affect the final detected image. As a result, future gold depositions were made on each piece individually and therefore negated the risk of trapped propanol between the

Ellipsoidal optic no.	Manufacture date	Intended use	Remarks
Ellipsoidal shell 1	October 2008	The ellipsoidal prototype	plating time 40 hours
Ellipsoidal shell 2	January 2009	Full optical metrology	plating time 40 hours
Ellipsoidal shell 3	February 2009	Actuator bonding tests	plating time 40 hours
Ellipsoidal shell 4	June 2009	Full optical metrology	plating time 80 hours
Ellipsoidal shell 5	July 2009	Full optical metrology	plating time 60 hours
Ellipsoidal shell 6	August 2009	Full optical metrology	plating time 45 hours

Table 4.2: Ellipsoidal shell production

sections. Generally after each deposition the mandrel had small scratches within the gold layer, often due to the wrapping of the pieces for transit: these small scratches did not hinder the removal of the electroform, although it is expected that there will be a maximum limit to this.

4.3.2 Nickel deposition

Due to the asymmetry of the mandrel, orientation within the tank becomes a consideration for repeatability over multiple replications. A decision was made to place the larger radius of curvature at the bottom of the tank, thereby positioning the mandrel's centre of gravity closer to the ground. A finite element analysis (FEA) map of the current density distribution was simulated to provide an indication of the thickness variation likely to be exhibited by the optic. Following the same method as for the cylindrical mandrel, the ellipsoidal mandrel was reproduced in the FEA software COMSOL MULTIPHYSICS: a potential of 5.25V was added to the electrode and the 'active' surface of the mandrel was set to ground. The ellipsoidal form of the mandrel and the insulating layers were reproduced within the FEA to provide an accurate representation of the experimental set-up.

Figure 4.13 displays the current density map for the ellipsoidal mandrel. The obvious discrepancy is the variation from the corner to the centre, which indicates a current density variation (and therefore a thickness variation) of $\sim$50%, i.e. the corners are 50% thicker than the centre. This is an improvement in comparison to the cylindrical mandrel, whose corners were $\sim$220% thicker than the centre, but unless the wasters are significantly larger an approximately uniform optic thickness will not be obtained.

A subtle difference that can be viewed in Figure 4.13, is the variation of current density from the top (165mm) of the mandrel to the bottom (169mm), viewed from the perspective of the tank. The bottom of the mandrel is $\sim$6% thicker than at the top; this variation is probably due to the conic nature of the mandrel, where the larger radius of curvature protrudes further towards the electrode than the top of the mandrel. This is actually a small discrepancy in current density and it would be prudent to note that the FEA merely provides an indication of the variation of thickness. Other factors such as: the position of the pump's jets, the presence of pitting/nodulation or the introduction of an impurity, all affect the rate of growth upon the mandrel's surface.

The deposition of the nickel followed the procedure as outlined in Chapter 3, and the only variants were: the current applied 5.25A, assuming an even current density of 0.01A cm^2 over a 525cm^2 surface area; shorter stainless steel rods used to hang the mandrel from the bus bar and the mandrel degreasing phase prior to submersion. The stainless steel rods were shortened to ensure that the mandrel could be positioned centrally in front of the anode basket, therefore

(a) The vacuum chamber used during deposition

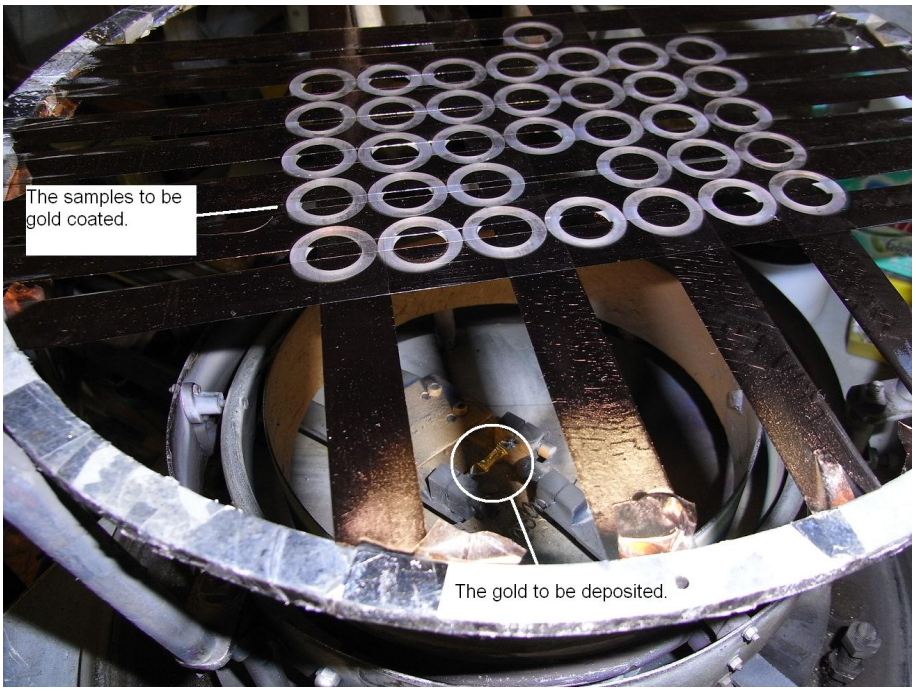

(b) The interior of the vacuum chamber

Figure 4.12: The vacuum chamber used for the gold deposition of the mandrel and wasters

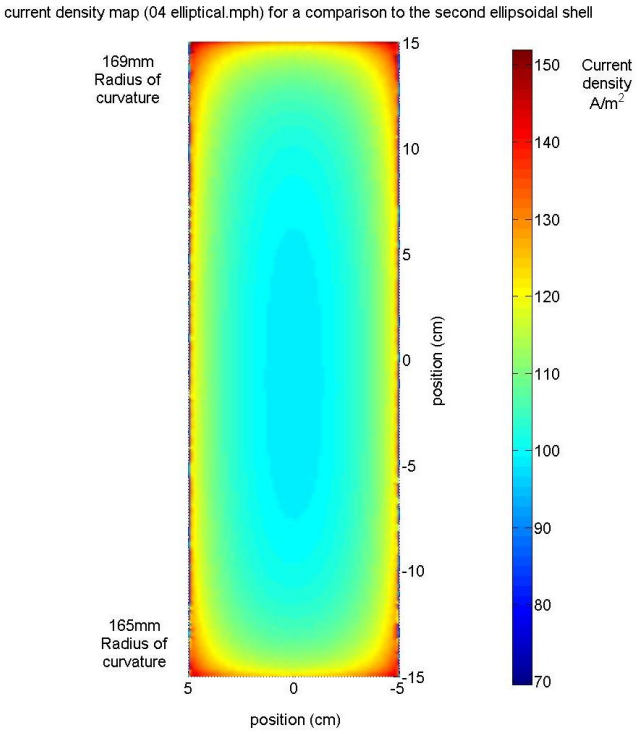

Figure 4.13: The current density map of the ellipsoidal mandrel

providing a symmetry in deposition. The degreasing phase was removed to prevent damage to the deposited gold layer, as the mandrel is thoroughly cleaned prior to vacuum coating; that was deemed adequate in the prevention of the foreign substances entering the electrolyte. Figure 4.14 displays the prepared ellipsoidal mandrel prior to submersion within the electroforming facility.

4.3.3 Optic removal

Removal of the electroformed optic from the mandrel was problematic. The electroformed deposit upon the wasters was removed with ease: as this was waste electroform a concentrated force could be applied. However, this approach could not be applied to the optic due to the necessity to retain the mandrel's morphology upon the optic. The removal problem stemmed from the ingress of nickel at the location of the polypropylene insulator; the nickel bonded to the kanigen sides that were not gold coated and subsquently fixed the optic to the mandrel. This excess nickel had to be scraped away before the optic could be removed and was a concern due to potentially damaging both the optic and mandrel. The final release was aided by a slight thermal shock of $\sim \Delta 50\,^{\circ}\mathrm{C}$.

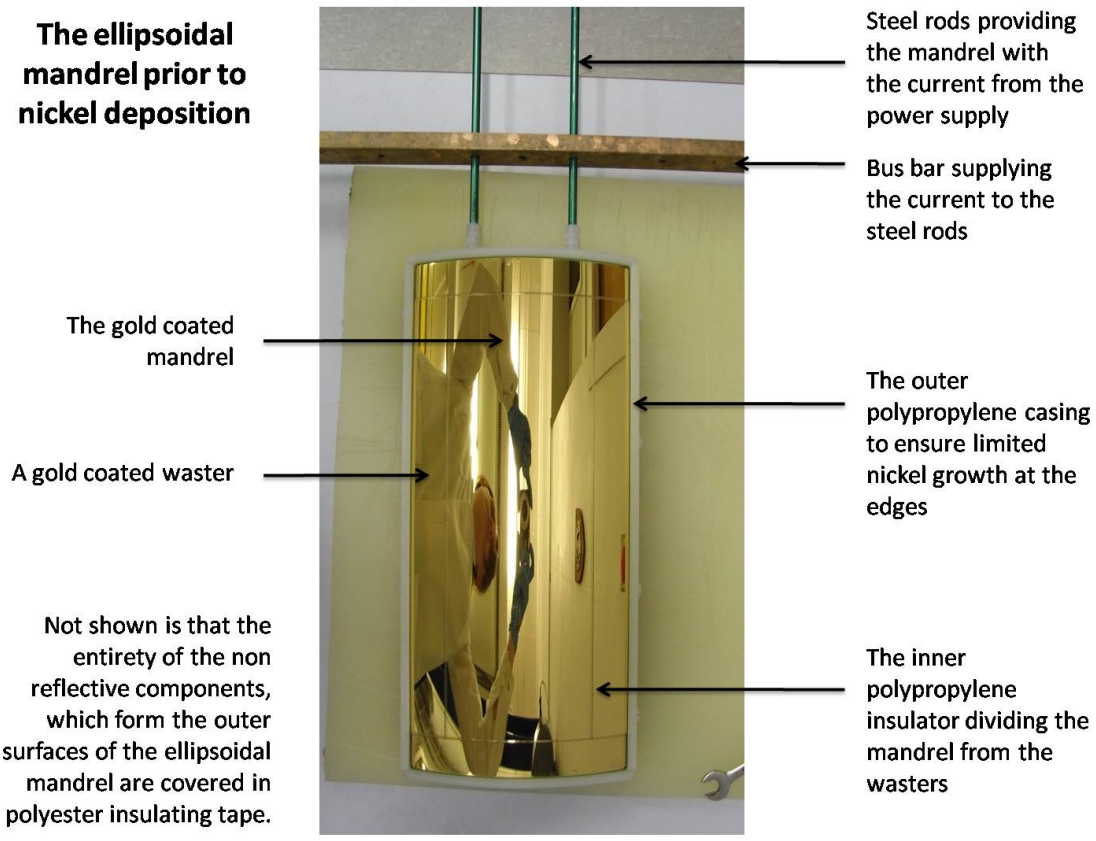

Figure 4.14: The ellipsoidal mandrel prior to nickel electrodepostion

4.4 Optic Metrology

The afore mentioned time constraints in the prototype's manufacture prevented the prototype's optic from having the benefit of a thorough metrology analysis, therefore the results presented relate to the second ellipsoidal shell, with the exception being for the outer radius of curvature (measurement 5), which was performed on the prototype's optic. The difference between the first two optics was that the mandrel had been further polished. However polishing does not significantly affect the form of the mandrel, only the surface quality and as a result the form of second optic can be considered representable of the prototype's optic (although the surface roughness will be different). The optic's measurements proceeded as outlined:

1. Surface roughness measurements using OSL's WYKO RST 500 microscope interferometer
2. Surface roughness measurements using DL's MicroXAM-5000 microscope interferometer
3. Long trace profiler (LTP) traces along the axial length (DL)

4. The inner radius of curvature (ROC) measurements in the azimuthal direction using the Talysurf profilometer

5. The outer radius of curvature (ROC) measurements in the azimuthal direction using the Talysurf profilometer

6. Thickness measurements using a digital micronmeter

For measurements 1 - 4 the second optic was situated upon the optic cradle component of the MSSL support structure thereby supporting the second optic in the same manner used during the X-ray tests. Measurements 2 and 3 were aided by AS and AG respectively.

4.4.1 Surface roughness measurements using the RST 500

Throughout the set-up of the interferometer it was obvious that vibrations were dominating the surface profile of the optic. Attempts to isolate the vibrations through damping were not successful, though they were reduced to a point where a surface profile image could be obtained but an accurate representation of the surface was still lacking. Figure 4.15 indicates the profile obtained, and the ripples indicate the presence of vibrations in the optic; however peaks are evident upon the surface and typically these are in the order of $\sim$9nm in height. The figure also highlights a Rq of 2.30nm rms and using Equation 1.14 and the variables mentioned in Section 4.2.1, a total integrated scatter (TIS) of 21% was calculated. Although the interferogram was affected by rippling, the decision to use it to calculate the TIS was based upon maintaining consistence with the previous cylindrical optic and mandrels.

4.4.2 Surface roughness measurements taken at the Daresbury Laboratory

The metrology laboratory at DL offers several advantages that are beneficial for the analysis of the optic's form; these are: good ground stability, the use of an optical bench and an enclosure around the metrology equipment. These factors help isolate the majority of ground and air disturbances. The MicroXAM-5000 interferometer was used to study the surface roughness in a number of locations down the axial length of the optic (unfortunately corresponding azimuthal coordinates were not recorded). Figure 4.16 displays a 2D interferogram of a 120μm by 180μm area. Clearly noticeable in the corresponding 3D image is that the troughs that were seen in the mandrel have been replicated as peaks upon the optical surface. The peaks observed in the optic are generally on the scale of 5 - 10 nm and these are concurrent with the troughs seen in the mandrel's interferogram.

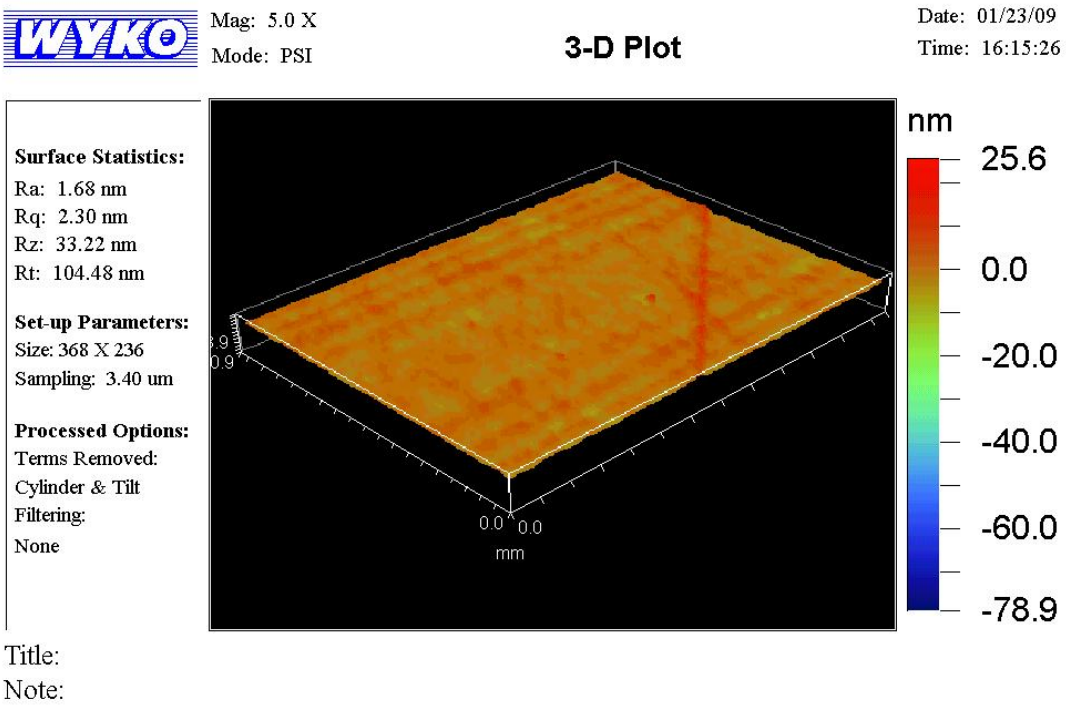

Figure 4.15: A RST 500 surface profile of the second ellipsoidal shell, the ripples indicate that vibrations are present in the profile

The line profiles from the five data sets, (an example can be seen in Figure 4.17), allow the Ra to be calculated for each of the five locations. Each line profile was first corrected in terms of tilt and then with a 2^{nd} order polynomial, in the case of three regions, a higher 8^{th} order polynomial was substracted to remove high order spatial frequency form distortions.

Table 4.3 displays the final Ra line data for each of the locations. A cumulative Ra of 2.04nm is calculated from the Ra at each location and in comparison with the mandrel average Ra of 2.09nm there is a clear agreement. A concern could be voiced with regard to the mandrel in fact having a worse surface than the optic which is not normally the case in electroformed surfaces. This anomaly could be a result of the deposited gold layer, where the gold has not penetrated and filled the entirety of the deep troughs and therefore these have been replicated as smaller peaks. Another consideration is that the sampling of both the mandrel and the optic may not have been adequate to provide an accurate representation of either surface, nor can two exact locations be matched.

4.4.3 Long trace profiler (LTP) traces along the axial length

The LTP was used to measure the axial curvature of the replicated optic. As with the mandel, the positioning of the optic was fundamental to obtain reliable data, as poor alignment would deflect

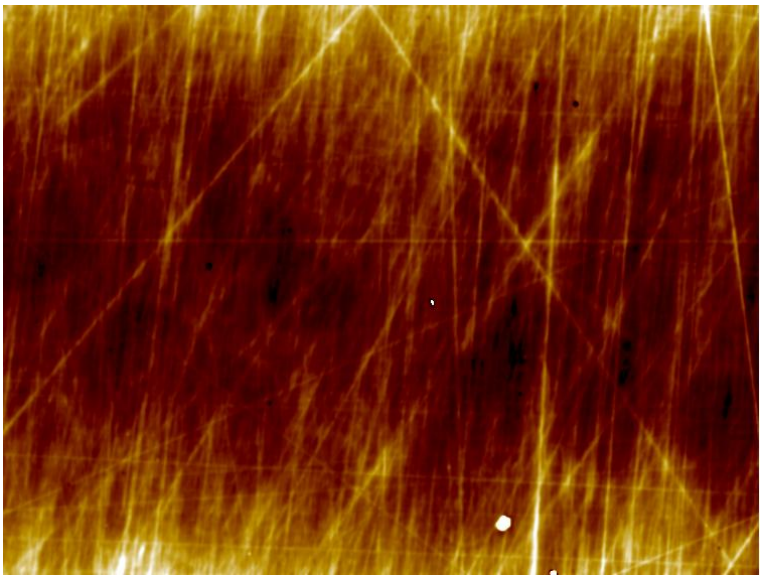

(a) Surface profile of the ellipsoidal optic 2D image

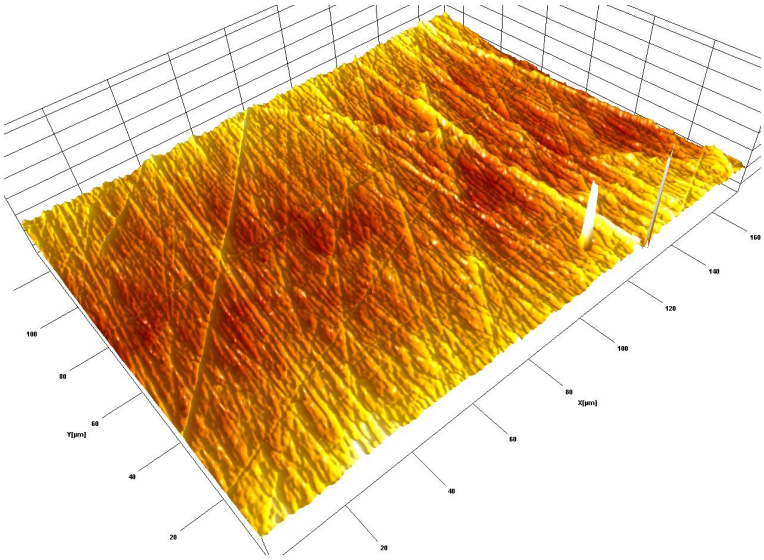

(b) Surface profile of the ellipsoidal optic 3D image

Figure 4.16: 2 and 3D profiles of the optical surface taken using the microscope interferometer at the DL (images courtesy of Anthony Gleeson from DL)

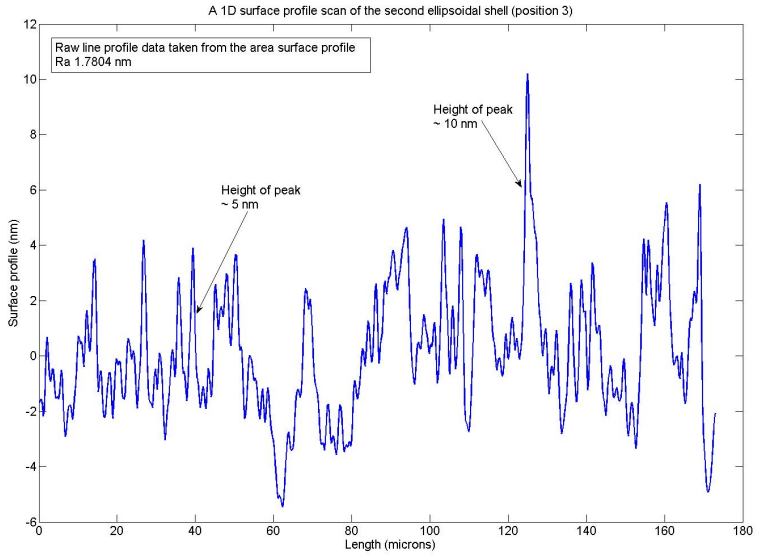

(a) Raw data, Ra 1.7804

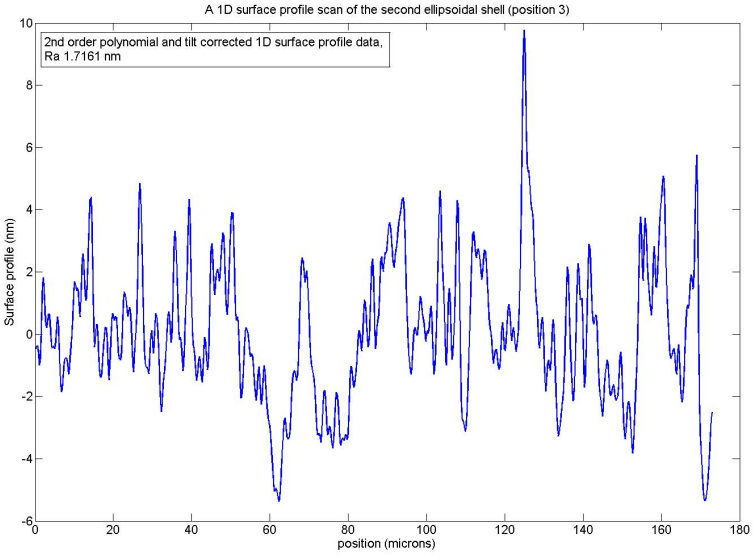

(b) Corrected data in terms of tilts and 2^{nd} order polynomial, Ra 1.7161

Figure 4.17: 1D surface roughness data taken from the second ellipsoidal shell (position 3)

Position	Raw - Ra (nm)	Tilt - Ra (nm)	2^{nd} order - Ra (nm)	8^{th} order - Ra (nm)
1	2.4648	2.4707	2.4721	2.2137
2	1.7804	1.7212	1.7161	n/a
3	1.6926	1.6846	1.5665	n/a
4	2.0142	2.0119	2.0243	1.7770
5	3.8499	3.8546	3.8643	2.9212
average	2.3604	2.3486	2.3287	2.3040

Table 4.3: The surface roughness (Ra) measurements taken from the second ellipsoidal shell

the reflected laser away from the sensor. Seven 270mm traces were taken in the axial length of the optic: one trace down the centre of the optic and three each side of the centre at 1mm intervals, as shown in Figure 4.18. The measurements indicate that 20μm of axial sag has been lost through replication. It is possible that this is an effect of internal stress within the nickel deposit which has warped the form of the optic, or, the result of applied force needed in optic's removal from the mandrel. It should also be noted that the support structure which holds the optic also provides an important role in the curvature of the optic and this consideration is discussed in Section 4.4.7.

4.4.4 The inner azimuthal radius of curvature

As the contact profilometer can only measure a maximum height displacement of 2mm, to obtain measurements of the inside radius of curvature, the optic and support structure had to be positioned at an angle. Two screws were added to the support structure to lift one side and position the optic at an angle of $\sim$14° to the horizontal (Figure 4.19(a)), this allowed the profilometer to measure the optic in two sections (Figure 4.19(b)). There was a gross difference measured in the RoC of the optic compared to that of the mandrel, suggesting either compressive stress within the deposited nickel or a deformation caused by the optic release. The measured values are displayed in Table 4.4. When these are compared against the theoretical values (Figure 4.20), the magnitude of the variation can be seen. The RoC of the optic is significantly tighter than that of the mandrel, and at one end of the mandrel it appears that the radius of curvature is becoming closer to the desired RoC in an anomalous manner. Subsequent measurements of shell 3 highlight this trend of a tighter post-release radius of curvature, though the variation in curvature varies according to the mandrel's form.

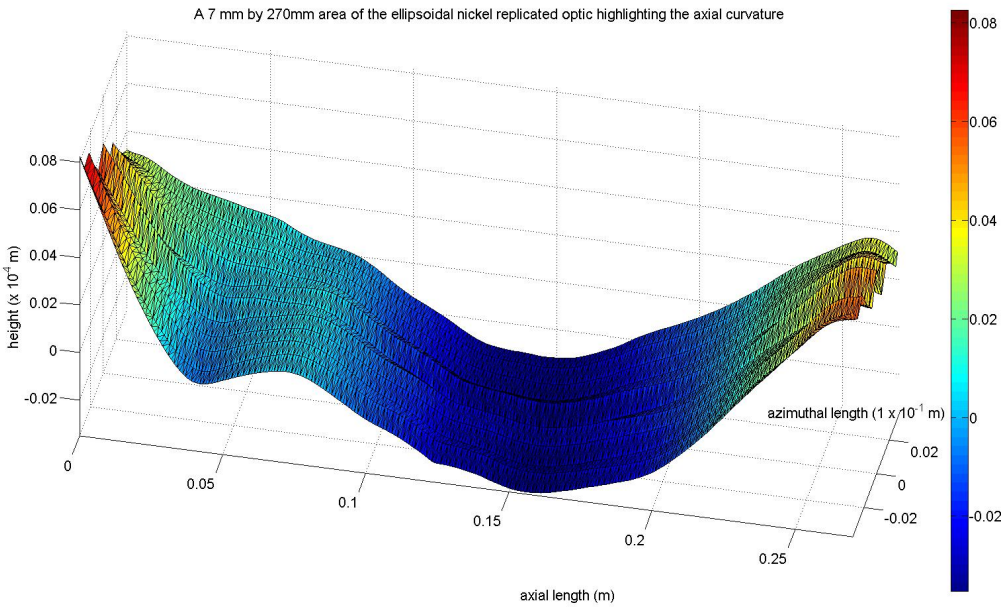

Figure 4.18: A 270mm by 6mm area of second ellipsoidal optic

4.4.5 The outer azimuthal radius of curvature

The outer radius alone was measured for the prototype's optic, as this was to be non-invasive upon the reflective surface and could be completed promptly in-house at UCL to prevent delays to the strict production schedule. The outer radius of curvature was measured by supporting the optic upon the mandrel with optical tissue used to protect the reflective surface of the optic from that of the mandrel. The measurement of the outer radius of curvature not only provided an indication of the form of the prototype's optic, but also provided a map upon which to position the actuators, should the actuators' radius of curvature be known. Figure 4.21 depicts the measured outer RoC against the desired inner RoC and an agreement is observed at the X-ray source end of the optic. However, at the detector end of the optic, the measured radius of curvature is tighter than the required form. This indicates the presence of compressive stress within the optic during electrodeposition; however this is difficult to quantify considering the chemical nature of the variables involved. The measurements of the prototype's optical form highlight that to improve the resolving capability of the optic, actuator adjustments will be required at the detector end of the prototype.

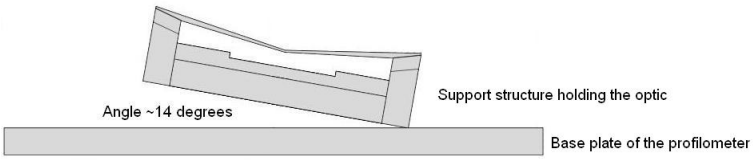

(a) 2D profile of the experimental set-up

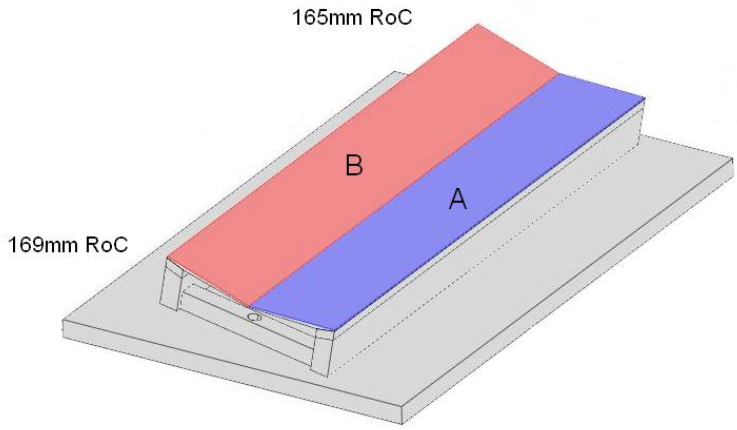

(b) 3D profile of the experimental set-up

Figure 4.19: The experimental set-up of the optic and cradle allowing the measurement of the optic's radius of curvature in two sections, A and B.

4.4.6 Thickness

The thickness of the ellipsoidal shell was measured using a contact digital micrometer with a maximum reach of 2cm. Measurements were taken every 1cm from the edge of the optic to a depth of 2cm. The results were repeated to ensure an accurate respresentation of the measurement area, which was often difficult to define. Figure 4.22 displays the thickness map of the shell in comparison with the FEA data.

The predictions from the FEA data in Section 4.3.2 suggested that there should be a 50% increase in the thickness of the corners in comparison to the centre: the average thickness of the corners was 535μm in comparison to $\sim$350μm in the central measured regions and this provides an increase in thickness of 53% at the corners compared to the centre.

The obvious anomaly in the thickness map is the variation in the thickness from one radius of curvature to the other. It was noted from the FEA data that a 6% increase in thickness was expected at the 169mm radius of curvature in comparison with the 165mm radius of curvature. The

Theoretical		Measured			
Position (mm)	Theoretical ROC (mm)	Position side A	ROC (mm) A	Position side B	ROC (mm) A
4	169.7	4	159.7	4	157.0
18	169.5	18	159.5	18	157.7
38	169.2	38	158.9	38	157.9
58	168.9	58	158.5	58	157.9
78	168.6	78	158.2	78	158.0
98	168.3	98	158.2	93	157.9
118	168.0	118	158.1	118	157.8
138	167.7	138	158.2	138	157.7
158	167.4	158	158.5	158	157.8
178	167.1	178	158.4	178	158.1
203	166.8	203	158.4	202	159.1
218	166.5	218	158.7	218	160.3
238	166.2	238	160.0	238	162.1
258	165.9	258	161.7	258	162.4
278	165.6	278	163.0	278	161.0
288	165.5	288	163.6	288	159.5
296	165.4	296	164.4	296	158.1

Table 4.4: Radius of curvature of the 2^{nd} ellipsoidal optic

measured data indicated the reverse: the 165mm end was significantly thicker than the 169mm end by approximately 38%, and this indicates that current density has not been the dominant effect in the deposition of nickel. It is thought that this variation is probably caused by an asymmetry in the placement of the pump's jets, which had to be repositioned in the tank after the previous plating run, due to the tank being used for alternative applications. Ill placement of these jets could have caused a preferential deposition (i.e. a higher rate) of the nickel upon the top of the mandrel (the 165mm end) in comparison with the bottom of the mandrel.

Comparing the extreme edges of the optic to the FEA can be difficult due to increased localised growths as a result of pitting/nodulation; therefore a comparison of the inner regions provide a

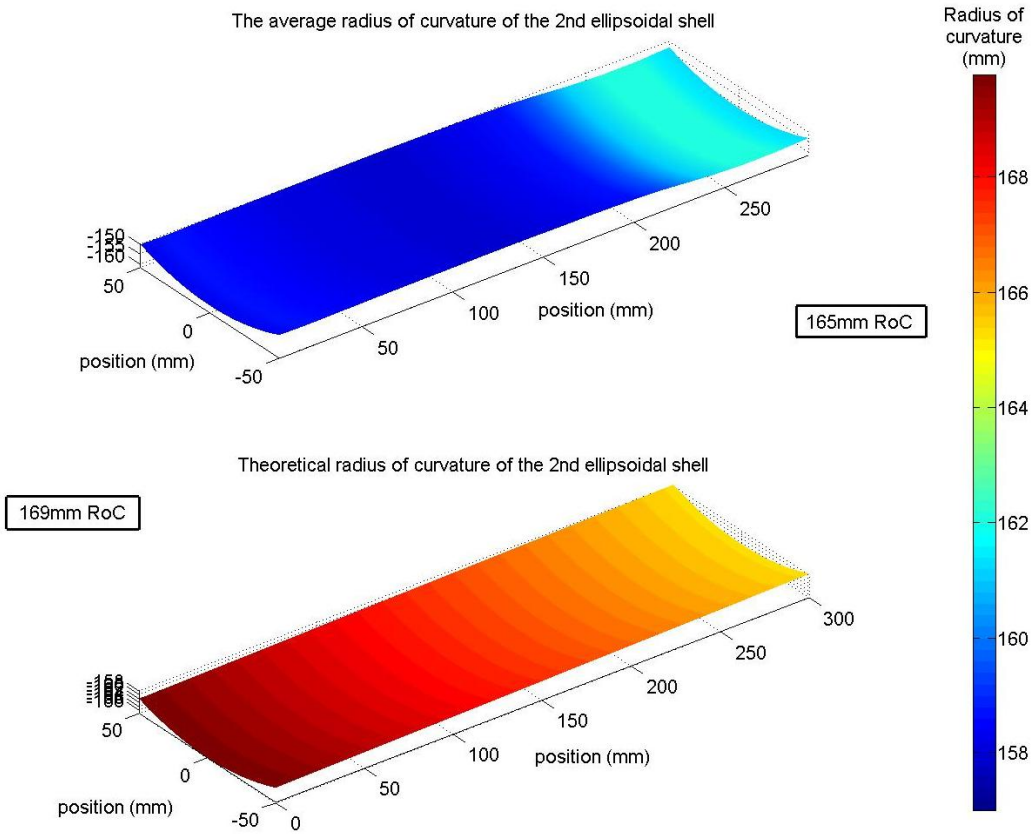

Figure 4.20: The radius of curvature of second ellipsoidal optic

better interpretation of the data. Comparing the inner 1cm and 2cm axial lines to the equivalent in the FEA, a close similarity is observed (Table 4.5). These lines represent the average of the data points at set azimuthal coordinates in the axial direction.

The results indicate that the growth of nickel upon the surface follows the current density upon the mandrel's surface, although other internal factors, such as agitation, dictate the rate of deposition. This is consistent with theory of *diffusion* as outlined in Section 3.2.4. For example, although the 165mm end was thicker than the 169mm end, it still had the thickness variation one would expect for the current density of the area on a global scale.

4.4.7 Optic summary

A comparison of the mandrel and the optic's metrology data clearly demonstrates that the optic's form has not replicated accurately from the mandrel. It is thought that these discrepancies are due to internal compressive stress within the deposited nickel. The surface roughness of the mandrel and

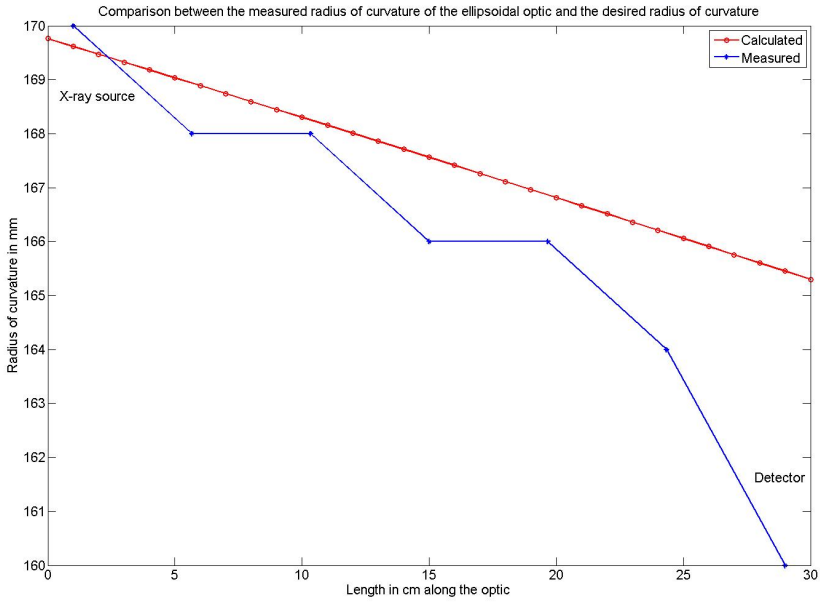

Figure 4.21: The measured outer, and the calculated inner, radius of curvature of the ellipsoidal optic used in the prototype

Line position (mm)	Current density (A/m^2)	Thickness (mm) A
2 cm line	108.5113	376.0323
1 cm line	115.0675	397.2527
8 cm line	108.0313	373.5323
9 cm line	114.6296	392.5323
ratio 2cm/1cm	0.94302	0.94658
ratio 8cm/9cm	0.94244	0.95160
average ratio	0.94273	0.94907

Table 4.5: Comparison between the measured thickness data and that of the FEA data

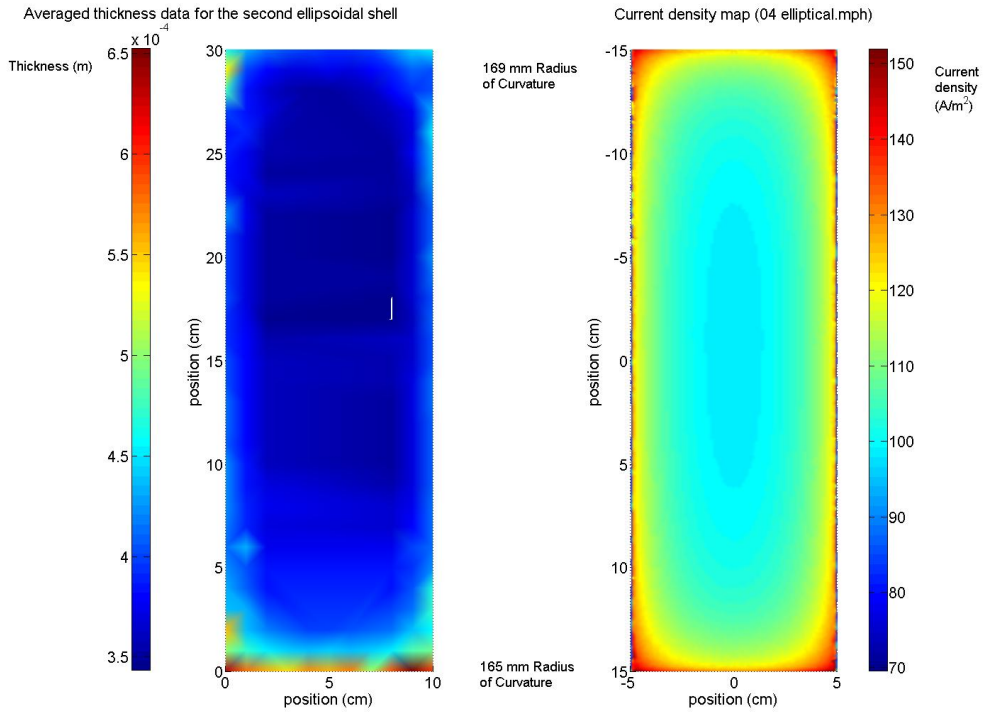

Figure 4.22: The measured thickness of the 2^{nd} ellipsoidal optic and its comparison to the FEA simulated current density map

the optic does appear to be in agreement, though the total number of data samples is in question. The calculation of total integrated scatter suggests that 21% of the incident X-rays would be scattered. Fortunately, this is a major reduction from the cylindrical optic which implied 98% of incident X-rays would be scattered.

The major scratch as detailed in Section 4.2.4 replicated as a peak in the optic and microscope images can be seen in Figure 4.23. The height of these peaks was measured using the Talysurf profilometer and the height varied between 0.2μm to $\sim$30μm. Unfortunately the presence of this peak is unavoidable and it is replicated with each shell, but as mentioned previously this should only produce a localised scatter.

It was noted that the radius of curvature of the optic did not vary as one would expect over the axial length: the optic was tighter at the 169mm end than the 165mm end and the 165mm end was actually approaching the desired radius of curvature. The subsquent optic (Ellipsoidal shell 3) showed a similar tightening effect though the change in radius of curvature varied in accordance with the mandrel (i.e. the 165mm end was tighter than the 169mm end). If the thickness of the

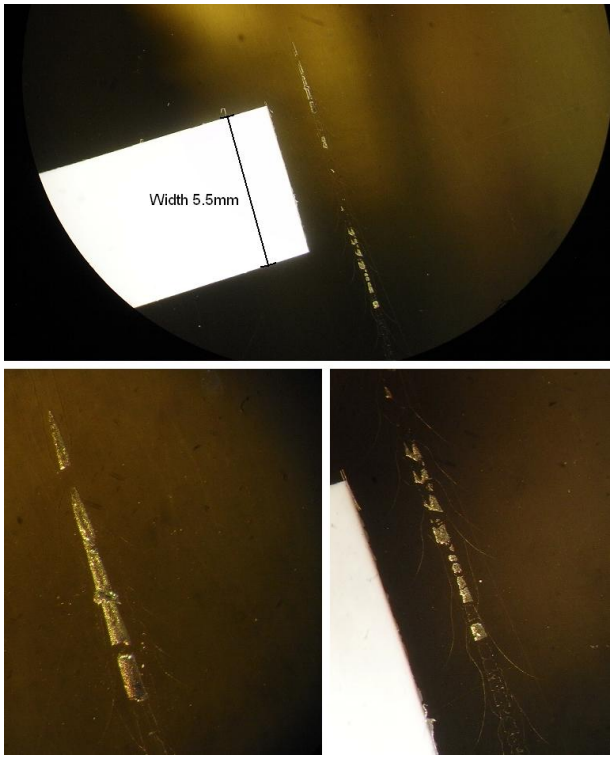

Figure 4.23: Peaks created on the optic's surface caused by the major scratch upon the mandrel

optic is taken in to account, it can be seen that the thicker end of the optic corresponds with the 165mm approaching the correct radius of curvature. It is thought that this thicker distribution of nickel has allowed the optic to retain some of its desired form in comparison with the 169mm end and this in part has led to the experiments to thicken future shells.

A further consideration is the support structure, which has been found to dictate much of the optic's form. This effect can be shown in measurements of the third ellipsoidal shell: it was held in a variety of positions to assess different support points (Figure 4.24). It can be seen from these profile plots that by positioning the optic on two points a dramatically larger axial sag can be obtained from the optic. This leads to the point that due to the flexible nature of the optic, the actual axial displacement is difficult to quantify as it differs according the mounting used. Therefore it should be possible to optimise the mounting to provide a larger axial sag (closer to the 30μm desired), although care would have to be taken to prevent adversly affecting the azimuthal curvature.

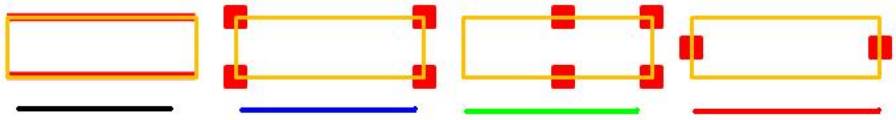

(a) Mounting positions used for the third ellipsoidal optic

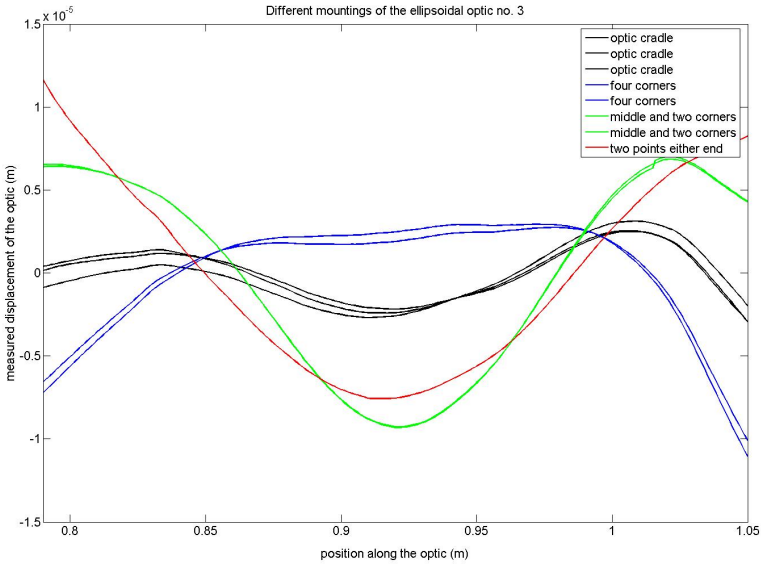

(b) Axial profiles measured for the different positions

Figure 4.24: Measured axial profiles for the different methods of mounting for ellipsoidal shell 3

4.5 Actuator bonding and harnessing

This section outlines the final stages of the prototype development where the actuators were bonded and the wires harnessed to the reverse of the nickel optic. Due to the time constraints some sacrifices in production were made and these will be outlined within the conclusion to this section; however, the primary concern was to complete the prototype system on schedule for delivery to Leicester for X-ray testing in November 2008.

4.5.1 Actuators for the ellipsoidal prototype

Changes were made to the ellipsoidal actuators with repect to the cylindrical prototype's actuators and these included both a morphology change and revision in fabrication methods. As the ellipsoidal prototype is 10cm longer in the axial direction in comparison with the cylindrical prototype the actuators had to be altered accordingly. The dimensions of the ellipsoidal actuators are 29mm in the

axial direction, 32mm in the azimuthal direction and ∼0.2mm thick: these dimensions provided an inter-actuator gap of ∼1mm in either direction. To achieve the desired azimuthal radius of curvature for the varying curvature of the optic, actuators were formed on both the cylindrical former[4] (radius of curvature 0.156m) and an ellipsoidal former (radius of curvature 0.167mm). It was found during production of the actuators for the cylindrical prototype that the radius of curvature of the former was not replicated upon the actuators and generally resulted in a larger radius of curvature than desired. Therefore it was hoped through the use of two formers that the production of the actuators could be completed on time (the use of two formers doubled the University of Birmingham's production ability) to provide a variety of radii which would match the curvature on the reverse of the nickel optic.

Unlike the cylindrical prototype's actuators the wires were not soldered to the electrodes prior to bonding. This was a benefit as problems had been encountered previously due to wires pulling the actuators during curing and the 60 wires becoming tangled making them difficult to harness. Therefore it was decided that the soldering of the actuators would form part of the harnessing phase of the prototype, taking advantage of the fixed position of the actuators upon the surface.

The final modification to the actuator fabrication process involved the cleaning of the actuators in an ultrasonic acetone bath. It was noted in the production of the cylindrical prototype that the acrylic tape did not bond to the actuators; it was later found that this was an effect caused by the oil used in their fabrication. Therefore a cleaning phase was included in the UoB's production scheme and test pieces provided a strong bond with the acrylic tape.

4.5.2 Actuator Bonding

The process for actuator bonding followed the same procedure as outlined in Section 3.6.3 of Chapter 3. The low shrinkage adhesive, EP30 (Masterbond), containing spherical glass beads of diameter 80μm was used as the bonding layer. The glass beads were present to maintain a minimum thickness of glue and thereby to ensure that each actuator's ground electrode was not in contact with the nickel optic.

Building on the experience gained in the production of the cylindrical prototype, the glue-bead suspension was produced three times, allowing the 30 actuators to be bonded in groups of 10 with a new glue batch for each group. This prevented the viscosity of the glue increasing over time due to its limited work life, a problem which had been encountered in the cylindrical prototype. Again the actuators were bonded by hand and care taken to ensure an even gap of 1mm between each of the

[4]The formers used in the production of the curved actuators were outlined in Chapter 3

actuators (Figure 4.25).

Figure 4.25: The bonding of the actuators in groups of 10 using the EP30-glass bead suspension.

4.5.3 Problems encountered

The primary problem encountered was the mismatch in radius of curvature between the actuators and the nickel optic.

As mentioned in Section 4.4 the outer radius of curvature of the optic was typically tighter than that which was required and previous experience had taught us that the actuators do not replicate off the zirconia former with the desired curvature: it was this mismatch in curvatures which led to the major problem. During bonding, time was not available to measure the radius of curvature of the actuators, therefore the actuators were positioned crudely according to which former they had been produced on (i.e. the actuators fabricated upon the cylindrical former were positioned at the 165mm RoC and those formed on the ellipsoidal former positioned upon the 169mm RoC end). Therefore the optimum positioning of the actuators could not take place and due to a limited supply of actuators (33 actuators for 30 positions) one could not be critically selective. This led to a poor fit between many of the actuators and the optic. This mismatch caused gaps in an otherwise uniform glue layer and these had to be accommodated by excess glue, therefore leading to an increase in the glue layer thickness. Filling the gaps between the actuators and the nickel shell was paramount and stemmed from two individual requirements. First, to benefit from the full displacement generated by the actuator under a potential difference, the total active area of the actuator had to be in contact with the glue layer. Second, due to the vacuum environment of the X-ray TTF, any air pockets

would outgas under vacuum and could potentially damage the prototype.

An adverse effect caused by the requirement for additional glue was in the positioning of the actuators accurately upon the reverse of the nickel optic. Due to the low viscosity of the glue, the actuators float upon the glue layer and due to the curved nature of the optic the actuators would readily shift position under gravity. As such, positioning the actuators with a uniform inter-actuator gap proved difficult to guarantee. However, these small positioning errors were unlikely greatly to affect the global influence function generated by all the actuators upon the optic.

4.5.4 Harnessing

The harnessing of the actuators' wires to the 37-D connector was undertaken by GW from MSSL. The actuators had been allowed to cure for approximately 24 hours prior to harnessing and this cure time provided 85% of the total glue strength[5]. Unlike the cylindrical prototype the wires were first harnessed to the connector and then soldered to the actuators. Indium solder was used to fix the 100μm diameter enamelled wires to the actuators' electrodes, due to its low melting point resulting in its ability to bond to the vacuum deposited gold layer.

The 60 wires were then fixed to the reverse of the prototype using the vacuum compatible acrylic tape and as the actuators had been thoroughly cleaned prior to bonding, the acrylic tape was able to provide a strong adhesion. The harnessed actuators are depicted in Figure 4.26(a) and the 60 wires can be seen positioned in two wire bundles that traverse the axial length of the optic to the 37-D connector.

4.5.5 The completed prototype

The ellipsoidal prototype was completed at the end of October ready for transit to Leicester X-ray beam line in early November (Figure 4.26(b) Atkins *et al.* (2009*b*)). Although no metrology of the completed prototype was performed prior to the X-ray tests, the axial length of the prototype was investigated upon the LTP in March 2009. These measurements were undertaken while the prototype was disconnected from the power supply and this is a condition that proves relevant in Section 5.3.3. Several LTP measurements were taken along the length of the prototype and the average of these can be seen in Figure 4.27. The measurement indicates two glue related features: first, the axial profile is $\sim$50μm in magnitude, assuming consistency with the optic mentioned in Section 4.4.3; this is a factor of 5 increase in magnitude. It is thought that this increase is an

[5] As stated by the EP30 - technical data sheet (`http://www.masterbond.com/tds/ep30.html`)

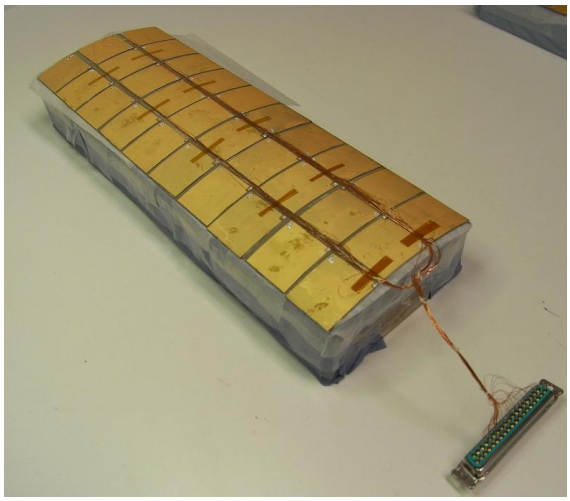

(a) The harnessed actuators

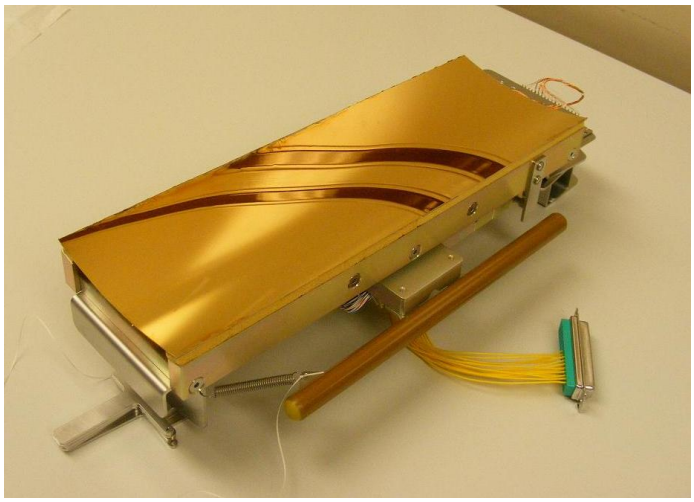

(b) The completed prototype resting upon the support structure

Figure 4.26: The final stage of the prototype fabrication was: **(a)** the harnessing of the actuators and **(b)** the completed prototype awaiting integration within the X-ray test tunnel facility.

effect caused by the adhesive layer, which has contracted as a result of shrinkage during curing. The second feature is the print-through of the actuators' form and this is evident as small bumps upon the LTP profile. Print-through is a highly undesirable effect as the distortion is on a spatial frequency scale that cannot be corrected for with the actuators.

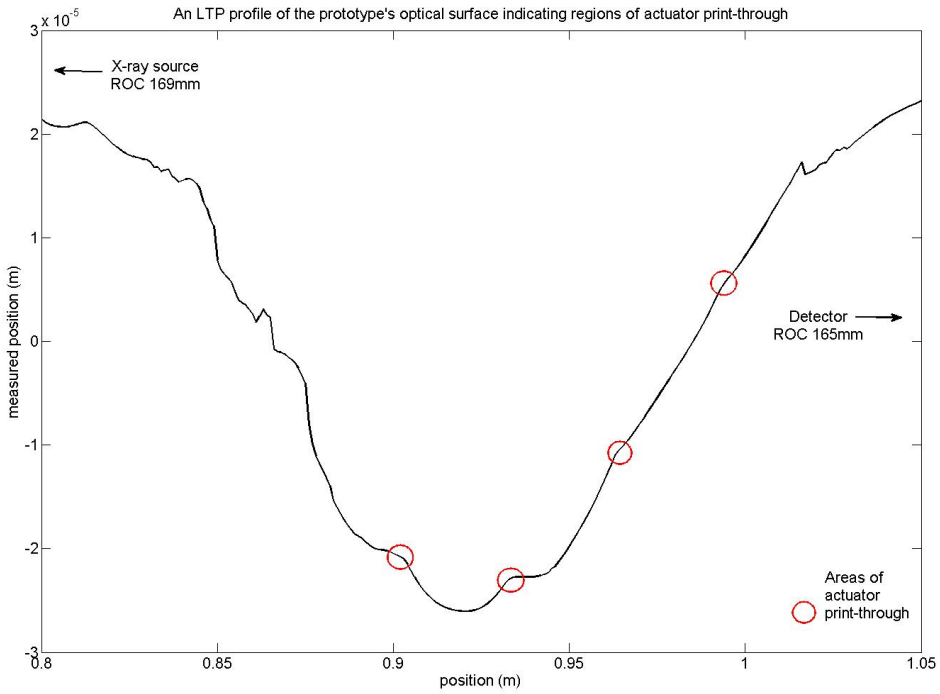

Figure 4.27: The axial curvature of the prototype

No additional metrology has been performed upon the prototype, for example: thickness measurements or azimuthal radius of curvature since this is a consequence of a desire to protect the reflective surface of the optic. However from the bank of data which has been collected within this chapter a prediction of the form of the prototype has been established.

Although an emphasis on time constraints has been regulary voiced throughout, efforts were made not to rush its production and, as such, care was taken. Prior to commencing the X-ray tests, the areas of concern for the prototype were primarily in regard to the optic's ability to reflect X-rays without a dominant scatter effect and if there was the presence of air pockets within the glue layer.

4.6 Chapter summary

This chapter has outlined the production of the prototype from the design of the mandrel to the bonding and harnessing of the actuators, which completed the prototype. This work was done on a tight time constraint, due to a specific test date available at the University of Leicester's X-ray beamline facility. In Chapter 5 the control of the actuators shall be outlined, both in terms of hardware and software, and the morphology and magnitude of the actuators' influence functions shall be discussed.

CHAPTER 5

PROTOTYPE CONTROL AND ACTUATOR INFLUENCE FUNCTIONS

Chapter 5 is divided into two components; Sections 5.1 and 5.2 discuss the hardware and the software which operate the prototype, and a description of the software from a user's perspective will be given. Section 5.3 describes the influence functions of the prototype as measured on the LTP and their comparisons with FEA models, therefore providing an understanding of the prototype's operation prior to the X-ray tests. This chapter has greatly benefited from the work from other members of the SXO consortium, in particular Section 5.2 and credit will be stated where appropriate.

5.1 Actuator hardware

The prototype control hardware was orginally purchased by SJT for the proof of concept SXO study (Doel *et al.* 2006) and it forms the physical link between the prototype (as described in Chapter 4) and the user/X-ray facilty. The hardware has the following two components (a graphical representation can be seen in Figure 5.1):

- 32 channel voltage output PCI card supplied by National Instruments (voltage range 0 - 10V)
- High voltage amplifier supplied by Starpoint (voltage amplification factor $\sim$20)

All 30 actuators are controlled via a desktop computer through the 32 channel voltage output card. To allow the piezoelectric material to expand and contract and therefore provide displacement

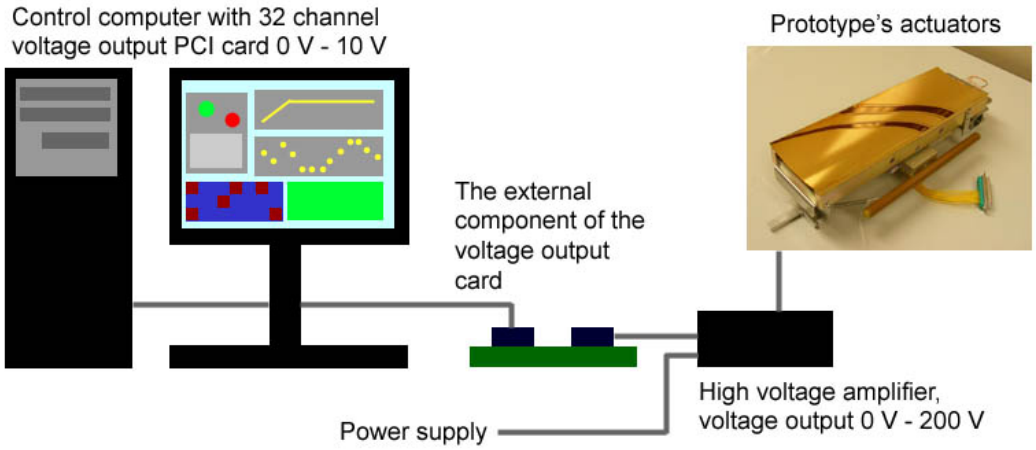

Figure 5.1: A schematic of the prototype's hardware

in a positive and negative direction, the common actuator ground is set to 5V, therefore allowing a potential difference range of -5V and 5V. To obtain a larger voltage range, each actuator output channel is amplified by a factor of ∼20 to provide an output voltage range of -100 V to 100 V. In total 31 out of the total 32 channels are used, 30 for the actuators' driving voltage and 1 for the common ground.

Each amplifier channel is connected directly to the actuators' electrodes, therefore considerations such as amplifier noise and variations in the amplifier gain on each of the channels need to be addressed to provide a realiable understanding of the prototype system.

5.1.1 Amplifier noise/ power supply stability

In this instant, the amplifier noise is defined to be the variation in voltage output over time and it was measured for each channel using a digital oscilloscope. The data was retrieved in `.csv` format via a floppy disk and then analysed using MATLAB. The first measurements investigated each channel in turn for a 10 second duration at 10V, an example of the oscilloscope display can be seen in Figure 5.2. The results from each channel can be seen in Table 5.1 and a statistical representation of the data is shown in Figure 5.3. An analysis of the data indicates a ∼5mV rms variation in voltage over 10s: using FEA simulations and LTP data (Section 5.3) this variation implies a ∼1nm change in magnitude.

An anomaly recorded from this first set of data was the unreactive nature of channel `AO16`.

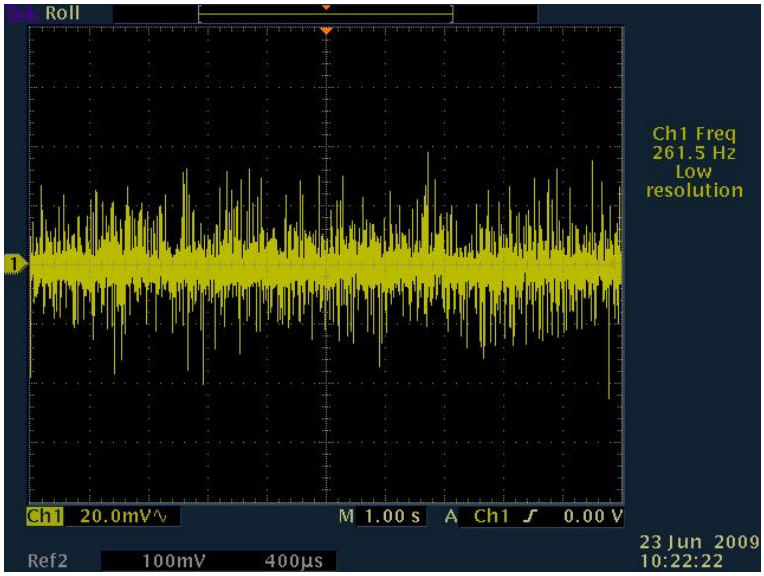

Figure 5.2: An example of the noise generated upon channel AO4 for a 10 second duration, the scale in the vertical direction is one tick equals 20mV

The channel did not provide any voltage output when tested, indicating a fault with the hardware. Fortunately this fault did not develop until after the X-ray tests. Independent measurements taken in October and December confirmed `AO16`'s operation and it was not until March 2009 that the fault became apparent.

A second set of measurements was taken to determine whether the noise varied as a function of voltage. The odd numbered channels were set to 100V and the voltage output was recorded for a 10s period: only the odd number channels were investigated in order to conserve time. The results are presented in Table 5.2 and Figure 5.4. The data indicates ∼4.6mV rms variation on each of the odd channels at 100V: this is consistent with the results obtained at 10V, implying that the noise is not a function of voltage, but rather an inherent characteristic of the prototype's hardware.

A point of interest was the presence of the mains frequency at 50Hz within the channel outputs: such an artefact would appear upon the timescale of 20ms. The hardware was connected to the mains power supply with the mains power turned on but the amplifier turned off, the 50Hz mains frequency is clearly evident, as shown in Figure 5.5(a). When the amplifier is turned on the 50Hz signal is removed and no longer an output feature, as demonstrated in Figure 5.5(b).

5.1.2 Amplifier gain

The amplifier gain is defined as the factor by which the voltage output from a single channel has been multiplied by the high voltage amplifier. The variation in amplifier gain across the output

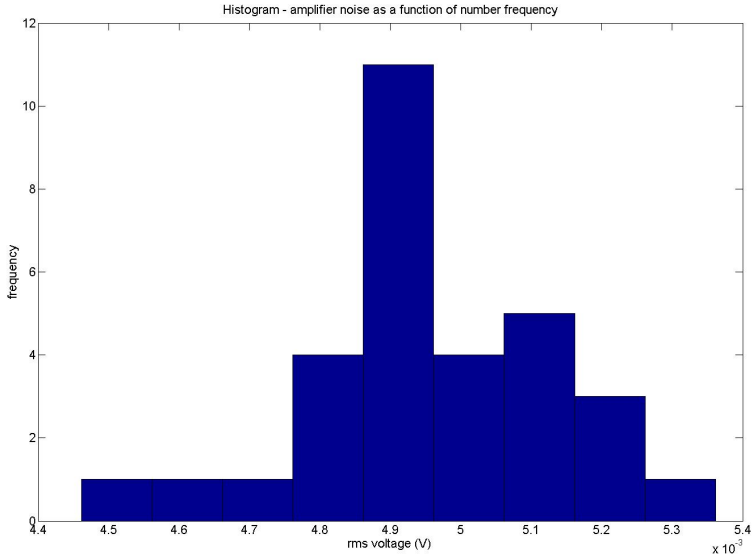

Figure 5.3: A histogram displaying the rms noise as a function of number frequency at 10V

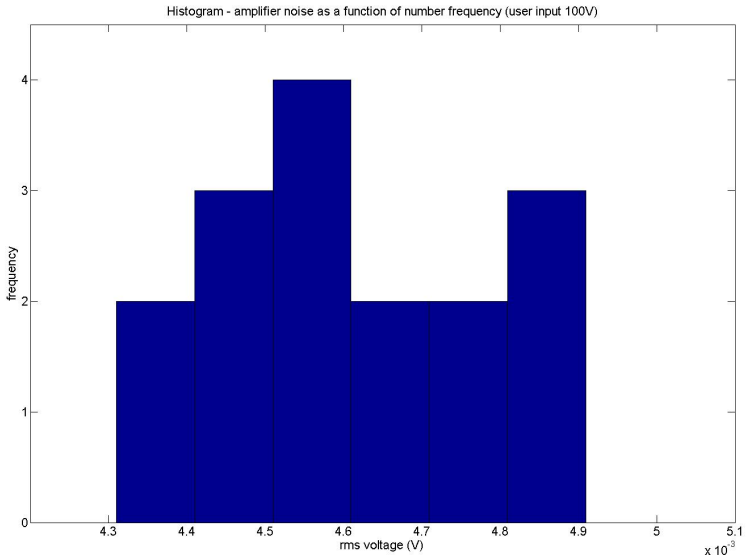

Figure 5.4: A histogram displaying the rms noise as a function of number frequency at 100V

Channel no.[a]	V	V rms	Channel no.	V	V rms
AO00	9.89	0.00511	AO16	`dead`	`dead`
AO01	9.90	0.00487	AO17	10.22	0.00489
AO02	9.75	0.00525	AO18	9.98	0.00494
AO03	9.64	0.00513	AO19	10.10	0.00486
AO04	9.91	0.00529	AO20	10.02	0.00482
AO05	9.77	0.00515	AO21	9.82	0.00488
AO06	9.20	0.00518	AO22	9.88	0.00498
AO07	10.30	0.00500	AO23	9.77	0.00498
AO08	10.24	0.00511	AO24	9.92	0.00483
AO09	9.38	0.00511	AO25	9.97	0.00493
AO10	10.20	0.00495	AO26	10.02	0.00500
AO11	10.00	0.00524	AO27	9.66	0.00492
AO12	10.01	0.00451	AO28	10.01	0.00492
AO13	9.59	0.00459	AO29	10.07	0.00484
AO14	10.08	0.00470	AO30	10.28	0.00495
AO15	9.88	0.00495	AO31	9.84	0.00495

Table 5.1: The power supply stability with each channel operated at 10V

[1]

channels is clearly evident from the output voltage in Tables 5.1 and 5.2, where the user input voltage was 10V. This variation in output can be accommodated for within the actuator control system, by utilising a multiplying factor which compensates for the effect at the initial user input.

Channel	Voltage V	rms Voltage	Channel	Voltage V	rms Voltage
AO01	99.2	0.004702	AO17	99.1	0.004605
AO03	99.6	0.004868	AO19	98.7	0.004395
AO05	98.8	0.004731	AO21	99.4	0.004844
AO07	99.8	0.004705	AO23	98.3	0.004600
AO09	98.1	0.004745	AO25	99.5	0.004360
AO11	99.4	0.004835	AO27	99.1	0.004438
AO13	99.8	0.004525	AO29	98.4	0.004454
AO15	99.8	0.004533	AO31	98.7	0.004435
Average voltage rms			0.00461		
Max voltage rms			0.00487		
Min voltage rms			0.00436		

Table 5.2: The power supply stability with the odd channels operated at 100V

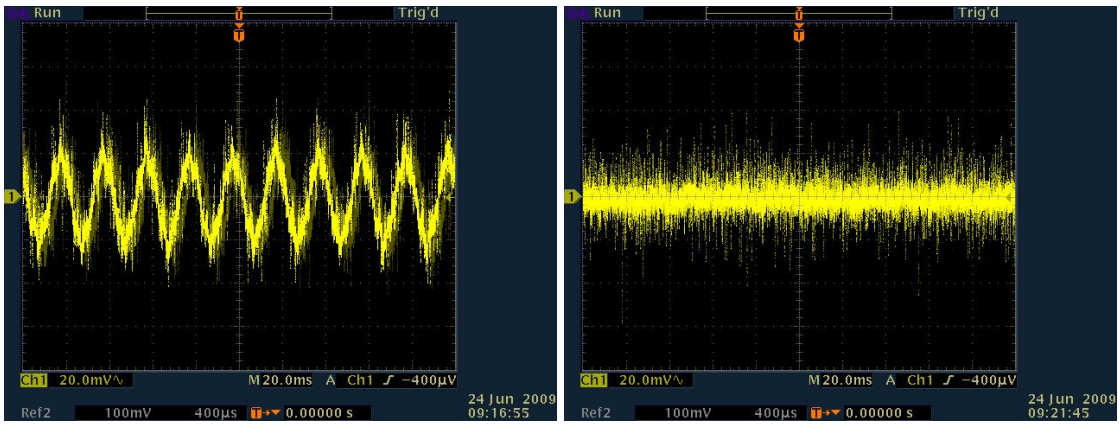

(a) Power supply turned off (b) Power supply turned on

Figure 5.5: The effect of the 50Hz mains frequency power supply

5.2 Software - Actuator control

The actuator control software and graphical user interface (GUI) were developed using LabVIEW, which is National Instrument's complementary software to its hardware. Therefore the design of the software significantly benefited from an archive of example code, which formed the foundation of the prototype's software. The majority of the software development was undertaken by HCW, with input from both UoB and the author. LabVIEW generates a virtual instrument (VI) GUI and the 'programming' is achieved through the linking of different operational blocks with 'wires' in a block diagram. This section will outline the functionality of the VI from a user's perspective, without an indepth discussion into the underlying program.

5.2.1 Requirements of the actuator control software

The software is built upon the user/hardware requirements for the prototype's operation and these are outlined below:

- An ability to compensate for the effect of piezoelectric hysteresis
- To provide an interface with the external optimisation routine in order to set the actuators to the correct voltage pattern.
- To compensate for the variation in channel amplifier gain
- To regulate the approach of each channel to their prescribed voltage
- An ability to operate continuously over a time period without user intervention

As mentioned in Chapter 2, the effect of hysteresis has to be removed from the actuators whilst optimising the detected image. Fortunately, due to the consistency of the hysteresis loop over time, hysteresis can be compensated for by adding a reference voltage in the operational procedure. In relation to Figure 5.6, the reference voltage (V_{ref}) is the maximum voltage of the system and its use within the operational routine is to always ensure a standard point from which to travel to the desired output voltage. Starting from V_{ref}, the output voltage (V_{out}) is approached via the solid line and the displacement per voltage does not deviate from this line. When a new voltage is required, the system is first taken to V_{ref} along one of the dashed lines and then the new output voltage can be selected. By using V_{ref}, only one side of the hysteresis loop is used for setting the output voltage and therefore this removes the loop's variation in displacement per voltage: an example of this process in operation can be seen in Figure 5.7.

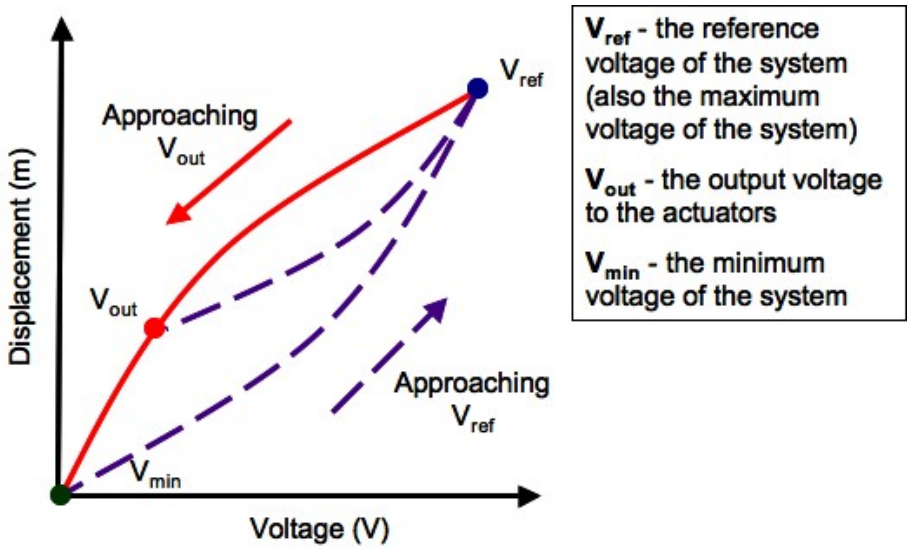

Figure 5.6: An example of the hysteresis loop and use of the the reference voltage

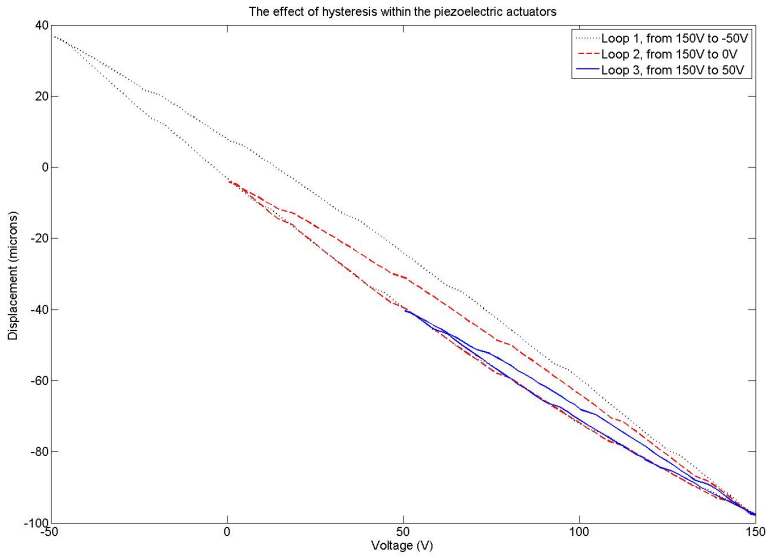

Figure 5.7: A practical example of the hysteresis and the use of the reference voltage

The optimisation routine determines the voltage patterns to be applied to the prototype: as these patterns are a function of an external computer and the counts obtained from the X-ray detector, a suitable link had to be established. The simplest approach was through the use of a `.txt` file with a standardised notation for the actuator configuration, therefore the input file represents Actuators 1 - 30 as a column vector with the actuators in numerical order.

The condition to approach the voltage gradually over a minute rather than to have an immediate jump to the desired voltage came from discussions with the UoB, who suggested that for better consistency in results (i.e. displacement per voltage) the desired output voltage should be approached slowly. The requirement for continual operation without user intervention stems from envisaged X-ray tests which may be carried out over many hours and the continual presence of an operator in these circumstances would not be an optimum use of time. With these conditions in mind, the software was developed and is discussed in the following section.

5.2.2 The graphical user interface of the prototype's control software

The actuator control software was developed by HCW and the graphical user interface (GUI) can be seen in Figure 5.8. The following is an explanation of the GUI's components and the numerical identification is in reference to this figure. In addition, the future numerical references to controls etc. within this chapter are also in reference to this figure.

- `Start` - The `run` command is operated using the arrow button; it initalises the VI and continues to operate until user intervention.
- `Stop` - The red circle stops the VI and rests the VI clock back to zero

1. `Secondary controls tab` - provides access to the secondary controls, such as: amplifier gain input, duration to desired voltage etc. (these shall be discussed in Figure 5.9).
2. `Actuator selector control` - cycles through the actuators 1 - 30 allowing their real time output to be displayed in `Plot 9`; in the figure Actuator 4 is selected.
3. `Finish indicator` - when the indicator is highlighted this implies that the actuators have reached their designated voltages; when dull the actuators are in transistion between voltage inputs
4. `Go to zero control` - quickly sends all the actuators to zero at the end of a session

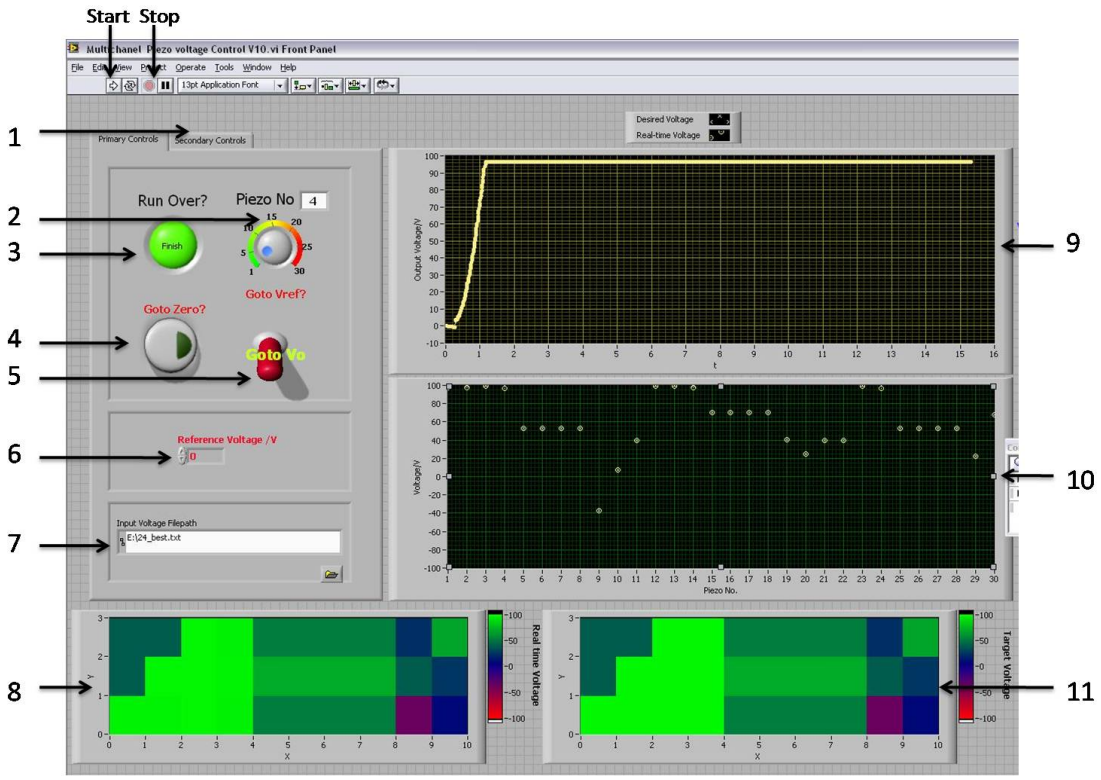

Figure 5.8: The user interface of the virtual instrument as developed by HCW.

5. `V`$_{out}$/`V`$_{ref}$ `control` - allows the operator to switch between the input file from the optimisation routine and the reference voltage V$_{ref}$.

6. `V`$_{ref}$ `input` - the reference voltage input is typically the maximum voltage of the system; however, when the software is first operated it is set to 0V.

7. `File Input` - allows the operator to use an external `.txt` input file for the voltage patterns from the optimisation routine.

8. `Real-time colour plot` - a plot depicting the real time voltage experienced by the actuators. Each square represents an actuator and the colour, which varies with time, represents the voltage, Actuator 1 is at coordinates (0,0) and Actuator 30 is at (10,3).

9. `Single actuator plot` - Real time voltage as a function of time for a single actuator as determined by `control 2` (in this example Actuator 4 is shown).

10. `Real time plot` - A real time plot depicting each actuator with its target and real time voltage; when the two markers are superimposed then the actuators have obtained their target voltage.

11. `Target plot` - A voltage plot highlighting the target voltages for each of the actuators, i.e. `plot 8` starts at a reference voltage and then over a minute turns into `plot 11`.

5.2.3 Operation of the virtual instrument graphical user interface

The operation of the prototype requires four stages as outlined below and a thorough description is provided in Figures 5.9 to 5.12.

1. Initiation (Figure 5.9) - This prepares the software for the session, in particular it allows the operator to select such variables as the time taken to reach the desired voltage and the maximum and minimum voltages of the system (i.e. the secondary controls). At the end of the stage all the actuators are set to 0V.

2. Reference voltage (Figure 5.10) - This stage sets all the actuators to the reference voltage V_{ref}, providing the point from which the desired output voltage is set.

3. Voltage pattern input (Figure 5.11) - At this stage the desired voltage (V_{out}) upon the actuators is set and this is determined from the voltage input file.

4. Finish (Figure 5.12) - This final stage sets all the actuators quickly to zero at the end of a session

Between each of the stages outlined above the `start` and `stop` commands are used. When the user interfaces with the program the `stop` command is active; however when the user sends the actuators to their desired voltages the `start` command is used and when new voltages are required the `stop` command is first used prior to the user's input. The importance of this stop-start routine is to set the software's iteration back to zero, which is needed to regulate the actuators' approach to their required voltages.

When operated within the X-ray facility, stages 2 and 3 will be repeated depending on the number of voltage patterns that can be achieved during that working day. The time taken therefore to change the actuators from one pattern to another is the time taken to perform stages 2 and 3, which is approximately 2 minutes.

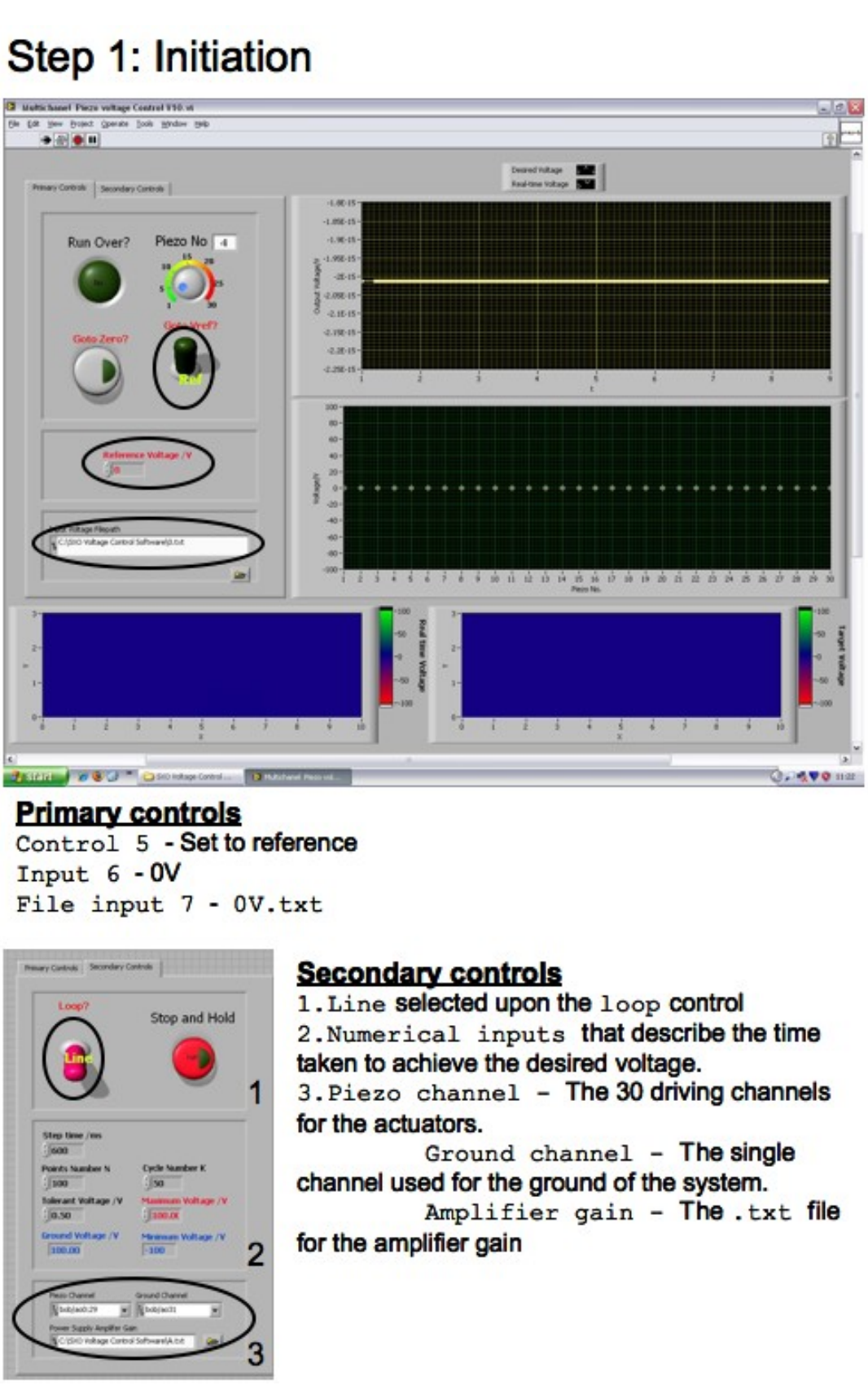

Figure 5.9: Step 1: Initiation

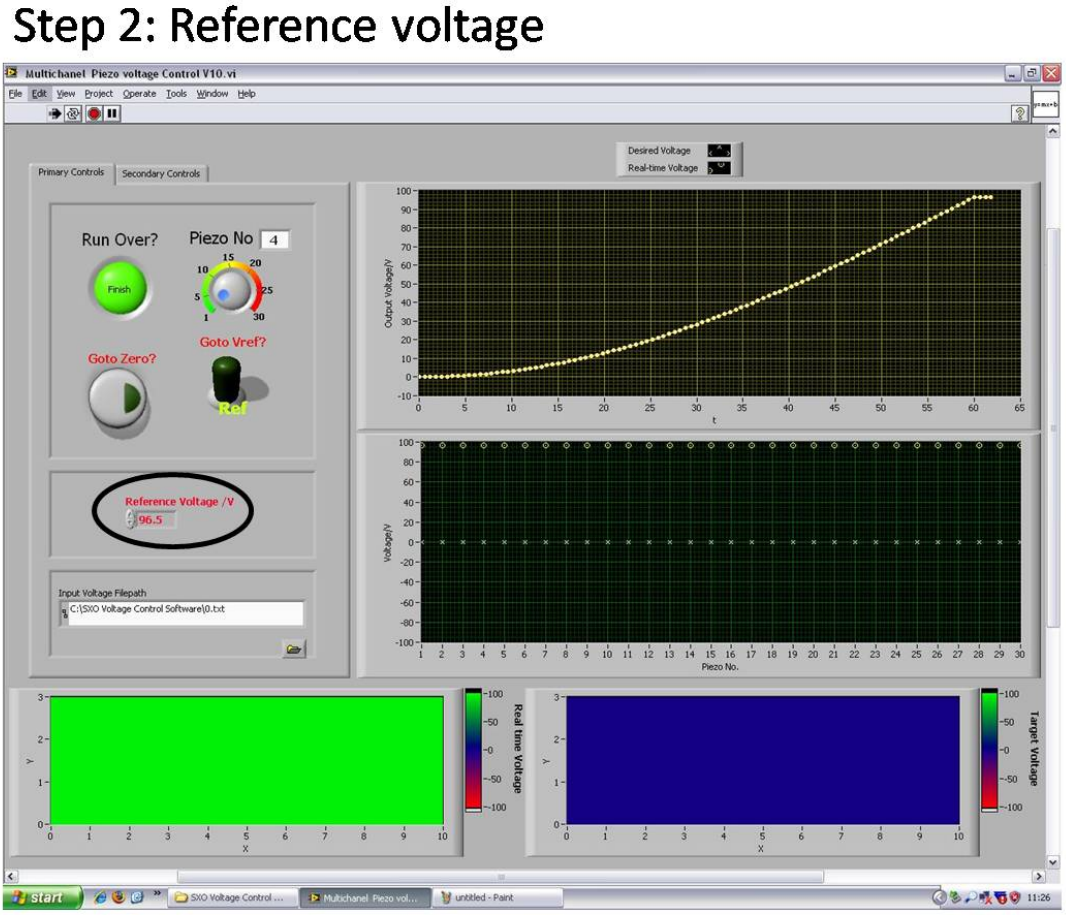

Primary controls

Input 6 – **100V (the GUI caps the value at 96.5V)**

Figure 5.10: Step 2: Reference voltage

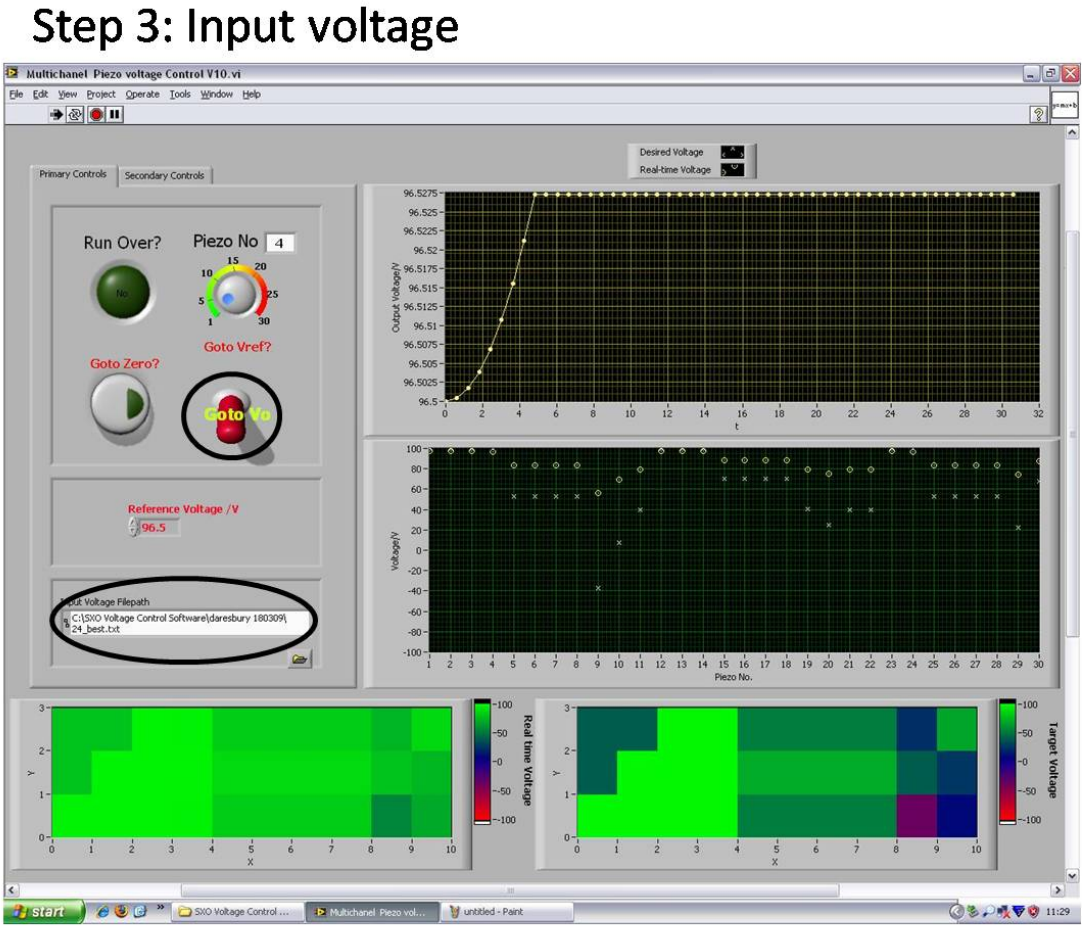

Primary controls

`Control 5` - **Set to** `Vo`

`File input 7` – **the desired voltage input pattern** ***filename*** `.txt`

Figure 5.11: Step 3: Input voltage

Figure 5.12: Step 4: Finish

5.2.4 Summary of the prototype's hardware and software

In Sections 5.1 and 5.2 the prototype's hardware and software have been discussed respectively. Considerations on the hardwares have been described, in particular in relation to the high voltage amplifier, where factors such as the amplifier noise and gain have been characterised. The software has been presented from a user's perspective introducing the requirements of the software and how the software is operated to set the actuators to their desired voltage pattern.

5.3 Prototype morphology and actuator influence functions

This final section in Chapter 5 describes influence functions generated by the prototype in a 1D format and it provides an indication of the physical form of the function which would not be otherwise visible in the detected X-ray images. The 1D profiles were obtained using the LTP at the DL (under the supervision of AS) in December 2008 (directly after the X-ray tests) and in March 2009 (a follow-up study). The LTP measurements are compared against FEA data and provide encouraging similarities. This section will begin with a discussion of the FEA model and then continue with the 1D profiles of the LTP data.

5.3.1 The finite element analysis model of the ellipsoidal prototype

Prior to discussing the metrology data obtained from the LTP it would be prudent to first provide an overview of the FEA model against which the LTP data was compared. The FEA model decribed is a simplification of the physical system, with the prototype modelled as a cylindrical rather than an ellipsoidal segment and the thickness of each component uniform. Though the cylindrical form does not represent curvature in the axial direction, it does allow the implementation of a cylindrical coordinate system that correctly models the piezoelectric properties in the azimuthal direction. This was considered to be a fair trade-off when considering the slight variation from a conic in the axial direction and the benefits obtained using the cylindrical coordinate system.

The FEA model, as shown in Figure 5.13, was comprised of three elements: the optic, the adhesive and the actuators. The dimensions of these components are outlined in Table 5.4 and all are a cylindrical approximation. The thickness of each of these components has been estimated and assumed to be uniform. As mentioned in Chapter 4 the thickness of the glue layer under each actuator and the thickness of the optical component are not uniform and the FEA model will not simulate the influence functions perfectly. The choice of 0.5mm was taken for the adhesive

	Optic	Adhesive	Actuators
axial length (m)	0.3	0.029	0.029
azimuthal length (m)	0.1	0.032	0.032
average radius of curvature (m)	0.1677	0.01682	0.01683
thickness (mm)	0.4	0.5	0.2
material	nickel	polyimide	PZT-5H

Table 5.4: The components of the FEA model describing the prototype system in terms of dimension.

thickness as it represents a mean value of the predicted range and this is based upon the actuator-optic curvature mismatch.

Boundary conditions proved to be an area of concern; in reality the prototype rests unconstrained upon its support structure. However, within FEA, boundary conditions have to be applied to provide the model a point(s) to react against. Therefore two sets of boundary conditions were used within the model; the first set fixed the four corners in x, y and z and the second set fixed at two points, separated by 300mm located down the centre of the axial length in x, y and z. Therefore the final FEA representation is the averaged version of these two data sets (Figure 5.13).

5.3.2 FEA model considerations

It has been established that over simplifications exist within the FEA model and in particular with regard to the adhesive thickness. The thickness is assumed to be uniform at 0.5mm; however, the actual range could be from 0.1mm (the absolute minimum due to the thickness enforcement via the spacing beads) to 1mm. Two additional models were created to observe the variation in displacement with adhesive thickness and the results can be seen in Figure 5.14. In each of the models 10V was applied to Actuator 15 and identical boundary conditions were applied. The 1D profile representing the axial centre of the prototype is displayed and variations in displacement are apparent between the models. There is a $\sim 0.5 \mu$m difference between the 1mm and 0.1mm case and although 1mm case is a worst case scenario the range in displacement provides an error margin for the FEA and LTP fitting.

Both LTP and FEA data represent the axial profile of the prototype and it assumes that the axial centre line as defined by the FEA model is identical to that which is measured. In reality it is

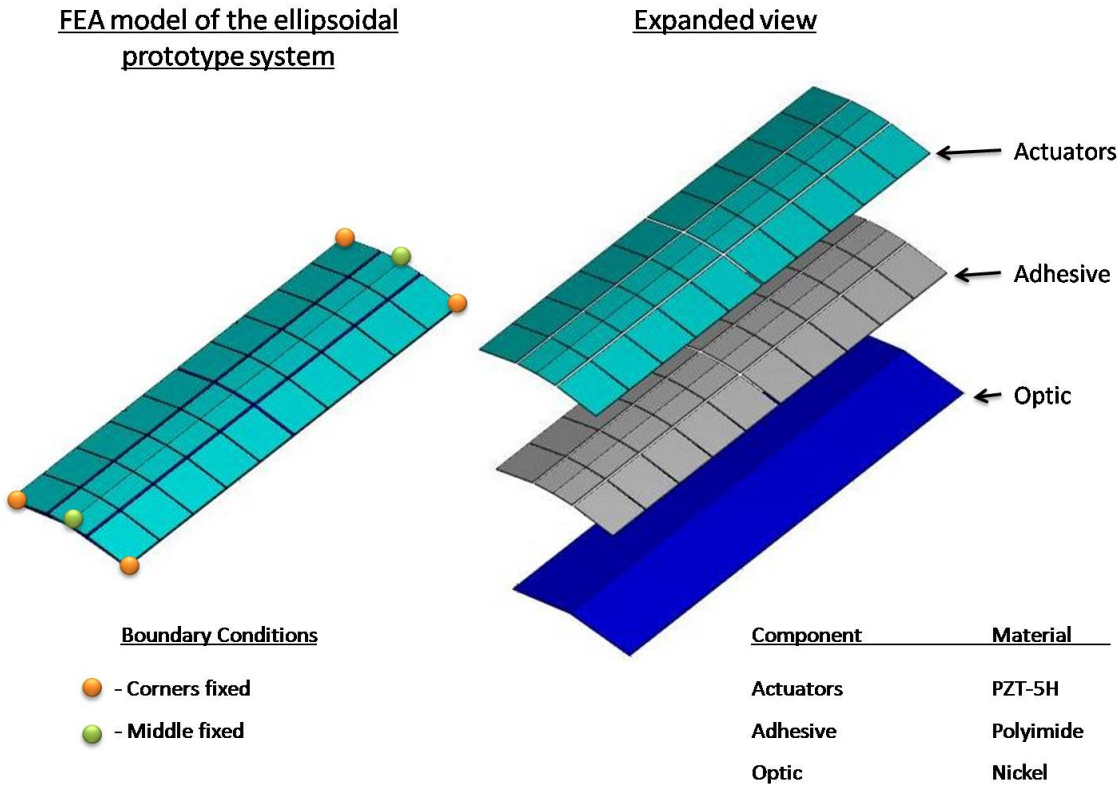

Figure 5.13: The FEA representation of the ellipsoidal prototype system

unlikely that the LTP will be completely in line with the FEA and as such there will be a difference in displacement. Figure 5.15 displays a 1D azimuthal trace across Actuator 15 at 10V (adhesive thickness 0.5mm) and it highlights how the magnitude of displacement decreases with increasing distance from the centre of the actuator. If it is assumed that the prototype can be aligned to the LTP to within 1-2mm, this would result in variations in the order of 0.01μm which is less than a 1% error. With such small variations in the azimuthal direction, exact positioning of the prototype will not be the dominant concern when comparing the two forms of data. However, care is required to keep the positioning within a 1-2mm error margin.

5.3.3 Axial LTP measurements - zero volts

These first measurements were used to investigate the subtle difference between having the power supply turned on or off and its effect upon the axial profile of the prototype. The axial profile when the power supply was turned off has been shown previously in Figure 4.27 and in this case the actuators can be considered as 'dormant' as no current is flowing in the system. However, when

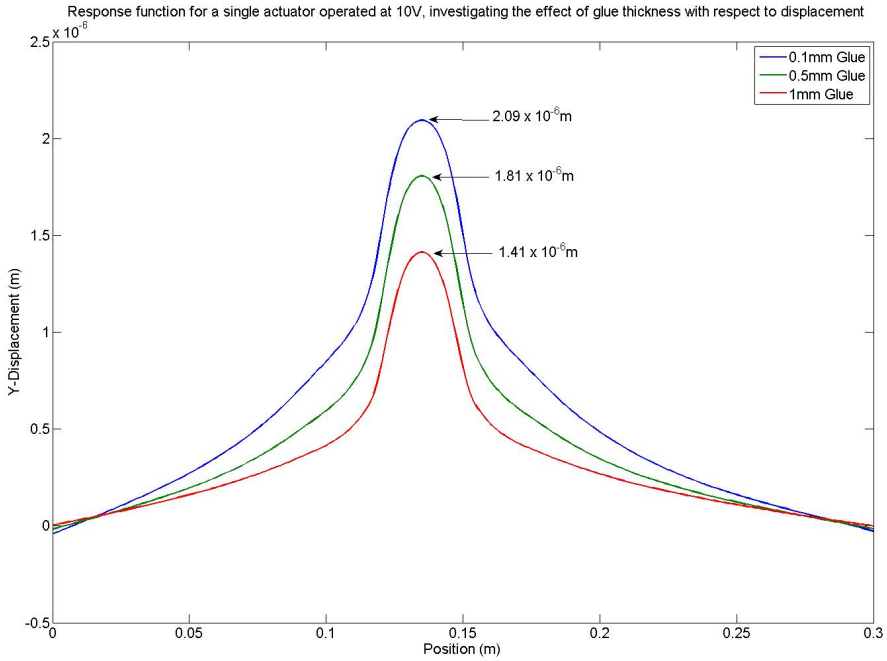

Figure 5.14: Displacement as a function of adhesive thickness with Actuator 15 set to 10V

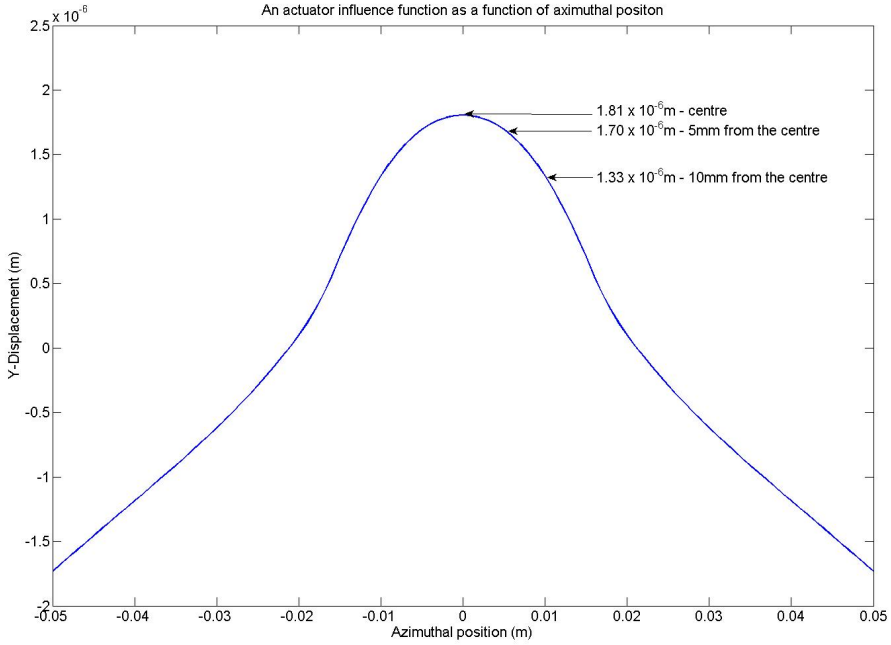

Figure 5.15: A 1D azimuthal profile of the of Actuator 15 at 10V, indicating the decrease in displacement with distance from the actuator central point

the power supply is turned on (the actuators can be considered as 'active') and the voltage on each channels is set to zero, there is actually a current flowing in each of the wires to provide 100V on each of the actuators' electrodes, resulting in a potential difference of zero volts. Considering the electrical difference between each case, a variation in the axial profile of the prototype would be expected.

Figure 5.16 displays a comparison between the two sets of power-on zero volts data taken in December 2008 and March 2009. As with the power-off, areas of actuator print-through are clearly visible; however, the axial sag has been reduced, from $\sim 50\mu$m (Figure 4.27) when the power is off, to $\sim 25\mu$m when the power is on. Therefore, allowing the actuators to exist in an active mode has resulted in a flattening of the prototype axial profile; in fact the axial sag is now closer to the desired form of $\sim 33\mu$m of the original optic prescription. The data taken in March closely resembles the data taken in December and the slight discrepancies could be accounted for by a small difference in the measured axial position.

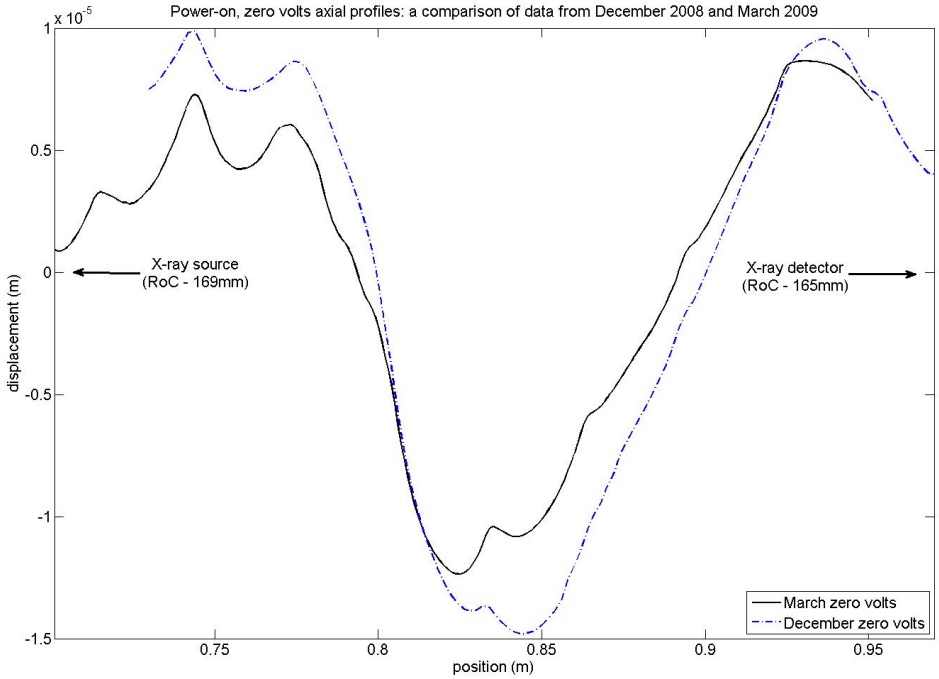

Figure 5.16: The axial profile of the ellipsoidal prototype

5.3.4 Axial LTP measurements - displacement per voltage

These measurements investigated the displacement per voltage for a given actuator with the intention of confirming the linear response expected from the piezoelectric material of the actuators. The first data sets, taken in December 2008, studied Actuator 17 by taking an 8cm LTP trace centralised upon its location. The actuator was then operated between 50V and -50V in 25V increments (the raw data can be seen in Figure 5.17(a)) and the data was then subtracted against a zero volts profile to provide the influence function of the actuator (Figure 5.17(b)). The maximum amplitude of the functions are recorded in Table 5.5 and a symmetry in the results can be seen. There is an approximate doubling in amplitude of the function at voltages 25V and 50V and the amplitude of -25V is a negative profile of 25V: these are effects that were anticipated prior to measurement due to the approximate linear relationship between voltage and displacement within a piezoelectric material. The -50V function appears to be an anomaly, as the displacement is $\sim$1.5μm larger than the equivalent 50V image; however, a definitive cause of this effect is yet to be determined. Figure 5.17 and Table 5.5 also display the FEA representation for the measurements, though there is a slight discrepancy in amplitude by approximately a quarter in the full form of the profile, these effects could be accommodated for by the unknown adhesive layer and false boundary conditions imposed upon the FEA model, but despite these effects there is a distinct similarity between the two sets of data.

Voltage V	maximum displacement μm	FEA 5mm glue thickness μm
50	6.619	8.620
25	3.347	4.310
-25	-3.144	-4.310
-50	-8.193	-8.620

Table 5.5: The maximum displacement of Actuator 17 operated between 50V to -50V in 25V steps

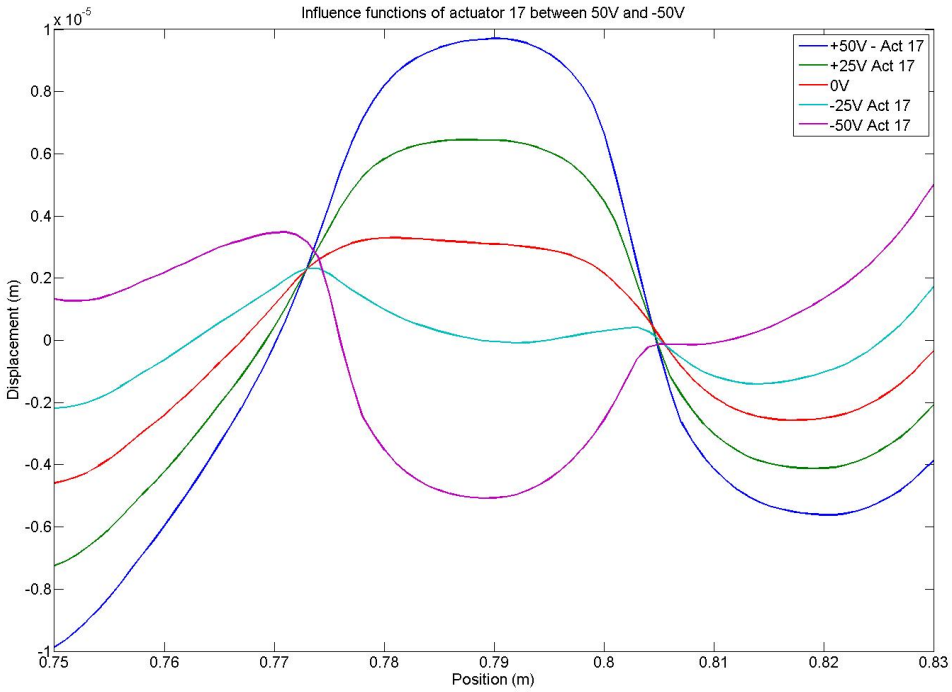

(a) Raw data for Actuator 17

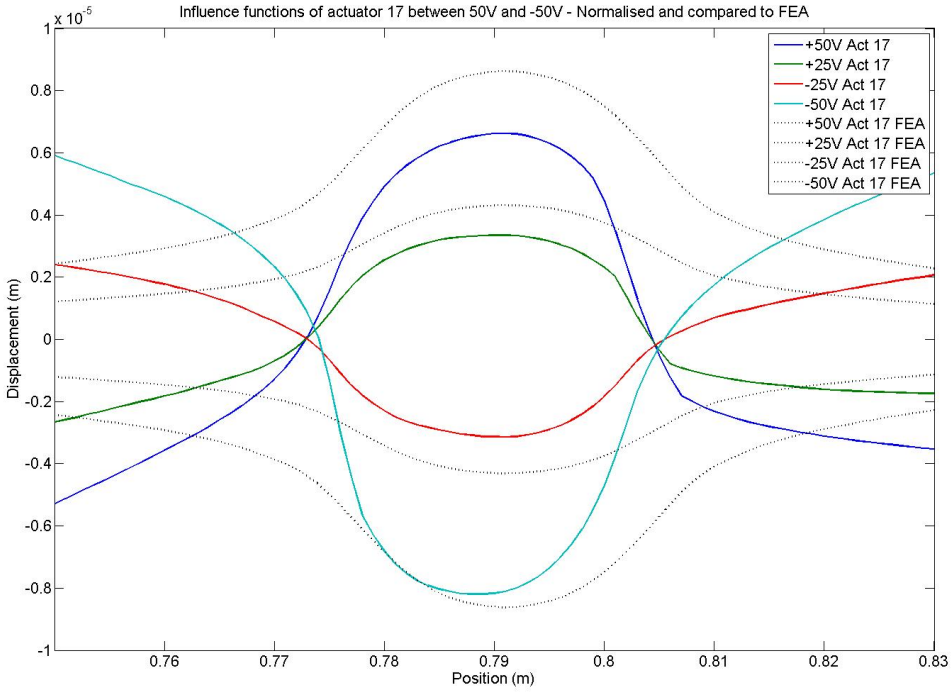

(b) Zero-subtracted data for Actuator 17

Figure 5.17: The influence functions of Actuator 17 operated between +50V and -50V, displaying raw and zero-subtracted data: all other actuators are at 0V

Further displacement per voltage measurements were undertaken in March 2009; these investigated Actuator 18 between +20V to -20V in 5V increments. Figure 5.18 displays the profiles taken over a 6cm range, centralised upon Actuator 18; the data has been subtracted from a zero volts image and compensated for in terms of tilt. As with the data taken in December there is an obvious symmetry and linear relationship within the results and this is emphasised by the numerical amplitudes recorded in Table 5.6.

The FEA data is superimposed upon the LTP data in Figure 5.19. There is some discrepancy between the maximum amplitude of the theoretical to that of the measured; however, the linear increase in amplitude with voltage is observed in the measured data. It is unlikely that such discrepancies in magnitude could be solely attributed to the unknown glue layer and it may be that other factors such as actuator thickness and the variant optic's thickness that have caused this decrease in displacement in comparison with the FEA data.

Voltage / V	Max displacement μm	FEA 5mm glue thickness μm
20	1.54	3.44
15	1.05	2.58
10	0.715	1.72
5	0.367	0.859
-5	-0.379	-0.859
-10	-0.742	-1.72
-15	-1.09	-2.58
-20	-1.50	-3.44

Table 5.6: Actuator 18 operated in the voltage range +20V to -20V in 5V steps

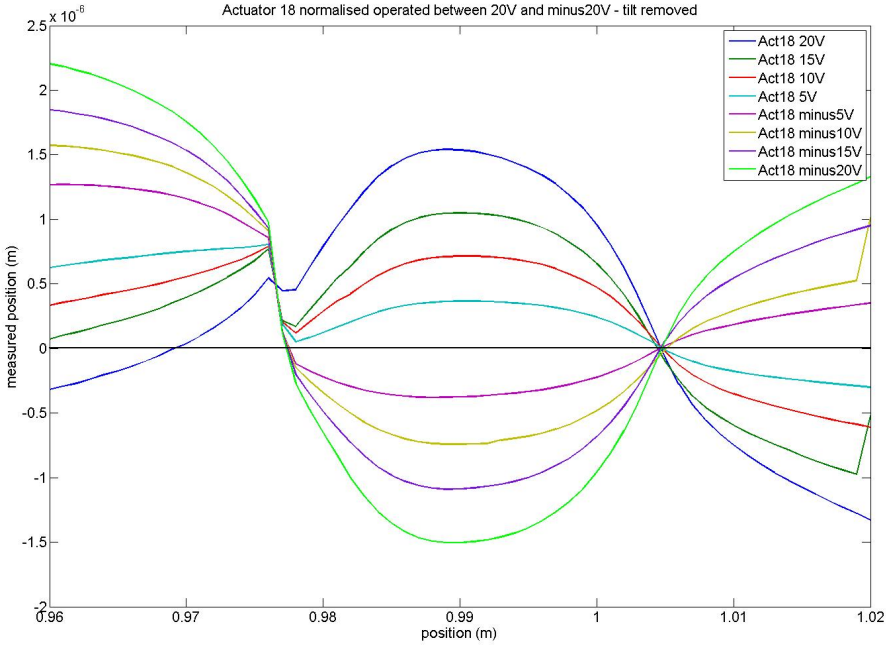

Figure 5.18: the profiles for Actuator 18 for the voltage range +20V to -20V in 5V steps that have been zero-subtracted and a tilt removed

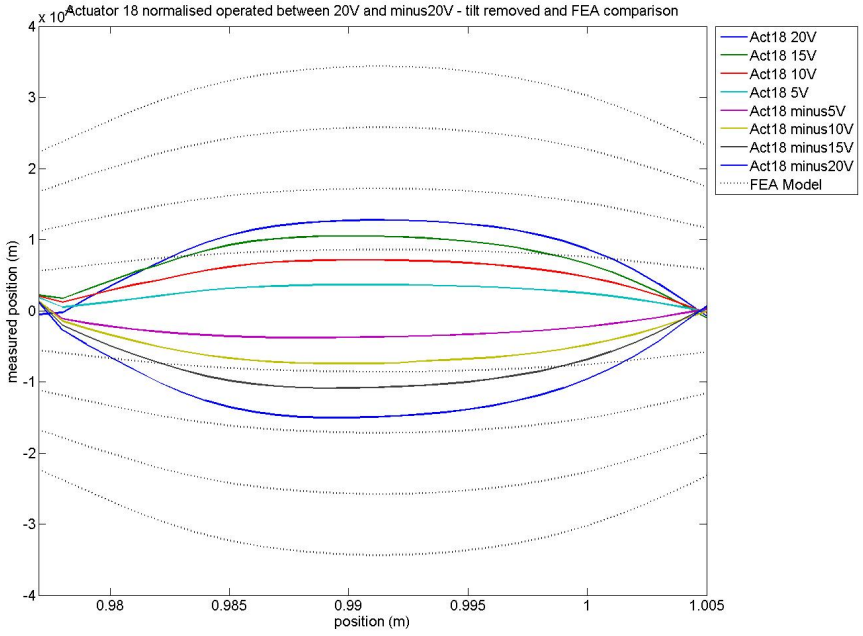

Figure 5.19: An FEA comparison applied to the active region of the LTP trace.

5.3.5 Axial LTP measurements - individual actuators

The following measurements (taken in December 2008) investigated the global effect of an individual actuator over the full length of the prototype. Actuators 11 - 18 were operated one at a time at 25V (Figure 5.20(a)) and subtracted against a zero volts profile; the LTP and corresponding FEA results can be seen in Figure 5.20(b) and Table 5.7. A comparison between the FEA and LTP data highlights a discrepancy in the amplitude for some of the functions: this again could be an effect of an unknown adhesive thickness which was estimated in the FEA models, though in the case of Actuators 16 and 13 there is a close match between the two data sets. The FEA predicts that the outer actuators will have a slightly smaller amplitude than the inner actuators by approximately 10%; this effect is mirrored in the LTP data, though to a greater extent. It is thought that this loss in amplitude in the edge actuators could have occurred from not only the unknown adhesive thickness, but also as an effect of the increase in nickel thickness at the outer regions of the optic (as discussed in Section 4.4.6), which resists the influence of the actuator.

Actuator no.	maximum displacement μm	FEA 5mm glue thickness μm
Actuator 18	2.8501	4.2972
Actuator 17	3.9380	4.4449
Actuator 16	4.3564	4.5135
Actuator 15	4.0406	4.5124
Actuator 14	3.5428	4.4432
Actuator 13	4.1035	4.2951
Actuator 12	3.2520	4.0366
Actuator 11	1.8160	3.9884
Average	3.2604	4.3164

Table 5.7: The maximum displacement of actuator operated at 25V one at a time

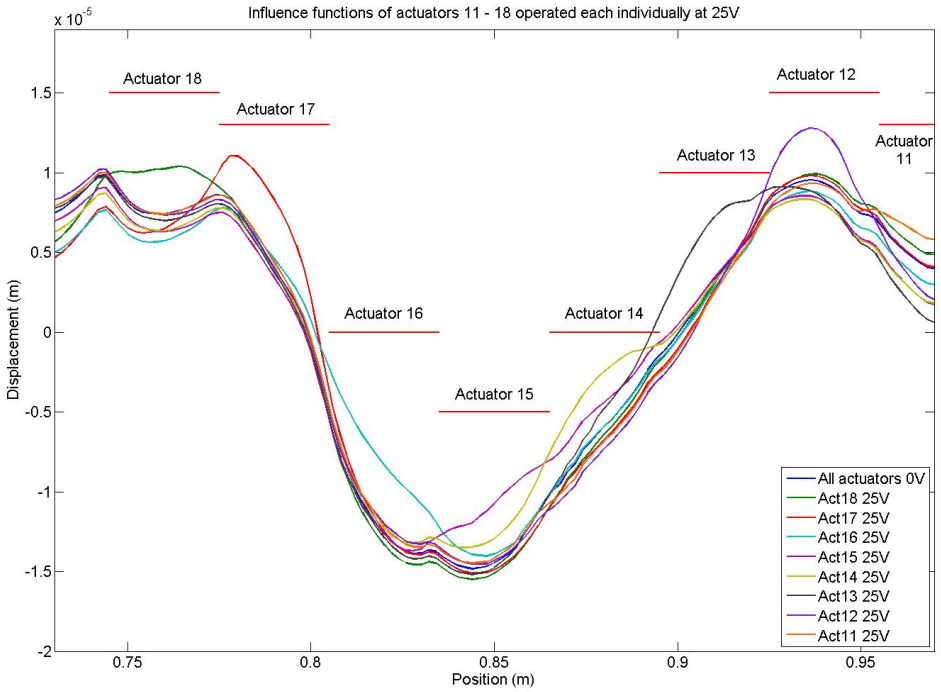

(a) Raw data for Actuators 18 - 11

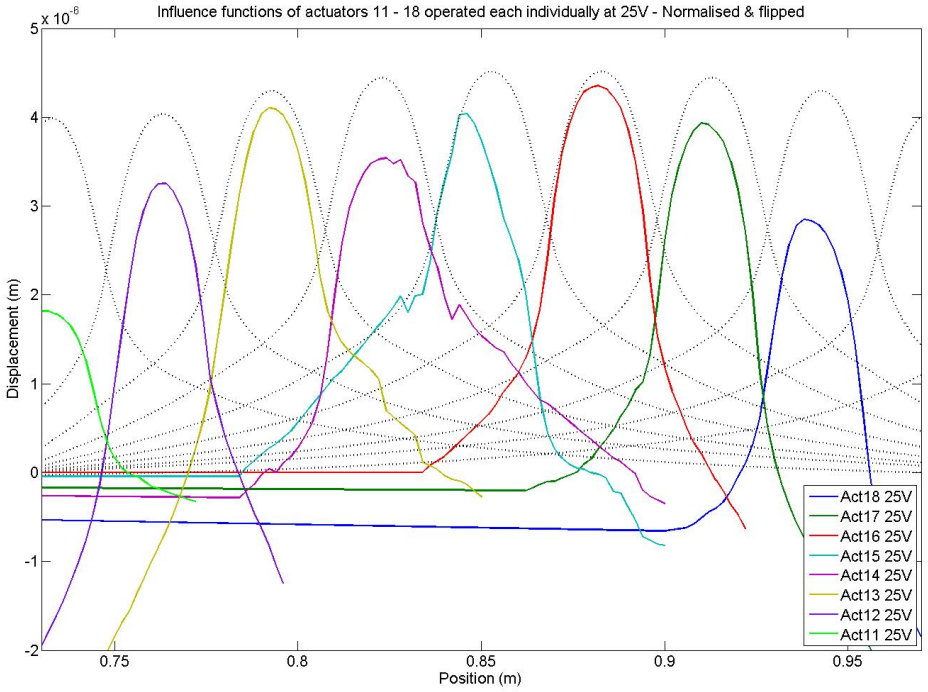

(b) Zero-subtracted data for Actuators 18 - 11

Figure 5.20: The influence functions of Actuators 18 to 11 operated at 25V one at a time while all other actuators are at 0V

The results from December were repeated in March over a similar axial length, allowing Actuators 12-20 to be studied (Figure 5.21(a)). To expand the data sets further, measurements were also taken at -25V to ensure that the inverse function provided a negative image (Figure 5.22(a)). Unfortunately, due to a different positioning of the prototype in relation to the LTP, the new data was more prone to errors caused by the reflected laser's position with respect to the LTP's detector; resulting in omission of some of the March data sets[2]. Figure 5.21(b) highlights the remaining influence functions and their comparison to the FEA data (see Table 5.8) for 25V. The March data does not appear to replicate amplitudes recorded from December: this could be due to the new position of the prototype with respect to the LTP. Therefore, the trace may not be along the centre of the actuator, which would provide the largest displacement, but rather shifted to the left or the right, though this has already been determined to be a minor effect in Section 5.3.2. Another argument could be that as the prototype is resting unconstrained upon the support structure, the actuators' influence has allowed it to shift position with respect to the original zero volts profile. However, there are similarities when compared against the FEA and December's LTP data and this is both in the form of the influence function and in the amplitude of the function with respect to its neighbours.

The negative data at -25V clearly demonstrates the expected inverse form of the influence function; however, in terms of symmetry, when compared against afore mentioned positive data, there are definite discrepancies within the amplitude of the functions. For example, Actuators 20 and 15 display an amplitude increase from the 25V data by 1.3μm and 0.8μm respectively, although it should be noted that this anomaly has been seen previously in the -50V profile in Figure 5.17. In addition the general variation of maximum amplitudes of the functions are consistent with those observed at 25V taken in March and December: the outer actuators provide a lesser displacement than those in the centre; however, Actuator 20 is inconsistent due to its 1.3μm increase in displacement.

[2]In addition, in the captions to Figures 5.21 and 5.22, *cut* refers to where the presented data tends to zero, this is an artificial effect implemented to remove poor data outside the main influence function location.

Actuator no.	+25V max displacement μm	FEA 5mm glue thickness μm	-25V max displacement μm	FEA 5mm glue thickness μm
Actuator 11	no data	3.9884	no data	-3.990
Actuator 12	2.6671	4.0366	-2.615	-4.039
Actuator 13	no data	4.2951	-4.297	-4.297
Actuator 14	2.8944	4.4432	no data	-4.445
Actuator 15	2.8426	4.5124	-3.6729	-4.514
Actuator 16	no data	4.5135	no data	-4.514
Actuator 17	no data	4.4449	no data	-4.445
Actuator 18	3.2500	4.2972	-3.2839	-4.297
Actuator 19	2.7840	4.0388	-2.5814	-4.039
Actuator 20	2.6597	3.9895	-3.9938	-3.990

Table 5.8: The maximum displacement of actuators 11 - 20 each operated at +25V and -25V one at a time

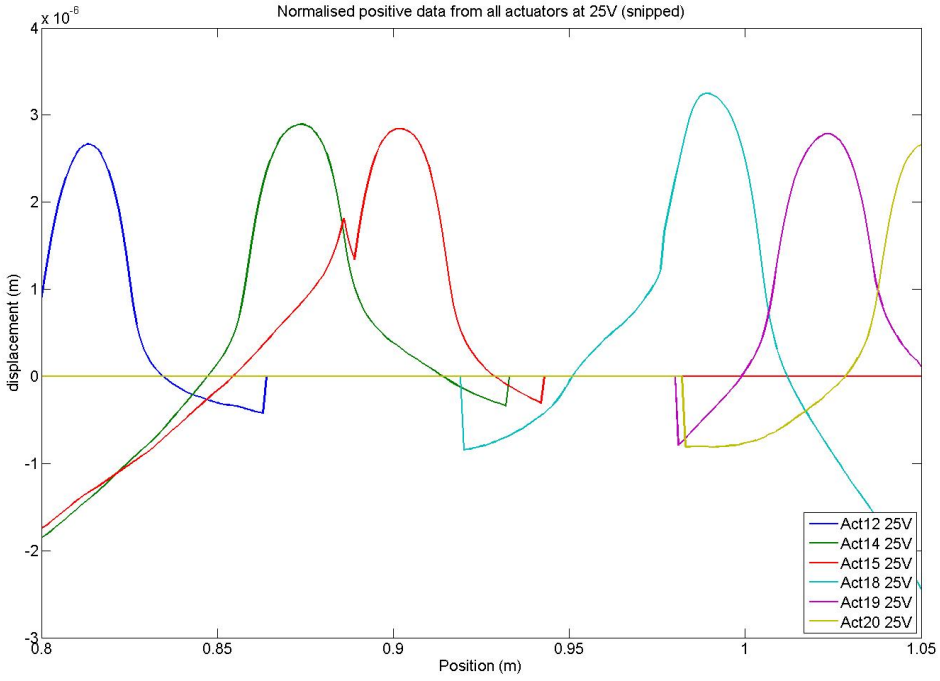

(a) Data for Actuators 20 - 12 25V (zero-subtracted and cut)

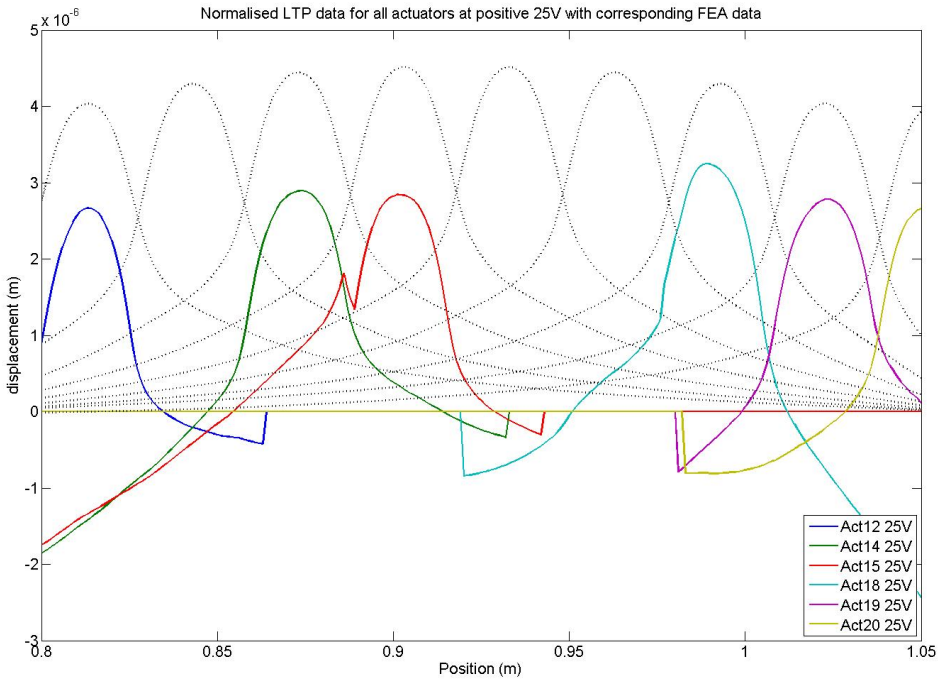

(b) Data for Actuators 20 - 12 25V (zero-subtracted and cut) including FEA comparison

Figure 5.21: Zero-subtracted and cut data for each actuator between 11 and 20 operated at 25V one at a time, including an FEA comparison

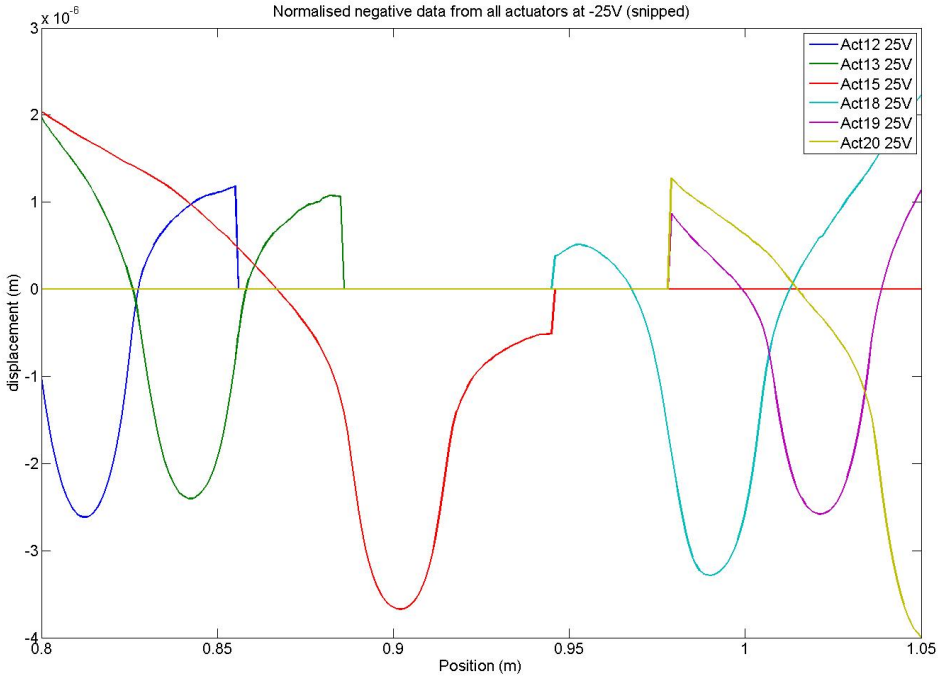

(a) Data for Actuators 20 - 12 -25V (zero-subtracted and cut)

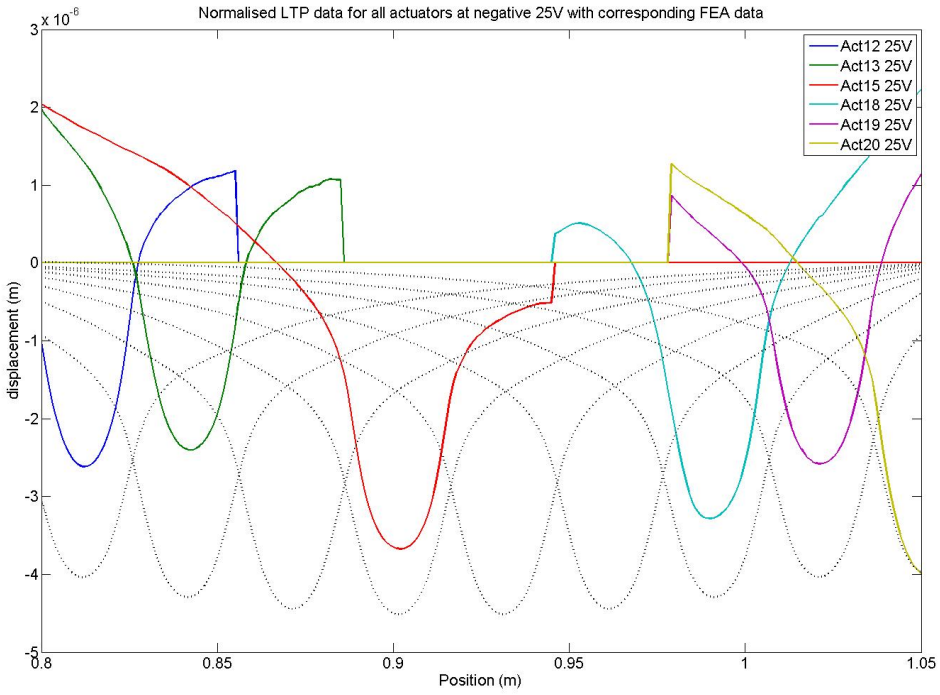

(b) Data for Actuators 20 - 12 -25V (zero-subtracted and cut) including FEA comparison

Figure 5.22: Zero-subtracted and cut data for each actuator between 11 and 20 operated at -25V one at a time, including an FEA comparison

5.3.6 Axial LTP measurements - neighbouring effects

Section 5.3.5 highlights the actuators' ability to influence beyond the confines of their physical size. To investigate this 'neighbouring effect', a trace was taken over the length of three actuators with Actuator 18 central within the profile. Two neighbouring effects were investigated: one in the axial direction, where Actuator 18's effect was studied upon Actuators 17 and 19; and the second measurement which investigated Actuators 8 and 28's effect upon Actuators 17-19.

The raw data for Actuator 18's effect upon Actuators 17 and 19 is displayed in Figure 5.23 (with applied voltages of -20V, 0V and 20V) and an initial observation indicates Actuator 18's ability to affect beyond its physical dimensions. Figure 5.24(a) represents the -20V and 20V data subtracted against the 0V profile and compared against the FEA simulation. From the figure a discrepancy in the magnitude of profiles is evident; however, the form of the profiles have a close similarity and Figure 5.24(b) displays the effect when the FEA data (displaying the full length of the prototype) is shifted down to fit with the LTP data. From the fitting, the similarity in form is clearly apparent, not only in the region of Actuator 18 but also in the region of Actuator 19, although the fit at Actuator 17 is less convincing. The measurements were intended to investigate the 'neighbouring effect' in the axial direction and the results indicate Actuator 18's ability to affect beyond its confines in the axial direction and with striking similarities in form when compared to the FEA data.

The same LTP trace was used to investigate Actuators 8 and 28's neighbouring effect in the azimuthal direction upon Actuators 17 - 19. Figure 5.25 displays the LTP measurements compared against the FEA for the four voltages applied: -20V, -10V, 10V and 20V, these profiles have been substracted from the 0V profile in the figure. It was noted during measurement that some of the data points were of poor quality, a result of the reflected laser with respect to the LTP detector; this has resulted in the rather disjointed form of the profiles. In comparing the LTP data to the FEA, there are similarities in the form and magnitude of the profiles when the voltage was negative, though this similarity is restricted to the central location of Actuator 18. The positive data is less convincing in terms of magnitude and form, however the profile does increase in magnitude from $\sim$-0.23μm to $\sim$-0.53μm, which shows the linear relationship between voltage and displacement. Although the fit of the LTP to FEA data is not of the quality of Figure 5.24, it does highlight how Actuators 8 and 28 have affected Actuators 17 - 19 and that the effect was a result of influence from the azimuthal direction.

The intention of this section has been to highlight the 'neighbouring effect' where an actuator affects a displacement beyond its physical dimensions. This effect has been demonstrated in both

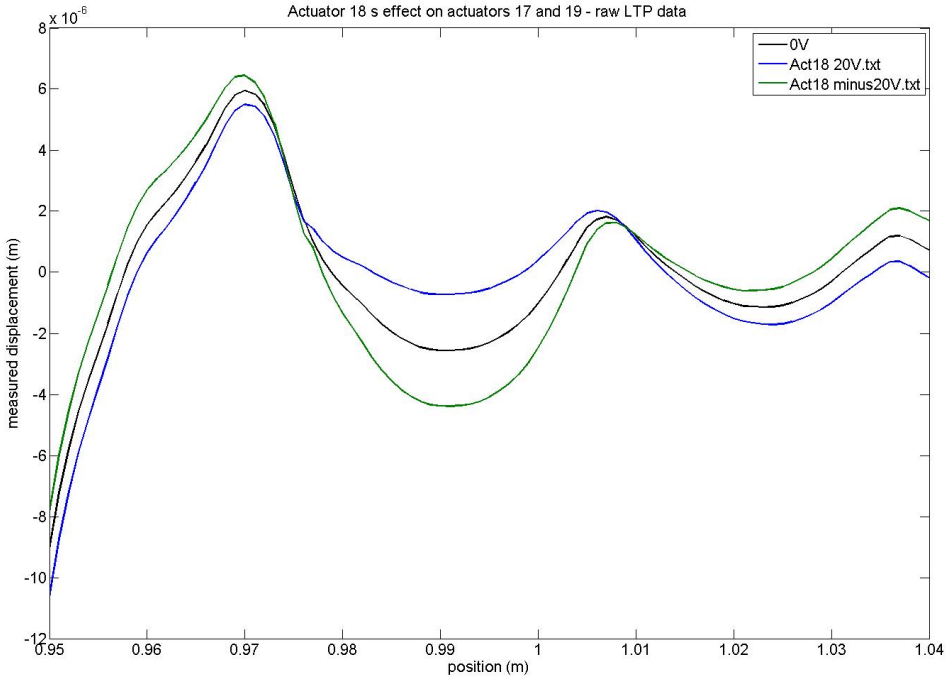

Figure 5.23: Raw LTP data taken over Actuator 17 to 19, centralised upon Actuator 18

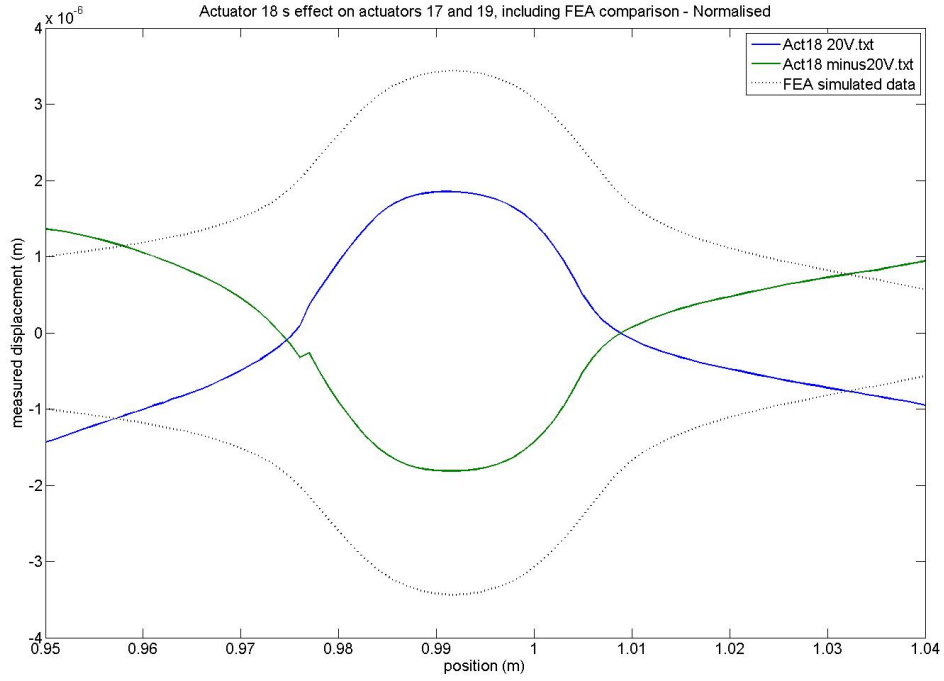

(a) Zero-subtracted data with FEA comparison

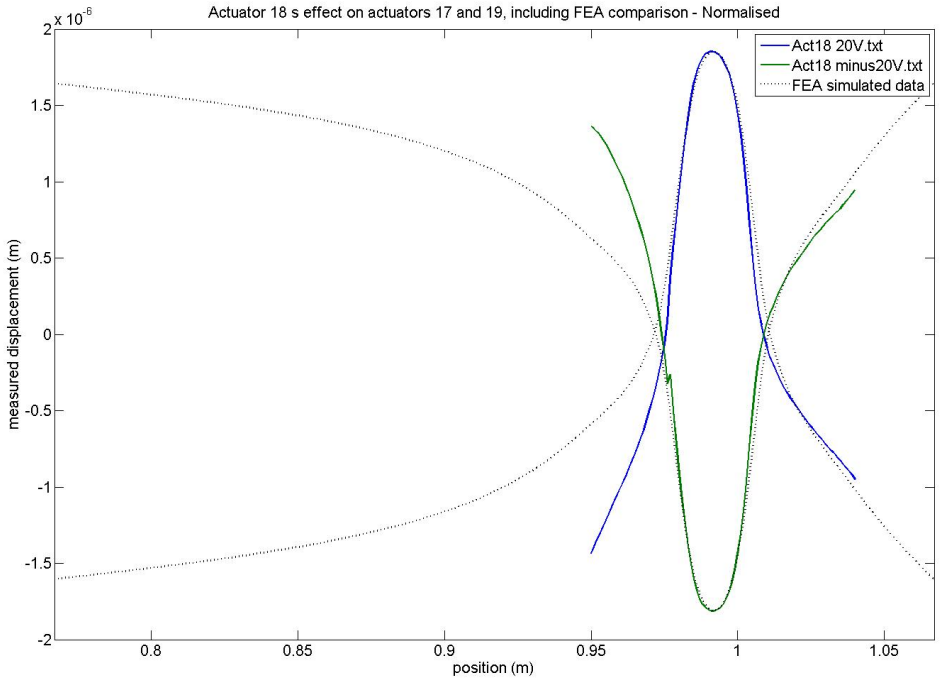

(b) Zero-subtracted data fitted to the FEA data looking at the full length of the prototype

Figure 5.24: Zero-subtracted data compared against FEA simulations.

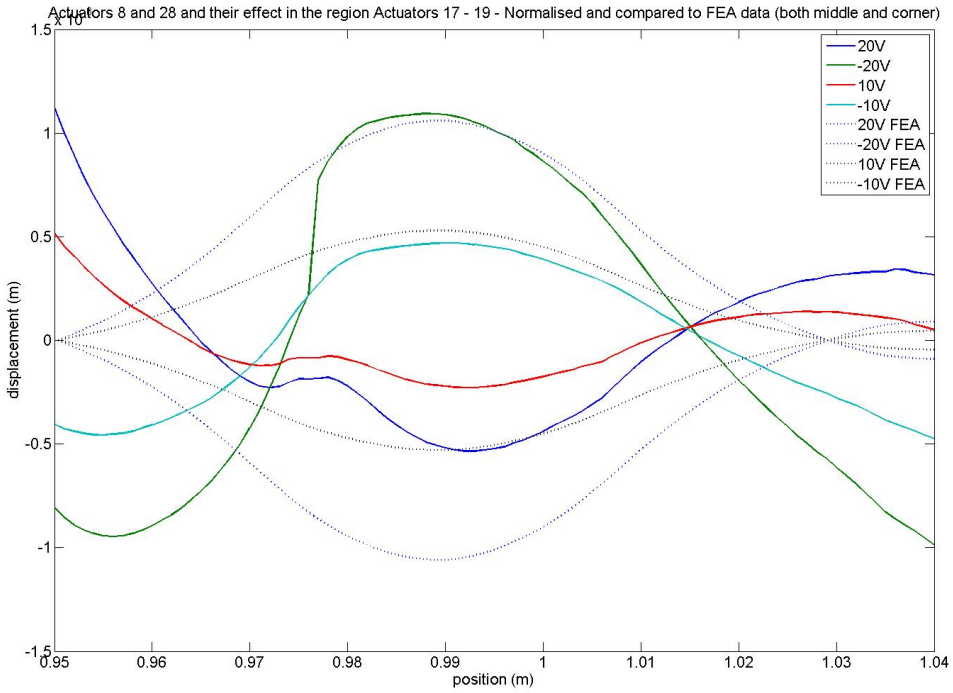

Figure 5.25: Actuator 8 and 28's effect upon Actuator 18 and its neighbours (zero-subtracted and compared to FEA data)

the axial (Figure 5.24(b)) and the azimuthal (Figure 5.25) directions and is consistent with the FEA representations outlined in Figures 5.14 and 5.15. These results therefore indicate that when the actuators are used simultaneously the displacement for a given actuator will not just be an effect of that actuator's voltage but also an effect of its neighbours' influence functions.

5.3.7 Axial LTP measurements - active to dormant decay in form

As mentioned in Section 5.3.3 there is a difference between the axial profile of the prototype between the actuators being dormant and active, therefore the decay of the prototype's form was investigated to determine the timescale of this change when the prototype goes from active to dormant. The LTP can take several consecutive measurements with only a short time delay between measurements (i.e. the time it takes for the probe to return to its start position), by using this feature a transition in form between active and dormant was hoped to be obtained. The same axial profile as in Section 5.3.6 was used and the LTP was set-up to take 11 consecutive traces, the first with the prototype in the active condition and in the latter traces in the dormant condition. The time between identical trace points was 75 seconds, this is the time taken for the probe to be in one position upon the prototype's surface and then to complete the rest of the trace, reverse and then obtain the same position in the following trace.

The results are highlighted in Figure 5.26, the solid black line indicates the axial profile when the power is on at 0V (active) and the coloured lines when the power is turned off (dormant): a clear change in profile is observed. The latter 10 profiles all have a similar form indicating the prototype relaxed on a shorter timescale than that which could be measured, in fact only the second profile shows any variation in comparison with the latter indicating that the profile was taken at the end of the prototype's transition. Therefore the results suggested that the transition between active and dormant occurs in the time taken for the probe to reverse and unfortunately could not be measured. However there is scope to investigate this transitional period further, a laser displacement sensor could be used to continuously sample a point upon the prototype's surface over the duration of the transition and assuming the sampling rate is greater than the decay a description of this transition could be established.

5.3.8 Prototype morphology and actuator influence functions summary

This section has presented the prototype's influence functions and how they compare to FEA simulations. The following conditions were investigated:

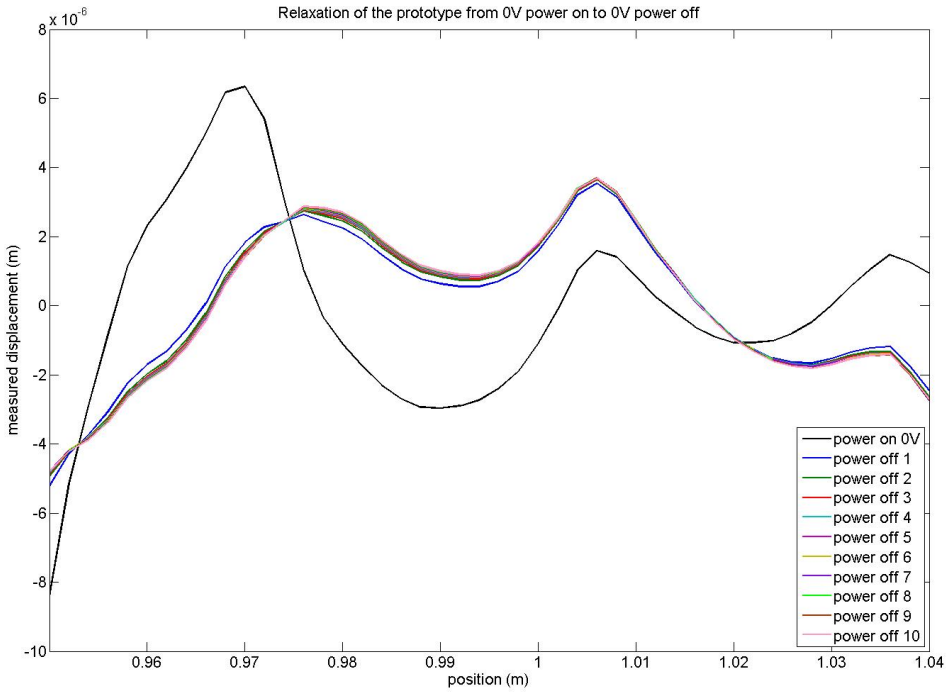

Figure 5.26: Relaxation of the prototype from 0V power on to 0V power off

1. the prototype's axial profile when the actuators are *active*
2. the linear relationship between displacement and voltage within the piezoelectric material
3. the difference in actuator influence function with position upon the prototype's surface
4. the 'neighbouring effect', where the influence of single actuator affects beyond its physical dimensions
5. the relaxation of the prototype's form from active to dormant

FUNCTION AMPLITUDE - The comparison of LTP and FEA functions in terms of amplitude was met with varying degrees of success. In some instances the match was almost identical (-25V for Actuator 20 in Table 5.8), but in some cases the amplitudes varied by $\sim 2\mu m$. Some of the discrepancy can be accounted for by the unknown adhesive thickness ($\pm 0.5\ \mu m$); however in many cases there is still a deficit to explain. Possible culprits could be: the boundary conditions imposed upon the FEA model; the prototype shifting position relative to the 0V profile and an inaccurate representation of the actuators within the model in terms of thickness and material properties.

FUNCTION FORM - Although there were discrepancies in the amplitude of the functions, the form of the functions, at least in the immediate vicinity of the actuator's dimensions (local form), proved to be consistent and Figure 5.24(b) highlighted this trend by fitting the FEA data to that of the LTP. In addition, if the full width half maximum (FWMH) of a LTP-FEA function pair is compared, as shown in Figure 5.27, the results are almost identical. The LTP trace in Figure 5.27(a) demonstrates a FWHM of ∼29mm, whereas in Figure 5.27(b) the FWHM is ∼31mm. Despite reinforcing the similarity in the local form of the functions, the figures highlight that half of the amplitude displacement is within the direct dimensions of the actuator (the actuators are 29mm in the axial length). However, these measurements may not be fully representative of the remainder of the data, as only one sample has been taken.

Comparisons of the global form of the functions (i.e. over the full length of the prototype) did not present a similarity between the LTP and FEA data. When considering the false boundary conditions applied within the FEA model this variation is not surprising. The FEA model provide fixed boundaries for the prototype to react against, whereas the actual prototype is free to move in all three axes.

FITTING FEA TO LTP - As mentioned in the previous paragraph, fitting FEA data to that of the LTP highlighted a similarity in the local form of the functions by correcting for the difference in amplitude. There is some justification in the realigning of the FEA data with respect to the LTP data due to the boundary conditions within the FEA model, which restrict the total movement of the prototype within the model. However, the author choose not to apply this correction to the remainder of the data, as the degree of realignment could not be accurately determined due to the number of variables to accommodate for.

The section has demonstrated the ability of the prototype and the FEA models to produce actuator influence functions that are similar in form and amplitude; however, limitations were encountered. The FEA model was just an approximation to the true system, it did not accurately represent the thickness of each component or the precise positioning of each element in relation to each other. The boundary conditions within the model were not represented upon the actual prototype and it is suspected that this could account for some of the discrepancies observed. It was not only the model which was inconsistent, it was thought that the prototype itself was shifting position, albeit slightly, upon the optic cradle; leading to errors in the function's amplitude/form due to a poor subtraction with a 0V profile.

There is scope for further analysis of this data. Alternative boundary conditions could be applied to the FEA model in an attempt to more accurately represent the real prototype. Measurements of

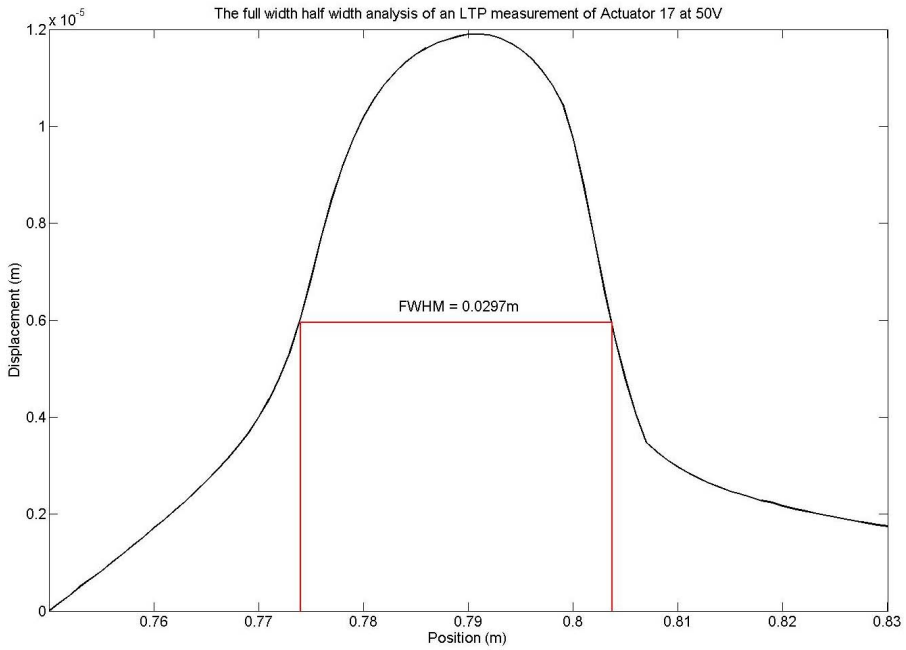

(a) LTP - FWHM measurement for Actuator 17 at 50V

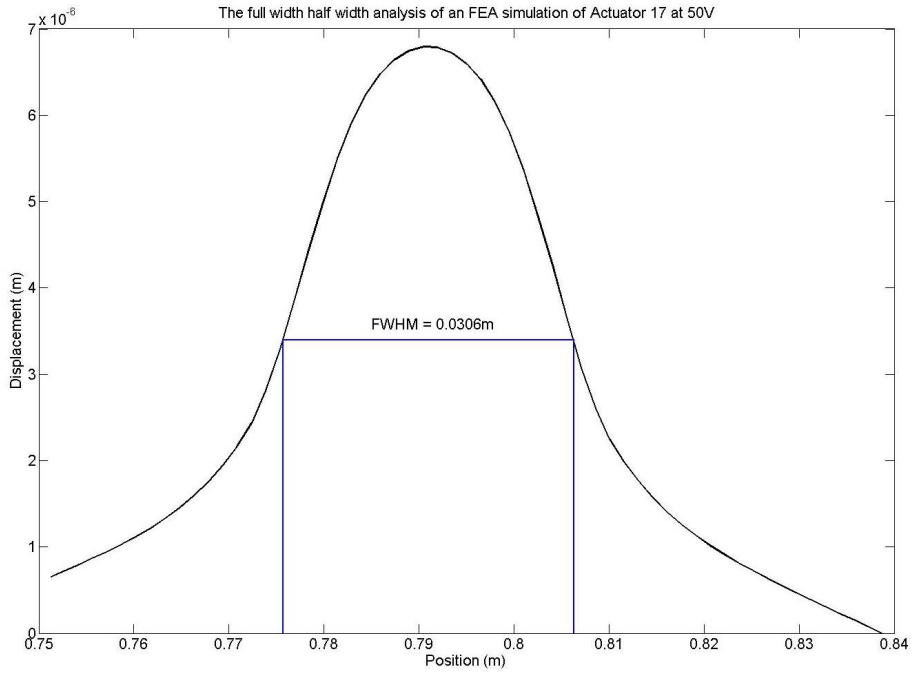

(b) FEA - FWHM measurement for Actuator 17 at 50V

Figure 5.27: A comparison of full width half maximum measurements of the Actuator 17 profile at 50V for the LTP (Figure 5.27(a)) and FEA (Figure 5.27(b)) data.

the thickness of the adhesive layer beneath each of the actuators could be determined, although current measurement techniques would damage the prototype's optical surface. Further analysis of the FWHM for the actuators could be undertaken. This would establish the effect of adhesive within the influence functions and the global function of the prototype when the actuators are operated simultaneously.

5.4 Chapter summary

Chapter 5 has described the operation of the prototype, starting with a discussion regarding the prototype hardware and software and concluding with a description of the actuators' influence functions and their comparison to FEA simulations. The following chapter presents the X-ray testing of the prototype, including: the experimental set-up, operation procedure, data taken and an analysis of the results.

CHAPTER 6

X-RAY TESTING AT THE UNIVERSITY OF LEICESTER

Chapter 6 outlines the performance of the ellipsoidal prototype within the an X-ray environment. The chapter will present an introduction to the X-ray tunnel test facility; the prototype's optimising routine; the four weeks of X-ray testing and will conclude with an analysis of the obtained data.

6.1 The University of Leicester's X-ray tunnel test facility

The X-ray tunnel test facility (X-ray TTF) is located in the basement of the Physics Department at the University of Leicester's main university campus in the centre of Leicester. The facility has its origins with the european ROSAT X-ray telescope and is currently being used to assess the optics for ESA's Beppi Colombo mission (Martindale *et al.* 2009). The following section will provide an overview of the facility including: the X-ray source, the MCP detector and the proposed integration of the prototype within the facility.

6.1.1 Specifications of the X-ray TTF

Figure 6.1 provides an approximate representation of the X-ray TTF, highlighting the source and detector at either end of the tunnel; the 28m length is in the axial length of the prototype. The X-ray TTF specifications are detailed below:

- Length of the tunnel - 28m
- Diameter of the tunnel at the source - 100mm

- Diameter of the tunnel at the detector - 200mm
- Environment within the tunnel - vacuum
- Thermal stability within the tunnel at a vacuum - $\pm 1\,^{\circ}\mathrm{C}$

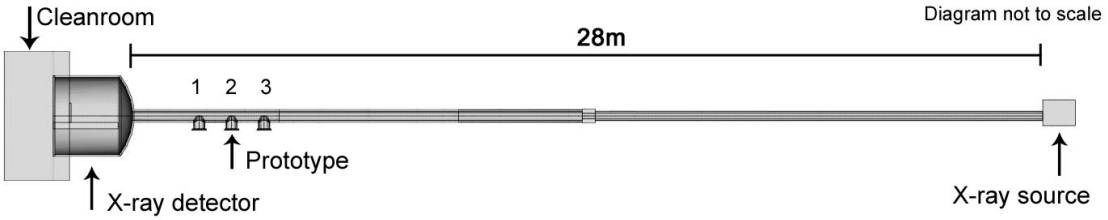

Figure 6.1: A schematic of the the X-ray tunnel test facility at the University of Leicester

Access to the interior of the tunnel is via a series of flanges that are located along the tunnel's length; only three have been depicted in Figure 6.1 and it is above the second of these flanges that the prototype will be positioned. The vacuum environment is obtained through an 8 hour 'pump-down', typically overnight, till a final internal pressure of $2 - 3 \times 10^{-6}$mbar has been achieved. The vacuum placed restrictions upon the components that could be placed within the facility; not only did they have to be vacuum compatible, but also clean to allow the vacuum to be obtained.

6.1.2 The X-ray source

A coated copper anode provides X-rays in the energy range from 0.1keV to 100keV. The coating of the anode dictates the energy of the X-rays: as the anode is heated the coating obtains enough energy to liberate photons from an excited state. For the X-ray tests the coating will be NaCl which provides X-ray energies of either 1.04keV (Na) or 2.64keV (Cl). The energy selected is determined by the current applied to the anode. The intention is to use the lower energy range 1.04keV, as it would reduce the magnitude of the scatter observed. Figure 6.2 highlights the housing of the X-ray source from an orientation of looking towards the detector and the copper anode used to generate the facility's X-rays.

The X-ray source can be interchanged with an optical laser for the alignment of the optics. This is advantageous as it allows the adjustments made to the position of the optic to be viewed in real-time, rather than waiting for the integration time required to obtain enough X-ray counts. A green Helium-Neon (HeNe) laser is used and this provides a point source to interact with the optic.

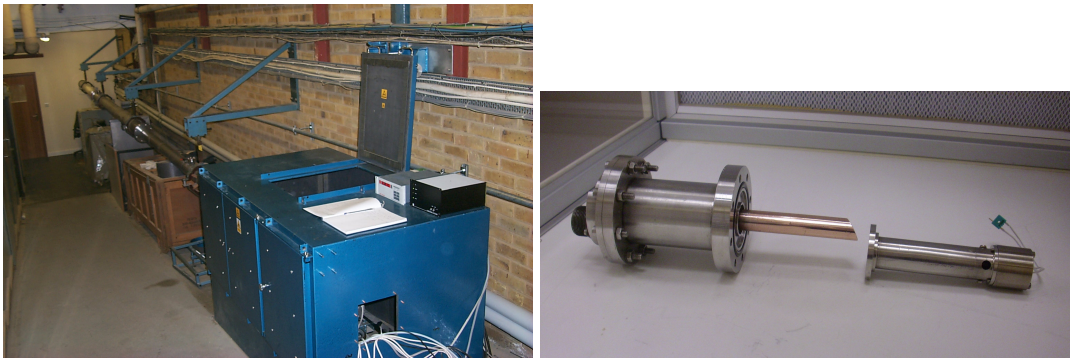

(a) The housing of the X-ray source (b) The copper anode coated in NaCl

Figure 6.2: Figure 6.2(a), courtesy of Dr J. Pearson from UoL, depicts the view from the X-ray source towards the detector, Figure 6.2(b), courtesy of CHF from UoL, displays the copper anode coated with NaCl which is used to generate the X-rays.

A diffuse source, similar to the X-ray cloud that will be generated, can be obtained by placing pin-holes or slits in front of the laser's aperture.

6.1.3 The MCP detector

The micro-channel plate (MCP) detector used within the X-ray TTF is shown in Figure 6.3(a); it has a surface area of 93mm^2 and has 0.8m of axial travel. An MCP detector works on the principle of electron cascade (Fraser 1989), where an incident X-ray liberates an electron from the channel's semiconductor surface, which then goes to liberate another electron and so on till an electron cascade is generated. A representation of a channel is shown in Figure 6.3(b); typically these channels are $\sim 15 \mu m$ in diameter. The X-ray images obtained will have to be compensated for in terms of the *pin-cushion* effect, an artefact of the read-out of the counts from the MCP detector which causes the image to become deformed, as shown in Figure 6.4.

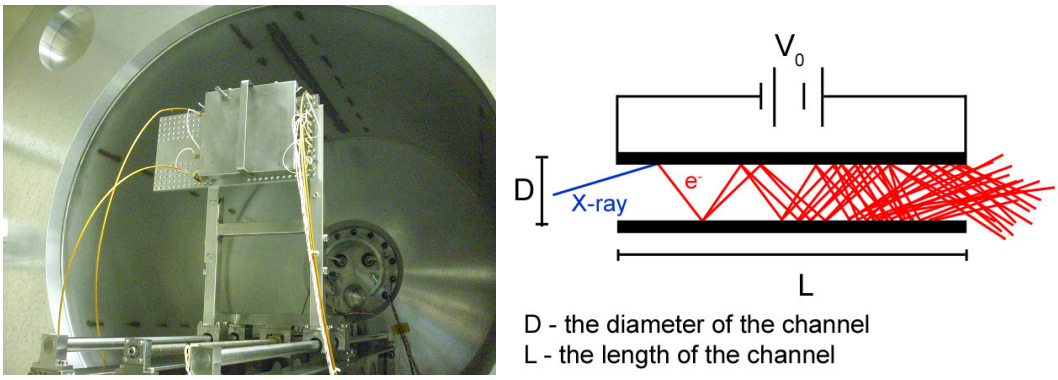

(a) A photo of the MCP detector

(b) A schematic of an MCP channel

Figure 6.3: Figure 6.3(a) displays the MCP detector at the UoL with a face guard protecting the detector. The detector is positioned upon two rails that provide the 0.8m of axial travel, photo courtesy of CHF from UoL. Figure 6.3(b) outlines a schematic of an individual channel of an MCP detector, where an incident X-ray liberates an electron and starts an electron cascade.

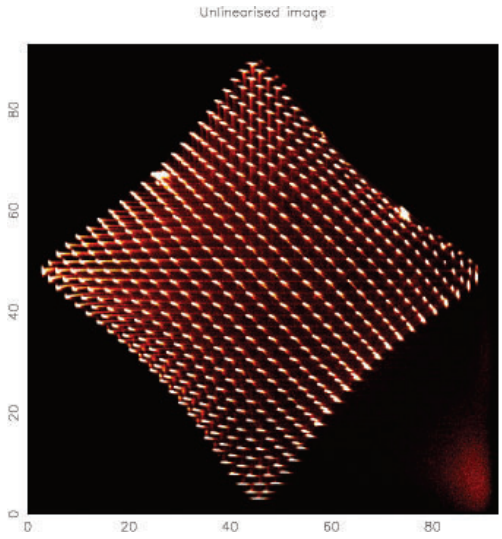

Figure 6.4: A pin hole image taken using the MCP detector demonstrating the pin cushion effect that has to be compensated for. The image mask used in this figure is a square array of pin holes, image courtesy of CHF from UoL

6.1.4 Integration of the prototype within the facility

The prototype and associated support structure are to be positioned within the X-ray TTF at the second flange approximately 4.5m from the detector, as shown in Figure 6.5. The flange support and remainder of the support structure, as outlined in Section 2.1.6 of Chapter 2, are positioned at the second flange independently of each other. The flange support is located externally by directly fixing the support to the open flange, whereas the remainder of the support structure is placed down the tunnel from the opening at the detector.

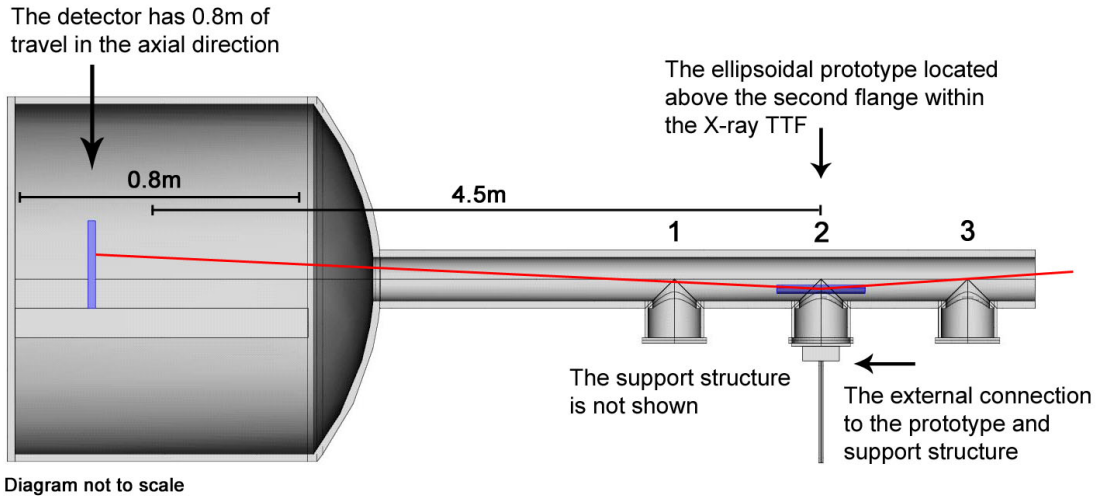

Figure 6.5: A schematic of the ellipsoidal prototype within the X-ray tunnel test facility: the prototype is located approximately 4.5m from the detector (when the detector is in the middle of its travel). The red line represents an incident X-ray upon the optic.

6.2 The optimisation routine

The routine to optimise the prototype's optic within the X-ray facility was developed by UoL and was presented in the paper by Feldman *et al.* (2008), therefore only a brief description shall be provided within this thesis.

The optimisation of the prototype within the X-ray facility is through voltage patterns; this allows all 30 actuators to be used simultaneously whilst trying to improve the resolution, instead of operating a single actuator at a time which would be time intensive. A series of fast fourier transform (FFT) patterns were produced, as shown in Figure 6.6. Each square within the patterns represents an actuator, the shade of the square indicates a value between 1 (white) and -1 (black).

Starting with Pattern 1 (the top left-hand image in Figure 6.6), the pattern is multiplied by 10 voltages between -100V to 100V in equal increments (providing the `.txt` file for the actuator control program). Between each voltage an X-ray image is taken. After the 10 voltages the optimum voltage for that pattern is calculated using a least squares fit method; this optimised voltage is then applied with Pattern 2 and the 10 voltages are repeated. Therefore after ∼160 observations the final optimum voltage is the cumulative effect of all the previous patterns at their optimum voltages. It is anticipated that the process of optimising the prototype will take several days to complete due to the low X-ray flux and the requirement of 5×10^5 counts per image.

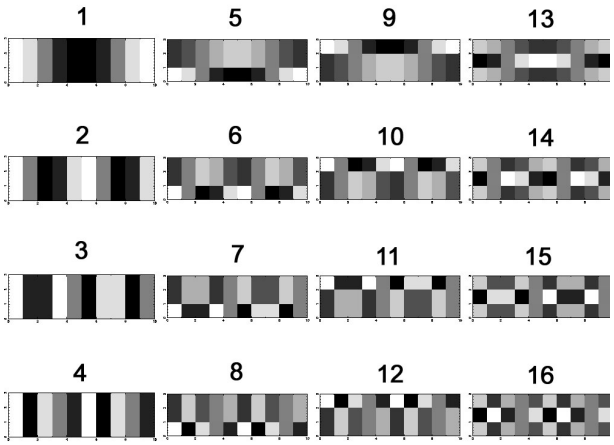

Figure 6.6: Fast fourier transform patterns, image courtesy of CHF from UoL.

6.3 X-ray testing at the X-ray TTF

The X-ray tests were undertaken for four weeks from the 10th of November 2008 to the 5th of December 2008. the X-ray tests were directed by CHF and Dr R. Willingale from UoL, with assistance from: Dr A. Martindale, Dr J. Pearson and Dr G. Butcher. HCW and author were present throughout the four weeks to provide assistance during the integration of the prototype within the facility and with the interface between the actuator control software and optimising routine.

The four weeks were utilised as below and the remainder of this section will present a narrative of the work undertaken:

WEEK 1 - Integration of the prototype within the X-ray facility and initial optical alignment.

WEEK 2 - X-ray first light, realignment of the prototype and initial actuator measurements.

WEEK 3 - Testing the optimisation routine and the development of new actuator patterns: the local group patterns.

WEEK 4 - Optimisation of the prototype using the new local group patterns.

6.3.1 Week 1 - Integration of the prototype within the X-ray facility and initial optical alignment

INTEGRATION OF THE PROTOTYPE WITHIN THE X-RAY TTF - The stainless steel plates, which formed the seal between the flange and external environment, were removed from the first and second flanges. The flange support, minus the connector base plate, was bolted to the second flange. A copper gasket was positioned between the flange support and the flange opening and this ensured a vacuum seal at the junction between components. The legs of the flange support were positioned at their minimum to provide a consistent starting position as well as reducing their obstruction within the tunnel during integration.

The prototype, resting upon its cradle, was attached to the active component of the support structure and pushed down the tunnel using the two plastic skis on the side of the active support to balance the system, as shown in Figure 6.7. When the prototype and carriage were in the vicinity of the flange they were lifted upon the three flange support legs and in doing so fixed the kinematic mount. The prototype and the support structure were viewed from the open flange to ensure the prototype had not shifted from its original position upon the foam as a consequence of its travel down the tunnel.

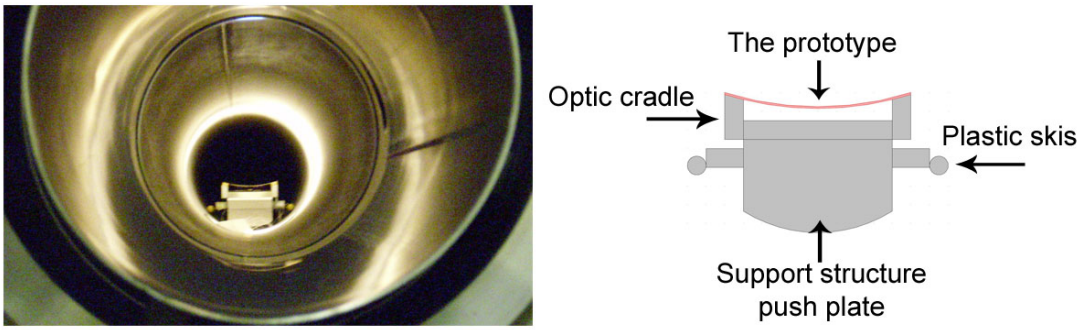

Figure 6.7: The photo on the left highlights the prototype positioned within the X-ray TTF as viewed from the detector towards the source (photo courtesy of CHF), the image on the right depicts the components of the prototype and support structure as seen in the photo.

OPTICAL ALIGNMENT - Crude alignment of the system was achieved through the use of the laser located at the X-ray source. At the detector a sheet of optical tissue covered the entrance to

the tunnel to provide a medium by which to view the laser. The laser light, as represented upon the optical tissue, was fixed to be in the centre of the tunnel's opening and then the legs of the support structure were used to lift the prototype to interact with the laser light (Figure 6.8). The objective was to optimise the reflected image in order to achieve as small a focus as possible.

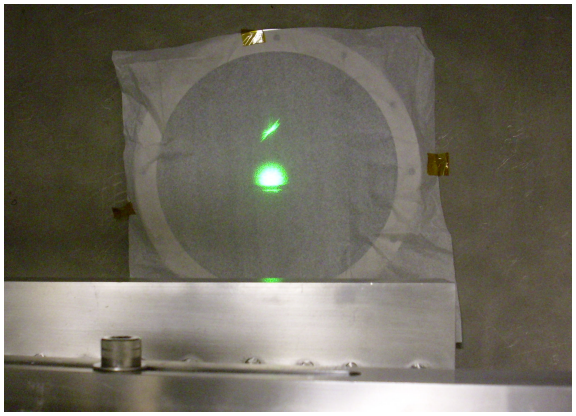

Figure 6.8: The laser interacting with the prototype's optic to produce a reflected image, photo courtesy of CHF from UoL

The legs of the prototype were first used to align the prototype; these were intended to correct for gross distortion errors. Once the optimum position was found, the connection to the drive computer was made and the pitch and yaw motors, of the active support structure, were used to provide fine adjustment. It soon became apparent that the pitch and yaw motors did not operate as intended and that they were prone to getting stuck and provided unreliable displacements: therefore, it was decided to view the X-ray image and then to realign if necessary. The final component of the flange support, the connector base plate, was connected and a vacuum seal established using a copper gasket. The detector chamber was closed and the facility brought down to a vacuum.

6.3.2 Week 2 - X-ray first light, realignment of the prototype and initial actuator measurements

X-RAY FIRST LIGHT - Figure 6.9 displays the first light X-ray image detected using the MCP. Unlike the laser images which could only sample a small area of the prototype's surface, the X-rays were able to illuminate the entire surface of the optic. The image is far from a point focus, indicating either a gross distortion of the optic, residual alignment errors or both. The pitch and yaw motors were used in an attempt to further align the optic; however, care had to be taken not to overheat the motors now that they were operating within a vacuum environment. The motors were able to shift the position of the detected image; however, the motors' unreliability prevented a predictable

cause-and-effect to be observed. As the motors could not correct for the gross distortion that was observed, the decision was made to bring the facility back up to air and to realign the optic using the laser.

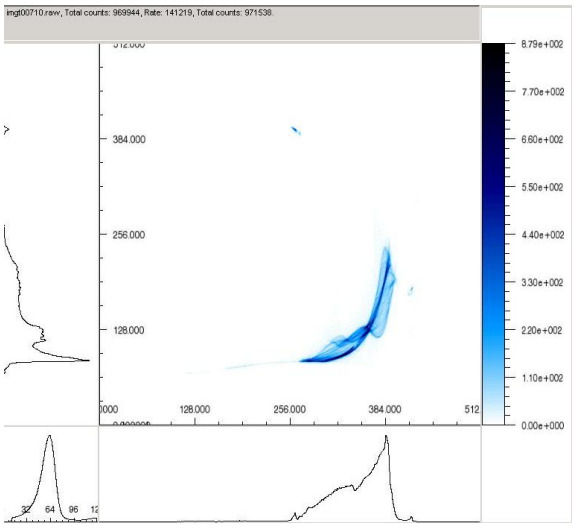

Figure 6.9: The first light X-ray image

OPTICAL REALIGNMENT - Upon further observation of the prototype upon its support structure it was noted that it was slightly off centre; adjustment led to an improved optical reflection. The adjustable legs were used to further optimise the reflection and the pitch and yaw motors were used to refine the image. Although the pitch and yaw motors were still unreliable, an improvement was obtained and the optimised optical image can be seen in Figure 6.10.

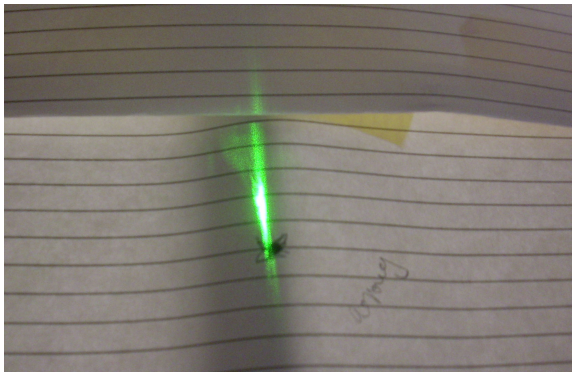

Figure 6.10: The improved realignment of the prototype using the optical laser.

X-RAY ALIGNMENT - Figure 6.11 highlights the X-ray image for the new alignment of the prototype. The reflected image is an improvement upon the more diffuse first light image and it is

now centralised upon the MCP detector. The detector was then used to 'focus' the X-ray image by positioning the detector at different locations upon its 0.8m of axial travel. The detected image was observed to come into focus (Figure 6.12) when the detector was at its most distant point from the source (i.e. when the detector was 4.9m from the prototype). Further fine alignment was attempted using the pitch and yaw motors. However, a predictable improvement could not be obtained.

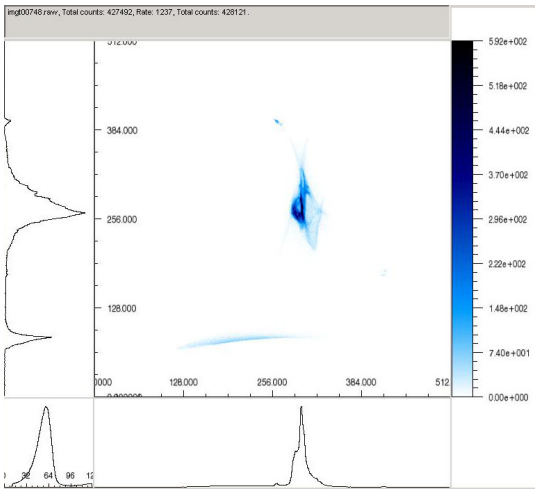

Figure 6.11: The first X-ray image of the realignment of the prototype. The image is centralised upon the detector and smaller than the previous first light image.

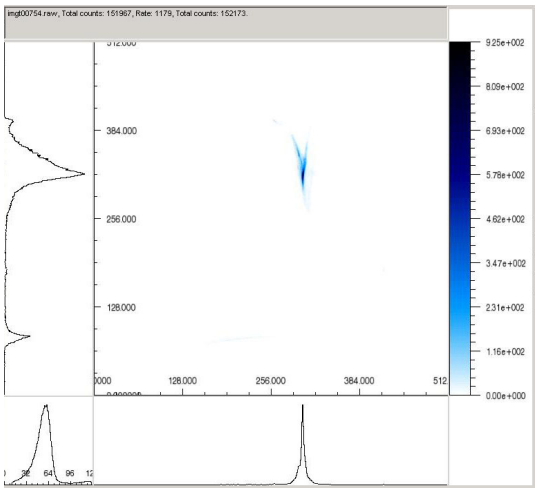

Figure 6.12: The realigned X-ray image brought into focus using the axial travel of the MCP detector.

ACTUATOR MEASUREMENTS - The piezoelectric actuators were tested prior to the FFT patterns in the hope that a change in the reflected image could be observed. An example of this initial actuator operation is shown in Figure 6.13, where a comparison is made between a 0V image and

an image obtained where the 15 actuators closest to the X-ray source are operated at 50V. In this example and several others, there was marked difference between the 0V and actuated images; this was encouraging as it highlighted the actuators' ability to manipulate the optical form of the prototype.

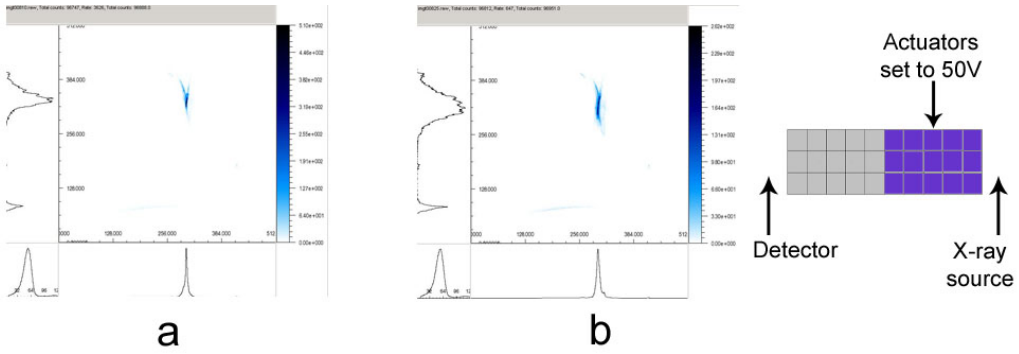

Figure 6.13: Image **a** represents the zero volts X-ray image, image **b** represents the effect of applying 50V to the 15 actuators located closest to the X-ray source while the other 15 actuators are at 0V. There is a marked difference in the form of the detected image.

6.3.3 Week 3 - Testing the optimisation routine and the development of new actuator patterns

OPTIMISATION ROUTINE - The low order distortions of the FFT patterns (Patterns 1 $\longrightarrow$ 4) were tested to determine their effect upon the detected image. However, it became apparent that they were too complex and that the detected image became decidedly worse. The FFT patterns were therefore abandoned for these tests in favour of more simple patterns where a row or column of actuators represented a single pattern. Several of these patterns were tested and their effect recorded, resulting in the development of the *local patterns*, 14 actuator patterns with a 1 (white) or 0 (black) designation, as shown in Figure 6.14. The local patterns were tested up to Pattern 5 using the optimising routine and an improvement in the full width half maximum (FWHM) of the detected image was observed.

FULL WIDTH HALF MAXIMUM - Measurements of the FWHM from each detected image provide the method in which the improvement in the image is determined. The detector software calculates the FWHM from a box that the operator draws around the image: the centre of the box provides the centre for the FWMH calculation. Figure 6.15 highlights the detector's graphical user interface. The FWHM is recorded in terms of horizontal (FWHM$_x$) and vertical (FWHM$_y$) components and the input to the optimising routine is the product of $\sqrt{FWHM_x^2 + FWHM_y^2}$.

Figure 6.14: Local patterns as developed during X-ray testing, image courtesy of CF from UoL

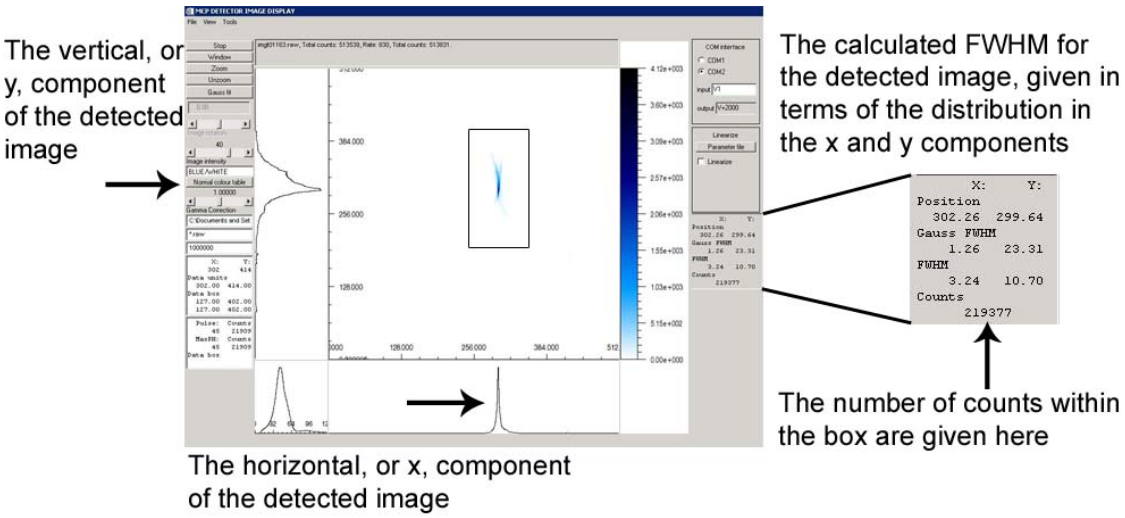

Figure 6.15: The graphical user interface of the detector control, the FWHM-input for the optimising routine is calculated from the x and y components of the image.

6.3.4 Week 4 - Prototype optimisation

OPTIMISING ROUTINE - The entire week was dedicated to optimisation of the prototype using the patterns as outlined in Figure 6.14. Due to time restrictions only 8 voltage steps were used. 5×10^5 counts were obtained for each image and this took approximately 15-20 minutes to achieve, typically 25 - 35 images were recorded each day.

ADDITIONAL DATA - Further X-ray data was taken to determine the stability of the prototype over time and the deformations within the optic caused by the actuators. The stability of the prototype is important as within a telescope system the optics could be held in a single position for several days/weeks/months at a time. To investigate the effect, the actuators were set to Pattern 16 from the FFT patterns and an image recorded every 20 minutes for 5 hours. The effect of the actuators upon the optical surface was determined by the series of zero volts images obtained during the 5 days of optimisation; these should be identical if no effect adverse effect is observed.

6.4 Data analysis

The analysed X-ray data from this section is courtesy of CHF from UoL. The majority of the results were presented within the paper by Feldman *et al.* (2009) and a thorough description is provided within the PhD thesis by Feldman (2009). The results are presented in terms of full width half maximum (FWHM) and half energy width (HEW) as both are relevant when describing the resolving capability of an optic. The distinction between the widths are outlined below for a function described by $f(x)$:

FWHM - is the width x_1 to x_2, whose points are defined as being half the of the maximum of function $f(x)$

HEW - is the width x_a to x_b, whose points are defined as containing half of the integral, between $+\infty$ and $-\infty$, of function $f(x)$.

6.4.1 Optimisation of the Prototype's form

OPTIMISATION ROUTINE - Measurements of the FWHM while obtaining X-rays images indicated an improvement from 6.931 arc-minutes to 3.438 arc-minutes. However, the data had to be linearised (compensated for in terms of pin-cushion effect) and then re-analysed within the software 'Q' [1]. Analysis of the linearised data indicated that FWHM as measured by the detector software

[1] The software 'Q' was developed by RW from UoL and was introduced in Section 2.1.3

had not provided a true representation of the width; this was an effect of the box drawn around the image where the centre of the box was assumed to be the centre of the FWHM.

The re-analysed results in terms of FWHM and HEW against the iteration number are shown in Figure 6.16. An improvement in both the HEW and FWHM was obtained: from 0V to optimised voltage the FWHM was observed to decrease from 0.786 arc-minutes to 0.686 arc-minutes and for Pattern 6 the HEW of the detected image was observed to decrease from 2.840 arc-minutes to 2.739 arc-minutes. Therefore the prototype succeeded in improving its resolution. However, the improvements were not the result of an 'optimised' prototype as determined by the routine, because the routine was correcting for erroneous values of FWHM.

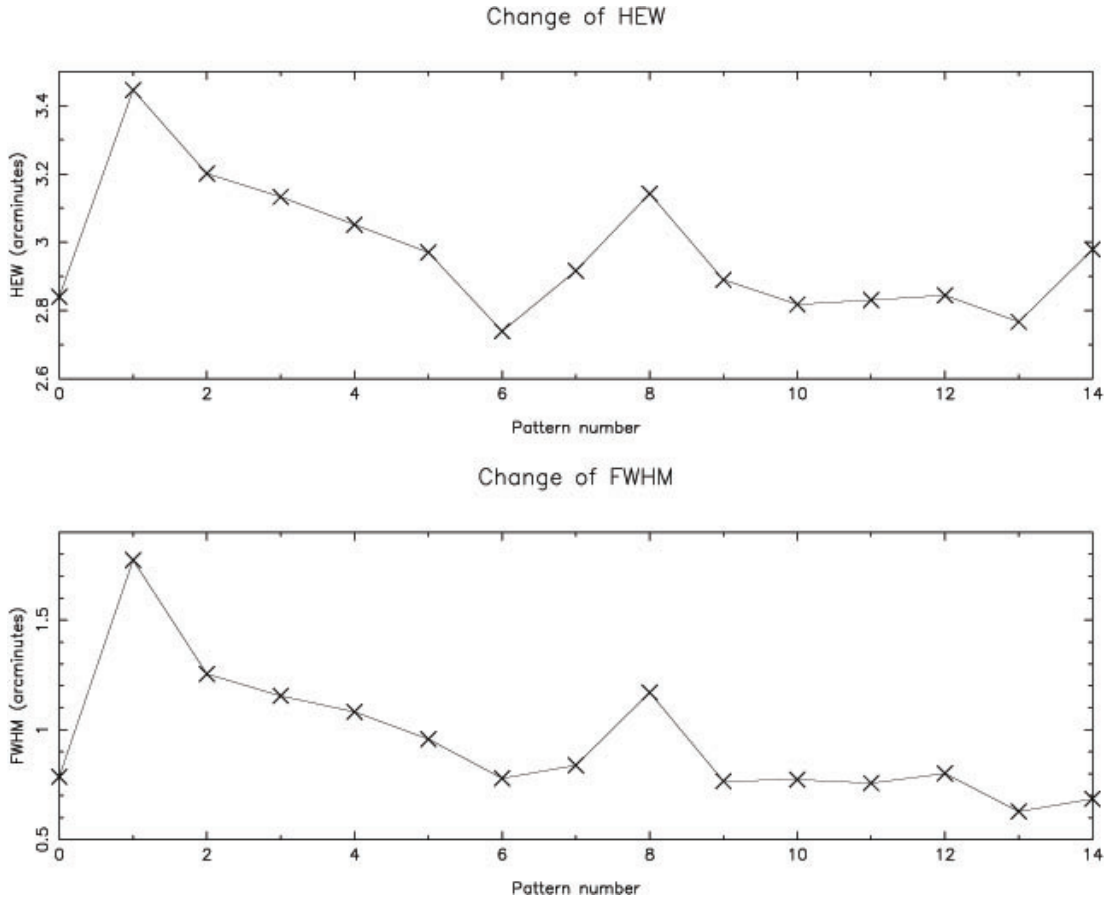

Figure 6.16: The analysis of the optimisation routine data. The half energy width (HEW) and the full width half maximum (FWHM) are shown against the iteration number of the optimisation routine, graphs provided by CHF.

LTP AND FEA DATA - In December 2008 the optimised voltage pattern (Figure 6.17) as obtained from the X-ray tests was applied to the prototype and the axial profile of the prototype measured on the long trace profiler (LTP) at the Daresbury Laboratory (DL). The profile down the

centre of the prototype was compared against a finite element simulation as is shown in Figure 6.18. The LTP trace and the FEA data highlight inter-actuator *kinks* and these are the direct effect of poorly interacting actuator influence functions. The FEA model used in simulations is the same as the model presented in Chapter 5 with a 500μm adhesive layer.

The significance of these results is that the actuators are removing the low spatial frequency errors, but are introducing high spatial frequency errors. It is thought that much of the filament structure seen in the X-ray images is a result of the inter-actuator kinks. FEA modelling suggested that the cause of these kinks was a combination of the thick adhesive layer as well as the $\sim$1mm of inter-actuator spacing; solutions to these problems will be presented in the final chapter.

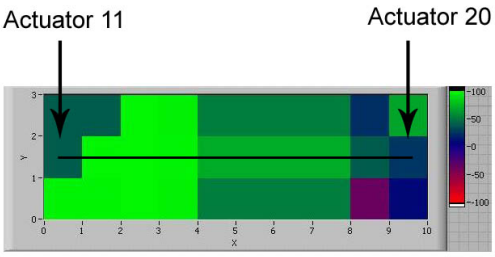

Figure 6.17: The voltage configuration of the prototype at the end of the optimisation routine. The black line indicates the trace of the LTP along the actuators. Green represents 100V and red represents -100V

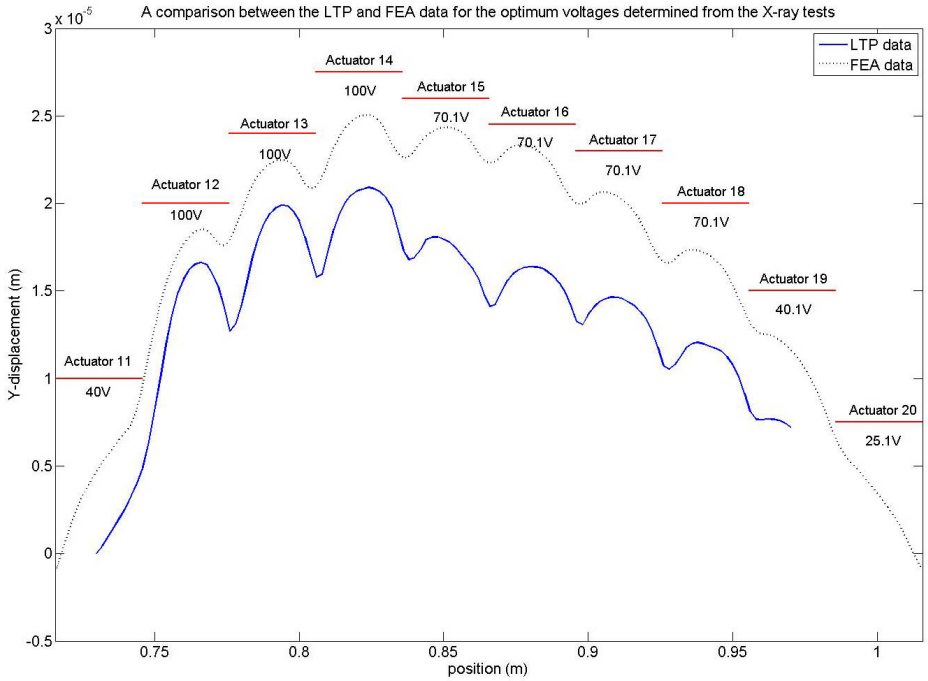

Figure 6.18: An LTP trace compared against finite element analysis data for the voltage pattern as determined by the optimising routine.

6.4.2 Prototype stability

Results from the stability of the optic over time indicate a drift in the detected image of 17.53", as shown in Figure 6.19 and this highlights that the optic was unable to maintain a constant form over the 5 hours. To rule out the effect of the high voltage amplifier in producing the drift observed, the prototype's hardware was connected to the digital oscilloscope for 5 hours and a measurement of a single channel was taken every 20 minutes, as shown in Figure 6.20. The average of the root mean square (rms) of the results over a 10 second duration indicated a voltage variation of 4.9mV; this translated to $\sim$1nm of displacement, calculated using FEA. The UoL calculated the effect of the voltage variation in terms of detected image and the results suggested a 1.29×10^{-3}" variation in the detected image over the 5 hours. Though only one channel was measured, the results from Chapter 5 implied that each channel was very similar in terms of rms voltage over the same time period. Therefore the effect observed could be caused by fluctuations within the piezoelectric material itself and this is an area of continuing study at the University of Birmingham.

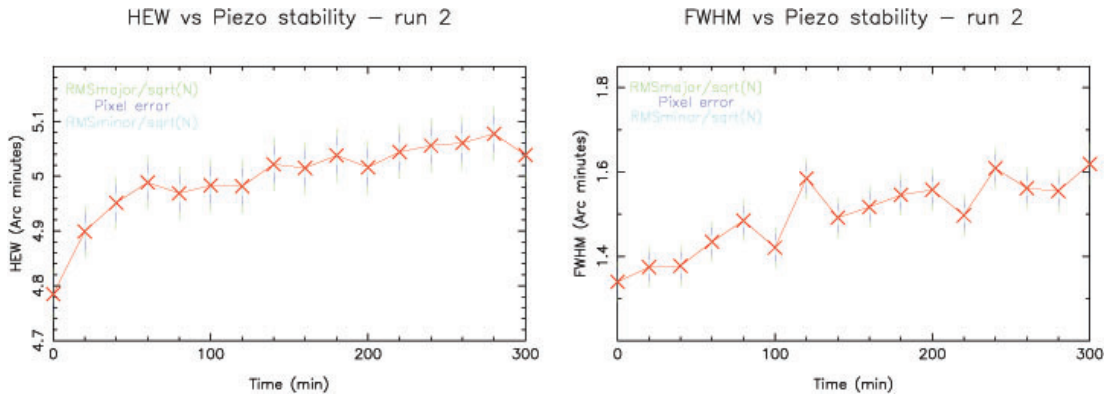

Figure 6.19: An analysis of the stability of the prototype over 5 hours given in terms of HEW and FWHM, graphs provided by CHF.

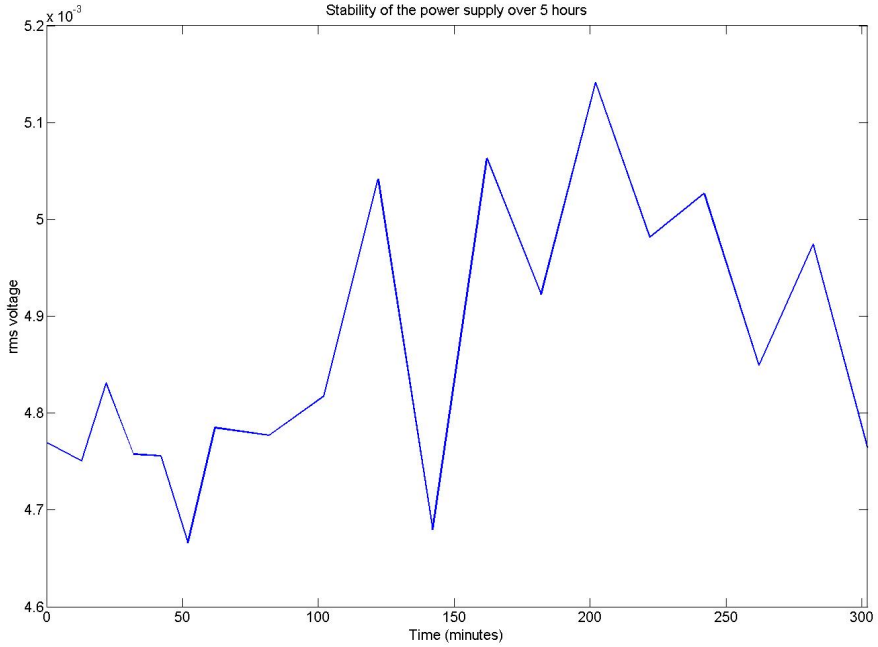

Figure 6.20: Stability of the power supply over 5 hours

6.4.3 Deformation of the optic over time

It was the intention of the actuators to provide a temporary adjustment to the optic, that is, when the applied voltage is removed that the optic returns to its original form. This quality was assessed by analysing the power on and power off zero volts images for the 5 days of the optimisation routine and the results are shown in Figure 6.21. The HEW width of the measurements decreased over time and the FWHM increased over time, therefore implying that the form of the optic had changed over the 5 days. As the prototype is unconstrained, it could have been an effect of a shift in the position of the prototype relative to the support structure. However, a linear trend is observed, therefore the effect could be from a plastic memory within the optic from the temporary influence of the actuators, or an environment effect (i.e. thermal stability) within the prototype and support structure. No definitive conclusions have be drawn and this effect will be a continued area of study in future prototypes.

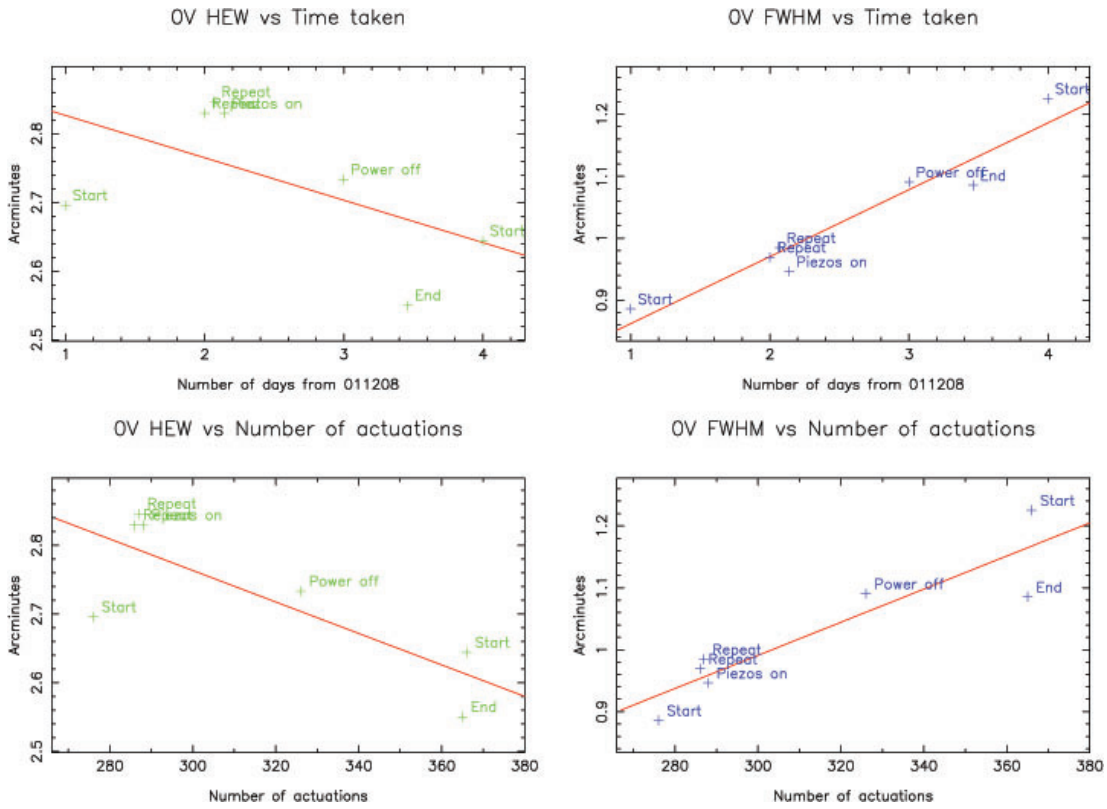

Figure 6.21: An analysis of the HEW and FWHM of the zero volts applied to the prototype during the 5 days of the X-ray optimisation. The images on the left display the variation in HEW of the prototype over number of day (top-left figure) and number of actuations (bottom-left figure). The images on the right are a FWHM representation of the HEW figures. The annotation within the figures relates to the type of zero volts measurement obtained as recorded within the log. `power off` is a zero volts image with the high voltage amplifier turned off. `Start` and `end` are zero volt images with the power on taken at the start and the end of the day respectively. `Piezos on` is identical to `Start`. Graphs provided by CHF from UoL.

6.5 Chapter summary

This chapter has outlined the X-ray testing at the University of Leicester's X-ray tunnel test facility detailing the four weeks of the X-ray testing and an analysis of the data obtained. An improvement in the resolving capability of the prototype was observed; however, not predictably. The following and final chapter provides a discussion of the prototype, the results obtained and their consequences in the design of future active X-ray prototypes.

CHAPTER 7

DISCUSSION AND FUTURE WORK

This final chapter shall review the chapters within this thesis; the ellipsoidal prototype and the X-ray results; the development of a second generation active X-ray prototype and the expansion of the technology towards an X-ray telescope system.

7.1 Chapters - review

This PhD thesis has outlined the manufacture and X-ray testing of an active X-ray prototype intended for the next generation of X-ray telescopes and the chapters are outlined below:

CHAPTER 1 - provided an introduction to the X-ray interactions with matter; X-ray optics and geometries; X-ray telescopes and the need to combine high resolution and high sensitivity and active X-ray optics within synchrotron facilities.

CHAPTER 2 - introduced the ellipsoidal and cylindrical prototypes, the role of each consortium member in the prototypes' production and finite element models of the ellipsoidal prototype.

CHAPTER 3 - described the method of electroforming in the fabrication of the prototypes' optics and presented the production of the cylindrical prototype.

CHAPTER 4 - presented the completion of the ellipsoidal prototype and its associated metrology.

CHAPTER 5 - discussed the actuator control software and the actuator influence functions compared against finite element models

CHAPTER 6 - detailed the X-ray tests at the University of Leicester; an analysis of the results and highlighted the prototype's ability to improve its imaging resolution through active control.

It was the objective of this research to demonstrate the ability of an active X-ray prototype to deform itself to achieve an improvement in angular resolution: this objective has been achieved; however, it is likely that the prototype has not been demonstrated to its full potential.

7.2 The active X-ray prototype and X-ray results - review

The X-ray testing demonstrated the ellipsoidal prototype's ability to deform its optical component to produce an improved resolution, albeit on the scale of arc-minutes. The improvements, from 0.786 arc-minutes to 0.686 arc-minutes full width half maximum (FWHM) and 2.840 arc-minutes to 2.739 arc-minutes in half energy width (HEW), were the result of the optimising routine. However, the rountine was not optimising the correct FWHM of detected images and therefore a true representation of the capability of the prototype was not obtained. The problems encountered during the test X-ray tests can be split into those relating to the prototype's design/manufacture and those encountered during the X-ray testing.

THE ELLIPSOIDAL PROTOTYPE - The majority of the problems associated with the prototype were determined via optical metrology after the completion of the prototype. The prototype's optic, and subsequent optics, were not replicated to the desired form and residual stress (compressive or tensile) has warped the optic's form from that of the mandrel's. The exact cause of the stress is difficult to establish, although contaminants within the electrolyte would be the obvious culprit; however, in electroforming some degree of stress is unavoidable. The problem of the prototype's optic's figure error was further aggravated by a lack of metrology undertaken to determine its actual form prior to actuator bonding and this was an effect of the time constraints imposed within the project.

It was not only UCL who were manufacturing to a deadline; the University of Birmingham (UoB) were also not able to measure the azimuthal curvature of each of the piezoelectric actuators prior to dispatch and as such a mismatch in the radii of curvature of the optic and actuators was inevitable. This mismatch led to excess adhesive being required to ensure that the whole surface of the actuator was in contact with the nickel optic. The excess adhesive caused an increased shrinkage effect, resulting in print-through of the actuators upon the optic's reflective surface.

The *kinking* effect as observed in Chapter 6 was not anticipated to the severity it was observed

prior to the long trace profiler (LTP) measurements. Through FEA modelling at UCL and UoB the effect is theorised to be a composite of the adhesive thickness and the inter-actuator gap. It was spectulated that much of the filament structure observed during the X-ray tests was a direct result of this inter-actuator kinking and although the prototype improved its resolution in terms of large scale distortions it introduced small scale distortions.

X-RAY TESTING - The alignment of the prototype with respect to the X-ray facility was more problematic than foreseen. The prototype was positioned upon the support structure with no constraints; this was to allow the actuators to move freely without fixed boundaries. However, pushing the prototype and support structure from the detector to the flange did cause the prototype to shift its position and it was difficult to rectify without direct access. Once positioned over the flange, coarse and fine alignment was to be achieved by the legs of the flange support and the pitch and yaw motors respectively. In reality only the adjustable legs provided a predictable improvement. The pitch and yaw motors did not operate consistently and therefore prevented an optimised alignment.

It was the detector software that prevented a true optimisation of the prototype from being obtained and this stemmed from the inaccurate calculation of the FWHM for each image. The box that was drawn around the image determined the centroid position as being the centre of the box and calculated the resultant FWHM from that point, whereas in reality the centroid position was unlikely to be in the centre of the box but at another location. The inability to determine the true FWHM for a given optical form prevented an accurate optimisation and therefore the prototype was not operated to its full potential.

7.3 Development of a second generation active X-ray prototype

The Smart X-ray Optics (SXO) project is currently in its final year of the four years of funding and it is the intention of the SXO project within the remaining time to manufacture and test a second ellipsoidal prototype, of identical dimensions, aiming to improve upon the initial results. The X-ray test date for the second active X-ray prototype is scheduled for late February 2010 and it is hoped that this second prototype will benefit from the enhancements outlined below.

ELECTROFORMS AND METROLOGY - Further optics have been, and are being, produced via nickel electroforming; optics produced in the summer of 2009 all demonstrate tensile stress and

metrology indicates that the optics are deformed in such a way as to diverge, rather than converge an incident beam. Efforts are now focussed upon removing suspected contaminants from the electrolyte and replicating optics with reduced stress to those already produced. One proposed method to improve the optics' form is to leave the optic unreleased from the mandrel and bond the actuators directly upon the reverse of the optic. It is thought that this would provide a dual solution, in that, the optic would retain the form of the mandrel during actuator bonding and that the adhesive-actuator composite would provide a rigid backing when the optic is released, therefore attenuate the effect from stress. However, problems could arise if the optic deforms significantly upon release (despite the backing) and the actuators fracture as a result. To prevent this eventuality pre-testing will be employed.

ACTUATOR BONDING AND CURVATURE MISMATCH - In addition to bonding the actuators to the optic prior to its release from the mandrel, it is proposed that the actuators will be bonded simultaneously via a vacuum chuck. The chuck would be figured to the inverse of the non-reflective side of the optic. The actuators would be positioned upon the chuck and conformed to the form of the chuck under the vacuum (Figure 7.1); this should reduce the effect of the curvature mismatch. It is proposed that vacuum will be maintained until the adhesive has cured thus preventing the movement of the actuators upon the low viscosity adhesive layer.

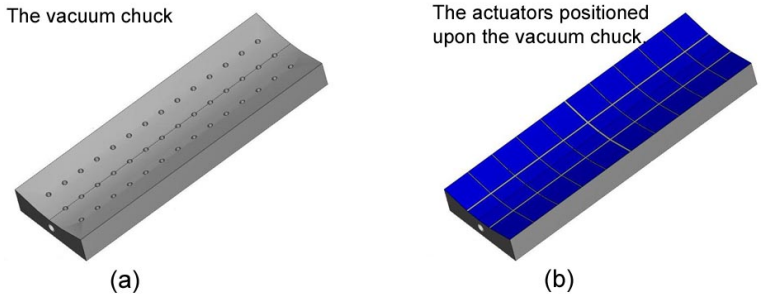

Figure 7.1: A vacuum chuck used to position actuators upon the non-reflective surface of the optic. Image **(a)** highlights the surface of the chuck which is figured to the same form as the optic, vacuum channels are then used to hold the actuator prior to bond. Image **(b)** depicts the actuator arranged upon the chuck. It is hoped that the vacuum will deform the actuators to the form of the chuck and therefore the optic, as a result improving the curvature mismatch.

ACTUATOR DIMENSIONS AND THE KINKING EFFECT - The dependence of the kinking effect upon the adhesive thickness and the inter-actuator has been demonstrated via finite element analysis in the papers Atkins *et al.* (2009*a*); Zhang *et al.* (2009*b*). Figure 7.2 is one example taken

from Atkins *et al.* (2009*a*) highlighting the effect of inter-actuator kinking as a function of prototype axial length and inter-actuator spacing. The model describes a cylindrical approximation to the ellipsoidal prototype's form and a 5 × 3 grid arrangement of actuators in the axial and azimuthal directions respectively. Within the model all the actuators are at 10V and the corners of the represented prototype are fixed in x, y and z. This model demonstrates that for decreasing size of the inter-actuator gap: the *kink* decreases. This effect is further demonstrated in the paper by Zhang *et al.* (2009*b*).

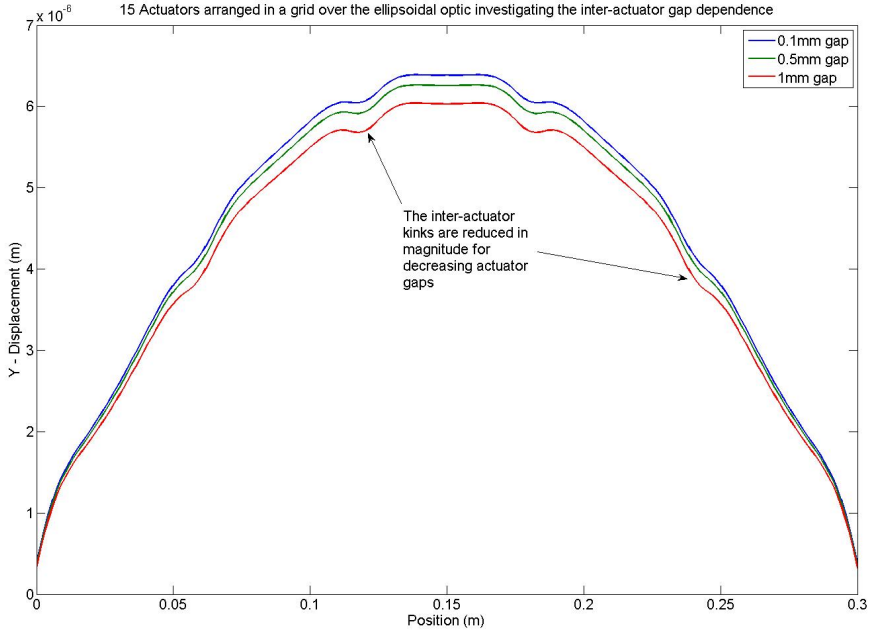

Figure 7.2: The effect of inter-actuator kinking represented as a function of prototype axial length and inter-actuator spacing.

The adhesive thickness is governed by the curvature mismatch and the glass spacing beads within the adhesive, but the inter-actuator gap can be altered by the manufacturer and minimising the gap is crucial to decreasing the inter-actuator kinks. An ideal scenario would have a single piece of piezoelectric upon the optic with sectioned electrodes and therefore all the gaps would be removed, but such an actuator cannot be fabricated within the constraints of the February 2010 test date. Nevertheless, within the time constraint concessions to the ideal scenario have be made; the second prototype will have 12 piezoelectric actuator pieces, but each actuator will have a two electrode regions that can be controlled independently (Figure 7.3).

Furthermore, the remaining inter-actuator gaps between the actuators will be minimised by

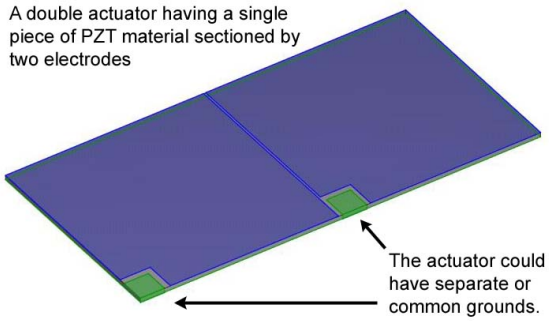

Figure 7.3: The double electrode actuator to decrease the number of inter-actuator kinks.

'butting' the actuators to one another. Care would have to be taken to prevent short-circuiting the actuators, but it should be possible to isolate the electrodes using the adhesive. To aid the process of 'butting' actuators the UoB intend to diamond/laser cut their actuators to provide an extremely sharp edge upon which to align. All remaining gaps will be filled, to ensure that the actuator layer is a smooth surface of uniform thickness.

ALIGNMENT OF THE PROTOTYPE WITHIN THE X-RAY FACILITY - Alignment errors prevented the prototype from being positioned within the facility to provide the optimum focus. To improve the initial alignment during the integration of the prototype within the X-ray facility, it is proposed that the prototype will be bonded to its support structure and therefore allowed to preserve its position relative to the tunnel. This concept could be developed further in that the support structure is bonded to the prototype while the optic is still upon the mandrel and therefore helping to preserve the optic's form.

The pitch and yaw motors of the active support structure are to be replaced. The problems generated by the motors were a result of the mechanical junction between the optic cradle and the active support structure and a poor specification of the motors' operational ability. It is hoped that a redesign of the junction between support structures and improved motors will provide the fine alignment required to optimise the prototype's position with respect to the X-ray source.

THE X-RAY DETECTOR SOFTWARE - The first X-ray testing results suffered from an inability to determine the true FWHM of the detected image. It is now proposed that the optimisation routine will be integrated within the detector software and that the detector software will determine the FWHM for the entire detector image without the need for operator intervention. These steps should provide a true optimisation of the prototype, allowing the actuators' ability to correct the optic to be thoroughly assessed.

7.4 An active X-ray telescope?

Although the current funding for the SXO project comes to an end next calendar year, it is hoped with the application of continuing-grants that the SXO consortium can proceed further in the growth of this technology. There is much scope for development of future prototypes and presented below are two of the avenues of research that could/will be followed:

A GLASS SLUMPED ACTIVE X-RAY PROTOTYPE - Working in collaboration with NASA's Goddard Space Flight Centre (GSFC) a slumped-glass variant of the nickel ellipsoidal prototype is under development. The thickness of glass and nickel are identical, but it is their differing densities which promotes glass as a favourable optic substrate: with decreased weight per effective area the sensitivity of an eventual telescope system would be increased per given weight. The GSFC have recently obtained an ellipsoidal mandrel upon which to start replicating a number of optics and with these telescope grade optics the SXO consortium hopes to achieve an improved resolution upon the scale of arc-seconds rather than arc-minutes.

NESTING THE OPTICS - Improving the angular resolution is only one goal. The second condition within the project mandate was to allow the optics to be heavily nested to increase the effective area and therefore the sensitivity. To achieve this second goal the active X-ray optics will have to be nested to increase the effective area of the system and this would provide additional validity in the use of active X-ray optics within an actual telescope system.

For this technology to find a place in future X-ray missions, such as Generation-X, it would have to demonstrate the ability to deform the optic's figure to provide a resolving capability to sub-arc-seconds. Although we are not there yet, with continuing prototype development at home and abroad, the goal of 0.1 arc-seconds could become a reality. Furthermore, there is a definite drive within the X-ray astronomical/telescope community to further this technology and this is evidenced by the technology's recent inclusion at the United States' Decadal Survey. In conclusion, despite the complexities inherent within the technology, there is a great desire to see this technology succeed and the author hopes to see its inclusion in missions to come.

Bibliography

Aschenbach, B., 1985, *Rep. Prog. Phys.*, **48**, 579

Aschenbach, B., Bruninger, H. & Kettenring, G., 1982, *Advances in Space Research*, **2**(4), 251

Atkins, C., Doel, P., Brooks, D., Thompson, S., Feldman, C., Willingale, R., Button, T., Sanmartin, D. R., Zhang, D., James, A., Theobald, C., Smith, A. D. & Wang, H., 2009*a* (SPIE), volume 7437, p. 74371H

Atkins, C., Doel, P., Brooks, D., Thompson, S., Wang, H., Feldman, C., Willingale, R., Button, T., Sanmartin, D. R., Zhang, D., James, A., Theobald, C. & Smith, A. D., 2009*b* (SPIE), volume 7360

Atkins, C., Doel, P., Yao, J., Brooks, D., Thompson, S., Willingale, R., Feldman, C., Button, T., Zhang, D. & James, A., 2007 (SPIE), volume 6721, p. 67210T
URL: *http://link.aip.org/link/?PSI/6721/67210T/1*

Atkins, C., Wang, H., Doel, P., Brooks, D., Thompson, S., Feldman, C., Willingale, R., Button, T., Rodriguez Sanmartin, D., Zhang, D., James, A. & Theobald, C., 2008, in *Society of Photo-Optical Instrumentation Engineers (SPIE) Conference Series*, volume 7011

Bowen, C. R., Stevens, R., Nelson, L. J., Dent, A. C., Dolman, G., Su, B., Button, T. W., Cain, M. G. & Stewart, M., 2006, *Smart Material Structures*, **15**, 295

Burrows, D. N., Hill, J. E., Nousek, J. A., Wells, A. A., Chincarini, G., Abbey, A. F., Beardmore, A. P., Bosworth, J., Bräuninger, H. W., Burkert, W., Campana, S., Capalbi, M., Chang, W., Citterio, O., Freyberg, M. J., Giommi, P., Hartner, G. D., Killough, R., Kittle, B., Klar, R., Mangels, C., McMeekin, M., Miles, B. J., Moretti, A., Mori, K., Morris, D. C., Mukerjee, K., Osborne, J. P., Short, A. D. T., Tagliaferri, G., Tamburelli, F., Watson, D. J., Willingale, R. & Zugger, M. E., 2004, in K. A. Flanagan & O. H. W. Siegmund (eds.), *Society of Photo-Optical Instrumentation Engineers (SPIE) Conference Series*, volume 5165, pp. 201–216

Citterio, O., Campana, S., Conconi, P., Ghigo, M., Mazzoleni, F., Poretti, E., Conti, G., Cusumano, G., Sacco, B., Braeuninger, H. W., Burkert, W., Egger, R., Castelli, C. M. & Willingale, R., 1996 (SPIE), volume 2805, pp. 56–65

COMSOL, August 2006, *COMSOL Multiphysics modelling guide* (COMSOL AB)

de Korte, P. A. J., Bleeker, J. A. M., den Boggende, A. J. F., Branduardi-Raymont, G., Brinkman, A. C., Culhane, J. L., Gronenschild, E. H. B. M., Mason, I. & McKechnie, S. P., 1981, *Space Science Reviews*, **30**, 495

Doel, P., Michette, A., Smith, A., Folkard, M. & Stevenson, T., 2006, *Proof of concept research on smart X-ray optics*, Smart X-ray Optics Consortium

Driggers, R. G., 2003, *Encyclopedia of Optical Engineering*, volume 2/3 (CRC)

Egle, W., 2000, *Innovation*, **8**, 12

Elson, J. M., Rahn, J. P. & Bennett, J. M., 1983, *Applied Optics*, **22**(20), 3207

Elvis, M., Brandt, W. N., Worrall, D., Fabbiano, G., Hornschemeier, A. & Brissenden, R., 2009, *Active galaxies and quasers*, Technical report, Harvard-Smithsonian Centre for Astrophysics **URL:** *www.cfa.harvard.edu/hea/genx/astro2010*

Feldman, C., 2009, *Smart X-ray Optics for large and small scale applications*, Ph.D. thesis, University of Leicester

Feldman, C., Willingale, R., Atkins, C., Brooks, D., Button, T., Doel, P., James, A., Sanmartin, D. R., Smith, A., Theobald, C., Thompson, S., Wang, H. & Zhang, D., 2009 (SPIE), volume 7437, p. 74371G

Feldman, C., Willingale, R., Atkins, C., Wang, H., Doel, P., Brooks, D., Thompson, S., Button, T., Zhang, D., Rodriguez Sanmartin, D., James, A. & Theorbald, C., 2008, in *Society of Photo-Optical Instrumentation Engineers (SPIE) Conference Series*, volume 7011

Fraser, G. W., 1989, *X-ray detectors in astronomy* (Cambridge University Press)

Friedman, E. & Miller, J. L., 2004, *Photonics Rules of Thumb - optics, electro-optics, fibre optics and lasers* (SPIE Press/McGraw-Hill), 2nd edition

Furuzawa, A., Ogasaka, Y., Kunieda, H., Miyazawa, T., Sakai, M., Kinoshita, Y., Makinae, Y., Sasaya, S., Kanou, Y., Niki, D., Ohgi, T., Oishi, N., Yamane, K., Yamane, N., Ishida, Y., Haba, Y., Tawara, Y., Yamashita, K., Ishida, M., Maeda, Y., Mori, H., Tamura, K., Awaki, H. & Okajima, T., 2009 (SPIE), volume 7437, p. 743709

Ghigo, M., Basso, S., Canestrari, R., Conconi, P., Citterio, O., Civitani, M., Dell'Orto, E., Gallieni, D., Pareschi, G., Parodi, G., Proserpio, L. & Spiga, D., 2009 (SPIE), volume 7437, p. 74370P

Giacconi, R., Branduardi, G., Briel, U., Epstein, A., Fabricant, D., Feigelson, E., Forman, W., Gorenstein, P., Grindlay, J., Gursky, H., Harnden, F. R., Henry, J. P., Jones, C., Kellogg, E., Koch, D., Murray, S., Schreier, E., Seward, F., Tananbaum, H., Topka, K., Speybroeck, L. V., Holt, S. S., Becker, R. H., Boldt, E. A., Serlemitsos, P. J., Clark, G., Canizares, C., Market, T., Novick, R., Helfand, D. & Long, K., 1979, *Astrophysical Journal*, **230**, 540

Glindermann, A., Hippler, S., Berkefeld, T. & Hackenberg, W., 2000, *Experimental Astronomy*, **10**, 5

Gubarev, M., Ramsey, B. & Arnold, W., 2009, in *Society of Photo-Optical Instrumentation Engineers (SPIE) Conference Series*, volume 7360

Gubarev, M., Ramsey, B., Engelhaupt, D., Speegle, C. & Smithers, M., 2005, in L. Assoufid, P. Z. Takacs & J. S. Taylor (eds.), *Advances in Metrology for X-Ray and EUV Optics. Edited by Assoufid, Lahsen; Takacs, Peter Z.; Taylor, John S. Proceedings of the SPIE, Volume 5921, pp. 55-62 (2005).*, volume 5921, pp. 55–62

Hart, A. C., 2000, *Working manual for setting up and operating a conventional nickel sulphamate process*, Hart Coating Technology/Nickel development institute

Hecht, E., 2002, *Optics* (Addison Wesley), 4th edition

Howells, M. R., Cambie, D., Duarte, R. M., Irick, S., MacDowell, A. A., Padmore, H. A., Renner, T. R., Rah, S. & Sandler, R., 2000, *Opt. Eng.*, **39**(10), 2748

Inoue, H., 1993, *Experimental Astronomy*, **4**, 1

Jansen, F., Lumb, D., Altieri, B., Clavel, J., Ehle, M., Erd, C., Gabriel, C., Guainazzi, M., Gondoin, P., Much, R., Munoz, R., Santos, M., Schartel, N., Texier, D. & Vacanti, G., 2001, *Astronomy and Astrophysics*, **365**, L1

Kim, I. & Mentone, P. F., 2006, *Electrochimica Acta*, **52**, 1805

Kirkpatrick, P. & Baez, A. V., 1948, *J. Opt. Soc. Am.*, **38**(9), 766

Koglin, J. E., An, H., Blaedel, K. L., Brejnholt, N. F., Christensen, F. E., Craig, W. W., Decker, T. A., Hailey, C. J., Hale, L. C., Harrison, F. A., Jensen, C. P., Madsen, K. K., Mori, K., Pivovaroff, M. J., Tajiri, G. & Zhang, W. W., 2009 (SPIE), volume 7437, p. 74370C

Lehmer, B., Brandt, N., Alexander, D., Brissenden, R., Elvis, M., Hornschemeier, A., Schwartz, D. & the Generation-X Team, 2009, *The Formation and Growth of the First Black Holes*, Technical report, University of Durham
URL: *www.cfa.harvard.edu/hea/genx/astro2010*

Lowenheim, F. A., 1974, *Modern Electroplating* (John Wiley), third edition edition

Martindale, A., Pearson, J. F., Fraser, G. W., Carpenter, J. D., Willingale, R., Stevenson, T., Whitford, C., Giannini, F., Fairbend, R., Seguy, J., Sclater, E., Delgado, I., Kaipiainen, M., Nenonen, S., Pilvi, T., Schyns, E., Bulloch, C., Sawyers, C. & Muinonen, K., 2009 (SPIE), volume 7441, p. 744117

Michette, A., Button, T., Dunare, C., Feldman, C., Folkard, M., Hart, D., McFaul, C., Morrison, G. R., Parkes, W., Pfauntsch, S., Powell, A. K., Rodriguez-Sanmartin, D., Sahraei, S., Stevenson, T., Vojnovic, B., Willingale, R. & Zhang, D., 2007, in *Advances in X-Ray/EUV Optics and Components II. Proceedings of the SPIE, Volume 6705, pp. 670502 (2007).*

Michette, A. G. & Buckley, C. J. (eds.), 1993, *X-ray science and technology* (Institue of Physics)

Pareschi, G., Attinà, P., Basso, S., Borghi, G., Burkert, W., Buzzi, R., Citterio, O., Civitani, M., Conconi, P., Cotroneo, V., Cusumano, G., Dell'Orto, E., Freyberg, M., Hartner, G. D., Gorenstein, P., Mattaini, E., Mazzoleni, F., Parodi, G., Romaine, S., Spiga, D., Tagliaferri, G., Valtolina, R., Valsecchi, G. & Vernani, D., 2008, in *Society of Photo-Optical Instrumentation Engineers (SPIE) Conference Series*, volume 7011

Pareschi, G., Basso, S., Citterio, O., Ghigo, M., Mazzoleni, F., Spiga, D., Burkert, W., Freyberg, M., Hartner, G. D., Conti, G., Mattaini, E., Grisoni, G., Valsecchi, G., Negri, B., Parodi, G., Marzorati, A. & dell'Acqua, P., 2005, in O. Citterio & S. L. O'Dell (eds.), *Optics for EUV, X-Ray, and Gamma-Ray Astronomy II. Proceedings of the SPIE, Volume 5900, pp. 47-58 (2005).*, volume 5900, pp. 47–58

Poizat, C. & Benjeddou, A., 2006, *Computers and Structures*, **84**, 1426

Rajan, N. & Cash, W., 2005 (SPIE), volume 5900, p. 59001F

Ramsey, B. D., 2005, *Exp Astron*, (20), 85

Reid, P. B., Murray, S. S., Trolier-McKinstry, S., Freeman, M., Juda, M., Podgorski, W., Ramsey, B. & Schwartz, D., 2008, in *Society of Photo-Optical Instrumentation Engineers (SPIE) Conference Series*, volume 7011

Riekerink, M. B. O., Lansdorp, B., de Vreede, L. J., Blom, M. T., van t'Oever, R., Ackermann, M. D., Collon, M. J., Wallace, K. & Bavdaz, M., 2009, in *Optics for EUV, X-Ray, and Gamma-Ray Astronomy IV*

Schwartz, D. A., Brissenden, R. J., Elvis, M., Fabbiano, G., Gaetz, T. J., Jerius, D., Juda, M., Reid, P. B., Wolk, S. J., O'Dell, S. L., Kolodziejczak, J. K. & Zhang, W. W., 2008, in *Society of Photo-Optical Instrumentation Engineers (SPIE) Conference Series*, volume 7011

Serway, R. A. & Beicher, R. J., 2000, *Physics for scientists and engineers with modern physics* (Harcourt College Publishers), 5th edition

Shklovsky, I. S., 1967, *The Astrophysical Journal Letters*, **148**, L1+

Signorato, R., Hignette, O. & Goulon, J., 1998, *Journal of Synchrotron Radiation*, **5**, 797

Signorato, R. & Ishikawa, T., 2001, *Nuclear Instruments and Methods in Physics Research*, **Section A**(467-468), 271

Sirohi, J. & Chopra, I., 2001, *Journal of Intelligent Material Systems and Structures*, **11**, 246

Skinner, G. K., Arzoumanian, Z., Cash, W. C., Gehrels, N., Gendreau, K. C., Gorenstein, P., Krizmanic, J. F., Miller, M. C., Phillips, J. D., Reasenberg, R. D., Reynolds, C. S., Sambruna, R. M., Streitmatter, R. E. & Windt, D. L., 2008 (SPIE), volume 7011, p. 70110T

Slane, P., Reynolds, S. P., Soderberg, A., Hughes, J. P., Vink, J., Ho, W., Patnaude, D., Pooley, D., Petre, R., Park, S., Badenes, C., Smith, R. & Brissenden, R., 2009, *Supernovae and their consequences: studies with the Generation-X mission*, Technical report, Harvard-Smithsonian Centre for Astrophysics
URL: *www.cfa.harvard.edu/hea/genx/astro2010*

Stein, B., 1996, in *AESF Electroforming Symposium*, AESF
URL: *http://www.finishing.com/Library/stein/strspaper.html*

Stockman, Y., Hansen, H., Houbrechts, Y., Tock, J. P., de Chambure, D. & Gondoin, P., 1999 (SPIE), volume 3739, pp. 298–309

Tan, Y.-J. & Lim, K., 22 April 2003, *Surface and Coatings Technology*, **167**, 255
URL: *http://www.ingentaconnect.com/content/els/02578972/2003/00000167/00000002/art00916*

Thompson, S. J., Brooks, D. & Doel, A. P., 2008, *Opt. Express*, **16**(2), 1321
URL: *http://www.opticsexpress.org/abstract.cfm?URI=oe-16-2-1321*

Thompson, S. J., Doel, A. P., Brooks, D. & Strangwood, M., 2008, in *Society of Photo-Optical Instrumentation Engineers (SPIE) Conference Series*, volume 7018

Wallace, K., Bavdaz, M., Gondoin, P., Collon, M. J., Günther, R., Ackermann, M., Beijersbergen, M. W., Riekerink, M. O., Blom, M. T., Lansdorp, B. & de Vreede, L. J., 2009, in *Optics for EUV, X-Ray, and Gamma-Ray Astronomy IV*

Weisskopf, M. C., 2003, *Advances in Space Research*, **32**, 2005

Weisskopf, M. C. & O'Dell, S. L., 1997 (SPIE), volume 3113, pp. 2–17

Willingale, R., 1999, *LNP*, **520**, 435

Willingale, R. & Spaan, F. H., 2009 (SPIE), volume 7437, p. 74370B

Windhorst, R. A., Cameron, R. A., Brissenden, R. J., Elvis, M. S., Fabbiano, G., Gorenstein, P., Reid, P. B., Schwartz, D. A., Bautz, M. W., Figueroa-Feliciano, E., Petre, R., White, N. E. & Zhang, W. W., 2006, *New Astronomy Review*, **50**, 121

Wolk, S., Brickhouse, N., Brissenden, R., Drake, J., Dupree, A., Elvis, M., Evans, N., Fabbiano, G., Feigelson, E., Gagné, M., Güdel, M., Kashyap, V., Linsky, J., Osten, R., Rosner, R., Smith, R., Townsley, L., Walter, F. & Wargelin, B., 2009, *X-ray studies of stars and planets with ultrahigh sensitivity and resolution*, Technical report, Harvard-Smithsonian Centre for Astrophysics
URL: *www.cfa.harvard.edu/hea/genx/astro2010*

Wolk, S. J., Brissenden, R. J., Elvis, M., Fabbiano, G., Hornschemeier, A. E., O'Dell, S. L., Bautz, M. W., Schwartz, D. A. & Juda, M., 2008, in *Society of Photo-Optical Instrumentation Engineers (SPIE) Conference Series*, volume 7011

Wolter, H., 1952, *Annalen der Physik*, **445**, 94

Yang, H. & Kang, S.-W., May 2000, *International Journal of Machine Tools and Manufacture*, **40**, 1065
URL: *http://www.ingentaconnect.com/content/els/08906955/2000/00000040/00000007/art00107*

Yang, J.-M., Kim, D.-H., Zhu, D. & Wang, K., 2008, *International Journal of Machine Tools and Manufacture*, **48**, 329

Zeilik, M. & Gregory, S. A., 1998, *Introductory astronomy and astrophysics* (Brooks/Cole), 4th edition

Zezas, A., Hornschemeier, A., Fabbiano, G., Brissenden, R., Elvis, M., Gallagher, J., Jenkins, L., Kalogera, V., Lehmer, B., Ptak, A., Strickland, D., Ward, M. & the Generation-X Team, 2009, *Accreting binary populations and ISM evolution in galaxies*, Technical report, Harvard-Smithsonian Centre for Astrophysics
URL: *www.cfa.harvard.edu/hea/genx/astro2010*

Zhang, D., Rodriguez-Sanmartin, D., Button, T. W., Atkins, C., Brooks, D., Doel, P., Dunare, C., Feldman, C., James, A., Michette, A., Parkes, W., Pfauntsch, S., Sahraei, S., Stevenson, T., Wang, H. & Willingale, R., 2009*a*, *Journal of Electroceramics*

Zhang, D., Sanmartin, D. R., Button, T. W., Meggs, C., Atkins, C., Doel, P., Brooks, D., Feldman, C., Willingale, R., Michette, A., Pfauntsch, S., Sahraei, S., James, A., Dunare, C., Stevenson, T., Parkes, W., Smith, A. & Wang, H., 2009*b* (SPIE), volume 7448, p. 744807

Zhang, W. W., 2009 (SPIE), volume 7437, p. 74370N

Zhang, W. W., J. Bolognese, G. B., Chan, K. W., Content, D. A., Hadjimichael, T. J., Hewitt, C., Hill, M. D., Hong, M., Lehan, J. P., Lozipone, L., Mazzarella, J. M., McClelland, R., Nguyen, D. T., Olsen, L., Petre, R., Robinson, D., Rohrbach, S. O., Russell, R., Saha, T. T., Sharp, M., Gubarev, M. V., Jones, W. D., O'Dell, S. L., Davis, W., Cladwell, D. R., Freeman, M., Podgorski, W. & Reid, P. B., 2009*c*, in *EUV and X-ray Optics: Synergy between Laboratory and Space*, SPIE

Zombeck, M. V., 2007, *Handbook of Space Astronomy and Astrophysics* (Cambridge University Press), 3rd edition

Zumdahl, S. S., 1989, *Chemistry* (D.C. Heath and Company), 2nd edition

LIST OF PUBLICATIONS

1. **Atkins. C.**, Wang. H., Doel, P., Brooks, D., Thompson, S., Feldman, C., Willingale, R., Zhang, D., Rodriguez Sanmartin, D., Button, T., James, A., Theobald, C. and Willis, G., "Active X-ray mirror developement for the next generation of X-ray space telescopes", 2009 in preparation.

2. **Carolyn Atkins**, Peter Doel, Hongchang Wang, David Brooks, Samantha Thompson, Charlotte Feldman, Richard Willingale, Tim Button, Daniel Rodriguez Sanmartin, Dou Zhang, Ady James, Craig Theobald, and Andrew D. Smith, "Advances in active X-ray telescope technologies", *Proc. of SPIE* 7437, 2009

3. Charlotte Feldman, Richard Willingale, **Carolyn Atkins**, Peter Doel, Hongchang Wang, David Brooks, Samantha Thompson, Tim Button, Daniel Rodriguez Sanmartin, Dou Zhang, Ady James, Craig Theobald, and Andrew D. Smith, "Advances in active X-ray telescope technologies", *Proc. of SPIE* 7437, 2009

4. Dou Zhang, Daniel Rodriguez-Sanmartin, Tim W. Button, Carl Meggs, **Carolyn Atkins**, Hongchang Wang, Peter Doel, David Brooks, Charlotte H. Feldman, Richard Willingale, Alan G. Michette, Slawka J. Pfauntsch, Shahin Sahraei, Ady James, Camelia Dunare, Tom Stevenson, William Parkes and Andrew D. Smith, "The fabrication and characterisation of piezoelectric actuators for active x-ray optics ", *Proc. of SPIE* 7448, 2009

5. Daniel Rodriguez-Sanmartin, Dou Zhang, Tim W. Button, Alan G. Michette, **Carolyn Atkins**, David Brooks, Camelia Dunare, Peter Doel, Charlotte H. Feldman, Ady James, Slawka J. Pfauntsch, William Parkes, Tom Stevenson, Andrew D. Smith, Shahin Sahraei,

Hongchang Wang, Richard Willingale, "The fabrication and characterisation of piezoelectric actuators for active x-ray optics", *Proc. of SPIE* 7448, 2009

6. **Carolyn Atkins**, Hongchang Wang, Peter Doel, David Brooks, Samantha Thompson, Charlotte Feldman, Richard Willingale, Tim Button, Daniel Rodriguez Sanmartin, Dou Zhang, Ady James, Craig Theobald, Graham Willis, and Andrew D. Smith, "Active x-ray optics for the next generation of x-ray telescopes", *Proc. of SPIE* 7360, 2009

7. Zhang, D., Rodriguez Sanmartin, D., Button, T., **Atkins, C.**, Doel, P., Dunare, C., Feldman, C., James, A., Michette, A., Parkes, W., Pfauntsch, S., Sahraei, S., Stevenson, T. Wang, H., Willingale, R.,, "Development of Piezoelectric Actuators for Active X-ray Optics", *Proc. of Electroceramics XI*, 2009.

8. **Carolyn Atkins**, Hongchang Wang, Peter Doel, David Brooks, Samantha Thompson, Charlotte Feldman, Richard Willingale, Tim Button, Daniel Rodriguez Sanmartin, Dou Zhang, Ady James, Craig Theobald "Future high resolution X-ray telescope technologies: prototype fabrication and finite element analysis", *Proc. of SPIE* 7011, 2008

9. Charlotte Feldman, Richard Willingale, **Carolyn Atkins**, Hongchang Wang, Peter Doel, David Brooks, Samantha Thompson, Tim Button, Dou Zhang, Daniel Rodriguez Sanmartin, Ady James, Craig Theobald, "Development of thin shell adaptive optics for high angular resolution X-ray telescopes", *Proc. of SPIE* 7011, 2008

10. Peter Doel, **Carolyn Atkins**, Samantha Thompson, David Brooks, Jun Yao, Charlotte Feldman, Richard Willingale, Tim Button, Dou Zhang and Ady James,"Large thin adaptive X-ray mirrors", *Proc. of SPIE* 6705, 2007

11. **Carolyn Atkins**, Peter Doel, Jun Yao, David Brooks, Samantha Thompson, Richard Willingale, Charlotte Feldman, Tim Button, Dou Zhang and Ady James, "Active X-ray mirror development at UCL: preliminary results", *Proc. of SPIE* 6721, 2007

ACKNOWLEDGEMENTS

I have discovered, like many others before me, that a PhD is by no means an individual pursuit. It requires academic guidance, perseverance, shoulders to cry on and most importantly cake! In the closing credits of this thesis, I would like to acknowledge the following:

First, my supervisor, Peter Doel, who introduced me to the world of active X-ray optics, gave me freedom to pursue my own interests and allowed me, often begrudgingly, to go on so many research trips. Second, my fabulous second supervisor Sam, who has patiently introduced me to FEA, read through many papers (and thesis) and was always prepared to listen to my woes. To David Brooks, without whom I would never have figured out the workings of an interferometer (plus every other piece of laboratory equipment) or that the simplest method is usually the best. Pola, without whose help the prototype would never have been operational and for always having a big smile on his face. To Jim and the guys in the MAPS workshop, for always manufacturing just the right part from the worse possible sketch. A thank you also goes to the members of the SXO consortium, for providing guidance and especially biscuits throughout this project. In addition the author would also like to acknowledge Tony Gee and Tony Hart for many useful consultations.

Sticking with the academic theme, I would like to acknowledge my A-level teachers, in particular: Mr Darlington, Miss Patterson and Mr Roberts, without whom I would not have made it to UCL and be where I am today. To Diane Smeed, whose patient reading of this thesis and introducing the author to the concept of grammar has infinitely improved this thesis. Thank you.

To the veterans of G15. First, the intrepid explorer Mich, for listening to my random rants, helping to initiate the OSL journal club and for flawless interpretation of Holly's commands. To the G15 class of '09: Manda, for many lunch time adventures; Bethan for shared appreciation of peanut butter cups and Shaun, my thesis writing comrade, for a sympathetic ear these past two months and many musical interludes.

At this point I offer an apology to all my friends, in particular the Astro&Physics Crew, who I have neglected over the past months to complete this thesis. Special thanks goes to Mark Shearsby, for putting a roof over my head last summer. To my housemates: Alison, Florian, Tom, James and the International Woman of Mystery who have made the past 7 years in London unforgettable.

To my partners in crime: Ms Dolphin, Ms Jarvis and Ms Pownall, frankly you guys rock! You have made made me cry with laughter on so many occasions and have always endured my madness with a smile on your face (probably due to all that hazard pay you get). To the ever fabulous Ms Bowman, for always being on the end of a letter/phone/text/email etc. and making me appreciate life outside my little bubble.

Finally, my family. To my brothers for always making me laugh and being more crazy than I am. To my mother, for love, support and enduring my impromptu road trips. Finally, my father, who has always supported me, placed a roof over my head, made me dinner, put petrol in the car, but most importantly for providing encouragement in all my scientific endeavours.